Fast Luminosity Monitoring Using Diamond Sensors for SuperKEKB

Dima El Khechen

Dima El Khechen. Fast Luminosity Monitoring Using Diamond Sensors for SuperKEKB. High Energy Physics - Experiment [hep-ex]. Université Paris Saclay (COmUE), 2016. English. NNT : 2016SACLS565 . tel-01522803

NNT : 2016SACLS565

THÈSE DE DOCTORAT
DE
L'UNIVERSITÉ PARIS-SACLAY
PRÉPARÉE À
L'UNIVERSITÉ PARIS-SUD

ECOLE DOCTORALE N° 576
Particules, Hadrons, Energie, Noyau,
Instrumentation, Imagerie, Cosmos et Simulation
(PHENIICS)

Spécialité : Physique des accélérateurs

Par

Mlle Dima EL KHECHEN

Fast Luminosity Monitoring Using Diamond Sensors For SuperKEKB

Thèse présentée et soutenue au LAL, le 16 Décembre 2016 :

Composition du Jury :

M. Stocchi Achille	Directeur, LAL, Orsay	Président
M. Baudot Jérome	Professeur, Université de Strasbourg	Rapporteur
M. De Conto Jean-Marie	Professeur, Université de Grenoble	Rapporteur
M. Funakoshi Yoshihiro	Professeur, KEK/Sokendai university	Examinateur
M. Uehara Sadaharu	Professeur Associé, KEK/Sokendai university	Examinateur
Mme Boscolo Manuela	Physicienne, INFN/Frascati	Examinatrice
M. Bambade Philip	Directeur de recherche, LAL, Orsay	Directeur de thèse
Mme Rimbault Cécile	Chargée de recherche, LAL, Orsay	Co-encadrante de thèse

Laboratoire de l'Accélérateur Linéaire LAL 16-246

université
PARIS-SACLAY

ÉCOLE DOCTORALE
PHENIICS

Titre: Monitorage rapide de la luminosité au moyen de capteurs diamant pour SuperKEKB

Mots clés: monitorage rapide de la luminosité, capteur diamant, Bhabha radiatif, collisionneur à très haute luminosité.

Résumé: SuperKEKB est un collisionneur à très haute luminosité construit pour l'expérience Belle II, constitué d' un anneau de basse énergie (LER) transportant des positrons de 4 GeV et d'un anneau de haute énergie (HER) où circulent des électrons de 7 GeV. Sa mise en service -ou commissioning- se déroulera en trois phases : La phase 1, durant laquelle des faisceaux circulent sans être focalisés au point de collision, a pour but de nettoyer la chambre à vide du gaz résiduel. La seconde phase, où le détecteur Belle II sera en partie installé, permettra le réglage du système de focalisation finale des faisceaux, jusqu'à atteindre une luminosité de 10^{34} cm^{-2} s^{-1} . La troisième phase correspondra au démarrage de l'expérience Belle II avec une luminosité visée de 10^{35} $\mathrm{cm}^{-2}\mathrm{s}^{1}$ à 8×10^{35} cm^{-2} s^{-1}.

Dans ce cadre, ma thèse porte sur la conception et la mise en place d'un système permettant le monitorage rapide de la luminosité, système nécessaire pour pouvoir corriger en temps réel les instabilités des faisceaux et ainsi maintenir une luminosité optimale. Afin d'atteindre la haute précision relative souhaitée, de l'ordre de 10^{-3} en 1 ms, la mesure sera basée sur le taux de comptage des particules issues de la diffusion Bhabha radiative à angle nul, processus bien connu et dont la section efficace est importante. Ces particules seront détectées au moyen d'un capteur en diamant, matériau résistant aux radiations et permettant une acquisition très rapide du signal, situé à l'extérieur de la chambre à vide et en aval du point d'interaction.

La première partie de cette thèse est consacrée à la recherche des localisations optimales pour le positionnement des capteurs diamants dans chacun des deux anneaux. Au moyen de simulations détaillées, nous avons étudié la dynamique des particules Bhabha lors de leur transport dans les anneaux ainsi que leur interaction avec la matière de la chambre à vide. Ces études ont permis d' une part d' identifier un emplacement à 11.9m dans le LER et un autre à 30 m dans le HER, et d'autre part de redéfinir pour l'une d' entre elle la géométrie locale du tube à vide.

La seconde partie, plus expérimentale, s'articule autour de la première phase du commissioning de SuperKEKB et des mesures réalisées au moyen des capteurs diamants que nous avons installés. Dans un premier temps, une étude détaillée des processus de perte single beam (Bremsstrahlung, effet Touschek, diffusion coulombienne) a été réalisée pour le LER en fonction des paramètres du faisceau et du collisionneur (courant, pression, taille transverse des faisceaux). Dans un deuxième temps les résultats de cette étude ont été comparés aux données que nous avons prises de février à juin 2016. Nous avons pu mettre en évidence un bon accord qualitatif et quantitatif entre nos simulations et nos mesures. Cela nous a permis d'estimer que le niveau de bruit de fond attendu dans le cadre des mesures pour le monitorage de la luminosité sera de plus de deux ordres de grandeurs inférieurs au taux du processus Bhabha radiatif à angle nul.

université
PARIS-SACLAY
ÉCOLE DOCTORALE
PHENIICS

Title: Fast luminosity monitoring using diamond sensors for SuperKEKB

Keywords: fast luminosity monitoring, diamond sensors, radiative Bhabha scattering, very high luminosity collider.

Abstract: SuperKEKB is a very high luminosity collider dedicated to the Belle II experiment, it consists of a Low Energy Ring (LER) of 4 GeV positrons and a High Energy Ring (HER) of 7 GeV electrons. The commissioning of this machine is split into three phases: phase 1 (single-beam phase) is dedicated to vacuum scrubbing, where beams circulate without focusing at the collision point. Phase 2, for which the major part of the Belle II detector will be installed, will enable the tuning of the final focus system to achieve a luminosity of 10^{34} cm^{-2} s^{-1} . During phase 3, Belle II physics runs will start with an aimed luminosity up to 8×10^{35} cm^{-2} s^{-1} .

In this context, the aim of my thesis is to develop and install a fast luminosity monitoring system, which is required for online correction of beam instabilities and maintenance of optimal luminosity. To reach the aimed relative precision of 10^{-3} in 1 ms, the measurement will be based on the radiative Bhabha process at zero photon scattering angle, whose cross-section is large and well-known. These particles will be detected using diamond sensors, resistant to radiation and enabling very fast signal acquisition, to be placed outside of the beam-pipe and downstream of the interaction point.

The first part of this work is dedicated to the investigation of the best locations for the diamond sensor positioning in both rings. Using detailed simulations, we studied the dynamics of Bhabha particles during their tracking in the rings and their interaction with the beam pipe material. This led to the identification of two positions, at 11.9 m in LER and at 30 m in HER, and to considering a new geometry for the vacuum pipe in the LER.

The second part is related to the phase 1 of the SuperKEKB commissioning and concerns the measurements performed with the diamond sensors that were installed. Single beam loss processes (Bremsstrahlung, Touschek, beam-gas Coulomb scattering) were studied in detail with respect to the LER beam and ring parameters (current, pressure, transverse beam sizes). The results of this study were then compared to the data collected from February to June 2016. We found good qualitative and quantitative agreement between our simulations and measurements. From this we could estimate that the level of background to be expected during luminosity monitoring will be two orders of magnitude smaller than the rate of the radiative Bhabha scattering signal.

Université Paris-Saclay
Espace Technologique / Immeuble Discovery
Route de l'Orme aux Merisiers RD 128 / 91190 Saint-Aubin, France

Monitorage rapide de la luminosité au moyen de capteurs diamant pour SuperKEKB

Introduction:

SuperKEKB est un collisionneur à très haute luminosité construit pour l'expérience Belle II, constitué d'un anneau de basse énergie (LER) transportant des positrons de 4 GeV et d'un anneau de haute énergie (HER) où circulent des électrons de 7 GeV. Sa mise en service -ou commissioning- se déroulera en trois phases : La phase 1, durant laquelle des faisceaux circulent sans être focalisés au point de collision, a pour but de nettoyer la chambre à vide du gaz résiduel. La seconde phase, où le détecteur Belle II sera en partie installé, permettra le réglage du système de focalisation finale des faisceaux, jusqu'à atteindre une luminosité de 10^{34} $cm^{-2}s^{-1}$. La troisième phase correspondra au démarrage de l'expérience Belle II avec une luminosité visée de 10^{35} cm^{-2} s^{-1} à 8×10^{35} cm^{-2} s^{-1}.

SuperKEKB a adopté le schéma de collision "nano-beam" qui implique une focalisation très forte au point d'interaction (IP) pour obtenir des faisceaux de très petites tailles verticales. Parce que la taille des faisceaux est de quelques dizaines de nanomètres seulement, la luminosité est très sensible à la stabilité des éléments de focalisation finale dont les vibrations provoquent un mouvement d'orbite qui pourrait être 4 ou 5 fois plus grand que la taille verticale des faisceaux. De telles vibrations provoquent des oscillations verticales du faisceau à l'IP à des fréquences allant jusqu'à 100 Hz, alors que les mouvements horizontaux sont attendus à quelques Hz. Les différences d'orbite des deux faisceaux à l'IP conduisent à une dégradation de la luminosité. Pour parer à cela, un système de «dithering» est dédié à la rétroaction (feedback) horizontale consistant principalement en un lock-in amplificateur, des bobines de dithering et un moniteur rapide de luminosité. Le moniteur rapide de luminosité se compose de deux différents détecteurs, des capteurs monocristallin en diamant (sCVD) utilisés par notre groupe au LAL, et les détecteurs Cherenkov et scintillateur en coïncidence utilisés par groupe Zero Degree Luminosity Monitor (ZDLM) au KEK. Le moniteur de luminosité mesure la luminosité relative à 1 KHz et les corrections de feedback sont appliquées à l'échelle d'une seconde. Les deux détecteurs sont placés l'un à côté de l'autre, juste à l'extérieur du tube à vide dans les deux anneaux de SuperKEKB, et mesureront le signal du processus de Bhabha radiatif à angle nul. La précision relative requise sur la luminosité en phase 3 est de 10^{-3}, avec moins de 1% de contamination par des bruits de fond.

Les positions des capteurs dans le LER et le HER:

Le choix des emplacements des capteurs dans chacun des anneaux a nécessité plusieurs étapes, de la génération des particules Bhabha et de leur dynamique (au moyen de GUINEAPIG++, outil de modélisation des interaction faisceau-faisceau) à leur transport dans les anneaux (en utilisant SAD), jusqu'à plusieurs dizaines de mètres en aval de l'IP. Les résultats ont montré que le meilleur emplacement pour positionner nos capteurs dans le LER se situe dans une section droite (drift) à 11.9m en aval de l'IP, le taux de Bhabha perdus y étant suffisant (potentiellement 4.7% de la section efficace totale) ainsi que l'espace libre disponible. L'interaction des particules perdues avec la matière de la chambre à vide a ensuite été simulé au moyen de GEANT4, pour pouvoir étudier et estimer le signal reçu par les capteur diamant. Dans le drift à 11.9m, la chambre à vide est un tube cylindrique de 3 mètres de long et de 6 mm d'épaisseur. Les positrons issus du processus Bhabha sortent de la chambre à vide avec un très petit angle (5 mrad), traversant 1.2 m de matériau, ce qui conduit à une grande absorption de la gerbe électromagnétique à la sortie du tube à vide et n'induit qu'un très faible signal dans le diamant.

Pour augmenter la gerbe électromagnétique et donc le signal dans les capteurs, l'inclusion d'une fenêtre à 45° a été suggérée par les physiciens de KEK en charge du vide dans la machine. Les simulations de cette fenêtre avec GEANT4 ont montré une amélioration de la précision sur la luminosité d'un facteur 10 par rapport au design initial. Cependant, une telle fenêtre est coûteuse et peut provoquer des champs de sillage (wakefields) et entraîner des instabilités du faisceau. En conséquence, différents types de matériaux (Aluminium, Berilium, Titane ,Cuivre) ont été simulés avec GEANT4 à différentes épaisseurs. Les simulations ont révélé que la fenêtre donne la meilleure précision parmi tous les autres modèles, et les simulations de wakefields effectuées au KEK ont montré des instabilités suffisamment faibles. Il a donc été décidé d'installer la fenêtre dans le drift à 11.9 mètres dans le LER pour la phase 2.

Pour augmenter la gamme de luminosités sur lesquelles des mesures précises peuvent être effectuées, nous souhaitons également utiliser des capteurs diamant (DS) dans le HER. De la même manière que pour les positrons dans le LER, les électrons issus du processus Bhabha ont été générés et leur transport dans le HER simulés jusqu'à 70m. Contrairement à ce qui se passe dans le LER, la déflection des positrons Bhabha le long du HER n'est linéaire avec leur énergie. Les particules perdues sont distribuées de manières stochastiques de part et d'autres de la chambre à vide, et quelque soit le positionnement des capteurs, la fraction des électrons Bhabha interceptée dans le DS est trop faible pour atteindre la précision visée.

Une autre méthode consiste à mesurer le signal des photons issus du processus Bhabha considéré avec le DS dans le HER. Les photons Bhabha sont produits à l'IP à très petits angles, de l'ordre de 0.4 mrad. Du fait de leur neutralité électrique, ils ne sont pas déviés par les champs magnétiques des éléments optiques, et sortent à un endroit précis de l'anneau.

Des simulations détaillées sont actuellement effectuées dans le groupe LAL en considérant l'optique du HER et la géométrie de la chambre à vide. L'analyse préliminaire montre que le spot des photons atteint le front de l'antichambre au milieu d'un sextupôle (à 27.4 mètres en aval de l'IP) à un angle moyen de 5.9 mrad. En raison de leur distribution transverse initiale, le spot projeté des photons sur la chambre s'étalent sur 2 à 3 mètres de part et d'autre du point de sortie nominal situé à 27.4m en aval de l'IP. L'espace libre le plus proche de ce point pour y placer les moniteurs de luminosité se situe à 30m en aval de l'IP. Comme les études en cours le montrent, une fraction importante de la section efficace de Bhabha radiatif peut être détectée à cet endroit.

Les capteurs diamant

Le diamant possède de nombreuses propriétés intéressantes qui lui permettent d'être l'un des meilleurs candidats aux détecteurs de rayonnement à l'état solide. Il a la plus grande conductivité thermique parmi les matériaux solides en plus d'une isolation électrique élevée. Le diamant a une énergie de liaison très élevée qui le rend très insensible aux rayonnements. De plus, le diamant se caractérise par un large écart de bande qui réduit le courant de fuite et diminue ainsi le bruit.

De plus, le diamant dispose de fortes mobilités des électrons et des trous, ce qui se traduit par une collecte rapide des charges et donc par des signaux rapides, dans la gamme de quelques ns. La largeur du signal dépend de l'épaisseur du diamant, par exemple une largeur de signal de 4-5 ns correspond à un diamant de 500 µm d'épaisseur. L'énergie minimale nécessaire pour créer une paire électron-trou dans le diamant est de 13 eV. Un MIP (Minimum Ionizing Particle) créé 36 paires électron-trou par µm dans le diamant. Un MIP est une particule chargée avec un taux de perte d'énergie proche du minimum, et l'énergie d'un électron au MIP est d'environ 1.6 MeV. Le champ électrique de polarisation que nous appliquons pour collecter les paires électron-trou est E = 0.8 V/µm. Normalement, nous pouvons appliquer une tension de polarisation jusqu'à 1 V/µm, cependant, grâce à la très bonne qualité du diamant, l'efficacité de la collecte de charge atteint 100% avant cette tension de polarisation (à ≈ 0,2 V/µm). Pour la sécurité, nous choisissons d'appliquer une tension un peu inférieure à 1 V/µm, soit 0,8 V/µm. Un désavantage du capteur diamant est la difficulté d'avoir une grande zone active, ce qui restreint nos mesures à une partie de la gerbe dans le cas d'une chambre à vide sans fenêtre.

Le fonctionnement et la lecture du DS sont simples. Une particule chargée traverse le DS créant des paires électron-trou en fonction de son énergie. En appliquant une haute tension aux électrodes du diamant, des charges opposées dérivent vers les électrodes. Le signal de sortie résultant de la chute de tension est lue par un oscilloscope. Dans le cas d'un petit signal, par exemple une faible intensité des particules incidentes et/ou des DS très minces , l'amplification du signal est nécessaire. Le dépôt d'énergie dans le DS suit une distribution Landau.

Pour mieux comprendre le comportement du signal dans le DS, nous avons effectué des tests en salle blanche en utilisant des sources radioactives. La configuration expérimentale se compose de la source β ^{90}Sr, un DS de 140 μm (qui sera utilisé en phase 3 de SuperKEKB), un amplificateur de charge de CIVIDEC dont la constante de temps de mise en forme est d'environ 10 ns, un scintillateur, une alimentation de basse tension de 12V pour l'amplificateur de charge, une alimentation haute tension pour le DS et un oscilloscope pour lire le signal. Étant donné que l'amplificateur de charge est unipolaire, la haute tension (-100 V) sur le DS est appliquée pour polariser négativement et pour obtenir des impulsions négatives à sa sortie.

Un support mécanique spécial a été préparé pour les tests. Le capteur de 140 μm est connecté à l'amplificateur de charge alimenté avec 12 V et les deux sont posés sur le banc central du support mécanique. Sur la partie supérieure, il existe une ouverture spéciale pour les électrons émis par la source radioactive pour atteindre directement la surface 4x4mm^2 du diamant situé en dessous. Juste au-dessous du diamant, un scintillateur est utilisé pour le déclenchement, afin de collecter uniquement les signaux des MIP, c'est-à-dire que le MIP traversera le diamant en déposant une partie de son énergie, sans être absorbé, puis atteindra le scintillateur et donnera un signal de déclenchement. Les données sont collectées pendant généralement 10 heures puis analysées. En plus de la reconstruction de la distribution de Landau du maximum de signal pour les diamants de deux épaisseurs (140μm et 500μm), nous avons vérifié que la position en temps du MPV (Most Probable Value) du signal ne se déplace pas significativement et ne dépend pas de l'amplitude du signal. Ceci est très important parce que dans nos mesures, nous échantillonnons à 1 GSPS (Giga Sample Per Second), ce qui signifie chaque 1 ns.

La phase 1 du commissioning de SuperKEKB

Lors de la première phase du commissioning du SuperKEKB, où la machine a fonctionné sans système de focalisation finale et sans le détecteur Belle-II, les faisceaux de positrons et d'électrons ont été produits avec succès, accélérés, injectés et stockés dans les anneaux principaux (LER et HER) de SuperKEKB.

Les objectifs principaux de cette phase étaient de démarrer chaque système de hardware de la machine (linac d'injection, système magnétique, système RF dans les deux anneaux, système de vide, ...) et définir un logiciel d'opérations du faisceau basé sur SAD. Au cours de cette période de mise en service, le lavage sous vide a été effectué dans les deux anneaux à différents courants, à partir de courants très faibles (30 mA) jusqu'à des courants élevés (1 A), afin de nettoyer les chambres à vide des gaz résiduels. Le gaz résiduel provoque une perte de faisceau due à la diffusion des particules du faisceau sur les molécules de gaz, soit par Bremsstrahlung (perte d'énergie de la particule en émettant un photon), soit par diffusion Coulombienne (diffusion à grand angle). Le lavage sous vide s'effectue par la circulation des faisceaux dans chaque anneau: le champ électromagnétique des faisceaux interagi avec la matière du tube à vide et en arrache des molécules qui sont ensuite extraites de la chambre à vide par un système de pompes NEG. Le lavage sous vide à des courants élevés (500 mA à 1 A) a été demandé par la collaboration Belle II pour protéger le détecteur des rayons de haute intensité lors des prises de données qui commenceront pendant la phase 2.

Des études spéciales dans les deux anneaux ont été menées dans le cadre de BEAST II, telles que la mesure des bruits de fond issus de la diffusion Touschek, de ceux résultant de l'interaction du faisceau avec le gaz résiduel, des bruits d'injection et les études de collimation. L'étude des Touschek a été réalisée en modifiant la taille verticale des faisceaux, par l'induction d'un couplage entre les émittances horizontale et verticale. Les études du bruit de fond faisceau-gaz ont été effectuées en induisant des «bumps» de vide en amont de l'IP dans des sections particulières des anneaux. Ces «bumps» de vide sont le résultat de la désactivation de quelques pompes NEG à des emplacements sélectionnés. Pour étudier l'effet des collimateurs sur les pertes du faisceau, les paramètres de certains collimateurs (largeur) ont été modifié.

Un autre objectif essentiel de la phase 1 du commissioning était de comprendre les problèmes qui peuvent survenir lors de l'opération à courant élevé (le blow up de la taille verticale du faisceau, l'avortement du faisceau, le comportement non linéaire de la pression avec le courant). Le groupe de mise en service de SuperKEKB a également de nombreuses études optiques.

Notre projet en phase 1:

Pour obtenir la précision visée sur les mesures de luminosité, nos capteurs doivent être placés dans des endroits où la contamination par des bruits de fond émanant du faisceau (bruits de fond single-beam) est minime (<1%). Par conséquent, l'étude des processus de perte single-beam est également importante pour notre projet.

Les capteurs diamant ont été installés aux emplacements que nous avons déterminés et nous ont permis durant la phase 1, l'acquisition de données permettant l'étude de plusieurs aspects:

- Vérifier le fonctionnement de nos capteurs et l'installation globale (électronique et mécanique) dans des conditions de fonctionnement de la machine.
- Mesurer les bruits de fond aux emplacements des capteurs choisis pour les mesures de luminosité dans les deux anneaux.
- Comparer les données à la simulation, et ainsi vérifier la fiabilité de nos simulations pour la phase 2.
- Une fois la fiabilité de la simulation confirmée, nous pouvons extrapoler nos simulations de bruits de fond à la phase 2 et estimer les fractions de signal de pertes single-beam et du processus de Bhabha radiatif dans nos capteurs.

Les bruits de fonds de Bremsstrahlung, la diffusion Touschek et la diffusion Coulombienne inélastique sont considérés comme des pertes single-beam, ils sont générés dans tout de l'anneau en raison de la diffusion des particules du faisceau sur le gaz résiduel ou de la diffusion des particules du faisceau les unes sur les autres. En plus d'être perdues à l'intérieur de la région d'interaction (IR) et d'engendrer des bruits de fond dans le détecteur, les particules provenant de pertes single-beam sont également perdues dans les anneaux, réduisant ainsi après un certain temps l'intensité et la qualité du faisceau. Dans des anneaux tels que SuperKEKB et en raison des courants très élevés et de leur très petites tailles, les faisceaux ont donc des durées de vie relativement courtes de l'ordre de 10 minutes. Les processus principaux déterminant la durée de vie des faisceaux sont l'effet Touschek et la diffusion Bhabha radiative à angle zéro à l'IP. Les faisceaux devraient donc être continuellement réinjectés pour maintenir leur intensité et donc maintenir une haute luminosité. Au cours de la phase 1 du commissioning de SuperKEKB, sans collision, les pertes principales étaient le Bremsstrahlung, la diffusion Touschek et la diffusion Coulombienne.

La diffusion Bremsstrahlung et les pertes résultantes sont proportionnelles au courant du faisceau et à la pression du gaz résiduel dans la chambre à vide. Pour l'effet Touschek, les pertes sont proportionnelles au carré du courant du faisceau et à l'inverse de la taille du faisceau. Comme pour Bremsstrahlung, la diffusion Coulombienne et les pertes résultantes sont proportionnelles au courant de faisceau et au niveau de vide.

Une version de SAD, écrite au KEK, a été utilisée pour simuler les pertes single-beam dans le LER. Les points de diffusion dans la version standard du code sont à l'entrée des quadrupôles, à l'exception des quadrupôles de focalisation finale pour les phases 2 et 3 et quelques aimants de courbure verticaux spéciaux . Le point d'observation est à l'entrée de chaque élément. Ainsi simulé, le spectre d'énergie des positrons Bremsstrahlung perdus dans le drift à 11.9 m, est discontinu et donc non physique. La raison de cette discontinuité est une résolution insuffisante des points de diffusion, qui ne permet pas d'obtenir une valeur correcte du taux de perte dans le drift.

Des modifications ont été apportées au code initial pour améliorer sa résolution, en ajoutant des points de diffusion à tous les éléments optiques et, pour les éléments longs, tels que les drifts et les aimants de courbure, en les découpant en tranches de longueurs égales. La diffusion des positons a ensuite été considérée à l'entrée de chaque tranche. Les aimants de courbure ont été découpés en petits tranches de ≈ 15 cm chacun, en gardant le même angle global de l'élément d'origine et les drifts ont été découpés en tranches de 10 cm chacune, de 50 mètres en amont à 13 mètres en aval de l'IP. De cette façon, nous avons récupéré tout le spectre d'énergie des positrons de Bremsstrahlung perdus dans le drift et obtenu une meilleure résolution sur les positions de diffusion. À l'aide de cette technique, le taux de perte obtenu dans le drift a été saturé tout en conservant le taux de perte dans l'ensemble de l'anneau: lorsque l'on augmente le nombre de positions de diffusion, nous augmentons la perte localement dans le drift alors que la perte totale globale dans toute l'anneau reste compatible dans les statistiques les erreurs.

Cette technique a ensuite été utilisée pour simuler et calculer les taux de pertes des diffusion de Bremsstrahlung, Touschek et Coulomb dans le drift, pour des pressions de vide, des courants et des tailles verticaux du faisceau différents. GEANT4 a été utilisé pour étudier les signaux de ces pertes dans le DS.

Pour pouvoir mesurer les pertes single-beam en phase 1, une installation expérimentale complète a été préparée au LAL et installée sur les deux anneaux de SuperKEKB, comprenant les supports mécaniques, les capteurs diamant et le système d'acquisition du signal.

Les supports mécaniques se composent de piliers dans chaque anneau. Chaque pilier prend en charge une plaque mobile avec deux capteurs diamant connectés chacun à un amplificateur de charge CIVIDEC et une plaque fixe avec les moniteurs ZDLM. La plaque mobile est associée à un moteur commandé à distance pour scanner dans la direction verticale sur une plage de 2.5 cm. Dans le HER, le pilier est installé à 30 mètres en aval de l'IP et les capteurs sont en face de l'antichambre dans le drift. Le pilier dans le LER est installé à 11.9 mètres en aval de l'IP et les capteurs sont en face à un tube de vide cylindrique normal dans le drift. En tout quatre capteurs diamant de 500 µm ont donc été installés pour la phase 1 du commissioning.

Deux procédures d'acquisition de signaux ont été implémentées, soit par des enregistrements continus de 10 ms pouvant être traités à la volée toutes les 5-6 secondes soit jusqu'à une cinquantaine d'enregistrements de 410 ms dont le traitement a lieu en différé et dure quelques heures. Les données brutes acquises par un oscilloscope Keysight ont ensuite été converties en fichiers ".mat" et traitées avec MATLAB. Les fonctions de traitement ont été construites pour rechercher les formes d'onde des signaux des DS. Une fois les formes d'onde définies, les maxima et leurs positions dans le temps ont été extraites, ainsi que le FWHM de chaque forme d'onde. De plus, nous avons créé notre propre archive EPICS pour sauvegarder les enregistrements des paramètres de la machine (comme le courant, la pression, la taille du faisceau, l'heure ...) et nous avons fusionné les données du DS avec les données EPICS après chaque acquisition.

Pendant la phase 1 du commissioning, nous avons pris des données principalement pendant les phases de nettoyage sous vide dans les deux anneaux et pendant des études de bumps de vide et les variations de la taille du faisceau dans le LER.

Les données prises pendant des bumps de vide ont été utilisées pour calculer la fraction des pertes liées au Bremsstrahlung dans des sections où les bumps ont été effectués et pour les comparer à des simulations. Les comparaisons ont montré que les données correspondent aux simulations au erreurs statistiques près.

Une étude de Touschek a été lors de l'augmentation de la taille verticale du faisceau. Les données ont été collectées pour six courants de faisceau différents dans le LER, I = 180, 360, 540, 720, 900 et 1000 mA et avec cinq taille de faisceau à chaque fois. Leur analyse a permis d'extraire les contributions de Bremsstrahlung et de Touschek. L'ajustement des pertes dans le diamant en fonction de l'inverse de la taille vertical du faisceau (σ_y^{-1}) permet de séparer les deux contributions de la manière suivante. Pour σ_y^{-1} proche de zéro, ce qui signifie que σ_y est très important, les pertes de Touschek devraient disparaître et donc toutes les pertes dans le DS devraient être issues du Bremsstrahlung.

Les pertes de Bremsstrahlung extraites des ajustements ont été comparées aux simulations en fonction du produit de la pression de vide et du courant du faisceau. Les résultats ont montré que les données sont toujours supérieures d'un facteur à ceux prédits par la simulation. Ce facteur s'explique par le fait que la valeur de la pression mesurée par le CCG (Cold Cathode Gauge) devrait être multipliée par un facteur 3 pour représenter correctement la pression réelle de CO au centre de la chambre à vide.

Les pertes de Touschek extraites des ajustements ont également été comparées aux simulations. Nous observons un facteur de simulation/données = 1.7 ± 0.37. Nous avons étudié les raisons possibles de cette écart, et exclu des erreurs possibles concernant l'estimation des tailles longitudinale et verticale du faisceau, cohérente avec la valeur estimée à l'aide de la modélisation basée sur les mesures des fonctions optiques dans le LER. Une raison plausible pourrait être l'emittance horizontal, mais malheureusement il n'existe pas de mesures fiables de la taille horizontale du faisceau à SuperKEKB pour vérifier cette hypothèse. Nous ne pouvons pas non plus exclure complètement qu'une partie de cet écart vient de la simulation elle-même.

Le bon accord qualitatif et quantitatif entre nos simulations et les mesures nous a permis d'estimer le niveau de bruit de fond dans le DS pour la phase 2. Les estimations ont montré que le niveau de bruit de fond résultant des pertes d'un seul faisceau devrait être d'environ deux ordres de grandeur inférieur au taux du signal de Bhabha radiatif pour la phase 2. Cela satisfait les conditions spécifiées pour obtenir une haute précision relative sur la mesure de luminosité.

Conclusion:

Le travail de ma thèse a été utile pour trouver les meilleurs positions pour les moniteurs de luminosité dans les deux anneaux de SuperKEKB afin d'atteindre la précision visée sur la mesure de la luminosité. En outre, les simulations effectuées pour les pertes single-beam sont cohérentes avec les données prises au cours de la phase 1, ce qui nous a permis d'estimer le rapport entre le signal et le bruit de fond dans le DS attendu en phase 2, compatible avec la précision visée.

To my parents and siblings first …
And to every marginalized and oppressed person in this world !

إلى أمّي وأبي وإخوتي أوّلاً
وإلى كلّ مظلوم ومهمّش على هذه الأرض !

Acknowledgements

I am honored to have been surrounded by great people during the three years of my PhD thesis work. It is difficult to mention all what they did for me in a short paragraph but I will never forget their direct or indirect contributions to my success.

Many thanks to the LAL director, Achille Stocchi, for hosting me almost 3 years and a half and for giving me the chance to work on this very interesting project. I would like as well to deeply thank the referees Jerome Baudot and Jean Marie De Conto for reading my thesis report and for giving nice comments on my work. Many thanks to Yoshihiro Funakoshi, Uehara Sadaharu and Manuela Boscolo for being the members of my thesis committee.

I would like to enormously thank my supervisors Philip Bambade and Cécile Rimbault for every single advice and for every information, discussion and support they gave me. I thank them for believing in me and my work and for their trust. Thank you for giving me the chance to participate on very important conferences and summer schools and thus acquiring a lot of experience in life.

Many thanks to every person in our group who without their help in every manner, I couldn't have achieved what I have today. Thanks to Didier Jehanno, Viacheslav Kubytskyi, Yann Peinaud, Patrick Cornebise, Alex Blin and Frederic Bogard.

Part of this work has been funded by the P2IO LabEx (ANR-10-LABX-0038) in the framework “Investissements d’Avenir” (ANR-11-IDEX-0003-01) managed by the French National Research Agency (ANR), so many thanks to P2IO, as well many thanks to the Ecole doctorale PHENIICS for funding the other part, many thanks to Fabien Cavalier and Elias Khan.

Many thanks as well to all the people of the administrative service at LAL for helping me in all the administrative issues related to my thesis.

I will not forget the great support I got from Japanese Scientists, I would like to enormously thank Funakoshi san for giving me the great chance as a student to participate on the SuperKEKB commissioning and for letting me participate on operation shifts, as well for the very interesting discussions and for replying on all my questions. Thank you for believing in my abilities and inviting me to return to KEK to work on SuperKEKB, I believe I will always be in your debt. Many thanks to Uehara san for the nice collaboration and for the very interesting discussions. Many thanks to Ohnishi san for your code and for your enormous help. Sincere thanks to Iida san, Muira san, Ikeda san, Flannagan san, Masuzawa san and Koiso san.

In addition, I would like to thank every single person in the accelerator department for the nice moments we shared in the lab. Special thanks to Robert Chehab, Walid Kaabi, Hayg Guler, Cynthia Vallerand, Iryna Chaikovska, Mathilde Court, Mohamed El Khaldi, Cristelle Bruni, Sophie Chancé, Nicolas Delerue, Noureddine El Kamchi and Jean-Noel Cayla. Special thanks also to Marica Biagini for all the nice moments and for the physics and “non-physics” discussions.

Very special thanks to Catherine Bourge for being the big sister in everything and for supporting me during every nostalgic moment during more than 4 years. Thanks to Dominique Bony for the nice lunch moments together as well.

Many thanks to all my professors at the Master 2 “NPAC” and for all my professors at the Lebanese university. Thanks to the first teachers who inspired me and guided me on the way of success, thanks to my teachers at “Asaad Abboud school”. Many thanks as well to my teachers at “Sohmor high school”.

Far from the office and the laboratory, special people were surrounding me and giving me a positive energy everyday to start. I cannot forget the memories we shared, the laughters which filled our small houses and the dances and “dabki” we performed which brought joy to my heart. Special, kind and lovely thanks to Fatima Al Reda, Marwa Zaarour, Marwa Koumaiha, Zeinab Koumaiha, Mohammad Tarhini, Mohamad Ayoub, Elie Saikaly, Mostafa Al Reda and Mayla Salman.

Infinite thanks to the one who considered me and still considering me as his daughter, for the one who taught me a lot of valuable things in life, who guided me while far from all the people I love, thank you Tokio Ohska, thank you my Godfather, I love you. Sweet thanks as well to my Classical singing teacher, for the lovely Keiko Nishimura.

For the people who were my family in Japan and will always be, thank you for being you and for every moment we spent together and for every support. Thank you Umberto Tamponi, Monica Frattari, Maryam Salihi, Hulya Hatmacan, Manca Mrvar, Bianca Scavino, Martin Ritter and Torben Ferber.

Many special thanks to the amazing friends Nuria Fuster Martinez, Thomas Vinatier, Shan Liu, Ping Chen, Renjun Yang, Chengguo Pang, Luca Garolfi, Sarah Bira, Alexis Gamelin and Hadda Rachidi for the nice moments and for every support.

Thank you Georges Audi and Ghislaine Audi for the nice moments we shared.

Special thanks to my aunt Inaam and her family and to my cousin Soha Salam and her husband Rayan Abdallah for being beside me in the very hard moments at the beginning of my thesis.
Thank you my cousin Imad for the support during these last years.

Infinite, enormous and lovely thanks to the people who considered me like their daughter and hosted me in their house for several special family gatherings, to the people who I owe a lot, to the kindest Bernard and Isabelle Thomas and their nice family.

To the piece of my heart, to my soul, to every spot of life in me, to my “Gods”, my parents Tarek and Fatima, you are everything and will always be. If I sacrifice my life, it will not be enough. I worship you and without you I have had never done any single step. To my sister Samah, you are the sunshine of my life, thank you for always being by my side. To my adorable brothers Maher and Ziad, you are my strength and you are my guards. To my adorable family, I say, I will always be me and I will always make you proud of me.

أمّي وأبي وإخوتي يا أغلى من الرّوح ، أنتم الأساس، أنتم البداية وكلّ الحكاية ... شكراً حتّى آخر نفس

”يظنّ النّاس أنّ الشّعور بالسّعادة هو نتيجة النّجاح ولكنّ العكس هو صحيح
النّجاح هو نتيجة الشّعور بالسّعادة"

إبراهيم الفقي

“ Money won't create success, the freedom to make it will”

Nelson Mandela

“If you can't explain it simply, you don't understand it well enough”

Albert Einstein

Contents

1 Introduction **1**
1.1 Accelerators for high energy physics 1
1.2 High luminosity colliders 2

2 The SuperKEKB collider **5**
2.1 Design and goals 5
2.2 Accelerator layout 7
2.2.1 Electron source 7
2.2.2 Positron source 8
2.2.3 Damping ring 10
2.2.4 Injection 10
2.2.5 Vacuum system for both rings 12
2.2.6 Nano-beam scheme 13
2.3 Belle II 14
2.3.1 Physics 15
2.3.2 Sub detectors 15
2.4 BEAST II 16

3 Fast Luminosity Monitoring **19**
3.1 Motivations And Specifications 19
3.1.1 Methods and Techniques 19
3.2 Evaluation of dithering algorithm 20
3.3 Our Project 23
3.3.1 CVD diamond sensors 24
3.3.1.1 Properties 24
3.3.1.2 Operation 25
3.3.1.3 Characterisation with radioactive sources 25
3.4 Position of the diamond sensor in both rings 35
3.4.1 Radiative Bhabha at zero photon scattering angle 35
3.4.2 Case of LER 37
3.4.2.1 Generation of Bhabha positrons with GUINEA-PIG++ 37
3.4.2.2 Particle Tracking 38
3.4.2.3 Simulation of signal in the sCVD 43
3.4.3 Design of new vacuum chamber insertion 45
3.4.3.1 Simulation of window at 45° 45
3.4.3.2 Simulation of different material and thickness beam pipe 50
3.4.4 Case of HER 52

3.4.4.1 Difficulties and restrictions . . . 52
3.4.4.2 Method implemented . . . 55

4 SuperKEKB single beam commissioning 59
4.1 Introduction . . . 59
4.1.1 General goals and achievements . . . 59
4.1.2 Next stages of SuperKEKB commissioning . . . 62
4.1.3 Goals for our fast luminosity project . . . 62
4.2 Beam Loss Monitors . . . 63
4.2.1 PIN diodes . . . 63
4.2.2 Ion chambers . . . 64
4.3 Vacuum scrubbing . . . 65
4.3.1 Electron cloud . . . 65
4.3.2 Non-linear pressure rise with beam current . . . 66
4.3.3 Countermeasures . . . 67
4.4 Beam size blow-up . . . 68
4.4.1 Description of the phenomenon . . . 68
4.4.2 Effect of permanent solenoids . . . 69

5 Single Beam Losses at Phase 1 71
5.1 Single beam loss processes . . . 71
5.1.1 Beam-Gas Bremsstrahlung . . . 72
5.1.2 Touschek scattering . . . 73
5.1.3 Coulomb scattering . . . 74
5.2 Simulation of single beam losses in phase 1 . . . 74
5.2.1 Beam-Gas Bremsstrahlung . . . 75
5.2.2 The Touschek process . . . 81
5.2.3 Coulomb . . . 84

6 Measurements of Single Beam Loss at Phase 1 89
6.1 Experimental configuration . . . 89
6.1.1 Mechanical setup . . . 89
6.1.2 Sensors and readout . . . 89
6.2 Single beam losses in the sCVD in phase 1 . . . 91
6.2.1 Losses as a function of different parameters . . . 92
6.2.1.1 Signals in the sCVD . . . 95
6.2.1.2 Losses as function of current and pressure . . . 96
6.2.1.3 Data from Cherenkov in LER . . . 97
6.2.2 Losses from vacuum bumps in the LER . . . 99
6.2.3 Losses for different vertical beam sizes . . . 102
6.2.3.1 Losses from beam-gas Bremsstrahlung . . . 104

6.2.3.2 Losses from Touschek scattering 105
6.3 Estimations of the ratio of radiative Bhabha signal and single beam losses in phase 2 108
6.3.1 Beam-gas Bremsstrahlung 109
6.3.2 Touschek scattering 110
6.3.3 Signal to Noise in the LER in phase 2 110

7 Conclusions and perspectives 111

7.1 Data from single beam losses at phase 1 112
7.2 Implications for phase 2 113
7.2.1 Signal to background ratio during luminosity monitoring 113
7.2.2 Vacuum chamber design and installation 113
7.2.3 Precision on luminosity 113
7.2.4 Readout electronics 113

8 Appendix A 115

8.1 Copper 115
8.1.1 6 mm 116
8.1.2 5 mm 118
8.1.3 4 mm 120
8.1.4 3 mm 122
8.1.5 2 mm 124
8.1.6 1 mm 126
8.1.7 Precision of $\mathcal{L}$ evaluation 128
8.2 Aluminium 129
8.2.1 Precision of $\mathcal{L}$ evaluation 130
8.3 Titanium 131
8.3.1 Precision of $\mathcal{L}$ evaluation 132
8.4 Beryllium 133
8.4.1 Precision of $\mathcal{L}$ evaluation 134
8.5 Comparison between different designs and final choice 135

Bibliography **137**

Chapter 1

Introduction

1.1 Accelerators for high energy physics

We live in a universe that behaves under well defined laws that may include some exceptions. It is very important to understand our universe, study about its constituents, its history and to predict its future. Scientists around the world participated on the foundation and development of the Standard Model (SM), the theory which concerns the electromagnetic, weak, and strong nuclear interactions, as well as the classification of all known subatomic particles. The SM gained its credibility by the confirmation of the existence of the quarks, and afterwards by the discovery of all its particles, in particular, the top quark [1] at the CDF (Collider Detector at Fermilab) and Dϕ at Tevatron (1995), the tau neutrino at DONUT collaboration (Direct Observation of the NU Tau) at Fermilab (2000) [2] and the Higgs Boson at ATLAS (A Toroidal LHC ApparatuS) [3] and CMS (Compact Muon Solenoid) [4] at LHC (Large Hadron Collider) at CERN (2012). However, the SM doesn't explain some phenomena like the gravitation theory, the neutrino oscillation, the expansion of the universe by dark matter, and questions about matter-antimatter asymmetry. In addition, still a lot of information on the origin of the Higgs mechanism and its properties are missing. So, more investigation on the Higgs boson and physics expected beyond the Standard model needs to be done. This requires upgrades of already existing accelerators like the LHC and the construction of new accelerators with high luminosities and energies.

Accelerators for high energy physics are mainly of two kinds: circular and linear colliders. These colliders are called hadron colliders if they collide hadrons like protons, and are called lepton colliders if they collide electrons and positrons. The advantage of circular colliders in general is that the beams can be reused for several turns, however in the linear colliders beams collide once and are then dumped. In hadron circular colliders, very high energies can be reached by improving high field super conductive magnets to bend the proton beams for a given ring radius, however the beam energies in lepton circular colliders (e^+e^- circular collider) are limited by synchrotron radiation due to the small electron mass. Thus lepton linear colliders are considered to achieve higher energies by extending the length of the accelerating lines. Lepton colliders in general provide a clean environment of interactions at the Interaction Point (IP), which helps the physicists to perform cleaner analysis of the produced events compared to the huge hadronic showers produced from the interaction of hadrons. As well, the initial state of the interacting particles is generally well known in lepton colliders, for instance the knowledge of the energy and momentum, and also the spin in the case of linear colliders, can be used to constrain the reconstruction of the final state, taking into account the conservation laws governing the physics process under study.

The HL-LHC (High Luminosity Large Hadron Collider) aims at a peak luminosity up to 5×10^{34} $\mathrm{cm^{-2}s^{-1}}$ and 14 TeV center of mass energy by reducing the beam sizes and upgrading the injector. The FCC-ee (e^+e^- Future Circular Collider) [5] is planned in a 100 km tunnel to be constructed in the Geneva area. It aims at a very high center of mass energy of 400 GeV. A 100 TeV FCC-pp (proton proton collider) with a peak luminosity of 5×10^{34} $\mathrm{cm^{-2}s^{-1}}$. The ILC is a 30 km long linear accelerator which aims to collide electrons against positrons at a luminosity of 10^{34} $\mathrm{cm^{-2}s^{-1}}$, with a 500 GeV up to 1 TeV center of mass energy. The CEPC [6] (Circular Electron Positron Collider) is a future circular e^+e^- collider ring of 50 Km circumference planned in China with a luminosity of 1.8×10^{34} $\mathrm{cm^{-2}s^{-1}}$ with beam energies of 120 GeV, aiming at a clean study of the Higgs boson (125 GeV). The CEPC can later be upgraded to a proton-proton collider enabling to achieve very high energies and discover new physics beyond the Higgs. CLIC (Compact LInear Collider) [7] is a future e^+e^- linear collider project based in CERN, aiming at a nominal luminosity of 6×10^{34} $\mathrm{cm^{-2}s^{-1}}$ by squeezing the beam sizes to 40 nm horizontally and 1 nm vertically, with center of mass energy up to 3 TeV.

1.2 High luminosity colliders

To achieve high precisions on the physics detected from particle collisions and to be able to see new particles, two very important parameters need to be optimised, the energy and the luminosity. High energies can be achieved by huge rings and long linear colliders (for lepton colliders). For future hadron colliders, the challenge is the development of very high field superconducting magnets. High luminosities require in general very small spot sizes at the IP and high currents.

SuperKEKB is an asymmetric B meson factory which aims to study the CP violation in the B meson sector and to search for new physics. It will collide electrons and positrons at a center of mass energy of 11 GeV, and it will achieve the highest ever luminosity in the history of high energy accelerators ($\mathcal{L}= 8\times10^{35}$ $\mathrm{cm^{-2}s^{-1}}$). This very high luminosity will be achieved thanks to a new scheme called the nano-beam scheme, where very strongly focused beams (σ_y= 60 nm) collide at a large crossing angle of 83 mrad. The beam currents will reach 3.6 A in the positron ring and 2.6 A in the electron ring.

To be able to keep a very high luminosity operation, a dithering system is employed to control the horizontal orbit of the beams at the IP. The dithering system consists of a set of magnets which will kick the beam at a frequency of 77 Hz. To monitor the effect of such kicks on the alignment of the beams and thus on the luminosity, a fast luminosity monitoring is required. The fast luminosity monitor is essential in the presence of dynamic instabilities, for feedback and optimisation.

At SuperKEKB, we perform fast luminosity measurements based on two technologies, the sCVD diamond sensors with our group at LAL and Cherenkov and Scintillator detectors with the ZDLM (Zero Degree Luminosity Monitor) group at KEK. We aim at a relative precision of 10^{-3} in 1 ms and we measure the signals from the Bhabha process at zero photon scattering angle, which has a large cross section at the IP about 200 mbarn. The sensors are placed in both rings just outside the beam pipe, several meters downstream of the IP. For high quality measurements, the signals in our sensors should not be contaminated by background signals from single beam losses. As a result, detailed simulations of single beam losses had to be performed as well, optimising the sensitivity of our devices to the Bhabha process.

We successfully installed our diamond sensors in both rings and took data during the single beam commissioning phase of SuperKEKB. A quantitative and qualitative agreement between the measurements and simulations was observed. This validated our simulation, giving credibility to our predictions for the levels of background and Bhabha signals expected in our sensors during the second and third phases of the SuperKEKB commissioning.

This thesis is organised in seven chapters including the introduction:

Chapter 2 defines the SuperKEKB project, its design, goals and different parts including the Belle II detector.
Chapter 3 defines the fast luminosity monitoring project, and describes the diamond sensors used and shows the results of characterisation tests performed in the clean room at LAL. As well, it describes in details the simulations performed to find optimal positions of the sensors in both rings and the results concerning the design of the vacuum chamber for phase 2.
Chapter 4 describes the different commissioning phases of SuperKEKB with their goals, and describes some phenomena and studies performed during the single beam commissioning.
Chapter 5 defines the processes of single beam losses at SuperKEKB and describes the simulations of these processes performed in phase 1.
Chapter 6 describes the overall mechanical and electronic setup of our project during phase 1 with the data acquisition and analysis, and compares the simulation results to the measurements.

Chapter 7 summarizes all the results and discusses the future prospects.

Chapter 2
The SuperKEKB collider

2.1 Design and goals

The KEKB electron-positron collider built at KEK, in Japan, achieved the world's luminosity record (more than 2.11×10^{34} cm^{-2}s^{-1}) in 2009. The analysis of the large amount of data taken by the Belle detector (1.5 ab^{-1}) from the collisions of the positron and electron beams has allowed the Kobayashi-Maskawa theory to be verified by observing the CP (Charge Parity) asymmetry in B mesons. The Kobayashi-Maskawa theory highlights differences between matter and anti-matter. At the beginning of the universe, equal quantities of matter and anti-matter were present, while almost no anti-matter is presently found in nature. This indicates that there are fundamental differences in the behaviour of matter and anti-matter. The Kobayashi-Maskawa theory alone cannot completely explain the deficit of anti-matter: More data and further research are needed. In this context, KEKB and the Belle experiment were upgraded to deliver higher luminosity and improve detection capabilities.

The upgraded machine, called SuperKEKB [8], consists of a 4 GeV positron ring and a 7 GeV electron ring and aims to reach a luminosity 40 times higher than that of KEKB (8x10^{35} cm^{-2}s^{-1}). It will be the highest luminosity particle collider that ever existed (fig. 2.1). It is an asymmetric collider with a center of mass energy equal to the $\Upsilon(4S)$ resonance energy to produce B meson pairs. With the asymmetric energies of the electron and positron beams, the B meson pairs are created with a Lorentz boost $\beta\gamma$ of 0.425 which allows the measurement of the decay time of the B meson by measuring its travelled distance from the interaction point (IP). Belle II [9] is the upgrade experiment and it expects to start data taking in 2018. SuperKEKB will reuse some components of KEKB, while other components need to be either modified or developed. The accelerator design of SuperKEKB (fig. 2.2) consists of a Photocathode RF-Gun to generate an electron beam, a positron source to generate a positron beam from the incident electron beam, a linear accelerator for both beams, a positron damping ring, an injector linac which will inject the electron beam in the high energy ring (HER) and the positron beam in the low energy ring (LER).

SuperKEKB will be able to achieve a very high luminosity by increasing the beam currents (twice higher than at KEKB) and by using the nano-beam scheme which allows

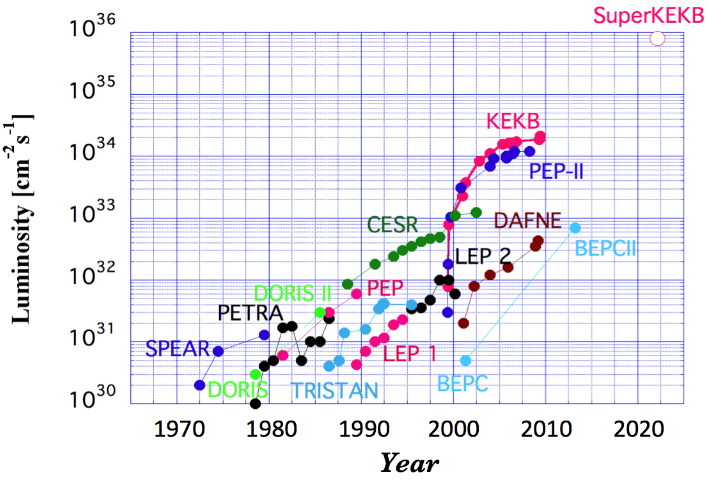

Figure 2.1 – Luminosity at SuperKEKB compared to other colliders

very strong focusing at the IP, to achieve very small vertical beam sizes (σ_y= 60 nm). The table 2.1 shows the comparison of some parameters between KEKB and SuperKEB. The very strong focusing at SuperKEKB will be achieved thanks to a final focus system (FF) [10] which includes superconducting magnets near the Interaction Point (IP) for each beam. The system of magnets is split into two cryostat boxes (fig. 2.3), and the closest magnets (in the LER) are at ± 935 mm from the IP.

SuperKEKB started its single beam commissioning in February 2016 and completed it in June 2016 (see chapter 4) during which both electron and positron beams were successfully injected and stored without collisions. During this commissioning, tuning of optics elements and parameters was performed and single beam background losses were measured by the BEAST II (see section 4) detectors and by the fast luminosity monitors (see chapter 3).

Parameter	KEKB (LER/HER)	SuperKEKB design (LER/HER)
Energy (GeV)	3.5/8	4/7
β_y^* (mm)	5.9/5.9	0.27/0.42
σ_y^* (μm)	0.94	0.059
Beam current (mA)	1.64/1.19	3.6/2.6
Luminosity ($cm^{-2}s^{-1}$)	2.11×10^{34}	8×10^{35}

Table 2.1 – Comparison between achieved parameters at KEKB and design parameters at SuperKEKB

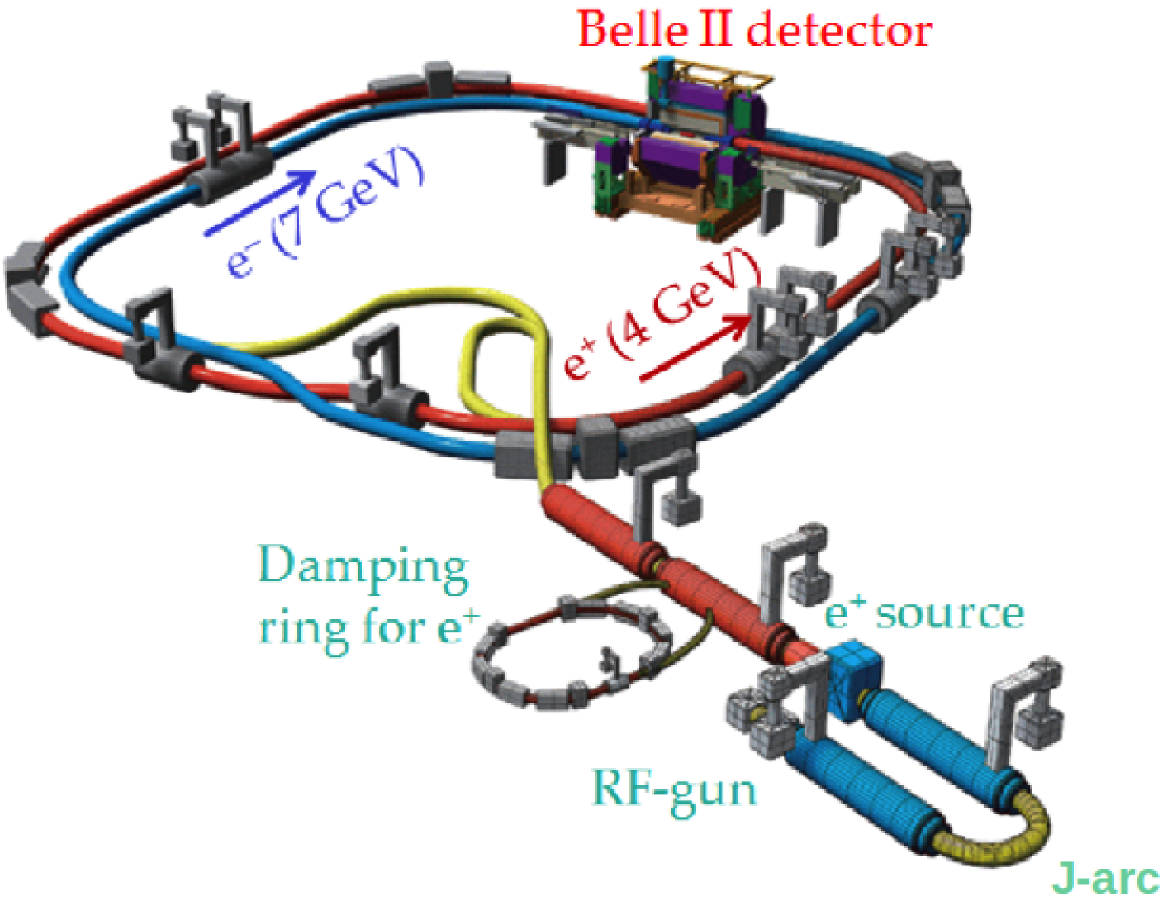

Figure 2.2 – Layout of SuperKEKB/Belle II experiment

2.2 Accelerator layout

2.2.1 Electron source

SuperKEKB requires a beam with very high charge (5 nC) and low normalised emittance (20 mm-mrad), for this reason a new RF gun [11] which generates the electron beam has been developed to achieve such requirements. The gun is installed at the start point of the J-linac (fig. 2.2). The RF gun (l.h.s of fig. 2.4) is designed with a very high focusing RF field to control the space charge effect from high beam charge. These high focusing fields are generated by seven QTW-SIDE cavities (quasi-travelling wave) [12] which are characterised by narrow gaps and responsible of keeping the beam size.

The choice of the photocathode material is essential to produce high charge beams for a long-term operation like that at SuperKEKB. The photocathode which will be used at

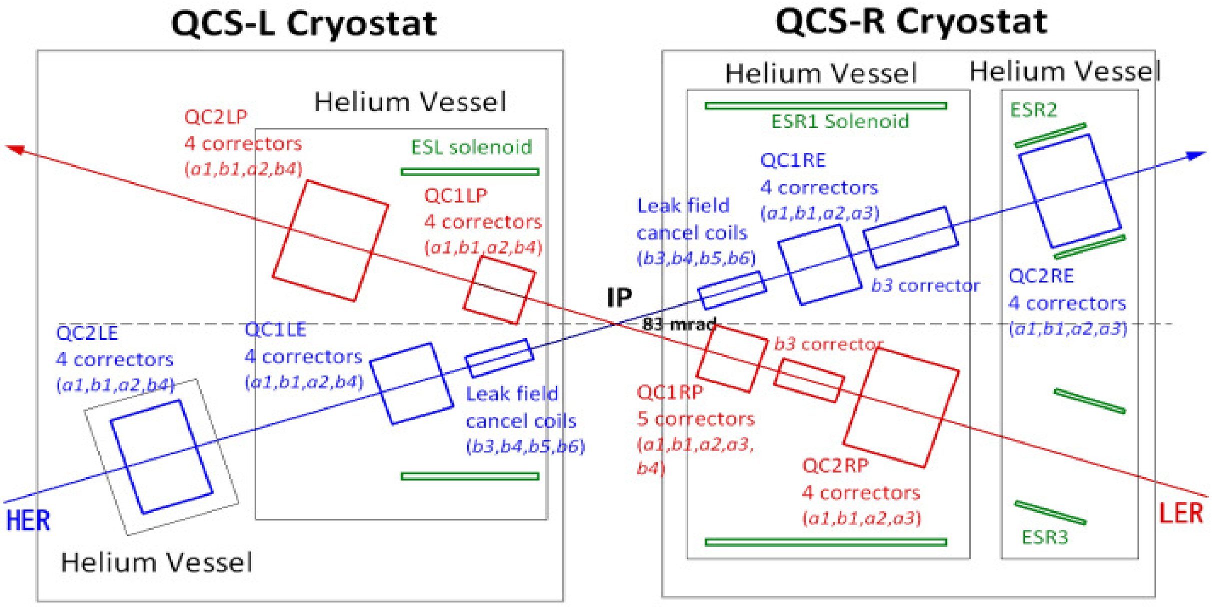

Figure 2.3 – The final focus Superconducting magnet system at SuperKEKB [10]

SuperKEKB is an Iridium Cerium cathode (r.h.s of fig. 2.4) thanks to its reasonably high QE (Quantum Efficiency=1.54×10^{-4} at 266 nm) and long lifetime.

To achieve high repetition rates of a double-electron bunch at SuperKEKB (50 Hz), a solid state laser system based on Neodymium-doped (Nd:YAG) and Ytterbium-doped (Yb:YAG) crystals [13] with emission wavelength of 1064 nm and 1030 nm respectively, is employed to prevent the thermal increase due to the increase of the source pump repetition rate.
On the other hand, the 10 nC primary beam used to produce the positron beam is generated by a thermionic gun, the beam line of which is merged to that of the RF gun by two vertical bends [14].

2.2.2 Positron source

The positron source upgrade [15] at SuperKEKB allows the increase of the positron bunch intensity from 1 nC to 4 nC and the achievement of very small beam emittance by introducing a damping ring. The 3.5 GeV accelerated double-bunch electron beam (10 nC each) hits a 14 mm thick amorphous tungsten target and produces positrons by a cascade shower. To protect the target from very high energy deposition due to the high intensity beams with very small spot sizes (0.4 mm), a beam spoiler [16][17] is introduced 3 m before the target to increase the beam sizes up to 0.7 mm.

After being produced, the positrons are focused by a flux concentrator [18] which is

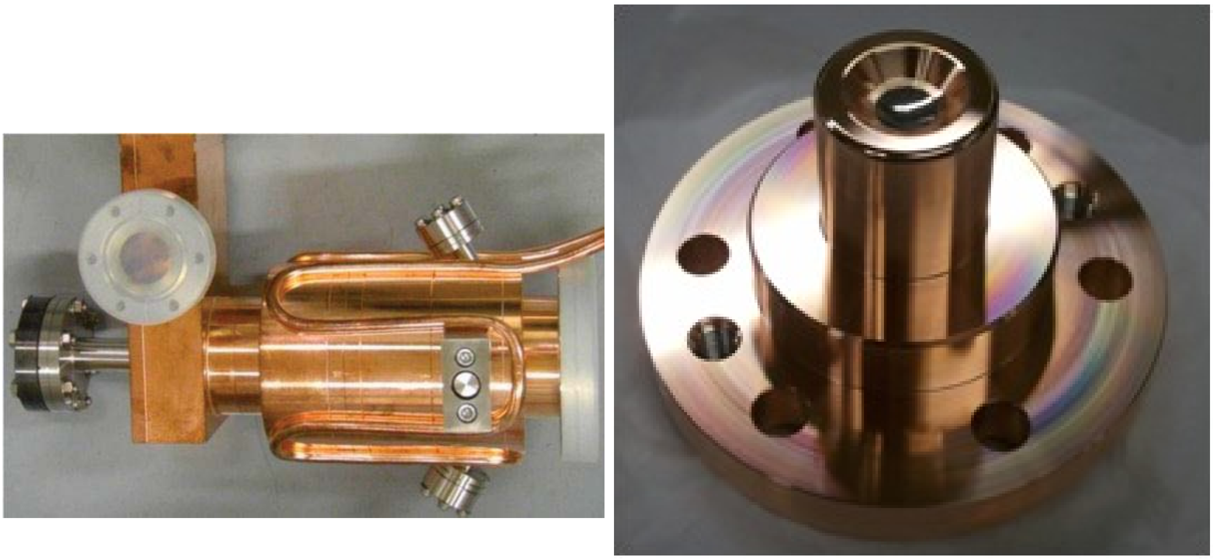

Figure 2.4 – The RF gun on l.h.s and the photocathode on r.h.s, at SuperKEKB

located 2 mm from the target. The positron beam is then accelerated to 110 MeV by six large aperture S-band (LAS) accelerating structures [19]. The scheme of the SuperKEKB positron source is shown on l.h.s of fig. 2.5 and a picture of the LAS accelerating structure on r.h.s of fig. 2.5

After the target, both secondary electrons and positrons are produced. After the LAS, the electron bunch is separated from the positron bunch by 175 ps due to the phase slippage. To be able to get pure positron beam, an electron/positron separator chicane is introduced after the LAS where secondary electrons are absorbed by a 60 mm thick tungsten-copper alloy block and positron beam continues.

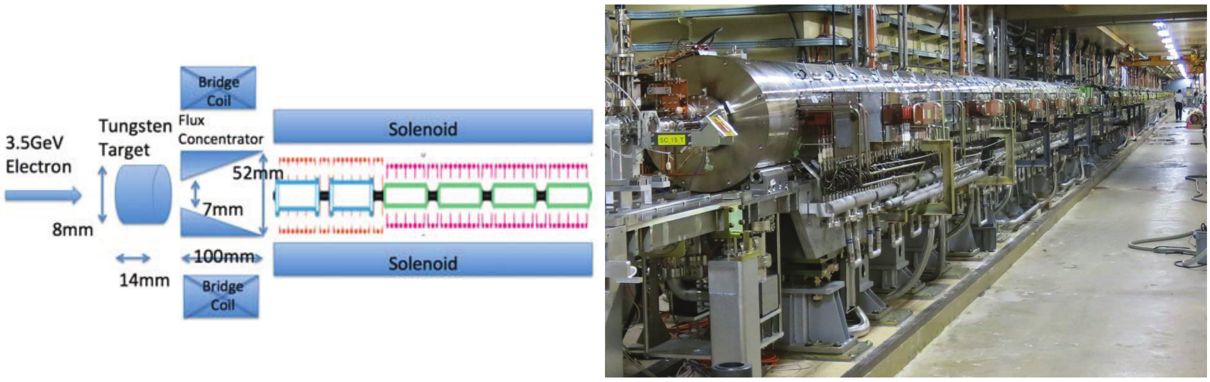

Figure 2.5 – The scheme of positron source on l.h.s and the large aperture S-band accelerating structure at SuperKEKB on r.h.s

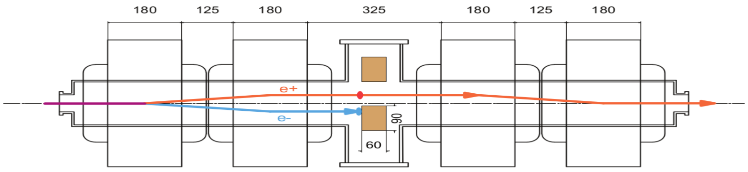

Figure 2.6 – Electron/positron separator chicane at SuperKEKB

2.2.3 Damping ring

As a result of very high electron/positron beam currents (2.6A/3.6A) at SuperKEKB and the adoption of the nano beam scheme which results in very small vertical beam sizes (60 nm), the Touschek lifetime in the LER becomes very short ($\approx$ 600 sec). In order to maintain the same beam current, a bunch intensity of about 8 nC needs to be continuously injected at a repetition frequency of 25 Hz. However, the generated and accelerated positron beam has a relatively large emittance and energy dispersion, larger than the aperture of the LER. Thus a damping ring (DR) [20] is needed to reduce the emittance before injection.

The DR has a circumference of $\approx$135 meters and a physical aperture of 34 mm. A pre-accelerated 1.1 GeV positron beam (emittance=1.7μm.rad) is injected to the DR passing through a transport line LTR (Linac To Ring) which contains an ECS (Energy Compression System) to compress the energy spread from 1.67% to 0.5%, to be within the energy acceptance of the DR. To achieve a short damping time, an optic design called "Reverse-bend FODO" [21] is used with relatively low field. The physical transverse emittances at the exit of the DR are ε_x=41.4 nm and ε_y=2.07 nm and the energy spread is 5.5×10^{-4}. After being damped, the positron beam exits the damping ring via the RTL (Ring To Linac) where its bunch length is compressed by the BCS (Bunch Compression system). After that, the positron beam is accelerated from 1.1 GeV to 4 GeV and reaches the injection point with horizontal emittance of 11.8 nm and vertical emittance of 0.86 nm. The layout of the damping ring with the LTR and RTL is represented in fig. 2.7.

2.2.4 Injection

The injector linac [22] (fig. 2.8) is 600 meters long, it starts from the RF photocathode, passing by the positron source and ending up at the injection point. This linac provides the positron beams for the LER (Low Energy Ring) and the electron beams for the HER (High Energy Ring) of SuperKEKB, and the PF-AR (Photon Factory Advanced Ring) and PF (Photon Factory) electron rings. In order to maintain a constant luminosity at SuperKEKB, simultaneous injections are needed among the mentioned rings. Consequently, SuperKEKB uses a continuous injection "top-up injection".

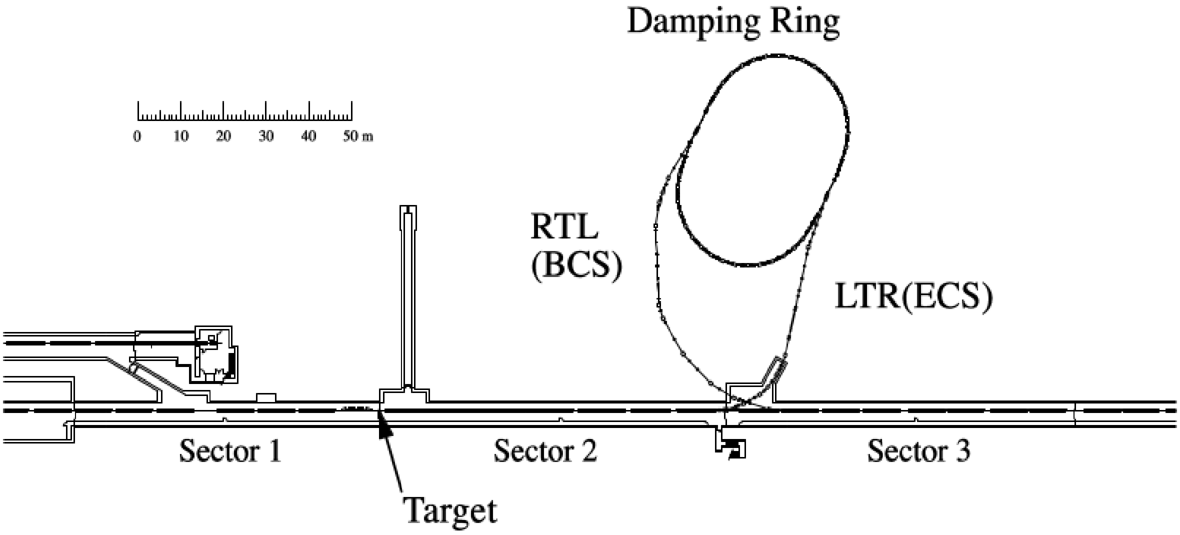

Figure 2.7 – The layout of the damping ring at SuperKEKB

The multi-turn injection scheme adopted at SuperKEKB, consists of a septum magnet where an orbit bump in the horizontal plane is provided by two kickers. During injection, two kicker units move the circulating beam to the septum and the injected beam is steered to minimize the coherent oscillation. The injected beam performs betatron oscillations around the circulating beam. These betatron oscillations are damped by synchrotron radiation and the bunch-by-bunch feedback system. This is called betatron phase space injection. The transverse damping time is 43 ms for LER and 58 ms for HER. The maximum injection rate is 25 Hz during continuous injection.

Since the injection is continuous and simultaneous among four rings, the injection ring needs to be changed frequently and the RF injection bucket needs to be controlled [23]. At SuperKEKB, the positron injection process cannot be finished before the next pulse is launched since the positron beam is damped for 40 ms before injection. Thus two processes go in parallel, the electron beam is injected while the positron beam is damped.

Concerning the bucket selection, a system that controls the injection into RF buckets to satisfy the requested fill pattern is controlled by the machine operator. This control is accomplished by introducing a delay time to the linac. Normally, the linac is synchronised to the revolution signal (the signal of one turn inside one ring, at SuperKEKB the frequency of one revolution is about 100 KHz).The delay time introduced to the linac corresponds to the desired time position of the injector RF bucket.

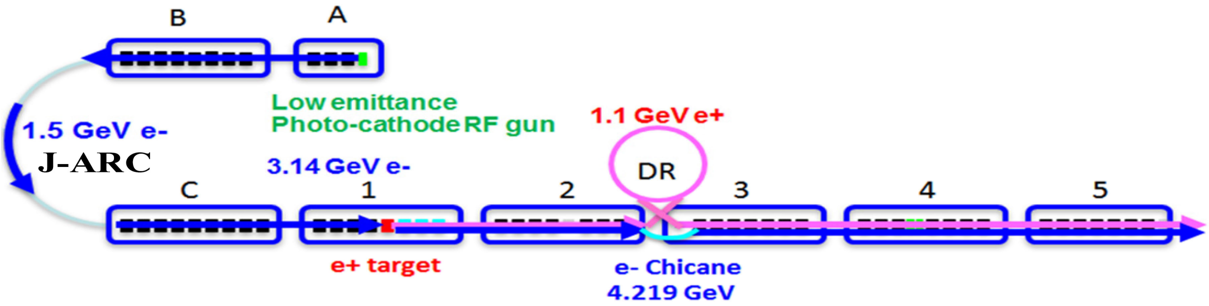

Figure 2.8 – The layout of the SuperKEKB injector linac

2.2.5 Vacuum system for both rings

In the upgrade from KEKB to SuperKEKB, there were many challenges in relation to the upgrade of the vacuum system [24], trying to use as much as possible the systems of KEKB. At SuperKEKB, 93% of the beam pipes are renewed for the LER and 82% of the beam pipes are reused for the HER. The main goal of the vacuum system is to achieve ultra-high vacuum ($P \approx 10^{-7}$ Pa with beams) in order to maintain small beam emittance and reduce the background noise in the Belle II detector due to the interaction of beam particles with the remaining gas molecules (for example: beam-gas Bremsstrahlung and Coulomb scattering).

In the presence of very high currents, the electron cloud effect [25][26] (see chapter 4) becomes very important in the LER and induces instabilities for the beam. In addition, the beam pipes are heated intensively due to the strong synchrotron radiation (SR). To cope with these effects, new beam pipes with antechambers were installed in the LER (fig. 2.9). By putting the NEG pumps and SR mask in the antechambers, the impedance of the beam pipe is reduced. As a result, new flanges and bellows were developed for these antechambers. To reduce the effect from the electron cloud, different measures were considered like roughening the antechamber wall, introducing solenoid fields and Tin coatings [27].

On the other hand, the energy reduction from 8 GeV to 7 GeV from KEKB to SuperKEKB for the electron beam makes the SR power tolerable with normal copper beam pipes. Consequently, the beam pipes from KEKB were reused in SuperKEKB, except in the wiggler section where the SR is stronger and where the normal copper beam pipes were replaced by beam pipes with antechambers.

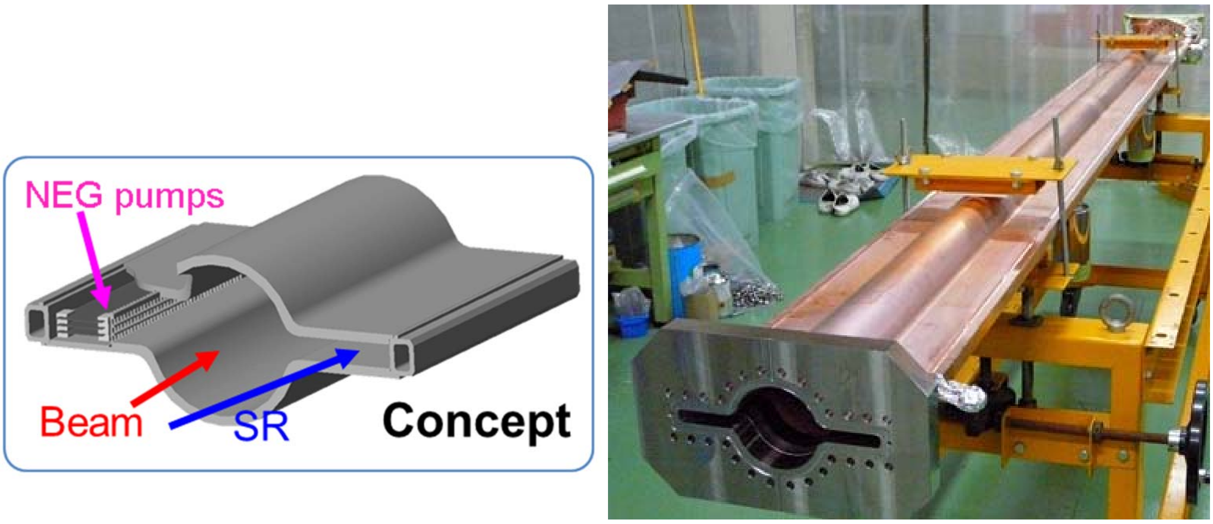

Figure 2.9 – The concept of antechamber on l.h.s and the antechambers for wigglers on r.h.s at SuperKEKB

2.2.6 Nano-beam scheme

The luminosity $\mathcal{L}$ can be represented in equation 2.1, where N_1 and N_2 are the number of particles in the two colliding bunches, f is the repetition frequency (colliding frequency), and σ_x and σ_x are the horizontal and vertical beam sizes respectively. This formula shows clearly that the luminosity is proportional to the beam currents and inversely proportional to the transverse beam sizes. Thus a high luminosity needs high beam currents and small beam sizes. The design luminosity at SuperKEKB is 8×10^{35} $\text{cm}^{-2}\text{s}^{-1}$ and the machine parameters are shown in the Table. 2.2.

$$\mathcal{L} = \frac{f N_1 N_2}{4\pi\sigma_x\sigma_y} \tag{2.1}$$

To achieve very small vertical beam size ($\sigma_y=\sqrt{\beta_y\varepsilon_y}$), the vertical β function must be strongly squeezed at the IP. But in the presence of relatively long beam sizes (5 mm and 6 mm), the hourglass effect [28] is an important limitation. It leads to the loss of luminosity for $\beta_y \leq \sigma_z$. In order to prevent the hourglass effect, beams are set to collide at a large Piwinski angle with very small spot sizes. The Piwinski angle is defined

Parameter	LER	HER
N	3.6×10^7	2.6×10^7
σ_x (μm)	10	11
σ_y^* (μm)	0.94	0.059

Table 2.2 – The machine parameters for a very high luminosity at SuperKEKB

in eq. 2.2, where θ_c is the total crossing angle, σ_x and σ_z are the horizontal beam size and the bunch length respectively. By colliding the two beams at an angle, the effective bunch length, representing the length of the overlap region, becomes much shorter. To satisfy the hourglass requirement (eq. 2.3) where ϕ is the half crossing angle i.e to be able to reduce the vertical β function, the horizontal spot size should be small and the crossing angle should be large. This is called the nano beam scheme (fig. 2.10) which was originally proposed in the context of the design of the SuperB collider [29]. SuperB was a high luminosity e^-e^+ collider aiming at the study of B meson physics, like SuperKEKB. It was supposed to be built near Rome, but was cancelled by the Italian government in 2012. The nano beam scheme is adopted at SuperKEKB where the vertical β functions will be ultra squeezed with superconducting focusing magnet systems at the IP, to attain vertical beam sizes of 60 nm, and the beams will collide at a large crossing angle of 83 mrad.

$$\theta_p = \frac{\theta_c \sigma_z}{2\sigma_x} \tag{2.2}$$

$$\beta_y^* \geq d = \frac{\sigma_x^*}{sin\phi} \tag{2.3}$$

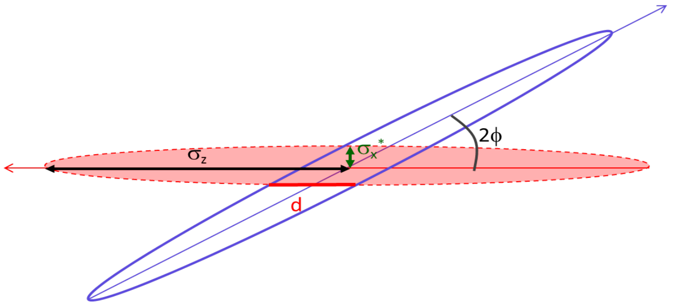

Figure 2.10 – The nano beam scheme at SuperKEKB

2.3 Belle II

Due to high currents and small beam sizes at SuperKEKB, an increase of the beam background level (10-20 times higher than KEKB) at the detector level is expected. In addition, the high luminosity will increase the event rate by 10 times which requires faster triggers, data acquisition and computing system. For all these reasons, the Belle detector is being upgraded to the Belle II detector (fig. 2.11).

2.3.1 Physics

The Belle II detector will start collecting data during first physics runs in 2018. It aims to accumulate 50 ab^{-1} of e^+e^- collision events by the middle of the next decade. Belle II will study the decays of the B meson to probe new physics scenarios, for instance through the search for new CP-violating phases, new physics with an extended Higgs sector (charged Higgs particle), also new physics directly at the tree-level such as right-handed currents. Unlike at hadron colliders like LHC, the clean environment at SuperKEKB allows the study of physics phenomena involving measurements of decays with multiple undetected particles like neutrinos. At SuperKEKB, B mesons are produced in pairs, so the momentum reconstruction of one of two B mesons by the full reconstruction of its daughter particles, allows the knowledge of the momentum of the other B meson even if it decays into undetectable particles.

At Belle II, the physics program is very wide and includes the study of several decays, and each decay corresponds to the probe of one or more physical phenomena. For example, the study of the CP violation in the decay modes of $B^0 \rightarrow \phi K_0$ and $B \rightarrow K^* \gamma$ allows the probe of new physics in the loop diagrams. The study of the decays $B \rightarrow D \tau^- \nu$ and $B \rightarrow \tau \nu$ allows the search of the charged Higgs boson. The semileptonic B decays allow to clarify the experimental situation of the CKM matrix element $|V_{ub}|$. In addition, the abundant production of $\tau^+ \tau^-$ pairs at SuperKEKB allows the search for lepton-flavour-violating (LFV) τ decays with one of the cleanest environments to probe new physics.

2.3.2 Sub detectors

The Belle II detector consists of several sub detectors [30], and each sub detector has its defined role. Here is a list of the Belle II sub detectors with a brief definition of their tasks.

- The vertex detector (VXD) detects the decay point of the B meson. It is made up of two parts, the inner layer is the Pixel detector (PXD) and it consists of two DEPFET layers (DEPleted p-channel Field Effect Transistor). The outer part is the Silicon Vertex Detector (SVD) and is made up of four layers of DSSD (Double Sided Strip Detectors). The VXD is the closest detector to the IP.

- The CDC (Central Drift Chamber) is the main tracking device for charged tracks. Its smaller cell sizes compared to Belle improves the momentum and dE/dx resolution.

- TOP (Time of Propagation) sub detector is used for the particle identification in the barrel region of Belle II. It consists of 16 modules, each module consists of two quartz bars, one mirror, one prism and an array of photo-detectors. The TOP detector measures

Cherenkov photons generated from charged tracks.

- ARICH (Aerogel Ring Imaging Cherenkov) is used for particle identification in the forward cap.

- ECL (Electromagnetic Calorimeter) is used to detect photons and π^0 from the B meson decay. It consists of 8736 CsI(Tl) crystals with typical dimension of $6\times6\times30$ cm^3.

- KLM (K_L-Muon detector) detects the K_L and muons, it consists of a large area of thin planar detectors interleaved with the iron plates of the 1.5 T solenoid's flux return yoke.

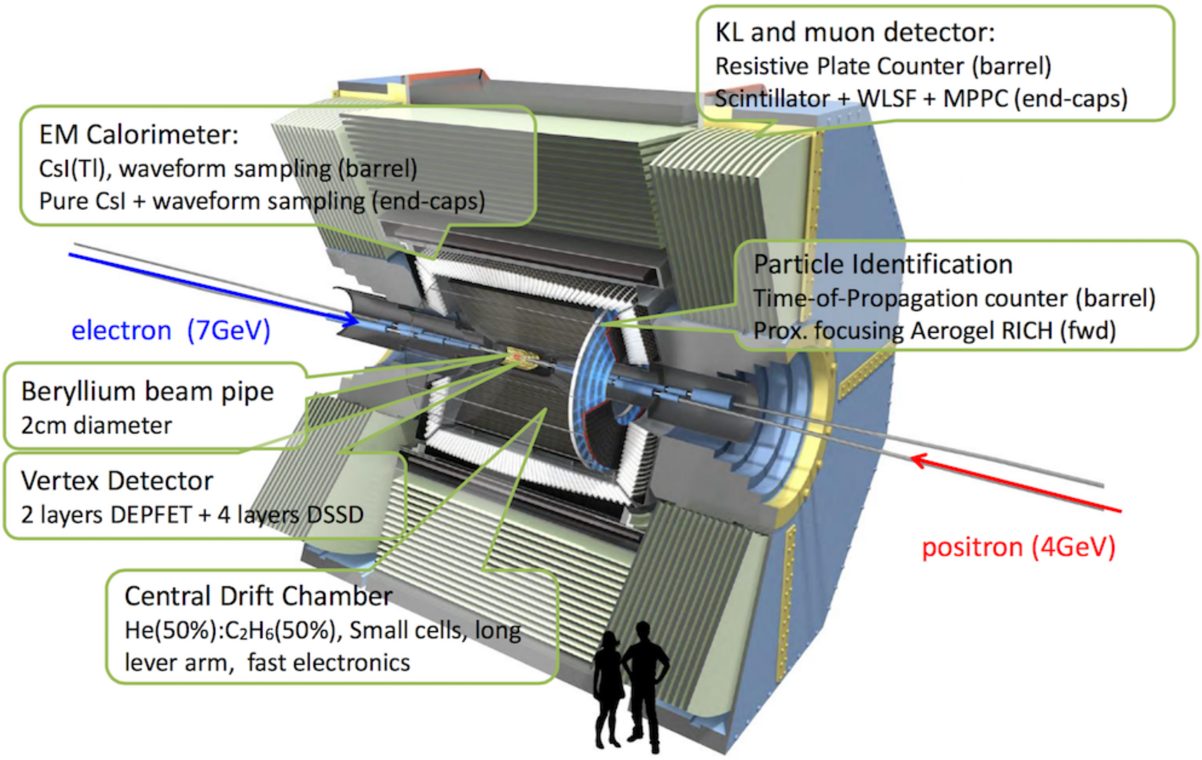

Figure 2.11 – The layout of the Belle II detector

2.4 BEAST II

The goals of the BEAST II (Beam Exorcism for a STable experiment project) [31][32] is to estimate, measure, mitigate and protect against beam backgrounds. In the presence of very high currents, very small beam sizes and high luminosity, the level of backgrounds increases in the interaction region (IR) and thus in the Belle II detector. These backgrounds may damage the sub detectors of Belle II and affect the precision of its measurements. The backgrounds considered are divided into two types, backgrounds from single beam processes like beam-gas Bremsstrahlung, Coulomb scattering, Touschek scattering, synchrotron radiation and injection noise, and backgrounds from non interesting collision events at the IP like radiative Bhabha scattering and 4-fermion final state QED processes.

BEAST II started its commissioning along with the phase 1 commissioning of SuperKEKB (see chapter 4). It aims to validate the MC (Monte Carlo) simulation of the backgrounds by comparing expected levels to measurements in dedicated sensor devices. It serves also to provide information on beam losses to SuperKEKB operators. The detector components of BEAST II measure the background levels by measuring the X-rays, fast/thermal neutrons, charged particles, etc ... BEAST II consists of seven sub detectors (fig. 2.13).

In the phase 1 commissioning of SuperKEKB, our fast luminosity monitors measured particle losses (see chapters 5 & 6) from single beam processes which are correlated to what was measured by BEAST II detectors. The same simulation tools were used to estimate the loss rates which enabled a cross check of the reliability of the simulation code. Data from our diamond sensors were integrated in the BEAST II ntuples to provide a feedback of beam losses at different locations in the rings.

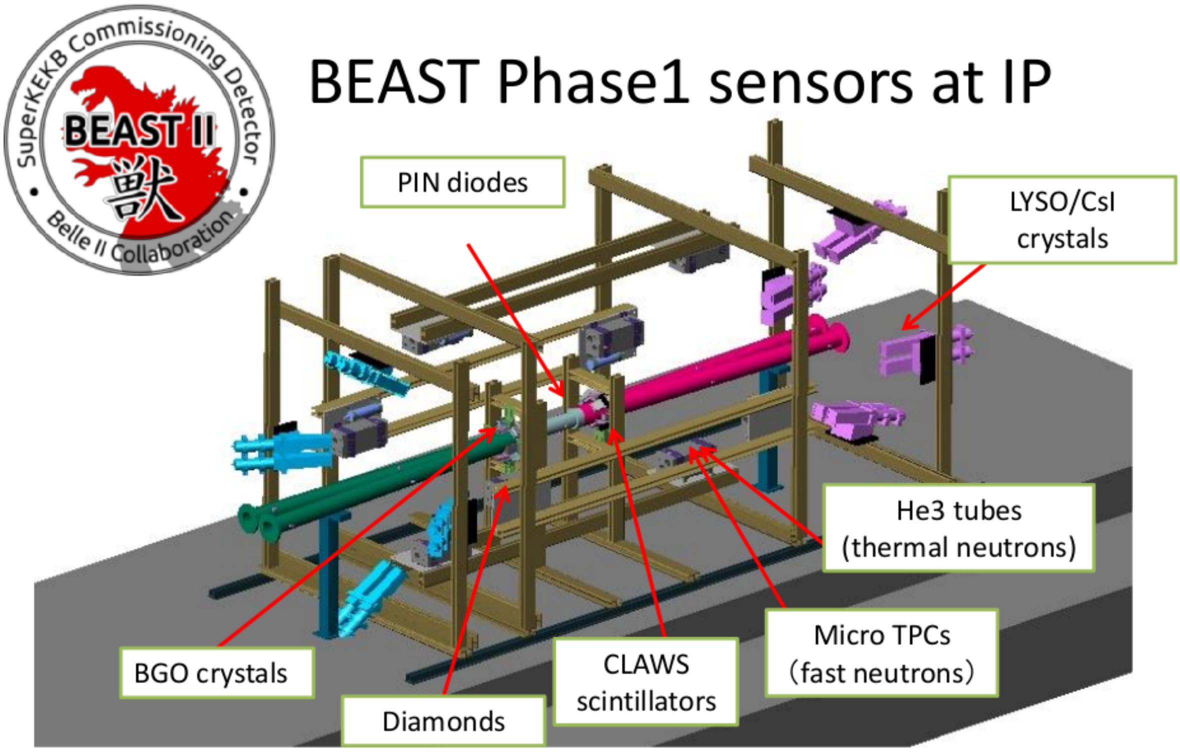

Figure 2.12 – The layout of the BEAST II in the interaction region of SuperKEKB at phase 1

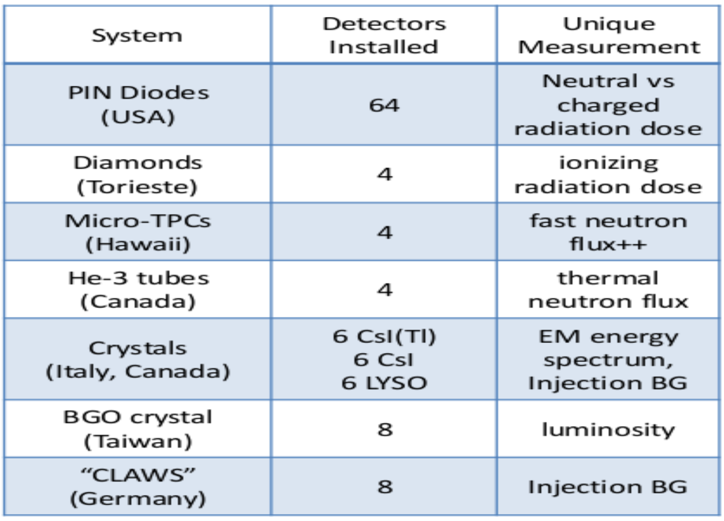

System	Detectors Installed	Unique Measurement
PIN Diodes (USA)	64	Neutral vs charged radiation dose
Diamonds (Torieste)	4	ionizing radiation dose
Micro-TPCs (Hawaii)	4	fast neutron flux++
He-3 tubes (Canada)	4	thermal neutron flux
Crystals (Italy, Canada)	6 CsI(Tl) 6 CsI 6 LYSO	EM energy spectrum, Injection BG
BGO crystal (Taiwan)	8	luminosity
“CLAWS” (Germany)	8	Injection BG

Figure 2.13 – The list of sub detectors of BEAST II [32]

Chapter 3
Fast Luminosity Monitoring

3.1 Motivations And Specifications

To achieve very high luminosity, and as mentioned and explained in chapter 2, SuperKEKB will adopt the nano-beam scheme which implies very strong focusing at the IP resulting in very small vertical beam sizes. Because the beam sizes are tiny, the luminosity is very sensitive to the stability of the final focusing elements whose vibrations cause an orbit motion which could be 4 or 5 times larger than the vertical beam sizes. Such vibrations cause vertical oscillations of the beam at the IP at frequencies up to 100 Hz, whereas horizontal movements are expected at few Hz. The resulting orbit differences between the two beams at the IP lead to a luminosity degradation.

3.1.1 Methods and Techniques

Orbit feedbacks in both horizontal and vertical planes are needed to minimise the losses [33]. The vertical orbit feedback is performed using four BPMs (Beam Position Monitors) around the IP to detect the vertical orbit offset. A dithering system is dedicated for the horizontal feedback, it mainly consists of a lock-in amplifier, dither coils (symmetric coils mounted on the normal cylindrical beam pipe and asymmetric coils mounted on Antechamber beam pipe (fig. 3.1)) and a fast luminosity monitor.

Eight sets of dither coils are placed in the LER. Each set consists of two pairs of coils, one kicks the beam horizontally at 77 Hz and the other gives a vertical kick to the positron beam in order to correct the x-y coupling caused by the misalignment of the horizontal coils. The fast luminosity monitor consists of two different detectors, single crystalline diamond sensors (sCVD) (l.h.s of fig. 3.2) used by our group at LAL, and Cherenkov and Scintillator detectors (r.h.s of fig. 3.2) used by the ZDLM (Zero Degree Luminosity Monitor) [34] group at KEK. The luminosity monitor measures the relative luminosity at 1 KHz and feedback corrections are applied on the second time scale. Both detectors are placed next to each other, just outside the beam pipe in both rings of SuperKEKB, and will measure the signal from the radiative Bhabha process at zero photon scattering angle.

Fast enough luminosity measurements are needed as input for luminosity optimisation and feedback in the presence of such dynamic imperfections. A relative precision of 10^{-3}

in 1 ms over all 2500 bunches in phase 3 ($\mathcal{L}= 8\times10^{35}$ cm^{-2}s^{-1}), with less than 1% contamination from non-luminosity scaling effects, is specified. In parallel, average single bunch luminosities are very important for beam dynamics studies, related for instance to the continuous top-up injection scheme used at SuperKEKB.

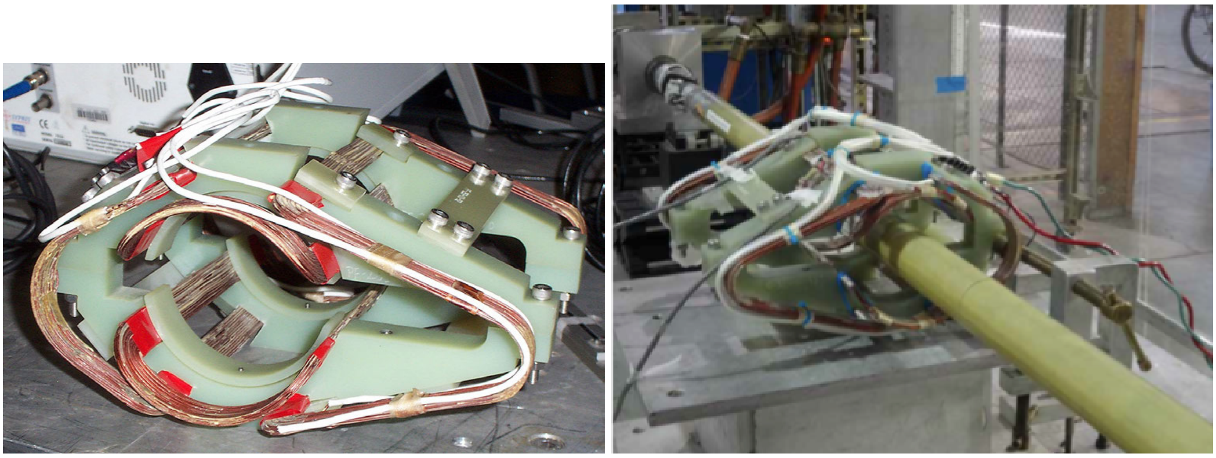

Figure 3.1 – Example of Ante-chamber asymmetric dithering coil at SuperKEKB

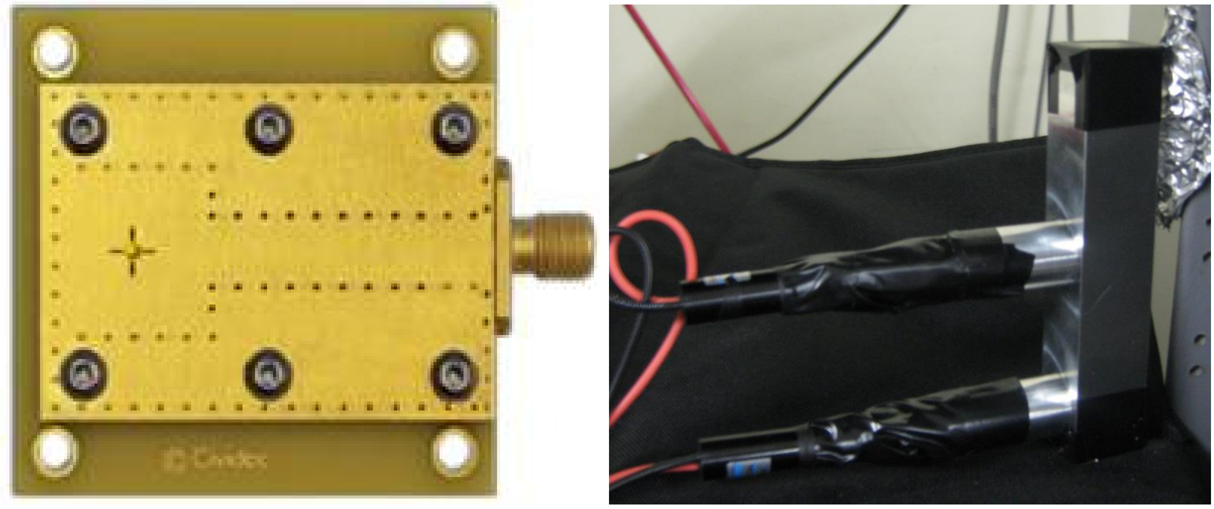

Figure 3.2 – Single crystalline diamond sensor (sCVD) on l.h.s and the Cherenkov and Scintillator detectors on r.h.s

3.2 Evaluation of dithering algorithm

A dithering system kicks the beam in the horizontal direction at 77 Hz (T $\approx$ 13 ms). In order to see the effect of such a kick on the luminosity performance of the SuperKEKB, fast luminosity measurement is required. In this case, we perform our fast luminosity monitoring using diamond sensors along with Cherenkov and Scintillation detectors. In order to reconstruct the modulation in the luminosity from the horizontal dithering, considering the conditions of the sampling theorem [35] which states that sampling frequency should at least be twice faster than the frequency of the signal itself, we choose to perform luminosity measurements each 1 ms (at 1 KHz)($\approx$ 13 times the dithering frequency).

In an attempt to estimate the minimum rate of luminosity events in the luminosity monitors required to give an efficient feedback on the luminosity, a Monte-Carlo simulation using Mathematica [36] was performed by S. Uehara at KEK. In the following, the main features of this simulation and its results are briefly summarized [37].

The dithering frequency "$\mathrm{f_0}$=77Hz" modulates the orbit of one of the two beams as "r=sin(2πft)". The Luminosity depends on this parameter with a Gaussian function given in equation 3.1 and represented in fig 3.3. Dithering quantities "p" and "q" represent the amplitude of dithering (the kick of the magnets) and the shift of the operation point from luminosity peak respectively. If $|q|$ >p, the operation point of the dithering system goes up and down on a side of the slope and thus we lose a quite large percentage of the luminosity, on the other hand if $|q|$ <p, it goes up and down across the peak with negligible luminosity losses. If we are at the top of the luminosity profile, the FFT (Fast Fourier Transform) of the luminosity measurement profile (fig. 3.4) gives a peak at $2\times\mathrm{f_0}$ (l.h.s of fig. 3.5), whereas as we go very far from the peak luminosity, the peak of the FFT is at $\mathrm{f_0}$ (r.h.s of fig. 3.5). Our aim is to evaluate the measurement rate (precision) needed to sufficiently decrease the peak at $\mathrm{f_0}$ while increasing the peak at $2\times\mathrm{f_0}$ to ensure maximal luminosity. The model of the lock-in amplifier [38] is employed, where the measured signal is decomposed into its Fourier components at the base frequency $\mathrm{f_0}$ and the double frequency $2\times\mathrm{f_0}$. The components at the base frequency are expressed as $\sum_{i=1}^{N}\cos(2\pi \mathrm{f_0 t}_i)$ and $\sum_{i=1}^{N}\sin(2\pi \mathrm{f_0 t}_i)$ whereas they are expressed as $\sum_{i=1}^{N}\cos(4\pi \mathrm{f_0 t}_i)$ and $\sum_{i=1}^{N}\sin(4\pi \mathrm{f_0 t}_i)$ at the double frequency, where t_i is each $\mathcal{L}$ measurement at a rate of 1 KHz and N is the total number of $\mathcal{L}$ measurements in a period of time sufficient to reconstruct the $\mathrm{f_0}$ and $2\mathrm{f_0}$ base and double frequencies via FFT. It is typically 1 second since feedback corrections are applied every second. The simulation considered different values of "p" at different counting rates. As a conclusion, a precision of 1.6×10^{-3} over 1 ms (event rate of 400 KHz in 1 ms) was found to be sufficient to control the horizontal orbit every 1 second based on the dithering feedback. Furthermore, the baseline frequency (l.h.s of fig. 3.6) information provides much better precision to pick up the true peak position than the double frequency (r.h.s of fig. 3.6).

$$\mathcal{L}(t) = exp(-\frac{(q + p \times sin(2\pi f t))^2}{2}) \tag{3.1}$$

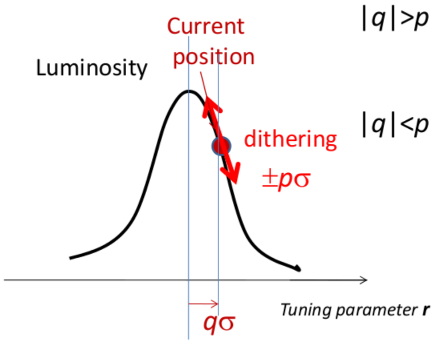

Figure 3.3 – The dithering parameters on the luminosity profile

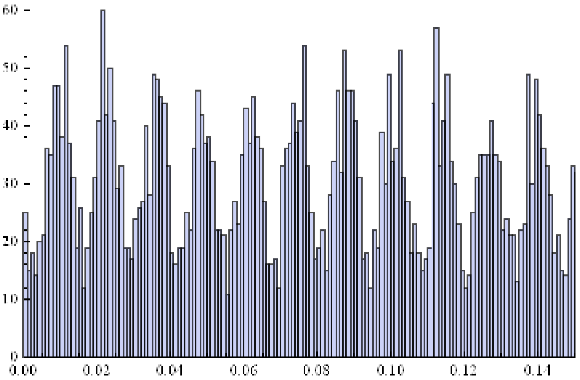

Figure 3.4 – The luminosity signal in the luminosity monitor from Monte-Carlo simulation at a given counting rate and dithering with modulation amplitude “p”

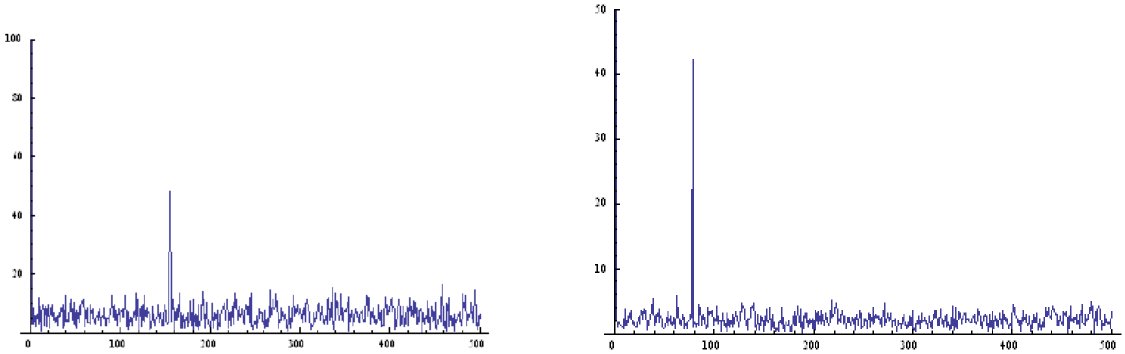

Figure 3.5 – The FFT of the square root of the measured luminosity profile with a peak at the double frequency (2×f_0) on l.h.s and a peak at the baseline frequency (f_0) on the r.h.s

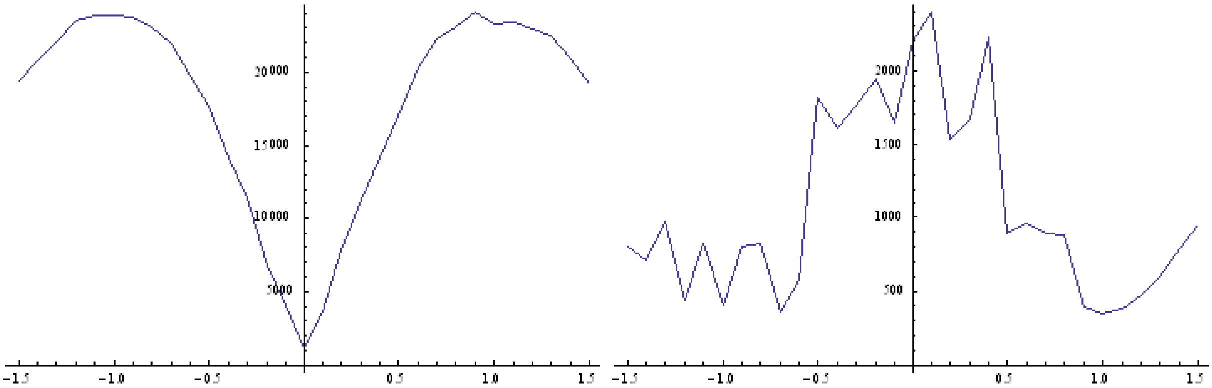

Figure 3.6 – The profile of the signal size at p=0.2 and rate=400 KHz per 1 ms of the baseline frequency on l.h.s and the double frequency on r.h.s

3.3 Our Project

Our group at LAL contributes to the orbit feedback project at SuperKEKB by supplying fast luminosity measurements using diamond sensors (DS) as input. We choose the DS thanks to its radiation hardness and relatively fast signals. The DS will measure signals from radiative Bhabha at zero photon scattering angle, by installing them just outside the beam pipe, downstream of the IP, at locations with event rates consistent with the aimed precision (Table. 3.1), and small enough contamination by backgrounds from single-beam particle losses. The number of Bhabha particles produced at the IP is proportional to the luminosity as given by equation 3.2, where N is the number of Bhabha particles produced at the IP, σ is the radiative Bhabha cross section at the IP in cm^2 (0.15 10^{-24} cm^2), $\mathcal{L}$ is the luminosity in cm^{-2} s^{-1} and $\mathcal{T}$ is the time in s. We aim at a precision of 10^{-3} in 1 ms. The fraction of the cross section which must be detected in the sensors to achieve the specified precision is shown in Table. 3.1. For the very high luminosity $\mathcal{L}$=8×10^{35} cm^{-2}s^{-1}, the simulation results reported in section 2 of this chapter show that a precision of 10^{-3} is needed for the dithering feedback in the horizontal plane. However, for a lower luminosity ($\mathcal{L}$=10^{34} cm^{-2}s^{-1}) the horizontal beam sizes are twice larger, which means that the precision on the luminosity measurement to control the horizontal orbit could be looser by some factor, which can be determined by the same simulation.

$$N = \sigma \times \mathcal{L} \times \mathcal{T} \tag{3.2}$$

Luminosity (cm^{-2} s^{-1})	Number of Bhabha	Aimed precision	Required fraction
8 x 10^{35}	1.2 × 10^8 in 1 ms	10^{-3} in 1 ms	8.3 x 10^{-3}

Table 3.1 – Minimum required fractions of Bhabha cross-section in the sensors

3.3.1 CVD diamond sensors

Diamond detectors are fabricated by the CVD (Chemical Vapour Deposition) process. In this process, a small amount of hydrocarbon gas such as methane is mixed with molecular hydrogen and oxygen gas. The mixture is then ionised so that carbon based radicals settle down on a substrate, normally silicon or molybdenum, and link together with σ-type bonds forming a diamond lattice (fig. 3.7) [39].

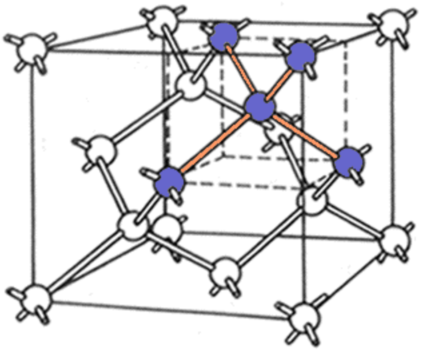

Figure 3.7 – The diamond lattice

3.3.1.1 Properties

The diamond sensor (DS) has many interesting properties which allow it to be one of the best candidates for solid state radiation detectors. It has the highest thermal conductivity among solid state materials in addition to a high electrical insulation. A detailed explanation of the diamond's properties, characterisation, functionality and types is found in [39]. Here, a few properties and advantages of the DS over other semiconductor materials are reviewed. A comparison among diamond, silicon and germanium is presented in (Table. 3.2).
The diamond has a very high binding energy which makes it very insensitive to radiation. As well, diamond is characterised by a large band gap which reduces the leakage current and thus decreases the noise. However, the large band gap in the diamond sensor also results in a weaker signal compared to Si and Ge for instance, but in our project, we are able to measure the signal from one electron using a 500 μm for a low luminosity, however for a higher luminosity, we will use a 140 μm with a window design (explained later in this chapter) which will increase the signal. In addition, diamond has high electron and hole mobilities which results in fast charge collection and thus in fast signals, in the range of few ns. The width of the signal depends on the thickness of the diamond, for example a signal width of 4-5 ns corresponds to a 500 μm diamond. The minimum energy needed to create an electron/hole pair in the diamond is 13 eV. One MIP (Minimum Ionising Particle) creates 36 e^-/h pairs per μm in the diamond. The bias field which we choose to apply to collect e^--h pairs is E=0.8 V/μm. Normally we can apply a bias voltage until

1 V/μm, however, thanks to the high quality DS, the charge collection efficiency reaches 100% long before this bias voltage (at $\approx$ 0.2 V/μm). For security, we chose to apply a voltage bias a bit smaller than 1 V/μm, let it be 0.8 V/μm.
One disadvantage of the diamond sensor is the difficulty of having large active area, which constraints our measurements to a part of the shower, however this is not a critical problem in the case of the window (see later in the chapter) where we will be able to achieve our aimed precision by increasing the electromagnetic shower.

Property	Diamond	Silicon	Germanium
Atomic number Z	6	14	32
Density ρ [g.cm^{-3}]	3.51	2.33	5.33
Radiation length X$_0$ [cm]	12	9.4	2.3
Relative dielectric constant ε	5.7	11.9	16.3
Band gap E$_g$ [eV]	5.47	1.12	0.67
Resistivity ρ_c [Ω cm]	$>10^{12}$	2.3×10^5	47
Electron mobility μ_e [cm^2 V^{-1} s^{-1}]	1800	1350	3900
Hole mobility μ_h [cm^2 V^{-1} s^{-1}]	1200	480	1900
Energy to create e$^-$h pair E$_{eh}$ [eV]	13	3.6	3 (at 77 K)

Table 3.2 – Properties of different solid state detectors at T=300 K

3.3.1.2 Operation

The operation and the readout of the DS is simple and is presented in fig. 3.8. A charged particle traverses the DS creating e$^-$/h pairs depending on its energy. A high voltage is applied at the electrodes of the diamond, opposite charges drift to the electrodes. The output signal resulting from the voltage drop is read by an oscilloscope. Amplification of the signal is necessary in the case of small signal, i.e low intensity of incident particles and/or very thin DSs. The energy deposition in the DS is a Landau distribution, as confirmed by performing a GEANT4 simulation using a 500 μm DS with a beam of incident electrons of 3 GeV (fig. 3.9). These electrons are considered as MIPs. A MIP is a charged particles with an energy loss rate close to the minimum, and the energy of a MIP electron is around 1.6 MeV.

3.3.1.3 Characterisation with radioactive sources

To better understand the behaviour of the signal in the DS, we performed tests in the clean room at LAL using radioactive sources.

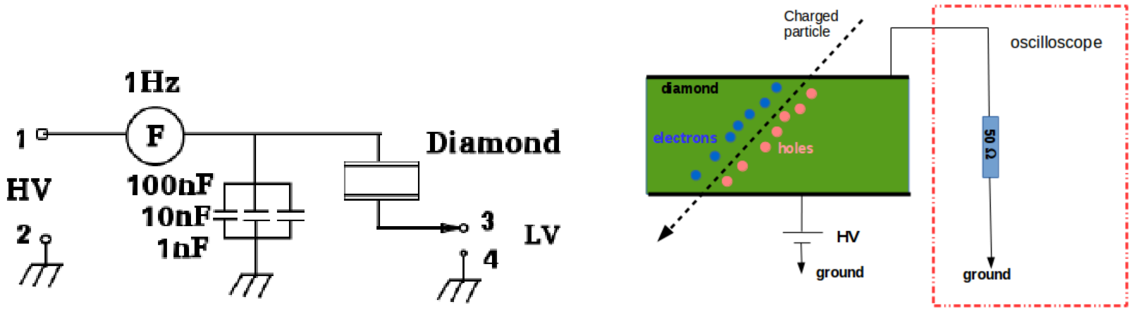

Figure 3.8 – The readout circuit on l.h.s and the operation scheme of the diamond sensor on r.h.s

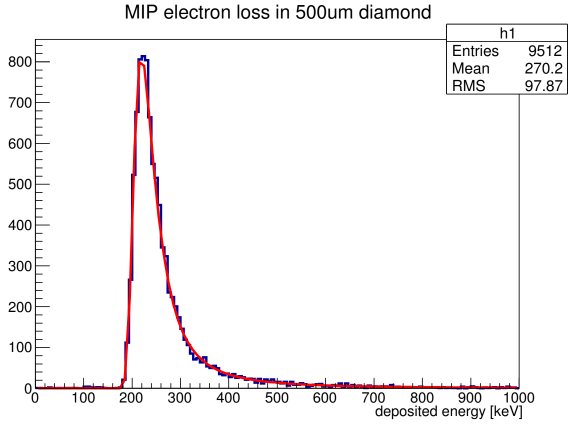

Figure 3.9 – Landau distribution of energy deposited by MIPs in 500 μm diamond sensor simulated by GEANT4

Experimental setup

Tests were performed on a 140 μm, 4x4 mm^2 DS from CIVIDEC [40] using the β radioactive source ^{90}Sr. The experimental setup is shown in fig. 3.10. It consists of the β source ^{90}Sr, the 140 μm DS (l.h.s of fig. 3.11), a charge amplifier from CIVIDEC whose shaping time constant is about 10 ns (r.h.s of fig. 3.11), a scintillator, a low voltage supply providing 12 V (l.h.s of fig. 3.12) for the charge amplifier, a high voltage supply for the DS (r.h.s of fig. 3.12), and an oscilloscope to read the signal. Since the charge amplifier is unipolar, the high voltage (-100 V) on the DS is applied to polarize negatively and to obtain negative pulses at output of the DS.

A special mechanical stand shown in fig. 3.10 was prepared for the tests on the DS. The 140 μm sCVD is connected to the charge amplifier which is powered with 12 V and both are laid on the middle bench of the mechanical stand. On the top part, there is a special opening for the electrons emitted by the radioactive source to hit straight the 4x4 mm^2 diamond below. Just below the diamond, a scintillator is used to trigger, in order to collect signals from MIPs only, i.e the MIP will traverse the diamond depositing some of its energy, without being absorbed, and will then hit the scintillator and give a signal to trigger. The ^{90}Sr undergoes a cascade of two β decays (fig. 3.13) resulting in electrons with a whole spectrum of energies. One MIP produces 36 e$^-$/h per μm in the DS, and since the energy to produce one e$^-$/h pair is 13 eV, then an electron with an energy $E_{e^-} < E_{min}$=65.52 KeV (13 eV $\times$ 36 e$^-$/h $\times$ 140 μm) will be absorbed in the 140μm thick DS. So the scintillator trigger makes sure that E_{e^-} is greater than E_{min}.

Two types of trigger are used, one is a trigger on all the events including signals from the MIPs and noise from the amplifier, and the second one is the multistage trigger. In the multistage trigger, a window of 6 ns is considered, this allows selecting only the events in the DS whose rising edge arrives 6 ns before the rising edge of the signal in the scintillator. The window of 6 ns is chosen after taking into account the delay of the signal in the scintillator due to the difference in the cable lengths connecting both the scintillator and the diamond to the oscilloscope, and the fact that the electron passes the DS before hitting the scintillator.

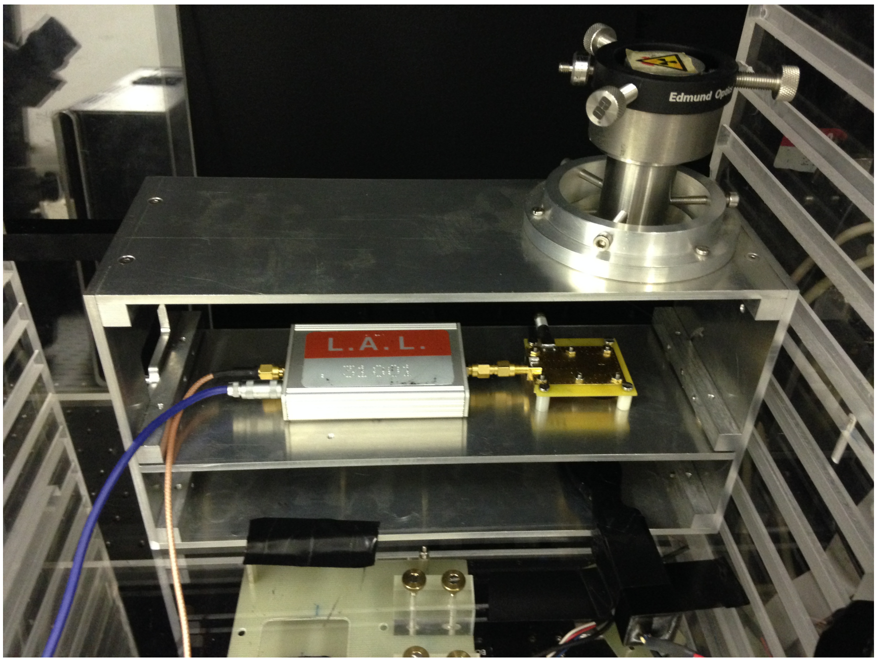

Figure 3.10 – The experimental setup of the tests on the diamond sensor in the clean room

Figure 3.11 – 140 μm CIVIDEC diamond sensor on l.h.s and the CIVIDEC charge amplifier on r.h.s

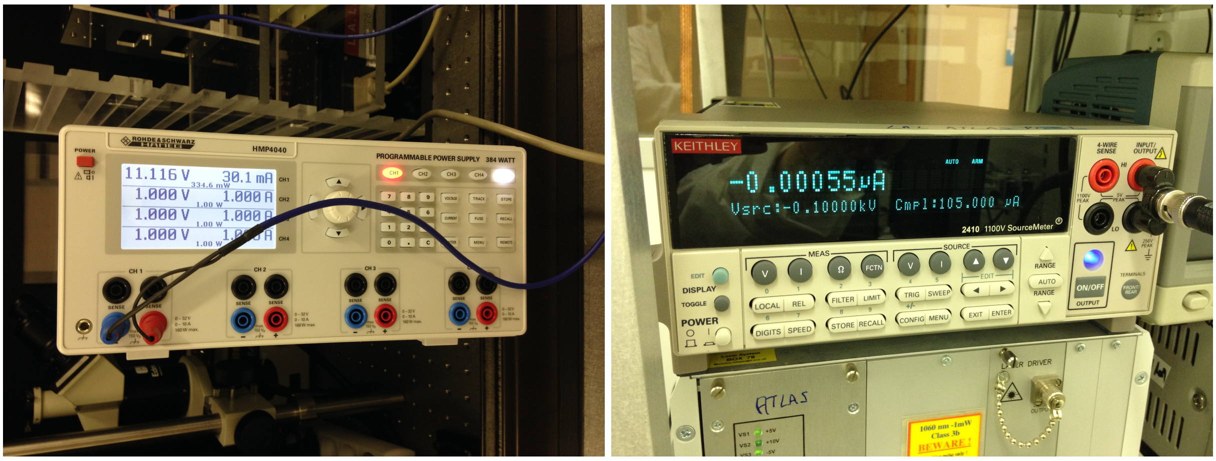

Figure 3.12 – Low voltage supply for the charge amplifier on l.h.s and high voltage supply for the diamond sensor on r.h.s

Signal characterisation with radioactive source

Data is collected during typically 10 hours and then analysed using Matlab and Root. One of the motivations of the data analysis was to reconstruct the Landau distribution of the MPV (Most Probable Value) of the signal. Using the trigger on all the events, screenshots of the oscilloscope are shown in fig. 3.14. The pink signal is the signal from the 140μm DS and the yellow signal is the signal from the scintillator. The MPV of the Landau distribution of the signal of one MIP in the 140 μm DS is 3.2 mV. This value is calculated after taking into account the gain of the charge amplifier which is 4mV/fC. One MIP creates 5040 e^-/h in 140 μm of diamond (36 e^-/h per μm × 140μm) , which corresponds to a total charge of $\approx$ 0.8 fC. When amplified, the signal gives a value of

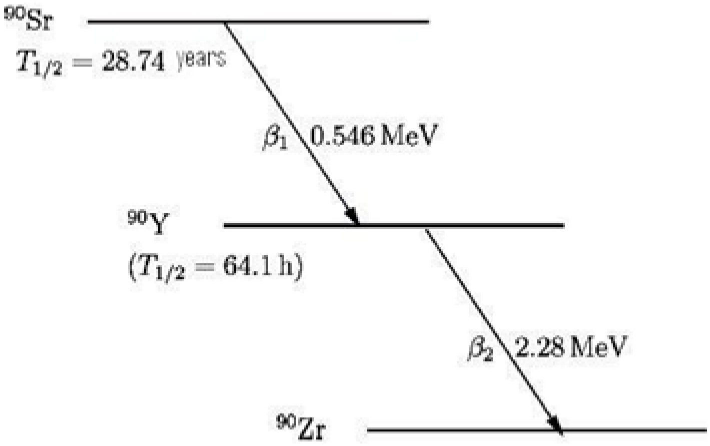

Figure 3.13 – The ^{90}Sr decay scheme

3.2 mV (0.8 fC × 4 mV/fC) and this could be read on the oscilloscope. The vertical sensitivity used is 5 mV/div. So this agreement implies that the 140 μm DS has close to 100 % charge collection efficiency for a bias voltage of 100 V. L.h.s of fig 3.14 shows a coincidence of the scintillator (yellow) with a signal from the sCVD (pink) at ≈ 10.5 mV, which corresponds to the tail of the Landau distribution, while r.h.s of fig. 3.14 shows a coincidence with a sCVD signal at ≈ 4 mV, close to the MPV of the Landau distribution. The noise of the charge amplifier is characterised by 1000 e$^-$ which corresponds to 0.64 mV. The MPV of the Landau distribution is at 3.2 mV which is just 5 times higher than the RMS of the noise and thus the reconstruction of the Landau distribution shows the signal attached to the noise and rather difficult to separate as shown on l.h.s of fig. 3.15. The large peak in fig. 3.15(l.h.s) represents part of the noise of the amplifier and the small peak represents the signal from the MIPs in the sCVD. The MPV of the signal is at ≈

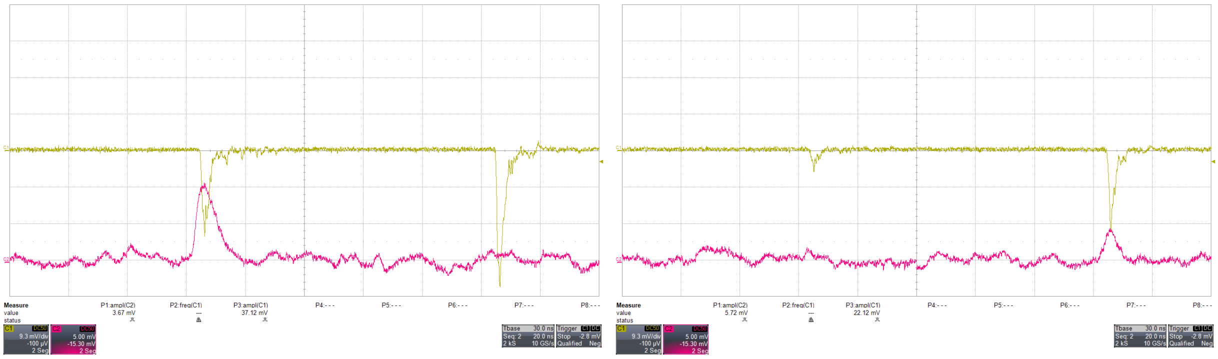

Figure 3.14 – Screenshots from the oscilloscope, pink: 140μm diamond and yellow: scintillator, diamond signal in the tail of Landau on l.h.s and diamond signal close to the maximum of Landau on r.h.s

3.8 mV ($>$ 3.2 mV). On r.h.s of fig. 3.15, the analysis of the noise of the amplifier shows a Gaussian distribution shifted by 0.36 mV, which represents a pedestal which should be subtracted from the signal. This pedestal explains the difference of 0.4 mV (3.8 - 3.2 mV) between the data and calculation and thus by shifting the data by this factor we will obtain the calculated value. The RMS (0.68 mV) of the analysed noise on r.h.s of fig. 3.15 matches to the given characteristics of the amplifier. The energy deposited in a 500μm DS is larger than in a 140μm DS due to the larger thickness, thus signal is well separated from the noise (fig. 3.16).

Using the multistage trigger mentioned before, the Landau reconstruction becomes easier since we just trigger on real signals. The l.h.s of fig. 3.17 shows the reconstructed signal distribution of MIPs in the 140 μm sCVD, where the Landau fit gives a MPV (Most Probable Value) of 3.5 mV. The r.h.s of fig. 3.17b shows the diamond noise from the data taken during the multistage trigger. The same scenario of the matching between data and calculation of the maximum of the Landau distribution explained before could be applied for this case as well.
In addition to the Landau reconstruction, we need to verify that the position in time of the MPV of the signal doesn't move significantly and doesn't depend on the magnitude of the signal. This is very important because in our measurements we are sampling at 1 GSPS (Giga Sample Per Second), which means each 1 ns. To be precise in the reconstruction of the shape of the signal amplified by the charge amplifier and to determine the maximum which represents the total charge collected in the diamond during the acquisition time, this maximum should move with an RMS less than 1 ns. For this study, we use a 500 μm sCVD biased with -200 V and we trigger using a multistage trigger at 6 ns using the same already described experimental setup.

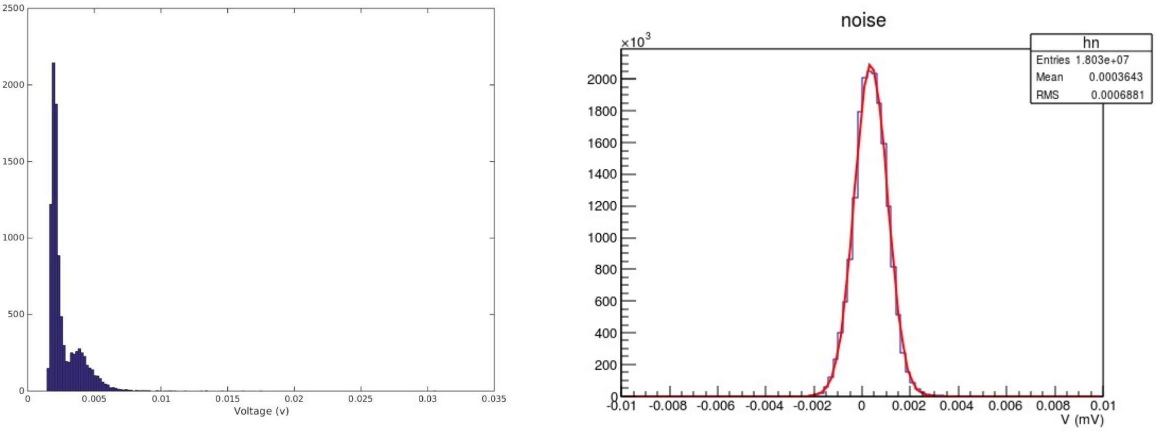

Figure 3.15 – Landau reconstruction of 140 μm sCVD on l.h.s and noise reconstruction of the charge amplifier on r.h.s in case of triggering on all events in the DS

The calculated maximum of the Landau distribution of the signals from the 500 μm

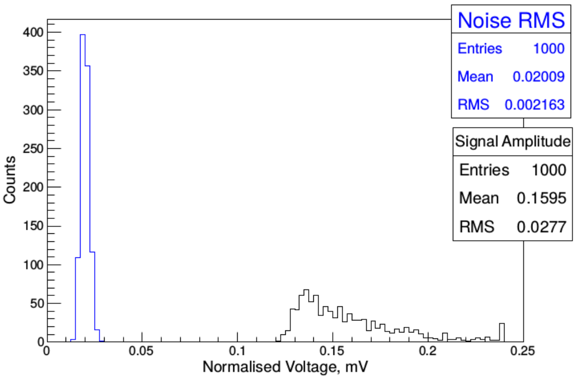

Figure 3.16 – Signal and noise amplitude distributions in the 500μm diamond sensor [41]

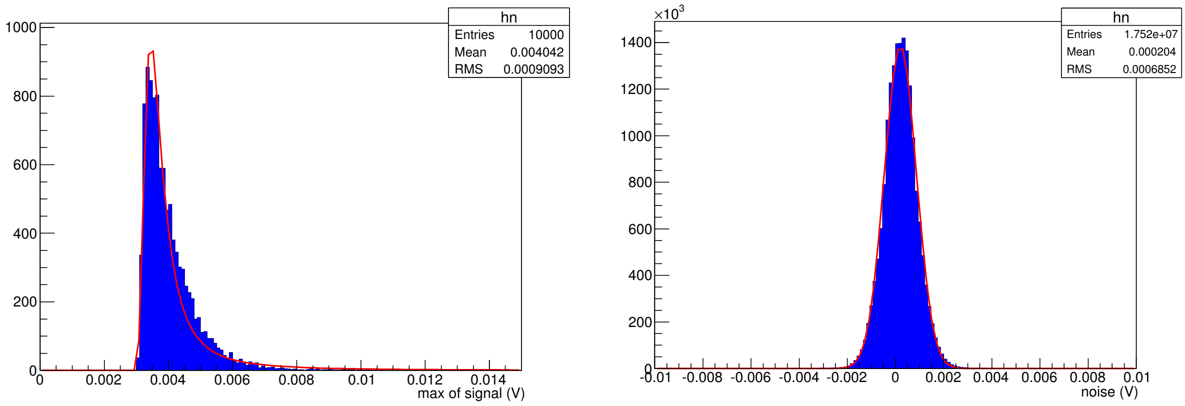

Figure 3.17 – Landau reconstruction of 140 μm sCVD on l.h.s and noise reconstruction of the charge amplifier on r.h.s in the case of multistage trigger

sCVD is 11.52 mV. The Landau reconstruction from the data is shown on the l.h.s of fig. 3.18, with a MPV at 12.3 mV. The distribution of the fitted RMS of the signal in the sCVD is shown on r.h.s of fig. 3.18. The plot shows an average RMS of ≈ 7 ns. The distribution of the position in time of the maximum of the signal is shown on l.h.s of fig. 3.19. The Gaussian distribution is centred at 0.8 ns with an rms of 1.67 ns (> 1 ns). Since we trigger on the scintillator, then the position in time of the maximum of the diamond may strongly depend on the position in time of the maximum of the scintillator. The r.h.s of fig. 3.19 represents the position of the maximum of the scintillator. We can clearly see from this figure that the position of the maximum of the scintillator moves a lot with an rms of 1.64 ns, in addition we can see three populations.

We subtract the position in time of the maximum of the diamond signal (l.h.s of fig. 3.19) from one population of the position in time of the maximum of the scintillator corresponding to times < 4 ns and we get the distribution shown in fig. 3.20. The RMS (1.5 ns) is still larger than 1 ns. But since the distribution of the position in time of the

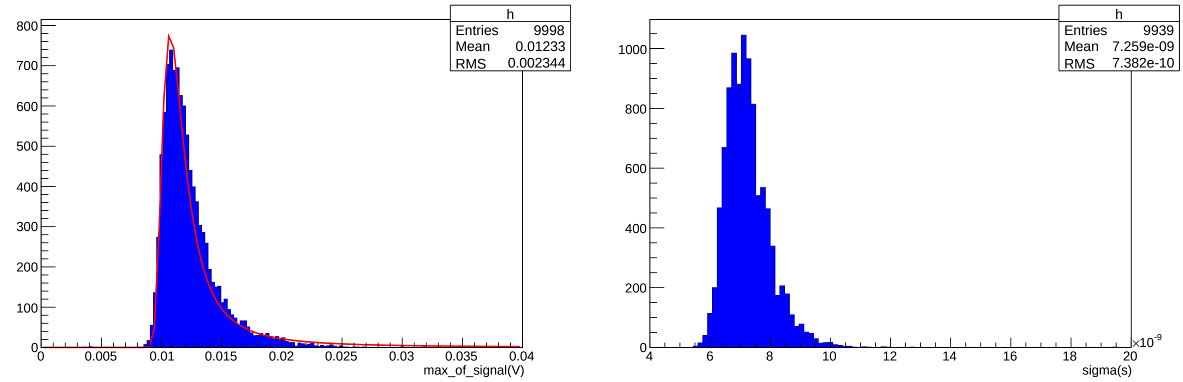

Figure 3.18 – Landau reconstruction of the signal from 500 μm sCVD on l.h.s and the width of the signal of the 500 μm sCVD on the r.h.s in the case of multistage trigger

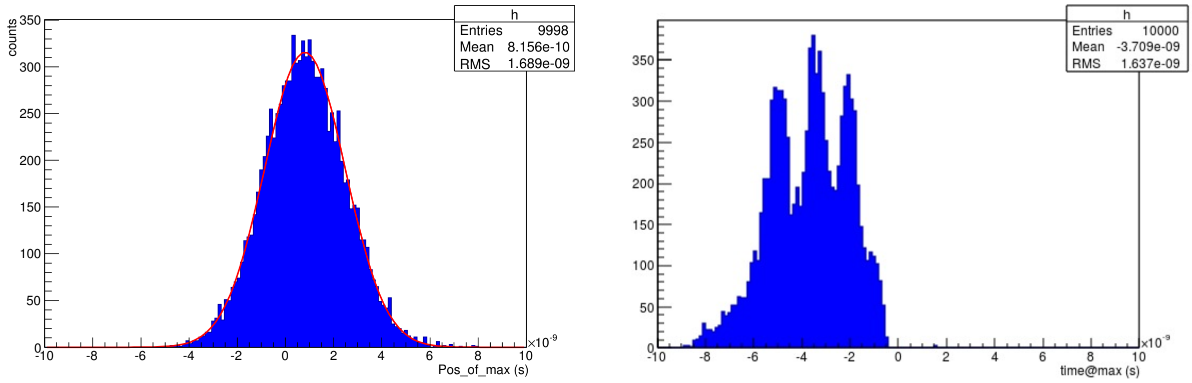

Figure 3.19 – Position of the maximum of the signals in the 500 μm sCVD on l.h.s and in the scintillator on r.h.s

maximum of the scintillator is a three population distribution, then it is very difficult to conclude on the RMS of the position of the signal in the sCVD.

To make sure that there are no other reasons behind the relatively large RMS of the position in time of the signal from the diamond other than that of the scintillator, we need also to check that there is no correlation between the maximum of the signal and its position in time. On l.h.s of fig. 3.21, we can see the maximum of the signal in the sCVD as a function of its position in time, and the plot shows no correlation between these two parameters which is a very good sign. As well, r.h.s of fig. 3.21 shows the maximum of the signal in the sCVD as a function of its width, also showing no significant correlation.

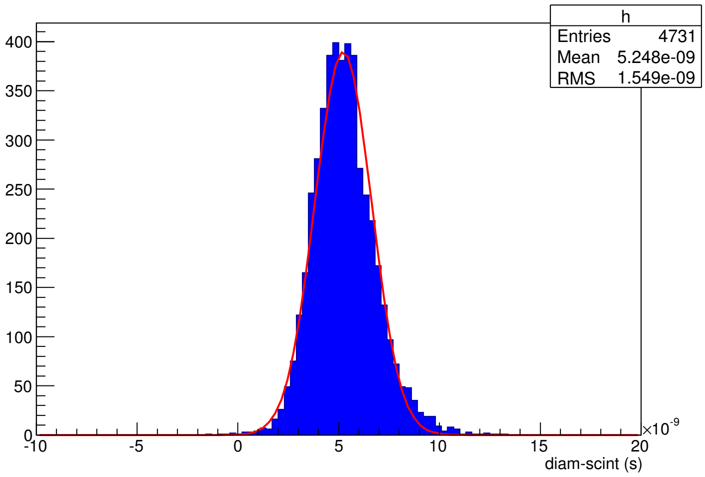

Figure 3.20 – Difference of the position of the maximum of the diamond and scintillator

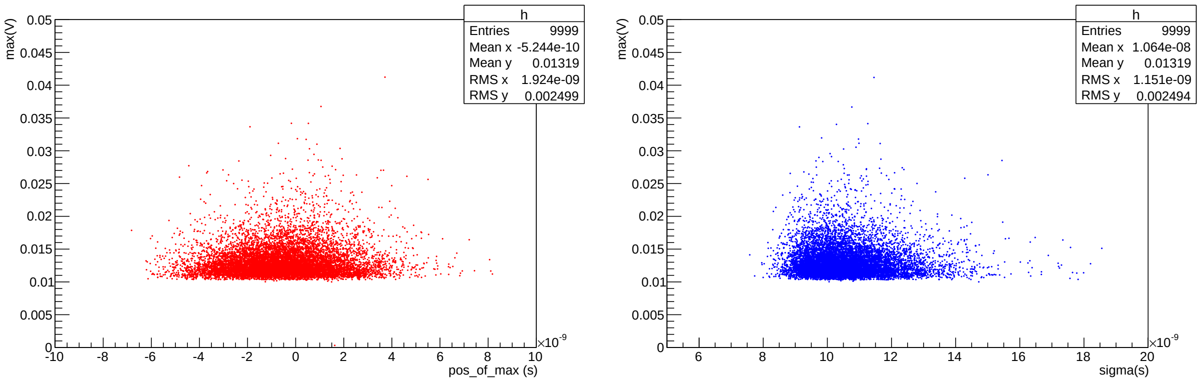

Figure 3.21 – The maximum of the signal as a function of its position in time in the sCVD on l.h.s and as function of its width on r.h.s

Data from LEETECH @ PHIL

Diamond sensors are not only tested in the clean room but also at PHIL (PHoto Injector at LAL) [42], where a new facility named LEETECH (Low Energy Electron TECHnique) [43] is installed. PHIL (fig. 3.22) is a photo-injector followed by a six-meter long beam line which delivers electron bunches up to 5 MeV with an intensity of 10^8 to 10^{10} particles per bunch and at a repetition frequency of 5 Hz. LEETECH (fig. 3.23) is a facility for detector R&D, which uses the electron beam of PHIL to deliver mono-chromatic low energy electrons with adjustable energy and intensity using a bending magnet with adjustable field in addition to collimators at its entrance and exit.

Among the tested detectors are a 500 μm CIVIDEC DS and another 500 μm DS prototyped and fabricated at LAL [44]. The data from the CIVIDEC DS were used to analyse the distribution of the position in time of the maximum of the signal. Unlike the tests with a radioactive source in which just one electron hits the DS at once, the tests at LEETECH correspond to 1,2,3,... electrons hitting the DS depending on the magnetic field and the collimator aperture. The distribution of the maximum of the signal of the DS is represented on l.h.s of fig. 3.24. The data taking from LEETECH is collected with a trigger on the laser of PHIL, the distribution of the position in time of the maximum of the laser's signal is represented on r.h.s of fig. 3.24. The maximum of the signal from the laser moves with an RMS of ≈ 1.7 ns. If we subtract the position in time of the maximum of the DS signal from that of the laser, we get the distribution shown in fig. 3.25. The

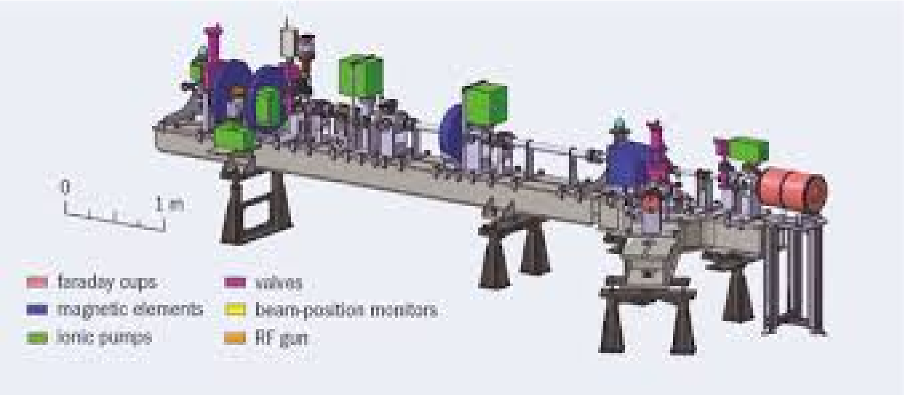

Figure 3.22 – The PHIL accelerator design

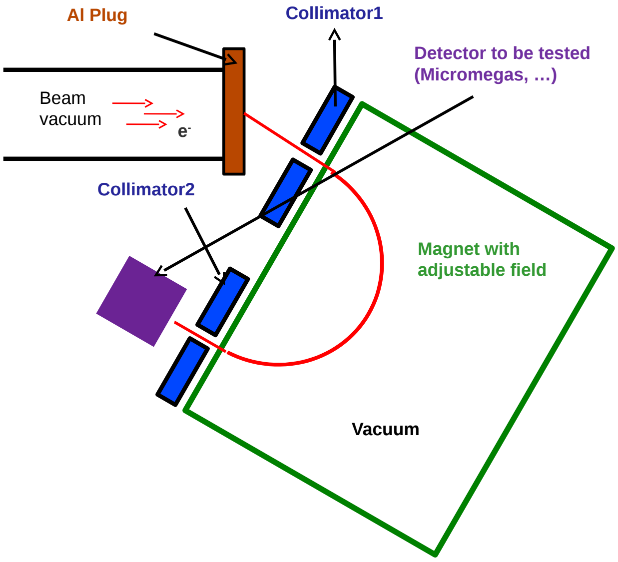

Figure 3.23 – The LEETECH facility design

RMS of the distribution of the difference is 1 ns, which is less than the RMS (1.5 ns) given by the same distribution when using the scintillator instead of the laser as a triggering apparatus. This confirms that the position in time of the maximum of the signal in the DS depends mainly on the position of the signal of the trigger.

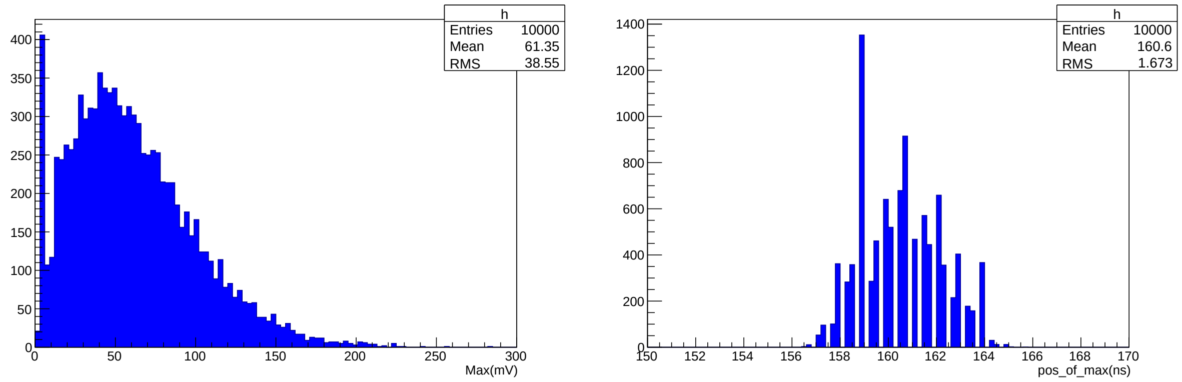

Figure 3.24 – The maximum of the signal in the sCVD on l.h.s and the position in time of the maximum of laser signal at PHIL on r.h.s

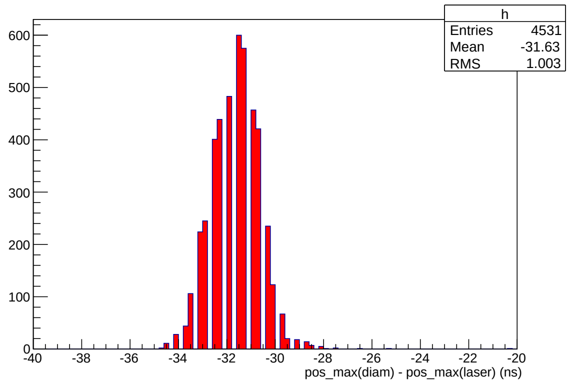

Figure 3.25 – Difference of the time position of the diamond and laser signals

3.4 Position of the diamond sensor in both rings

3.4.1 Radiative Bhabha at zero photon scattering angle

To measure luminosity, we need to collect events produced at the IP with rates proportional to the luminosity. We choose to measure events from a well known physical process: radiative Bhabha at vanishing photon scattering angle (fig. 3.26), which has a large cross section (≈ 200 mbarn). The considered process is one of the main sources of particle losses in a very high luminosity e^+e^- collider such as SuperKEKB. The particles of the electron and positron beams scatter through the exchange of a quasi-real photon at almost zero angle. The virtual photon interacts with a particle of the other beam and loses energy by emitting a real photon. The particle which emits the virtual photon, called spectator, keeps its energy and stays in the beam, however, the scattered particle loses part of its energy and will be deflected downstream of the IP at different locations, mainly after bending magnets, and will exit the vacuum chamber (fig. 3.27). The diamond sensors placed just outside the vacuum pipe measure the signal from the charged secondary particles, resulting from the interaction of the lost Bhabha particles with the material of the vacuum pipe.

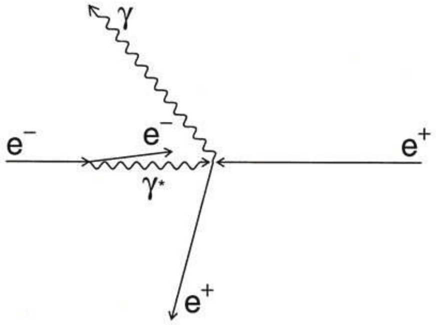

Figure 3.26 – Radiative Bhabha process at zero photon scattering angle

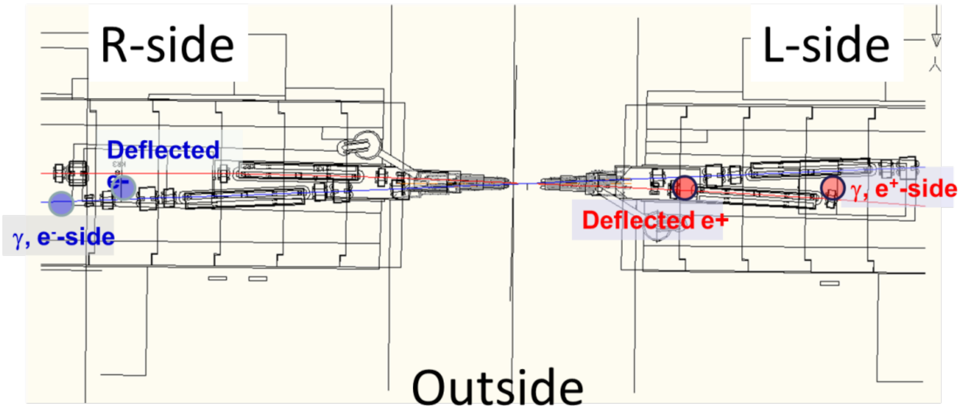

Figure 3.27 – Deflected Bhabha particles after optical elements downstream of the IP at SuperKEKB

3.4.2 Case of LER

3.4.2.1 Generation of Bhabha positrons with GUINEA-PIG++

GUINEA-PIG is a program to simulate beam-beam interactions in high-energy e^+e^- linear colliders, written in C language by D. Schulte [45]. It includes pinch effect, beamstrahlung, pair creation and calculation of hadronic backgrounds. It was upgraded to GUINEA-PIG++ [46] at LAL, which is its C++ version. This code is very important for the R&D of future linear colliders. It is able to simulate the interaction of an electron beam with a positron beam and predict the luminosity of the collision in the presence of pinch and disruption effects resulting from the very dense charge distributions in such colliders.

The input file of GUINEA-PIG++ contains the parameters of both beams, including the energies, intensities, β functions, emittance and bunch length. Normally, the code is prepared to simulate head on collisions, but in the case of SuperKEKB, the collision is at an angle. This is taken into account by replacing the total intensities by the intensities within the overlap region, and replacing the bunch length (σ_z) by the effective bunch length ($\sigma_{zeff}=\frac{\sigma_x}{sin\theta}$, where θ is the crossing angle (2θ=83 mrad)). The output files contain the energies and angular distributions of the incident beams, the Bhabha particles (electrons and positrons) and the Bhabha photons. The energy of the Bhabha particles extends from very low energy to the beam energy (4 GeV for e^+ and 7 GeV for e^-) (fig.3.28). The angular distributions of the Bhabha particles are shown in fig. 3.29 & 3.30. These distributions are similar to the angular distributions of the beams ($\sqrt{\frac{\varepsilon_x}{\beta_x}}$,$\sqrt{\frac{\varepsilon_y}{\beta_y}}$), electron beam: ($2\times10^{-4}$, 6.2×10^{-5}) and positron beam: (2.1×10^{-4}, 8.7×10^{-6}).

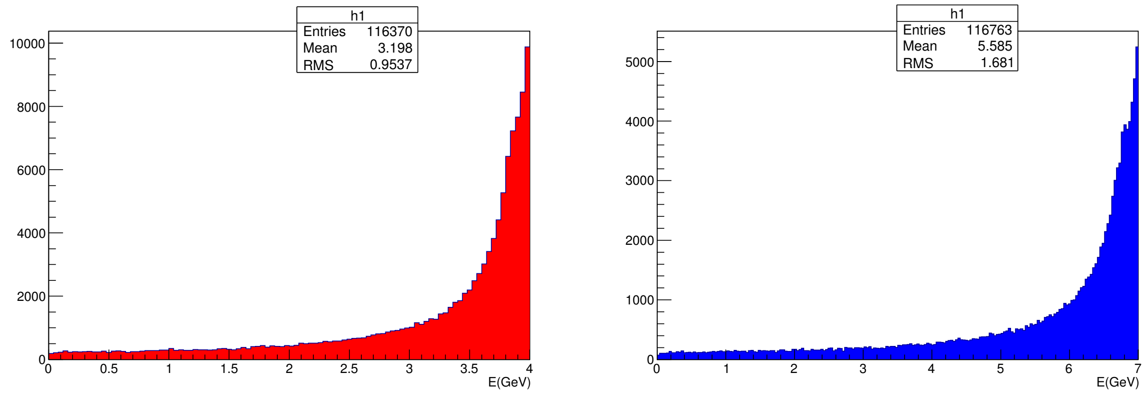

Figure 3.28 – The energy distribution of Bhabha positrons on l.h.s and of Bhabha electrons on r.h.s

3.4.2.2 Particle Tracking

After being generated and to be able to choose the optimal location of our DS in the LER, Bhabha positrons are tracked to different locations downstream of the IP. The updated lattices of both rings were provided by Y. Funakoshi. Tracking took place using SAD (Strategic Accelerator Design) [47]. SAD is developed at KEK in Japan, and is used by scientists at KEK and elsewhere. SAD is a very powerful tool for simulation, design and commissioning studies. All the simulation codes for the SuperKEKB commissioning were prepared within the SAD framework.

As shown on l.h.s of fig. 3.28, the energy of Bhabha positrons ranges from very low energies to the beam energy (4 GeV). Very low energy Bhabha positrons will be lost after traversing the first optical elements in the lattice downstream of the IP.
When a bunch of particles passes through the uniform field of the bending magnet, particles with the beam energy will bend on the correct trajectory, high energy particles will bend less and take the longest trajectory inside the magnet, whereas low energy particles will bend more (fig. 3.31). In the case of Bhabha positrons, the magnitude of the energy deviation due to the emission of a photon can be large and results in the loss of the particle.

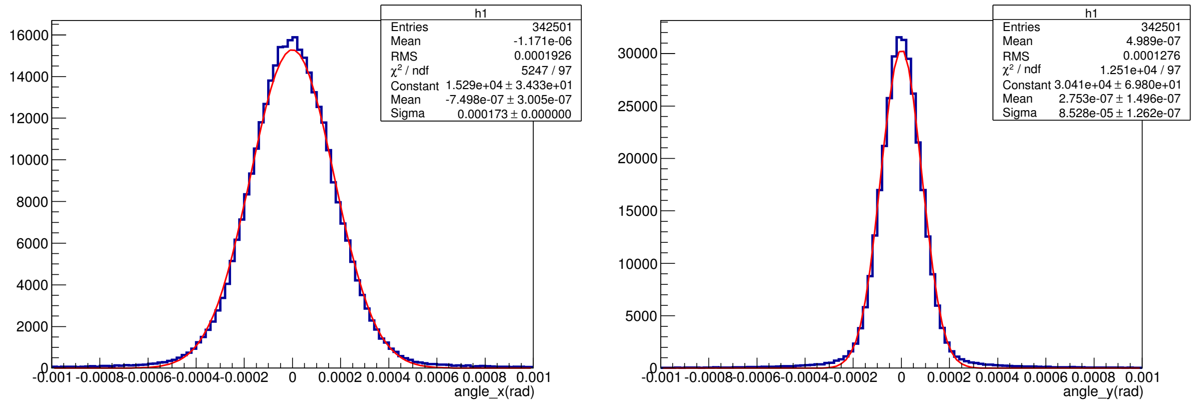

Figure 3.29 – Angular distributions of Bhabha positrons in the horizontal plane on l.h.s and in the vertical plane on the r.h.s

At the IP, the produced Bhabha particles are still inside the beam, the separation of the Bhabha particles from the beam particles is clearer after bending magnets, we can see that for example in fig. 3.32 after tracking the beam positrons (blue) and Bhabha positrons (red) to the exits of the third and fourth bending magnets. I tracked the Bhabha positrons to various locations downstream of the IP, after bending magnets, after quadrupoles and in drifts. The physical aperture of the beam pipe is 40 mm starting from ≈4 m downstream from the IP. In the following, I show few plots of the tracked

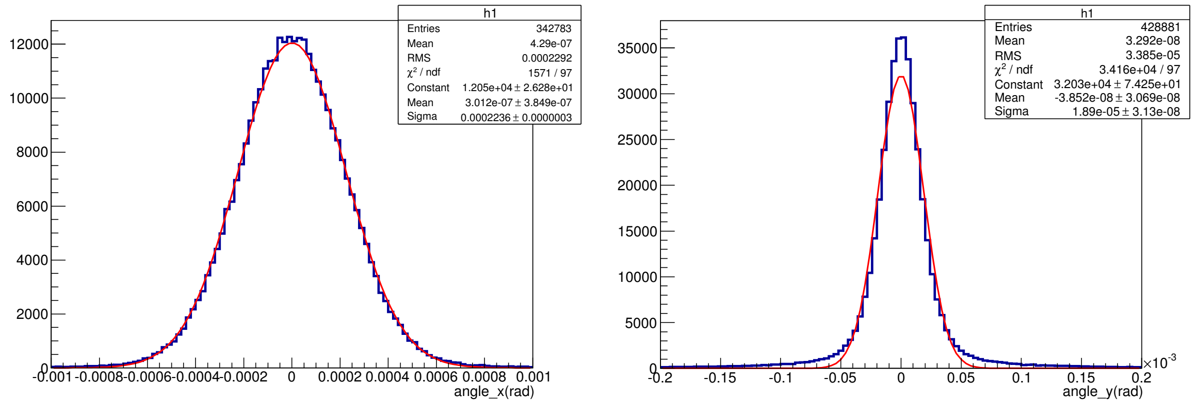

Figure 3.30 – Angular distributions of Bhabha electrons in the horizontal plane on l.h.s and in the vertical plane on r.h.s

Bhabha positrons after bending magnets. In fig. 3.33, we can see the horizontal position distribution of the Bhabha positrons as a function of their energies after the third and fourth bending magnets. We can see a very nice linearity in the E-x plane, in which low energy particles go close to the edge of the vacuum chamber and high energy particles stay close to the center of the vacuum chamber. It is clear from the plots that the low energy side is at +x and it is where we have installed our DS. Fig. 3.34 represents the en-

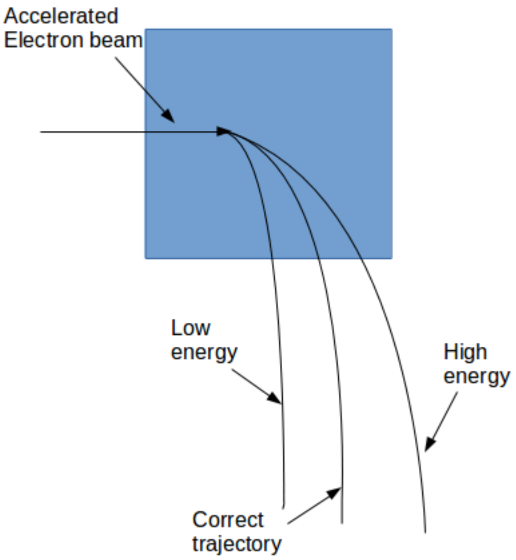

Figure 3.31 – Accelerated beam in a bending magnet

ergy spectrum of the Bhabha positrons after the third and the fourth bending magnets, the green represents the particles that have been already lost before the magnets, the blue represents the particles intercepted in the DS and the red represents the particles that remain in the beam pipe. We can see that after the fourth bending magnet we don't detect any Bhabha positron in the DS, this is explained by the fact that the fourth bending magnet is a very big magnet (Table. 3.3) and far from the IP, which means that very few low energy particles will reach it and will get lost inside it. On the other hand, after the third bending magnet 72 particles out of 10000 produced Bhabha positrons are intercepted in the DS. This fraction is close to the fraction required to attain the specified precision, but there is no adequate geometry and not enough space for the equipments as shown in fig. 3.35. Fig. 3.35 shows the β functions and dispersion functions in the horizontal and vertical planes of the LER lattice 27 meters downstream of the IP.

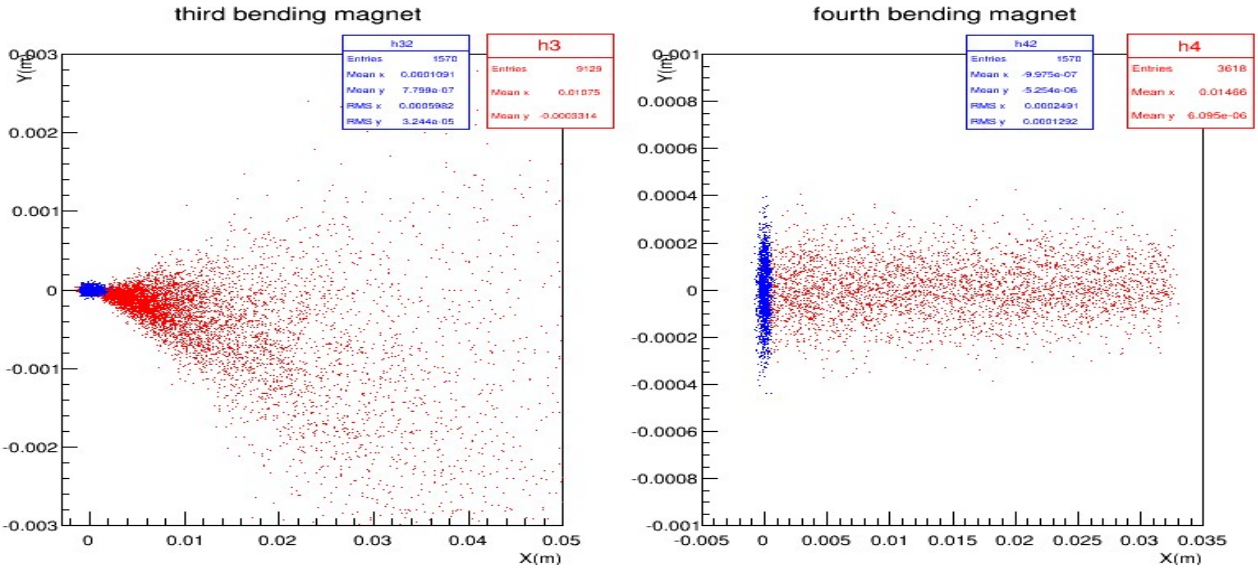

Figure 3.32 – Transverse distribution in x and y of beam positrons (blue) and Bhabha positrons (red) after third and fourth bending magnets

Unlike the third and fourth bending magnets, the horizontal position distribution of the Bhabha positrons as a function of their energies shows a strange tail after the first and

Name	Number	Length (m)	Position from IP (m)	Type
BC1LP	First	0.34	4.03	vertical
BLC1LP1	Second	1.5	5.48	horizontal
BLC1LP2	Third	2.23	7.53	horizontal
BLC2LP	Fourth	4.18	22.17	horizontal

Table 3.3 – The list of the first four bending magnets downstream of the IP in the LER

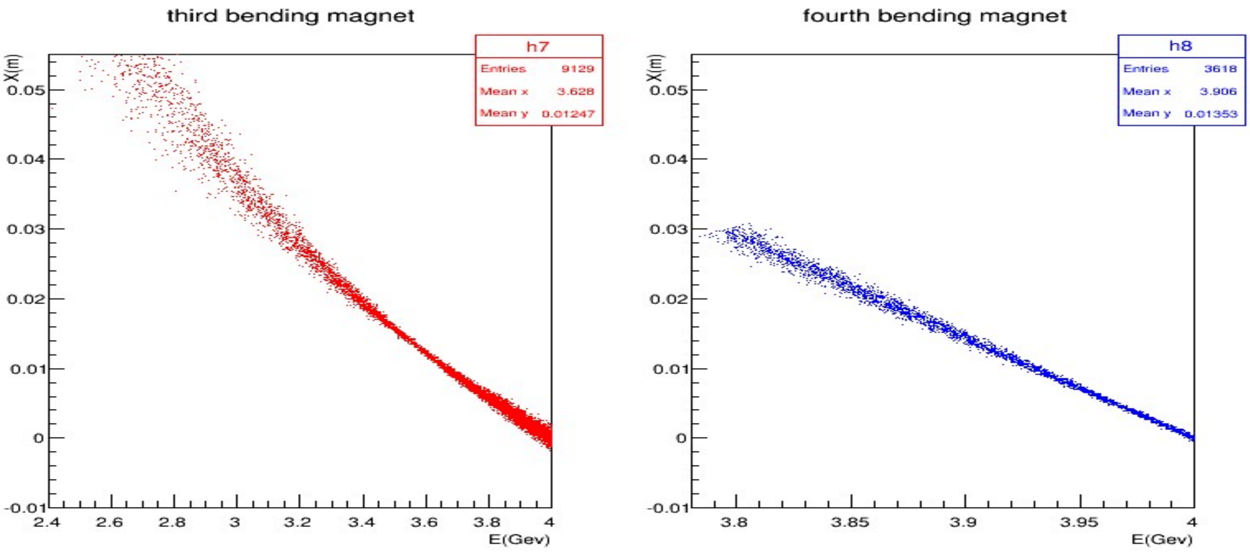

Figure 3.33 – The horizontal position distribution of Bhabha positrons as a function of their energies, after third and fourth bending magnets

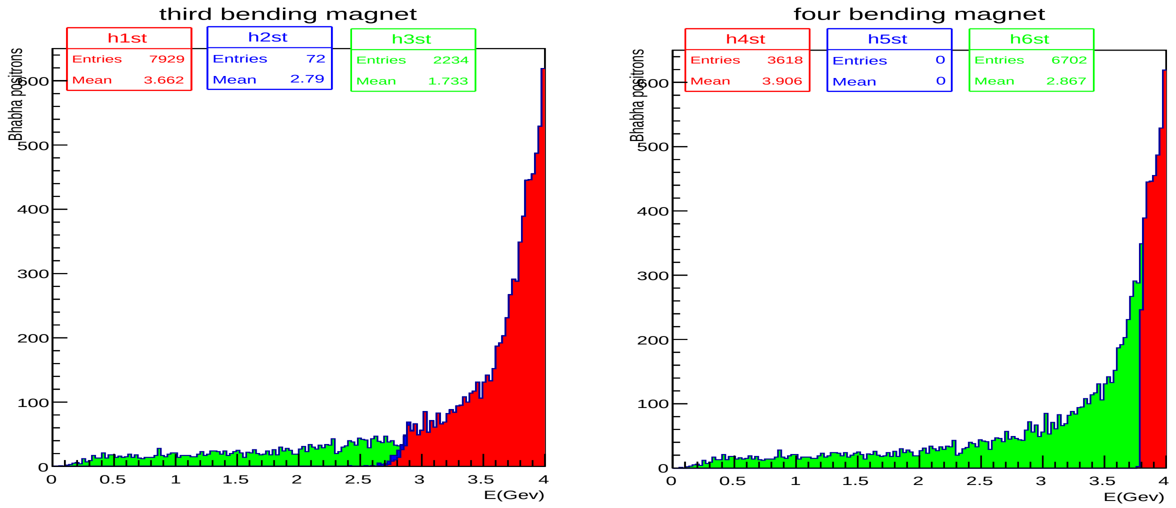

Figure 3.34 – Energy distribution of Bhabha positrons which are already lost (green), detectable in the DS (blue) and still remaining in the beam pipe (red) after the third bend (BLC1LP2) and fourth bend (BLC2LP)

second bends (fig. 3.36). This is mainly due to the fact that the first bending magnet is a vertical bend. This strange tail extends in the +x and -x direction and thus a negligible number of Bhabha positrons is detectable. As a result, bending magnets are not good candidate locations for the DS and we need to search for other candidates. I tracked in

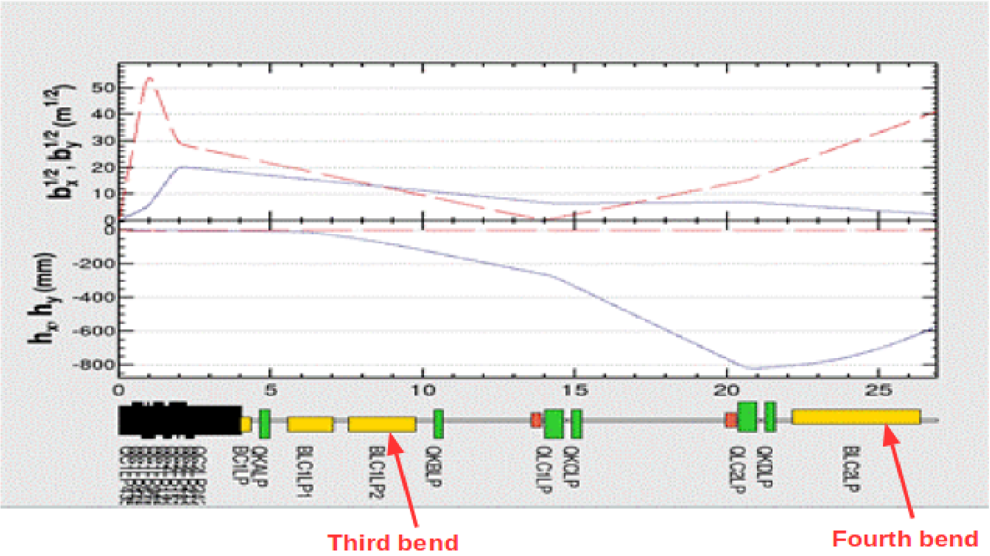

Figure 3.35 – Beta functions and dispersion functions over first 27 m downstream the IP for the LER

different drifts between the magnets and I found the best candidate place at 13.9 meters downstream of the IP.

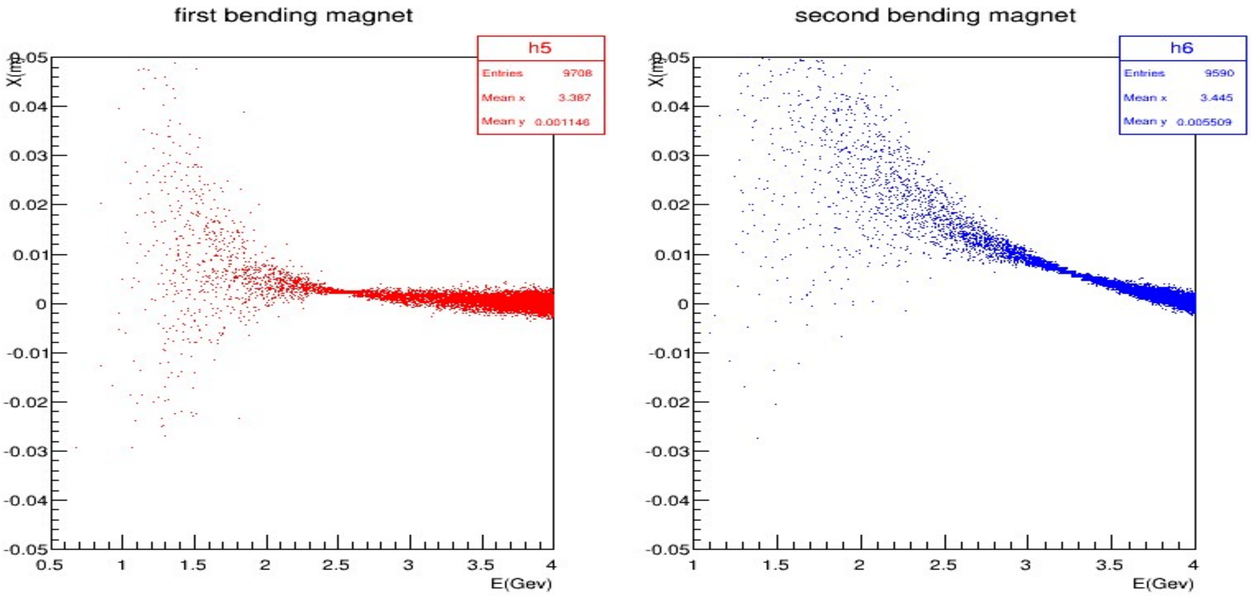

Figure 3.36 – The horizontal position distribution of Bhabha positrons as function of their energies after first and second bending magnets

The DS is perfectly placed in the middle of the distribution x-E at 13.9 m shown on the l.h.s of fig. 3.37 and detects ≈ 4.7% of the total radiative Bhabha cross-section (r.h.s of fig. 3.37). In addition, the location has a 3 meter drift with enough space for the DS, the Cherenkov and Scintillator detectors, with their mechanical setup and cables.

SAD doesn't take into account the beam pipe, its material and geometry, only the tracking in the optics of the accelerator, thus for a precise estimate of the signal in the DS we need to perform further simulations using GEANT4 [48].

3.4.2.3 Simulation of signal in the sCVD

After choosing the best candidate of the DS, it is very important to study the signal considering the lost Bhabha positrons themselves, their energies and exiting angles, the geometry of the beam pipe including its material and thickness. For this reason, a detailed simulation in GEANT4 is considered. The beam pipe at 13.9 meters is a 3 m long cylindrical Copper chamber of 6 mm thickness. The simulation uses the output of the tracking with SAD after the quadrupole QKBLP as its input. The input Bhabha positrons are defined by their energies (l.h.s of fig. 3.38), their positions and their horizontal angle (r.h.s of fig. 3.38). The Bhabha positrons hit the 6 mm Cu pipe at a very small angle of 5 mrad, which would lead then to cross 1.2 m of the material, corresponding to ≈ 80 radiation lengths (X_0=1.436 cm). Most of the particles produced in the showers induced by the interaction of the scattered positrons with the beam pipe are hence absorbed, and the probability for having charged secondaries exiting the beam pipe is

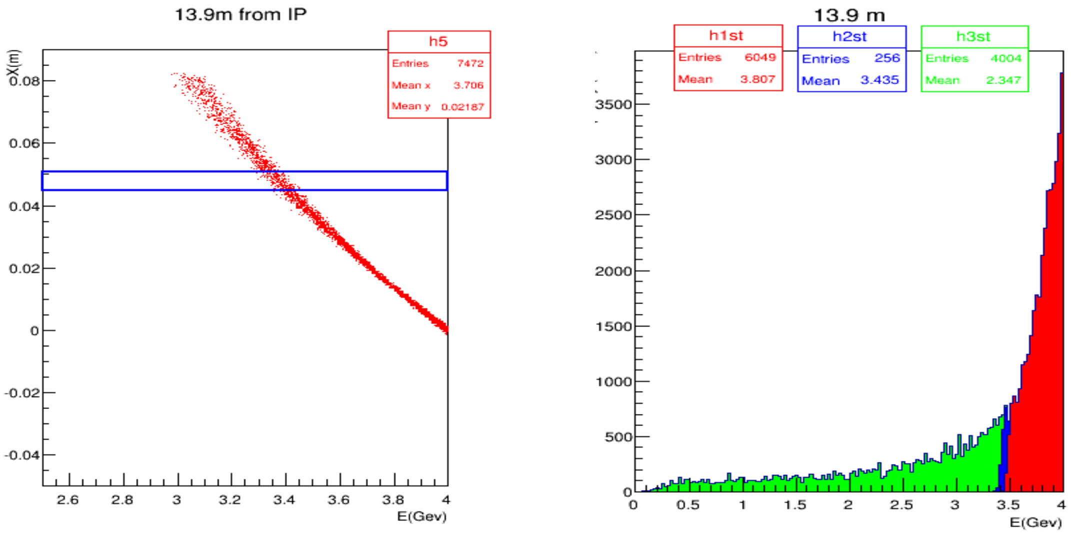

Figure 3.37 – The x-E distribution of the Bhabha positrons on l.h.s and the energy distribution of Bhabha positrons which are already lost (green), detectable in the DS (blue) and still remaining in the beam pipe (red) on r.h.s, in the drift at 13.9 meters

very small. Nevertheless, the lateral extent of the electromagnetic showers, quantified in terms of the Molière radius (R_M=1.176), enables a few of them to exit (fig. 3.39) with a horizontal angular distribution shown in fig. 3.40, mainly on the low energy side (+x) and in the plane of the accelerator, although a few of them also exit elsewhere due to back-scattering. I considered two different orientations for the DS, one parallel and the other perpendicular to the beam pipe (fig. 3.41). Both orientations give almost the same precision P (equation. 3.3), where N is the total number of detected Bhabha positrons, 4.7% is the fraction of the total Bhabha cross section exiting the 3 m drift, $\mathcal{L}$ is the luminosity (10^{34} cm^{-2}s^{-1} at phase 2 & 8×10^{35} cm^{-2}s^{-1} at phase 3), σ is the total cross section of the radiative Bhabha process and f is the fraction of exiting Bhabha particles hitting the DS and resulting in a detectable signal. In the simulation, a Bhabha positron is considered detectable if it deposits an energy of at least 50 KeV in the 500μm DS, corresponding to 2.43 mV or 3σ of the charge amplifier noise (see section 4.2.1.1 of this chapter). In the case of the parallel orientation, and due to their angular distribution after the 6 mm Cu tube, the secondaries may cross less than 500 μm and thus deposit less energy than the normal Landau distribution of the 500μm DS, or may cross more than 500 μm and deposit higher energies and thus appears in the very end of the extended tail of the distribution.

$$P = \frac{1}{\sqrt{N}};\ N = 4.7\% \times \mathcal{L} \times \sigma \times f;\ f = \frac{N_{diamond}}{N_{exiting}} \tag{3.3}$$

The fractions of detected exiting Bhabha positrons are the same for parallel and perpendicular sensors as a function of the distance from the beam pipe (fig. 3.42). It can also be

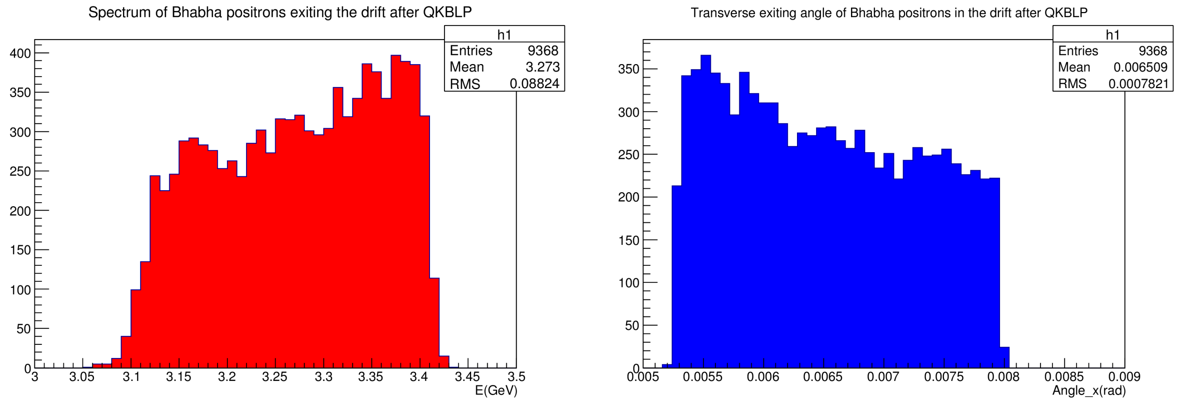

Figure 3.38 – Energy spectrum on l.h.s and exiting angle distribution on r.h.s of the lost Bhabha particles in the drift after QKBLP

seen in fig. 3.42 that this fraction decreases rapidly with distance to the beam pipe. Due to mechanical restrictions, we chose to position the DS as close as possible and parallel to the beam pipe.
The precision expected using the normal beam pipe is 6.3 x 10^{-2} at phase 2, this value is far from the aimed precision. The reason behind this bad precision is the thickness of the beam pipe and the very shallow angle of the exiting Bhabha positrons. Consequently, we may try to change the thickness of the beam pipe and study the precision at each thickness. Further GEANT4 simulations were done with cylindrical beam pipes of different thicknesses (1, 2, 3, 4, 5 and 6 mm). Results show that precision changes with thickness and that a thickness of 1 mm (minimum thickness) improves the precision by just a factor of 2, which is still far from the aimed precision, even at phase 3 (fig. 3.43).

3.4.3 Design of new vacuum chamber insertion

Since neither the normal beam pipe nor a beam pipe as thin as 1 mm allows the aimed precision to be achieved, K. Kanazawa from the vacuum group at KEK suggested a special insertion with a window at 45° in the drift where we will place the DS.

3.4.3.1 Simulation of window at 45°

The suggested window (fig. 3.44) starts at 81.5 cm from the center of the QKBLP. It is a 1.5 cm deep inclination at 45° of 6 mm thick Copper. It is 48 cm long with symmetric edges to reduce the beam pipe impedance, in order to limit beam instabilities due to wakefields. Such a window permits the exiting Bhabha positrons to traverse much less material than the normal beam pipe. Particles exiting the window at 5 mrad will cross 8.5 mm Cu only and thus most of the electromagnetic shower will be able to exit. Since the distance crossed by the charged Bhabhas is very short compared to the shower maximum

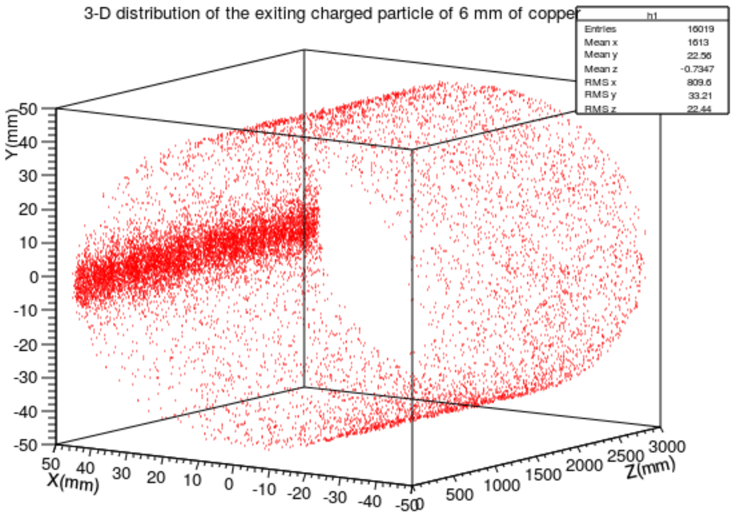

Figure 3.39 – The 3D plot of the charged secondary particles resulting from the interaction of the exiting Bhabha positrons with the 6 mm thick Cu cylindrical beam pipe

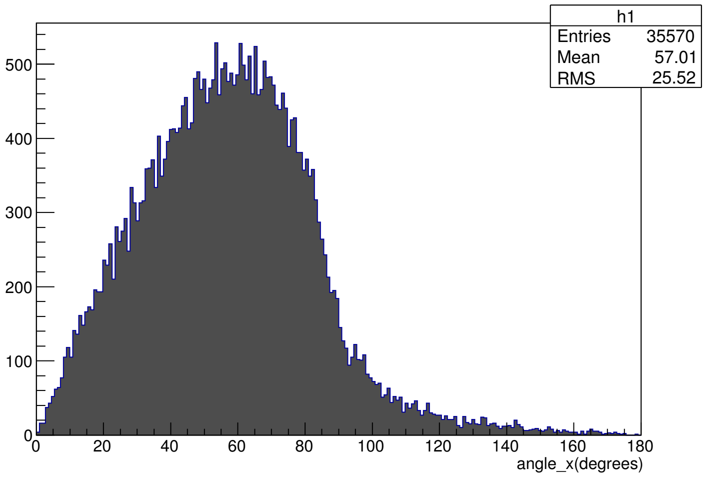

Figure 3.40 – The transverse angular distribution of the exiting charged secondaries from the 6 mm Cu beam pipe

in copper ($X_{Cu} \approx 7.4$ cm (fig. 3.45)), a very small shower is developed at the exit of the window which results in few secondaries hitting the DS, thus producing a small signal. In order to increase the shower and thanks to the design of the window, we can put a radiator of a heavy material with a thickness equal to its shower maximum, at the exit of the window (l.h.s of fig. 3.46). I simulated an inclined surface with the dimensions given in fig. 3.44 and I added an iron (Fe) radiator (Z=26) at its exit with the 5x5 mm^2 DS centred in the middle of the radiator (r.h.s of fig. 3.46). The Bhabha positrons intercepted

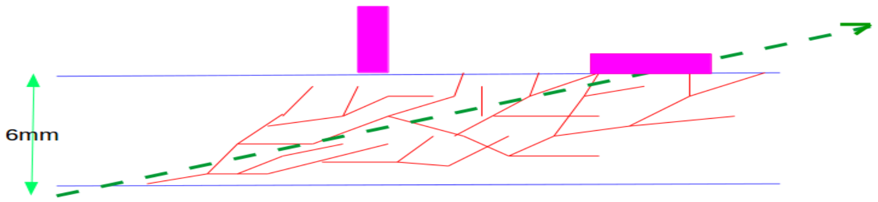

Figure 3.41 – Illustration of an electromagnetic shower of a Bhabha positron exiting the 6 mm Cu beam pipe and of the parallel and perpendicular positioning of the DS (violet)

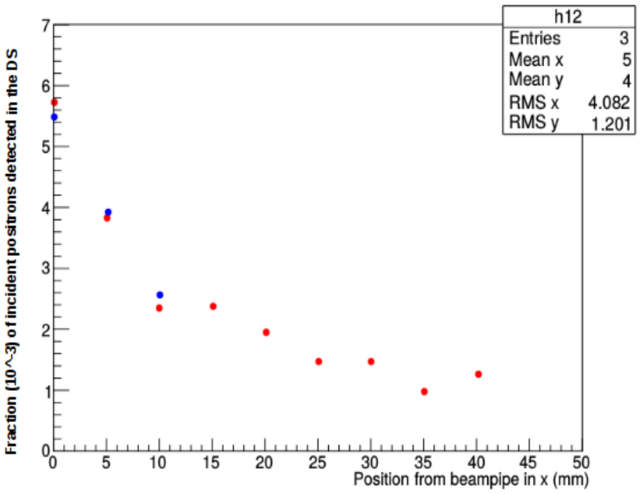

Figure 3.42 – The fraction f of exiting Bhabha positrons with a detectable signal in the DS for a parallel sensor (blue) and perpendicular sensor (red) as a function of the distance from the beam pipe

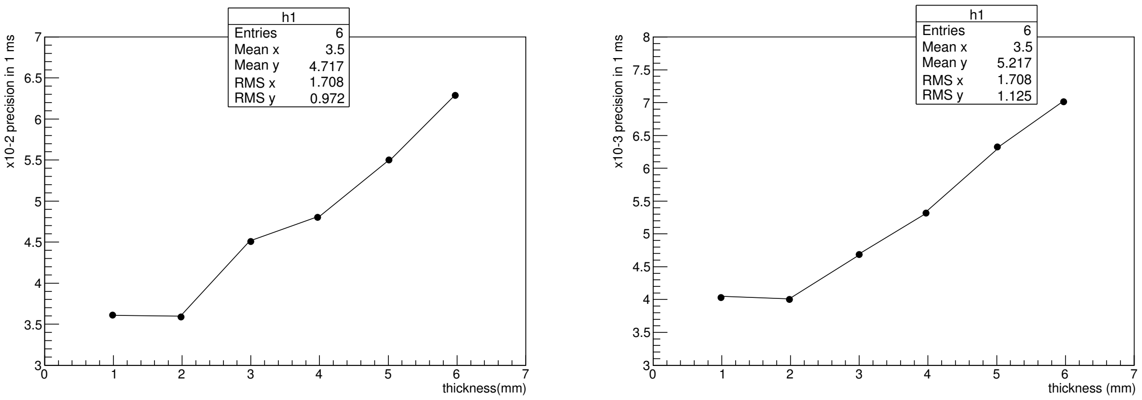

Figure 3.43 – Precision on luminosity in 1 ms in phase 2 ($\mathcal{L}$=10^{34}cm^{-2}s^{-1}) on l.h.s and in phase 3 ($\mathcal{L}$=8 x 10^{35}cm^{-2}s^{-1}) on r.h.s

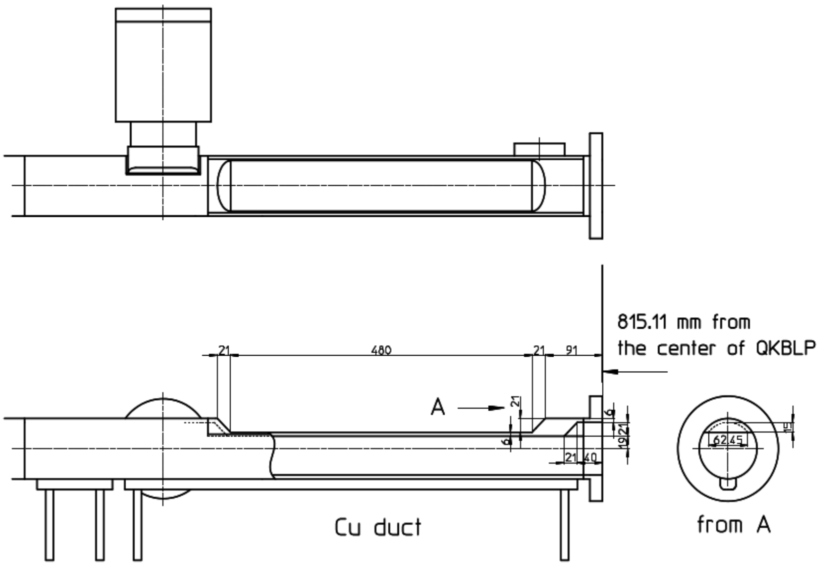

Figure 3.44 – The design of the window at 45° suggested by K. Kanazawa

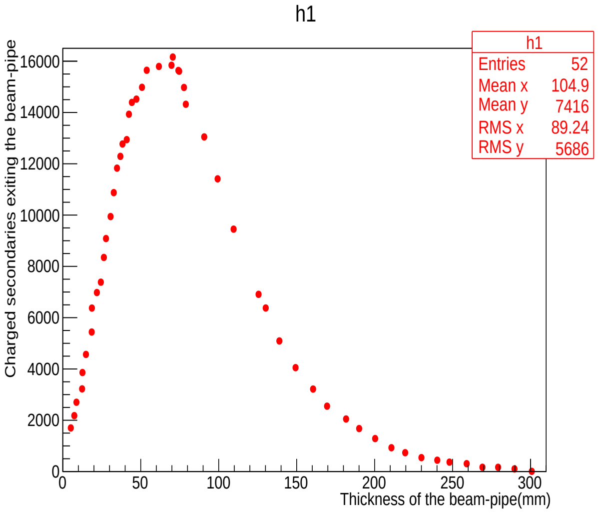

Figure 3.45 – The number of exiting charged secondaries per 1000 incident positrons crossing a given thickness of Cu beam pipe

in the window represent 8.8% of the total radiative Bhabha cross section which is 2 times more than the fraction of the positrons exiting the 3 m long drift. The average energy of the exiting particles is around 3.3 GeV (fig. 3.47). The Bhabha positrons giving a signal in the DS represent 52% of the intercepted Bhabha positrons in the window and are at the center of the energy spectrum (fig. 3.48).

As mentioned before, the radiator will increase the shower and consequently increase the

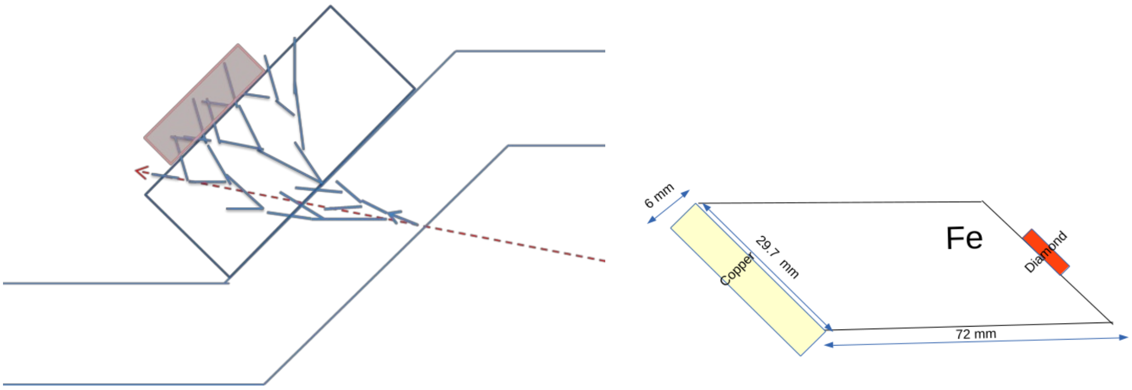

Figure 3.46 – The development of the shower in the radiator on l.h.s and the simulated window with an iron radiator at its shower maximum on r.h.s

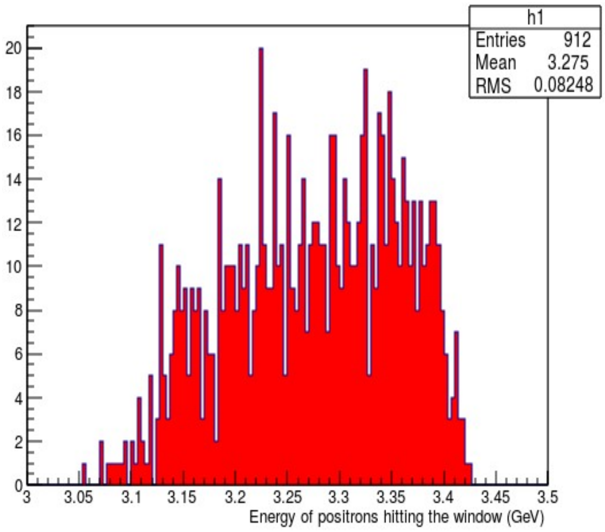

Figure 3.47 – The energy spectrum of the particles exiting the window and the radiator

number of charged secondaries per incident particle intercepted in the DS. The average number of secondaries per exiting incident particles intercepted in the DS is 3.5 (l.h.s of fig. 3.49) for the case of the window with the radiator, whereas it is 2.11 (r.h.s of fig. 3.49) for the case of window without radiator After performing all the already mentioned simulations for the different designs of the beam pipe, I found that the design of the window improves the precision by a factor of 10 compared to the normal 6 mm thick Cu cylindrical beam pipe. Table. 3.4 shows the precision on luminosity for different designs of the vacuum chamber and at different phases of SuperKEKB. The table shows that the window with the radiator is the best candidate to attain the aimed precisions at different phases.

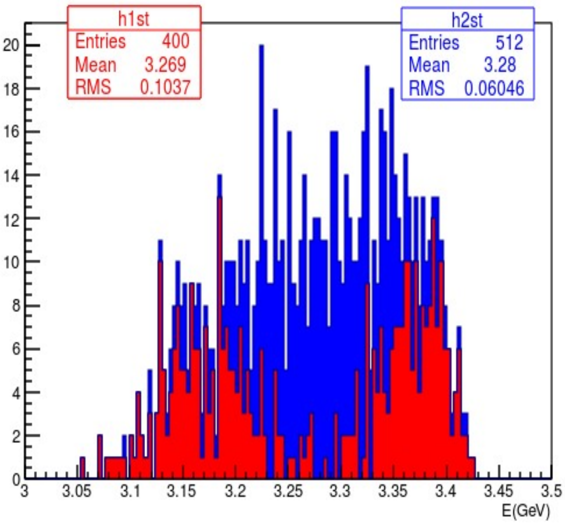

Figure 3.48 – The energy of the incident particles giving signal in the centred 5x5 mm^2 DS (blue) and with no signal (red) in the case of the window with a radiator

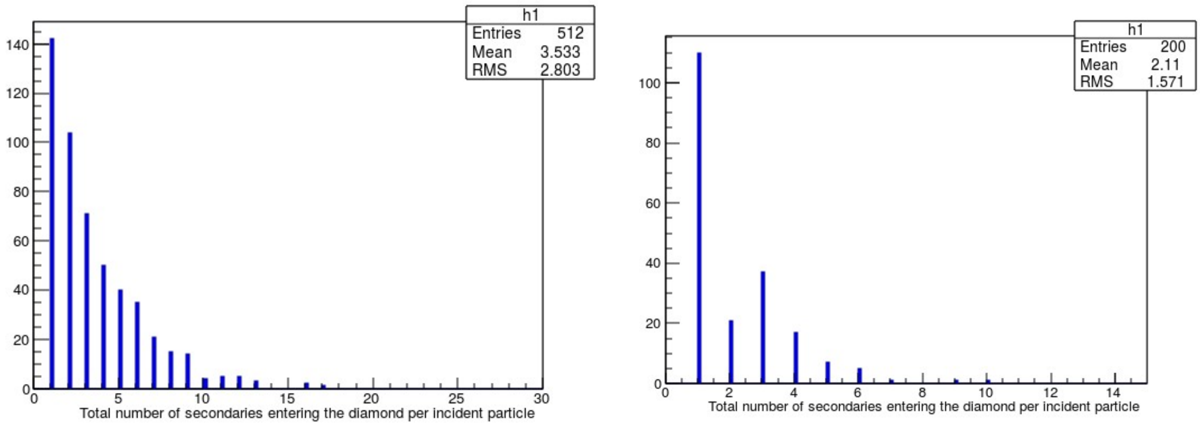

Figure 3.49 – Histograms of the number of charged secondaries in the DS per incident exiting Bhabha positron for a window with radiator on l.h.s and for a window without a radiator on r.h.s

3.4.3.2 Simulation of different material and thickness beam pipe

The simulation of the suggested window proves clearly the improvement of the precision on the luminosity. With the window and the radiator, we should achieve the aimed precision. On the other hand, such a design has a cost besides introducing some potentially detrimental wakefields affecting the stability of the beams. A less expensive solution could be using another material for the beam pipe at a suitable thickness. For quantitative assessment of the expected precisions, GEANT4 was used to compare performances with a regular cylindrical beam pipe, considering also different materials (Cu, Al, Be, Ti),

Design	phase 2 (10^{34} cm^{-2}s^{-1})	phase 3 (10^{35} cm^{-2}s^{-1})	design (8×10^{35} cm^{-2}s^{-1})
cylinder 6 mm Cu	6.3×10^{-2}	2×10^{-2}	7×10^{-3}
cylinder 1 mm Cu	3.6×10^{-2}	1.1×10^{-2}	4×10^{-3}
window at 45°	6×10^{-3}	1.89×10^{-3}	6.7×10^{-4}
window + radiator	3.7×10^{-3}	1.2×10^{-3}	4×10^{-4}

Table 3.4 – Precision on luminosity at different phases of SuperKEKB and different designs

different thickness of the beam pipe (1, 2, 3, 4, 5 and 6 mm) as well as different orientations of the diamond sensor. In table 3.5, the characteristics of the different materials considered for the vacuum chamber are recalled.

For each material I studied the dynamics of the interactions of the exiting Bhabha positrons along the 3 m long drift as a function of its thickness, as well as the signal in the DS and thus the precision on luminosity as a function of the different orientations of the DS with respect to the vacuum chamber (0°,45° and 90°).

Material	Copper (Cu)	Aluminium (Al)	Beryllium (Be)	Titanium (Ti)
Z	29	13	4	22
Density (g.cm^{-3})	8.96	2.7	1.85	4.506
Radiation length X_0 (cm)	1.47	8.985	35.28	3.655
Shower max X (cm)	7.2	35.76	110.2	17
Molière radius R_M (cm)	1.176	3.38	4.86	2.25

Table 3.5 – Characteristics of the different materials considered for the design of the vacuum chamber

The secondaries exit the thickness of the beam pipe uniformly over the 3 m drift, this means that wherever the DS is placed in the drift, we will get the same result. The average value of the number of secondaries per incident particle that exit the beam pipe changes with the material of the vacuum chamber and its thickness. When the distance travelled by the incident Bhabha inside the thickness of the beam pipe is close to the shower maximum of the material, the number of secondaries per incident particle is large and vise versa. This is simulated and shown in the plots in Appendix A.

The secondaries exit the beam pipe with an energy profile ranging around few tens of MeV. They exit with different angular profiles depending on the material of the beam pipe and its thickness, this is because of the different paths traversed by the incident particle. The different number and angular profiles of the secondaries result in variations in the number of secondaries in the DS depending on its orientation. This affects the precision on the measured luminosity. The results of the simulations for the different materials (Cu, Al, Be, Ti) are represented in Appendix A along with the comparison with the design of the window at 45°. The decision on the design of the local vacuum chamber is discussed as well.

The results showed that among all the different materials/thickness/geometries of the beam pipe and different orientations of the DS, the window at 45° is the best choice to achieve the specified precisions in phases 2 and 3 (fig.20-21). Thus, the window will be installed in the LER for phase 2.

3.4.4 Case of HER

The HER (High Energy Ring) is the electron ring with a beam energy of 7 GeV. We aim to use diamond sensors in the HER as well as in the LER to increase the range of luminosities over which precise measurements can be performed. The HER was studied in the same way as the LER to find the best possible locations for the DS. Bhabha electrons were generated using GUINEA-PIG++ and then tracked using SAD.

3.4.4.1 Difficulties and restrictions

Bhabha electrons are tracked to different locations after bending magnets and in the drifts to 24 meters downstream of the IP (fig. 3.50). The list of the first four bending magnets downstream of the IP in the HER is given in table 3.6. Unlike the LER which shows a nice linearity of the energies of the tracked Bhabha positrons with respect to their transverse positions, the HER shows strange distributions in the E-x plane (fig. 3.51, 3.52, 3.53).

Name	Number	Length (m)	Position from IP (m)	Type
BLC2RE	First	2.23	8.2	horizontal
BC1RE	Second	0.344	14.6	vertical
BC2RE	Third	0.344	17.7	vertical
BC3RE	Fourth	0.344	23	vertical

Table 3.6 – The list of the first four bending magnets downstream of the IP in the HER

This strange distribution in the E-x plane is mainly due to the fact that the second, third and fourth magnets are vertical bends, in addition to the existence of sextupoles to correct the chromaticity of the final focusing quadrupoles. The disadvantage of such distributions is that the Bhabha electrons will be lost on both sides of beam pipe (low energy side (LES)(+x) and high energy side (HES) (-x)). In the case of installing the DS on the LES to prevent the hits of high energy photons, the intercepted fractions of

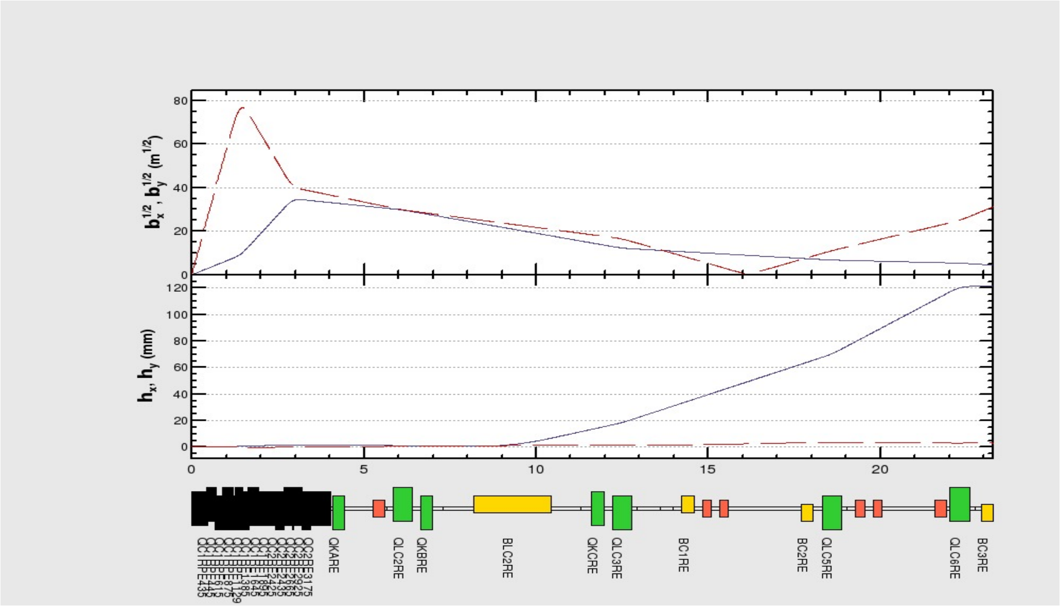

Figure 3.50 – The β and dispersion functions of the lattice of the HER up to 24 meters downstream of the IP

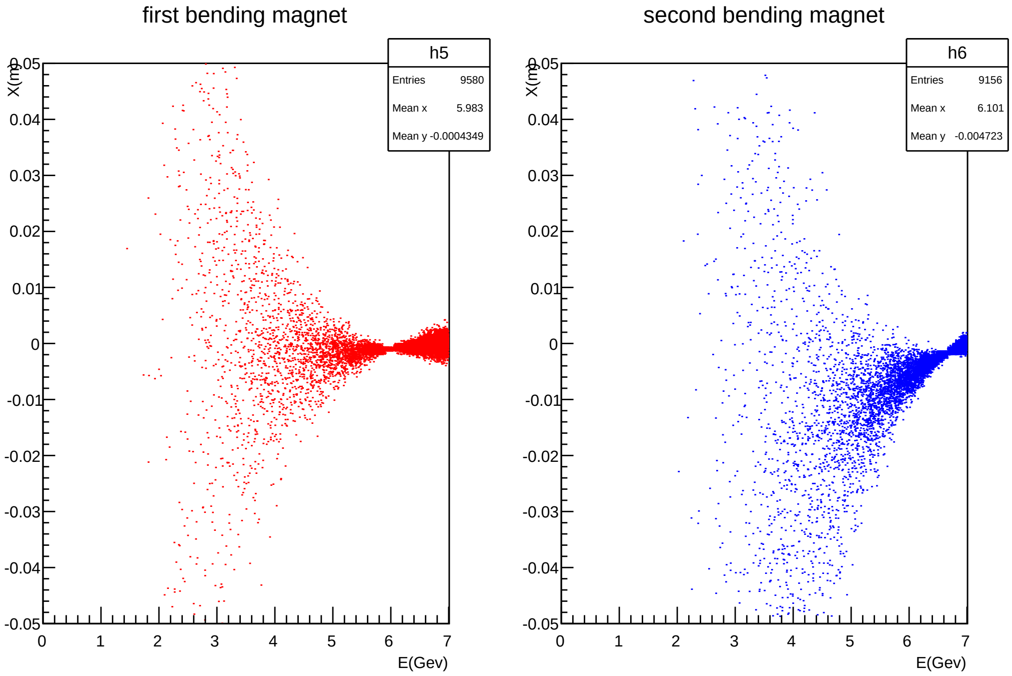

Figure 3.51 – The energies of the Bhabha electrons as a function of their transverse position x after first bending magnet (l.h.s) and second bending magnet (r.h.s)

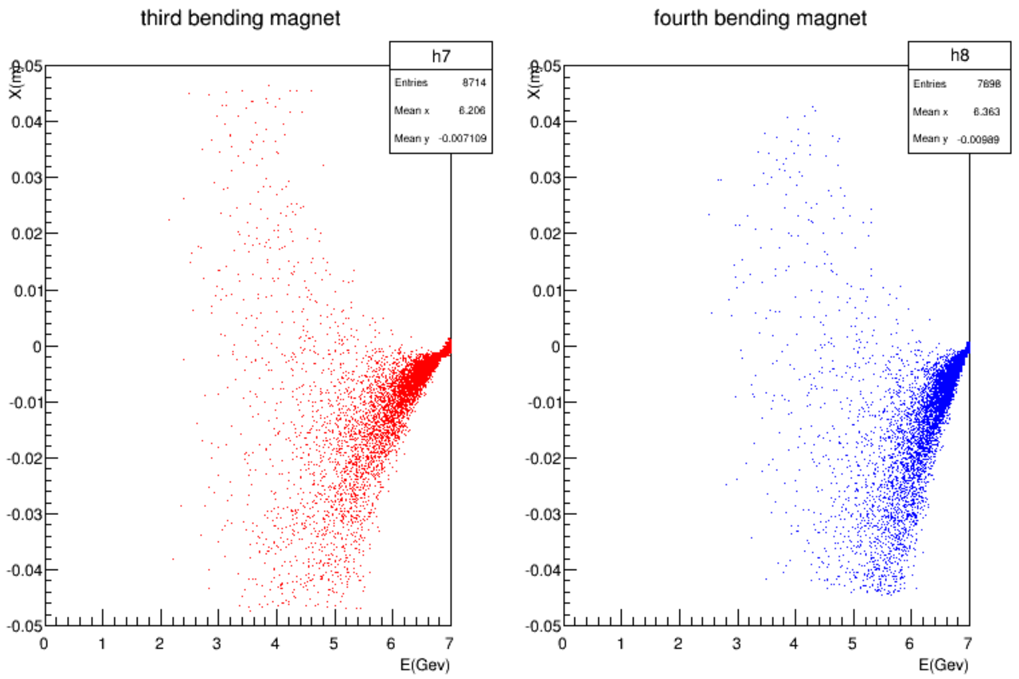

Figure 3.52 – The energies of the Bhabha electrons as a function of their transverse position (x) after third bending magnet (l.h.s) and fourth bending magnet (r.h.s)

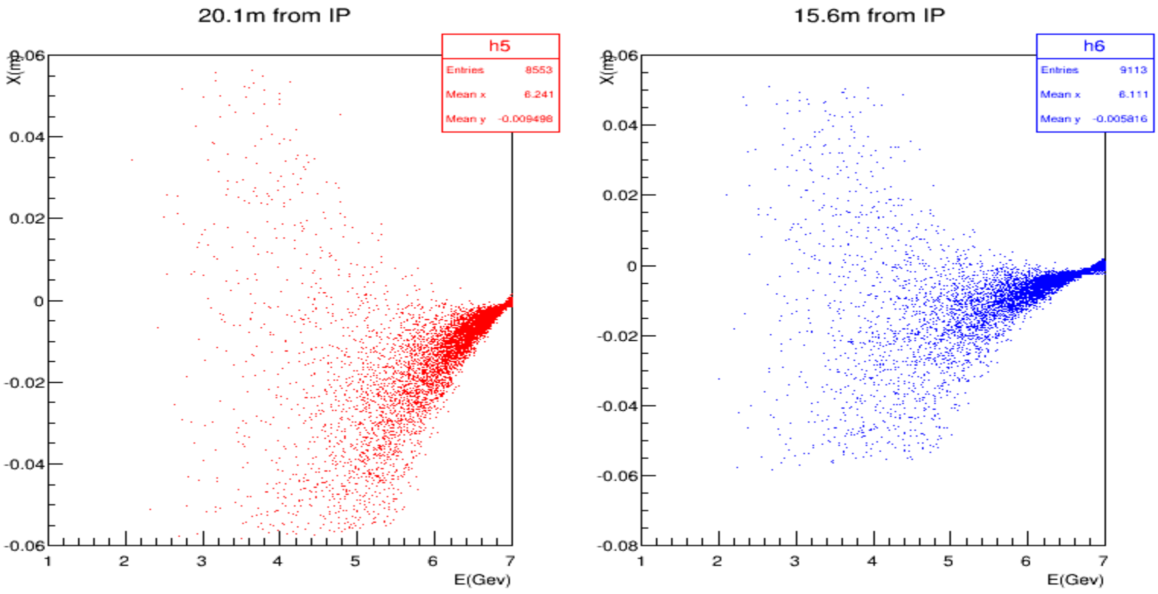

Figure 3.53 – The energies of the Bhabha electrons as a function of their transverse position x in the drift at 20 m (l.h.s) and at 15.6 m (r.h.s)

Bhabha electrons in the DS will be very low, in the range of 0.5% of the total Bhabha cross section. These fractions are insufficient to attain the aimed precision. Thus we tried to search for another method to measure the luminosity in the HER.

3.4.4.2 Method implemented

Since that Bhabha electrons don't satisfy the conditions for our fast luminosity monitoring, we may think about measuring the signals from the Bhabha photons. The energy of Bhabha photons in the HER varies from very low energy to 7 GeV as shown on l.h.s of fig. 3.54. They are produced at the IP with a very small transverse angular distribution with an RMS of 0.4 mrad (r.h.s of fig. 3.54). The advantage of the photons is that they are neutral particles and will not be deflected by the magnetic fields of the optical elements, so they continue straight and exit the beam pipe at well defined distance from the IP.

Detailed simulations are currently being performed in the LAL group considering the lattice of the HER and the geometry of the beam pipe. The preliminary analysis shows that the γ spot hits the antechamber edge in the SLYTRE sextupole (at 27.4 meters downstream of the IP) (fig. 3.55) at an average angle of 5.9 mrad. Due to the transverse angular distribution of the photons, some photons will hit the vacuum chamber several meters on both sides of the nominal exit point at 27.4 meters downstream from the IP (fig. 3.57). The closest free space for the DS is just after the exit of the sextupole

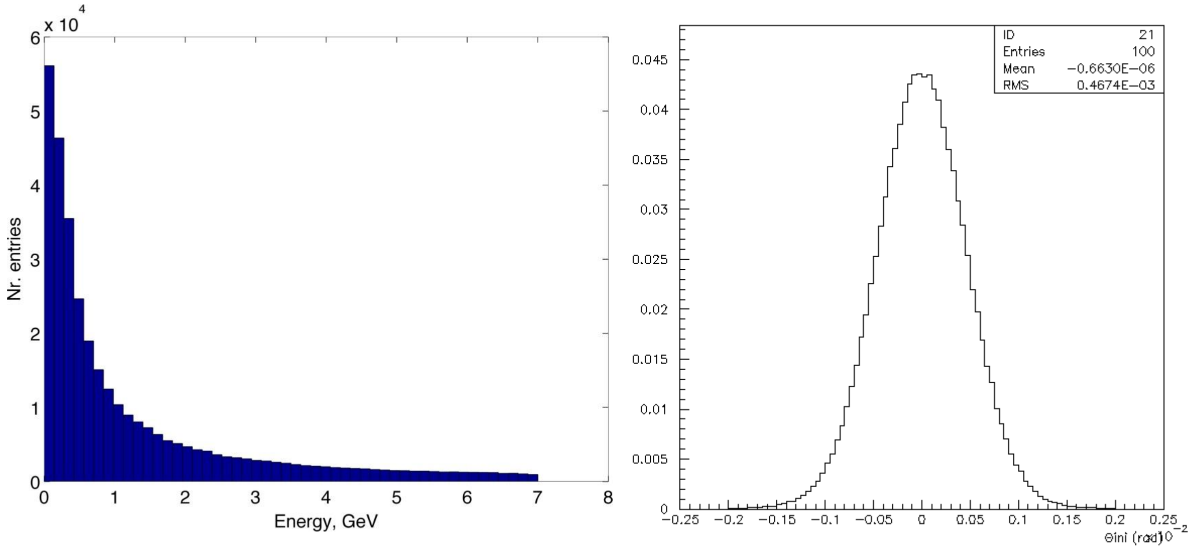

Figure 3.54 – The energy spectrum of Bhabha photons in the HER on l.h.s and their horizontal angle distribution on r.h.s

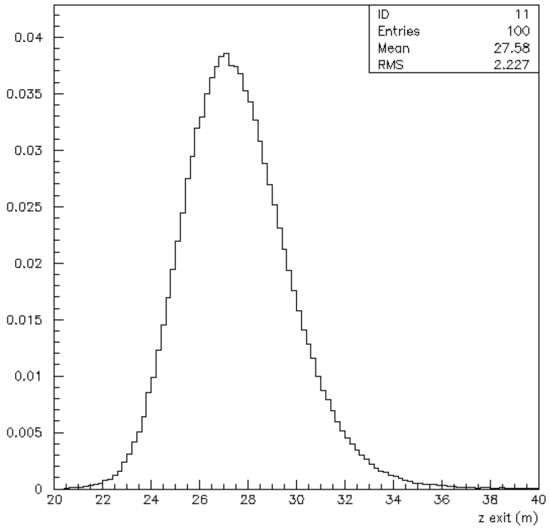

Figure 3.55 – The distance from the IP at which the photons exit the HER beam pipe

SLYTRE. It is a very small drift of 2.5 cm, which is insufficient to install both the DS and the ZDLM sensors with the mechanical stand, in addition the photons will traverse a thick mask which will absorb greatly the electromagnetic shower. Other free spaces are represented in fig. 3.56. Finally, the luminosity monitors were installed at ≈30 meters downstream of the IP in the HER. As what on-going studies are showing, a sizeable fraction of the Bhabha cross section can be detected at that location.

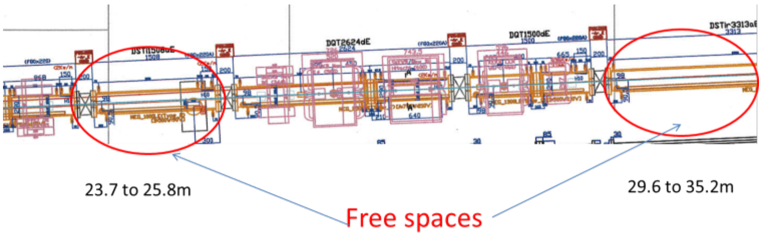

Figure 3.56 – The lattice of the HER where the γ spot hits, showing the free spaces for the luminosity monitors

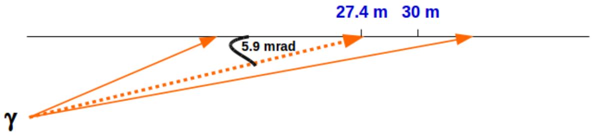

Figure 3.57 – The distances at which the Bhabha photon spot hits the vacuum chamber in the HER

Chapter 4

SuperKEKB single beam commissioning

4.1 Introduction

The SuperKEKB commissioning is split in three phases and each phase has its defined goals. The single beam commissioning took place starting from February until June 2016. This commissioning went in parallel with the BEAST II commissioning to study the backgrounds from single beam losses in the interaction region. Our fast luminosity monitors (diamonds + ZDLM monitors) also took data during that period.

4.1.1 General goals and achievements

The single beam commissioning of SuperKEKB, which represented the phase 1 of the commissioning, took place without the final focus system and without the Belle II detector, during which both positron and electron beams were successfully produced, accelerated, injected and stored in the main rings (LER and HER) of SuperKEKB.

The main goals of this phase [49] were to start each hardware system of the machine (injector linac, magnet system, RF system in both rings, vacuum system, ...) and to establish the beam operation software based on SAD. During this period of commissioning, vacuum scrubbing was performed in both rings at different currents, starting from very low currents (30 mA) to high currents (1 A), in order to clean the vacuum chambers from residual gases. The residual gas causes beam loss due to the scattering of the beam particles on the gas molecules, either by Bremsstrahlung (energy loss of the particle by emitting a photon) or Coulomb scattering (scattering at large angle). Vacuum scrubbing (fig. 4.1) is performed by circulating the beams in each ring, the interaction of the electromagnetic field of the beams with the material of the pipes leading to the extraction of molecules off the surfaces of the vacuum chambers, and by using the NEG pumps these residual molecules could be removed from the vacuum pipes. Vacuum scrubbing at high currents (500 mA to 1 A) was demanded by BelleII to protect the detector from high beam backgrounds during the physics runs which will start during phase 2.

During phase 1, BEAST II (beam background group) performed background studies with all its sub-detectors. Special studies in both rings were dedicated to background studies of BEAST II (Touschek study, beam-gas backgrounds, injection background and collimation studies). The Touschek study was performed by changing the vertical beam size, using the ECK (Emittance Control Knob). Changing the setting of the ECK means changing the field of the skew quadrupole component of the sextupoles, which induces a coupling of the horizontal emittance into the vertical emittance all over the ring and thus results in the change of the vertical beam size. The beam-gas background studies were performed by inducing vacuum bumps in both rings in sections upstream of the IP. These vacuum bumps are the result of deactivating a few NEG pumps at selected locations. To study the effect of collimators (fig. 4.2) on the beam losses, parameters of some collimators (collimator widths) have been modified each time. From these studies, the BEAST II group aimed to test its detectors under beam conditions, and to compare the data with the simulation, in order to validate the simulation in view of extrapolating it to phases 2 and 3. Another main goal of the phase 1 commissioning was to understand the problems that may arise during the high beam current operation (vertical beam size blow up, beam aborts, non-linear vacuum pressure behaviour with current). The commissioning group at SuperKEKB performed a lot of optics studies and corrections during phase 1. These corrections were mainly based on using the BPM's (Beam Position Monitors), e.g. the close orbit corrections. Optics corrections were performed in the context of low emittance tuning, such as the X-Y coupling correction and the dispersion correction. To achieve a low vertical emittance in the LER (fig. 4.3), several steps have been considered including the installation of few permanent skew quadrupole magnets and the optimisation of their strength.

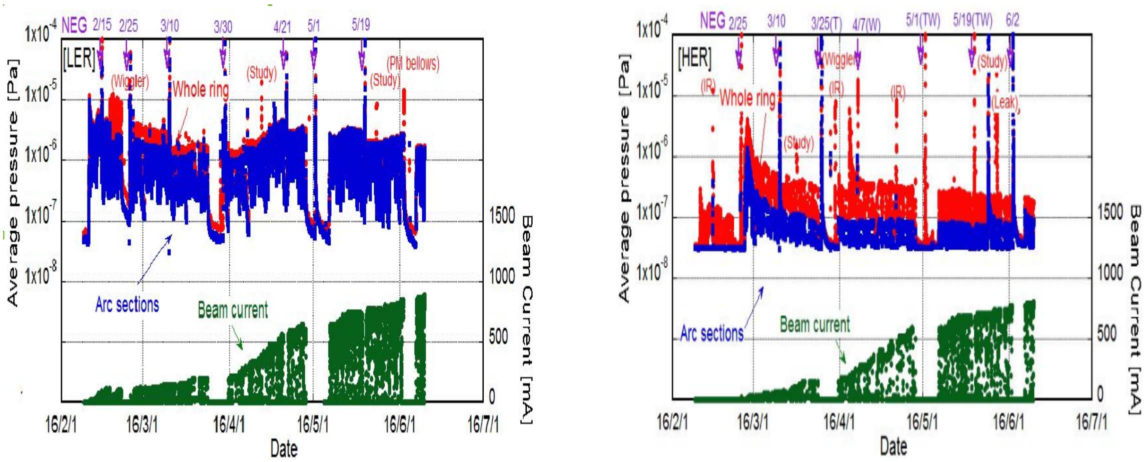

Figure 4.1 – History of the vacuum scrubbing in SuperKEKB during phase 1, in the LER on l.h.s and in the HER on r.h.s

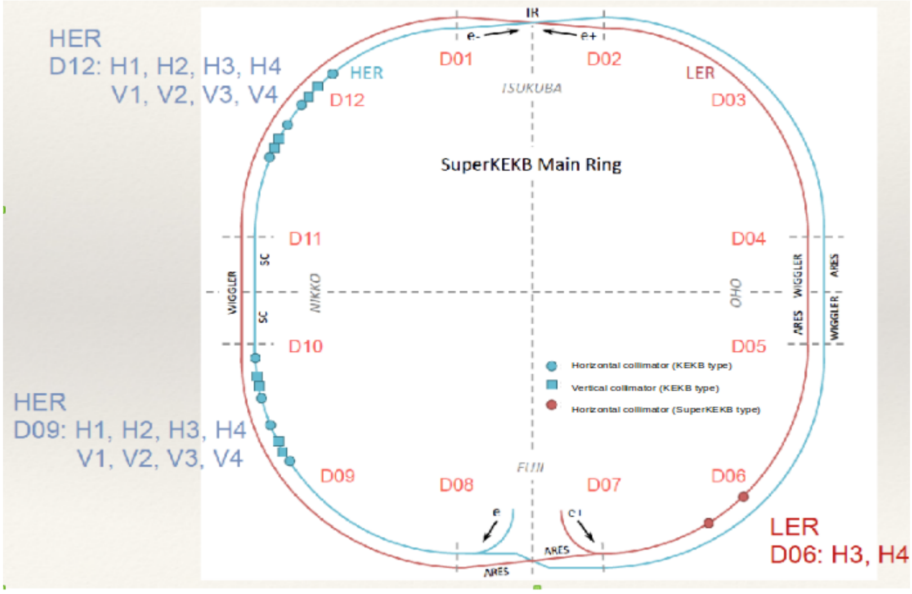

Figure 4.2 – The position of collimators in SuperKEKB rings during phase 1

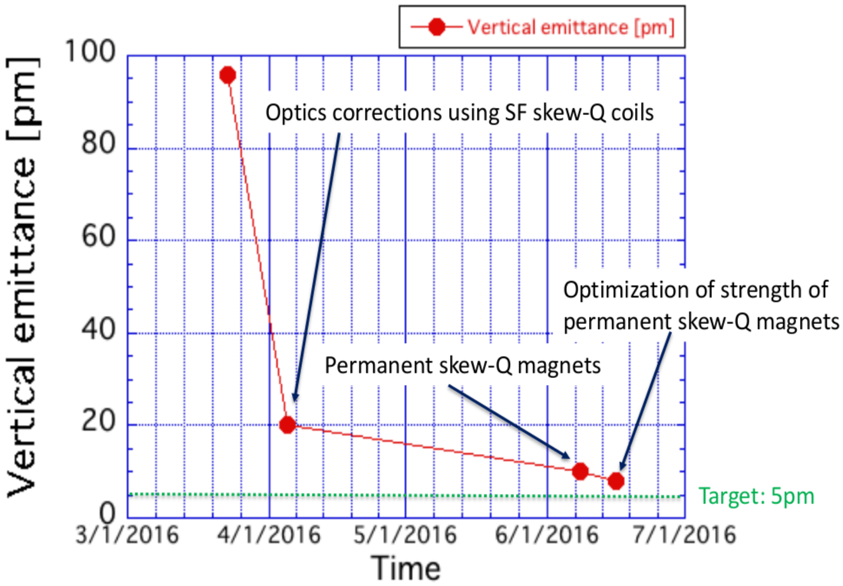

Figure 4.3 – The physical vertical emittance in the LER during phase 1 after several corrections [49]

4.1.2 Next stages of SuperKEKB commissioning

The phase 1 commissioning was successfully accomplished and finished in June 2016.

For the phase 2 commissioning, which is planned to start in the end of 2017 and beginning of 2018, the last final focus quadrupoles (QCS) will be installed in the IR along with the Belle II detector without its vertex detector. An increase of the background level mainly due to Touschek is predicted due to focusing to small beam sizes at the IP. This could be dangerous for the vertex detector which is the closest to the IP among the Belle II sub detectors, for this reason it will not be installed until the background level is confirmed and assured to be under the threshold that could damage the vertex detector. During this phase, the commissioning of the damping ring will take place in order to achieve a small emittance positron beam before injection into the LER. Background studies with the BEAST II detectors will be performed mainly to give feedback on the radiation levels in order to protect the Belle II detector. Luminosity tuning will start and the target luminosity is 10^{34} cm^{-2}s^{-1}.

During phase 3, the Belle II detector will be fully installed and the physics run will resume, this time with the vertex detector. The beam currents will be increased in both rings and the luminosity tuning will continue to achieve a luminosity of 10^{35} cm^{-2}s^{-1} and up to 8×10^{35} cm^{-2}s^{-1}.

4.1.3 Goals for our fast luminosity project

Our project is to perform fast luminosity monitoring as part of the dithering feedback system in the horizontal plane at SuperKEKB. We aim at a precision of 10^{-3} in 1 ms by measuring signals from the radiative Bhabha process at zero photon scattering angle with our diamond sensors in both rings. Our sensors need to be placed at locations where contamination from single beam backgrounds is minimal ($< 1\%$). Therefore studying the single beam loss processes is important for our project as well.

Our diamond sensors were installed and took data during phase 1 commissioning. We aimed from this data acquisition to address several aspects:
- To check the operation of our sensors and overall installation (electronics and mechanics) under machine conditions.
- To measure the backgrounds at the locations of the sensors chosen for the luminosity measurements in both rings.
- To compare the data to the simulation, and thus to check the reliability of our simulations for phase 2.
- Once the reliability of the simulation is confirmed, we can extrapolate our background simulations to phase 2 and estimate the fractions of signal from single beam losses and

from the radiative Bhabha process in our sensors.

The simulation was also used to compute the amount of Bhabha signal in the sensors, this is the detected fraction of the Bhabha cross section, which determines the precision to be expected for the luminosity measurement in different beam pipe geometries, materials and window designs. These predictions will also be validated once the simulations are confirmed.

During phase 2, the window at 45° will be installed in the drift at 11.9 meters in the LER. We will continue the backgrounds measurements before the luminosity tuning starts. The main aim of our project in this phase is to start the fast luminosity measurements with a modification of the data acquisition system which will enable us to monitor the train and the bunch integrated luminosities in real time, and thus provide input to the feedback system based on the horizontal dithering. We will pursue the fast luminosity measurements during the phase 3 as well.

4.2 Beam Loss Monitors

The BLMs (Beam Loss Monitors) at SuperKEKB are in charge of the measurement of the particle loss levels at a number of locations along both rings, in order to provide a protection of the hardware systems and the Belle II detector. The loss monitor system is a very important part of the abort system at SuperKEKB. Due to higher currents and smaller beam sizes compared to KEKB, the simulated beam losses are 50 times higher at SuperKEKB. These losses are mainly concentrated in the IR and around collimators. The beam loss monitors used at SuperKEKB are the PIN photodiodes and the ion chambers [50]. During phase 1, 101 PIN diodes and 32 ion chambers were activated. Each BLM signal can generate an abort signal. Signals from BLMs all over the rings are sent to 4 LCRs (Local Control Rooms). Along with the BLM signals, other signals like the beam intensity, signals from the RF cavities, injection trigger timing signals and others are fed to data loggers which are used to analyse data collected over 600 ms, diagnose the abort signals and give the reason behind each abort. The loss monitor system is shown in fig. 4.4.

4.2.1 PIN diodes

The PIN diodes (PD) used at SuperKEKB are 2.65×2.65 mm^2, and they are placed mainly around the collimators (l.h.s of fig. 4.5) to detect the losses in all directions. They are characterised by high speed and high radiant sensitivity, their interlock signal is fast enough to protect the collimators. They are also installed near the bellows (r.h.s of

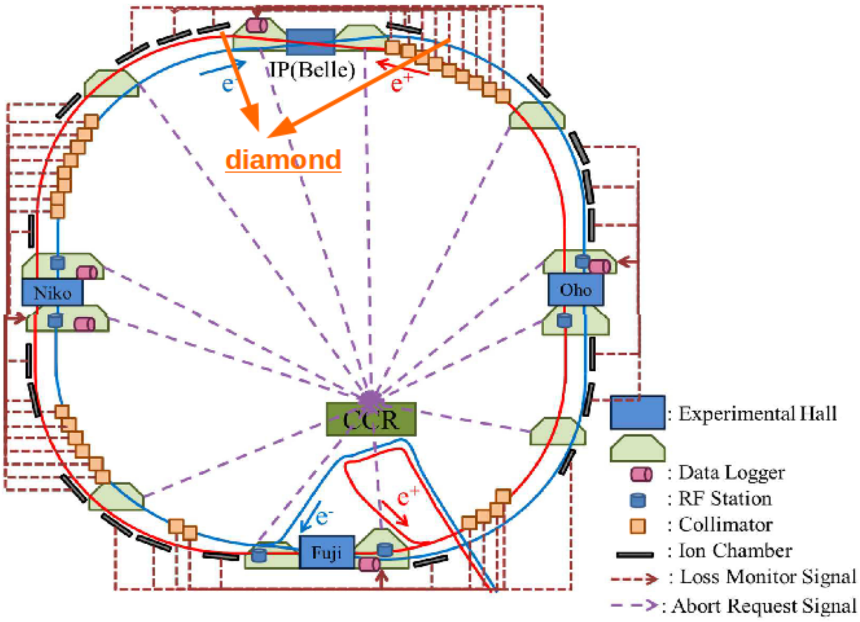

Figure 4.4 – Loss monitor system at SuperKEKB

fig. 4.5). The rise time of a PD is 60 μs.

4.2.2 Ion chambers

The Ion Chambers (IC) at SuperKEKB are 5 m long FC-20D coaxial cables (fig. 4.6) and they are placed on the outer wall of the tunnel. The inner and outer conductors of the IC are separated by an air gap. The loss signal from the IC is logged at 1 Hz in a 16 bit ADC. The IC is sensitive to very small loss rates of 0.1 mA/s.

During the phase 1 commissioning of SuperKEKB, I participated in operation shifts on the machine in the KEKB control room, and assisted with the beam loss monitors. My task was to integrate the beam loss monitors, considering their type and position, in the lattices of both rings of SuperKEKB. The aim of such a work, which was done in the framework of the SAD software, was to enable monitoring through EPICS (Experimental Physics and Industrial Control System) the values of each channel of the beam loss system at a given frequency (1 Hz for example), to quickly provide information about the position of the beam loss abort signal.

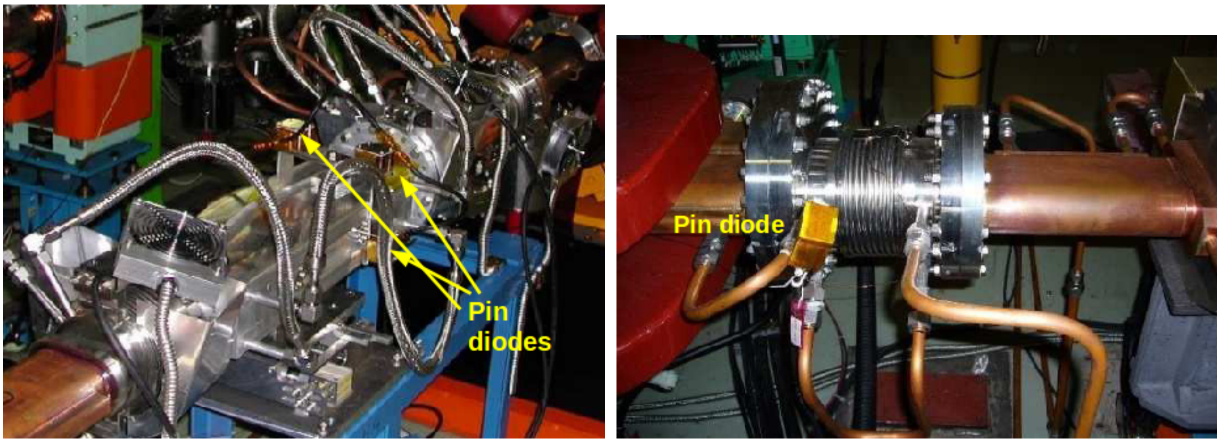

Figure 4.5 – PIN diodes at SuperKEKB, around the collimator [50] on l.h.s and near a bellow [50] on r.h.s

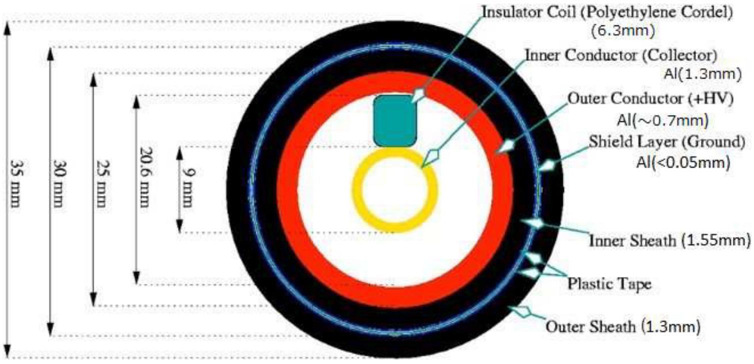

Figure 4.6 – The cross section of the ion chamber at SuperKEKB [50]

4.3 Vacuum scrubbing

Since a large part of the beam pipes has been replaced by new one, especially in the LER, vacuum scrubbing was a major task during the phase 1 commissioning [51], to increase the beam lifetime and decrease the beam background in the Belle II detector during the physics run of phases 2 and 3. The vacuum scrubbing took place successfully, with vacuum pressures of less than 1×10^{-7} Pa achieved in both rings. The stability of the new vacuum components (antechambers, bellows, flanges, ...) was checked and confirmed. No extra heating and abnormal pressure rise were observed in these components.

4.3.1 Electron cloud

The synchrotron radiation emitted by the positron beam in the LER generates photons which are intercepted by the material of the vacuum chamber. In that process, electrons can be extracted by photo-emission. Such electrons can then be attracted and interact with the positron beam, later hitting the chamber and extracting more electrons. In the presence of multi-bunch operation with narrow bunch spacing, these electrons accumulate in the vacuum chamber and build up the electron cloud. The electrons of the electron cloud thus create a current along with the passage of the positron beam. The antechambers and the TiN coatings (fig. 4.7) were observed to have an important effect on decreasing the electron current in the LER compared to other types of beam pipes.

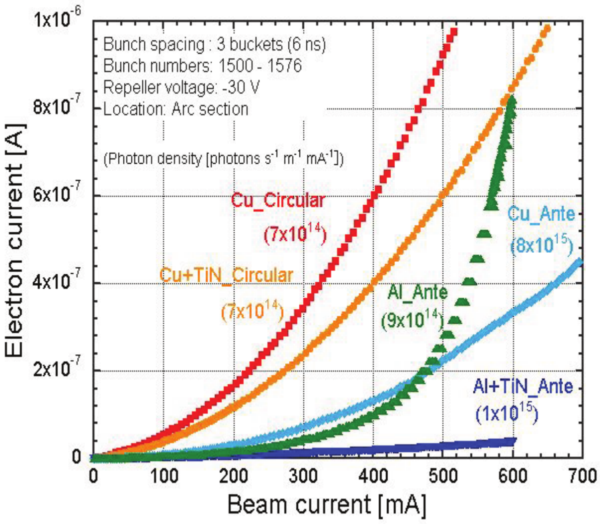

Figure 4.7 – The electron current measured in the LER as a function of the beam current for different types of the beam pipe [51]

4.3.2 Non-linear pressure rise with beam current

One problem encountered during the vacuum scrubbing in phase 1 commissioning was a non-linear pressure rise [52] against the beam current in the LER, starting from a beam current of 500 mA (fig. 4.8). This behaviour is similar to the behaviour of the electron current in the region of aluminium parts without the TiN coatings. The reason behind this non linear behaviour of the pressure can be explained by the multipacting of the electrons in aluminium bellows. In the LER, the aluminium bellows are 0.2 m long and are placed each 3 m on average, so they represent more or less 5% of the ring circumference. When the positron beam passes by the bellows, the electrons of the electron cloud are accelerated by the field in the bellows. These accelerated electrons hit the vacuum chamber thus introducing secondary electrons. When the transit time of the electrons crossing the vacuum pipe is comparable to the bunch spacing, multipacting occurs [53] thus leading to a non-linear vacuum pressure rise.

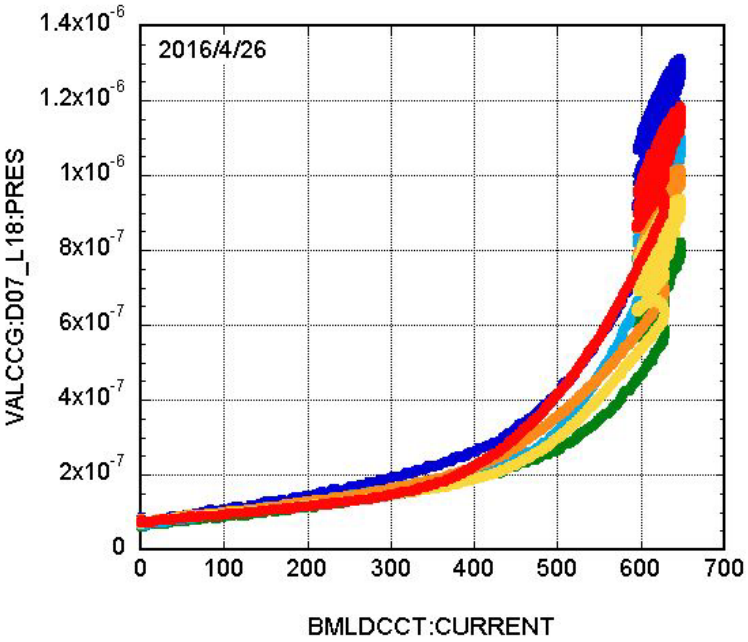

Figure 4.8 – The non-linear pressure rise at nine different gauges at the arc section as a function of beam current in LER

4.3.3 Countermeasures

As an attempt to mitigate the non-linear rise of the vacuum pressure with respect to beam current, a magnetic field of axial direction was applied with solenoids (l.h.s of fig. 4.9) or permanent magnets (r.h.s of fig. 4.9) at nine aluminium bellows, which represent a 30 m long section. The pressure rise in that section was observed to relax (l.h.s of fig. 4.10). In the maintenance period of 2-4 June, 800 permanent magnets were installed around most of the aluminium bellows in the arc sections of the LER, as a result the pressure rise was observed to relax all over the ring (r.h.s of fig. 4.10). However, the non-linear behaviour of the pressure remains at a high beam current (> 700 mA). To deal with this problem, permanent magnets were installed afterwards in part of a drift region.

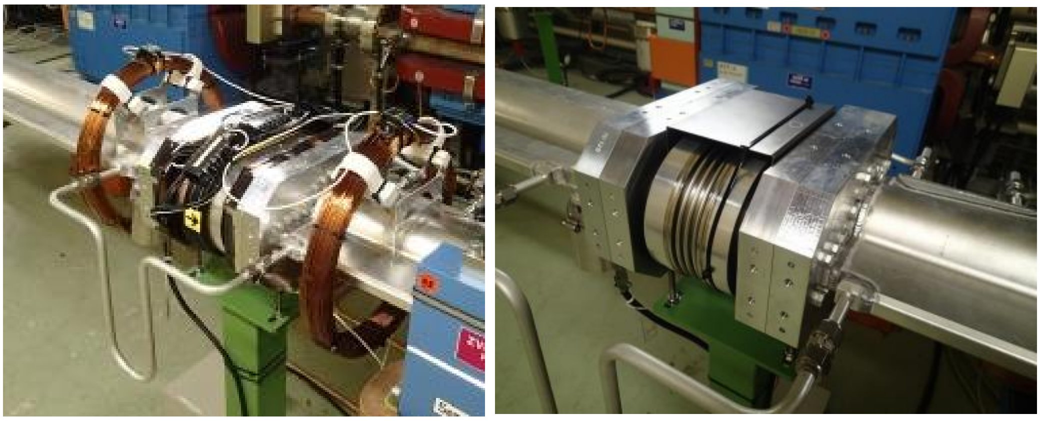

Figure 4.9 – A solenoid magnet on l.h.s and a permanent magnet on r.h.s at an aluminium bellow at SuperKEKB

4.4 Beam size blow-up

4.4.1 Description of the phenomenon

In the LER, when the positron beam passes through the electron cloud, the electrons oscillate and this oscillation induces a short range wake field. These wake fields are responsible for strong head-tail instabilities which result in the vertical beam size blow up [54]. This phenomenon has a great effect on reducing the luminosity of the affected bunches, thus it must be controlled.

To decrease the density of the electron cloud, normal cylindrical chambers are replaced by ante chambers. In the presence of ante chambers, the interaction between the positron beam and the emitted electrons is reduced since it is hard for the electric field to enter the chamber slot.

During the phase 1 commissioning of SuperKEKB, beam size blow up was observed at an early stage [55]. A dedicated study of this phenomenon was performed as a function of different parameters as the beam current and the fill pattern (bucket spacing), each time the vertical beam size was monitored by the SRM (Synchrotron Radiation Monitor) [56]. The beam current threshold of the beam size blow up varies for different fill patterns (l.h.s of fig. 4.11).

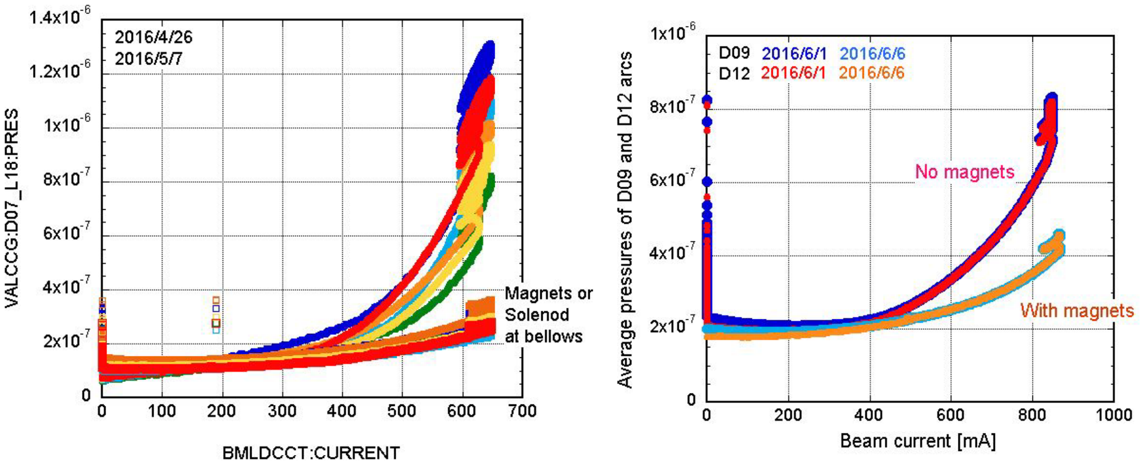

Figure 4.10 – The pressure rise against the beam current, at the 30 m bellow section before and after applying the solenoidal magnetic fields on l.h.s and in two arc sections before and after the installation of 800 permanent magnets around the aluminium bellows in the arc section on r.h.s [52]

4.4.2 Effect of permanent solenoids

One important motivation of the installation of the permanent solenoids at the Aluminium bellows was to see their effect on the beam size. Beam size blow up study was performed after the installation of the solenoids as well. It was observed that the solenoids had a great effect to raise the blow up threshold by a factor of 1.5 for the different bunch spacing patterns (r.h.s of fig. 4.11) [49]. Thus it was confirmed that the beam size blow up is mainly due to the electron cloud, which is dense at the Aluminium bellows due to the multi-pacting effect.

For the high currents planned in SuperKEKB during phase 3, where the bunch spacing will be reduced to 4 ns, more solenoids will need to be installed in order to control the electron cloud density and thus to control the beam size blow up for the high luminosity operation.

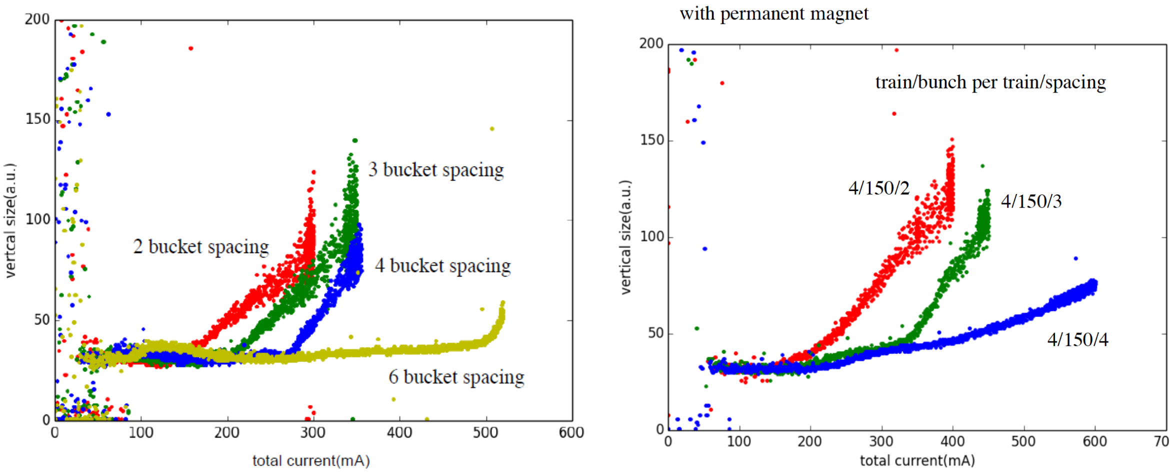

Figure 4.11 – The vertical beam size in the LER as a function of the total beam current for different bucket spacing, before the installation of permanent solenoids at the Al bellows on l.h.s and after the installation of permanent solenoids at the Al bellows on r.h.s [49]

Chapter 5

Single Beam Losses at Phase 1

5.1 Single beam loss processes

In SuperKEKB at very high luminosity, the beam backgrounds in the Belle II detector (fig. 5.1) are estimated to be much higher than at KEKB. These backgrounds deteriorate the detector resolution and analysis performance at phases 2 and 3 of the SuperKEKB project. The major sources of these backgrounds are synchrotron radiation (SR), scattering of the beam on residual gas (Bremsstrahlung and inelastic Coulomb scattering), Touschek scattering, radiative Bhabha scattering and electron-positron pair production via the two photon process $e^+e^- \rightarrow e^+e^-e^+e^-$ [57] [58] [59]. The main reasons behind these high backgrounds are the high currents (3.6 A in the LER and 2.6 A in the HER) and very small beam sizes in SuperKEKB compared to KEKB. To cope with the various kinds of backgrounds different measures will be considered. Movable horizontal and vertical collimators are to be installed along the rings to stop the deviated particles before they reach the detector. The inner surface of the Beryllium beam pipe are coated with gold to absorb the SR before it reaches the inner detector. Backgrounds from Bremsstrahlung,

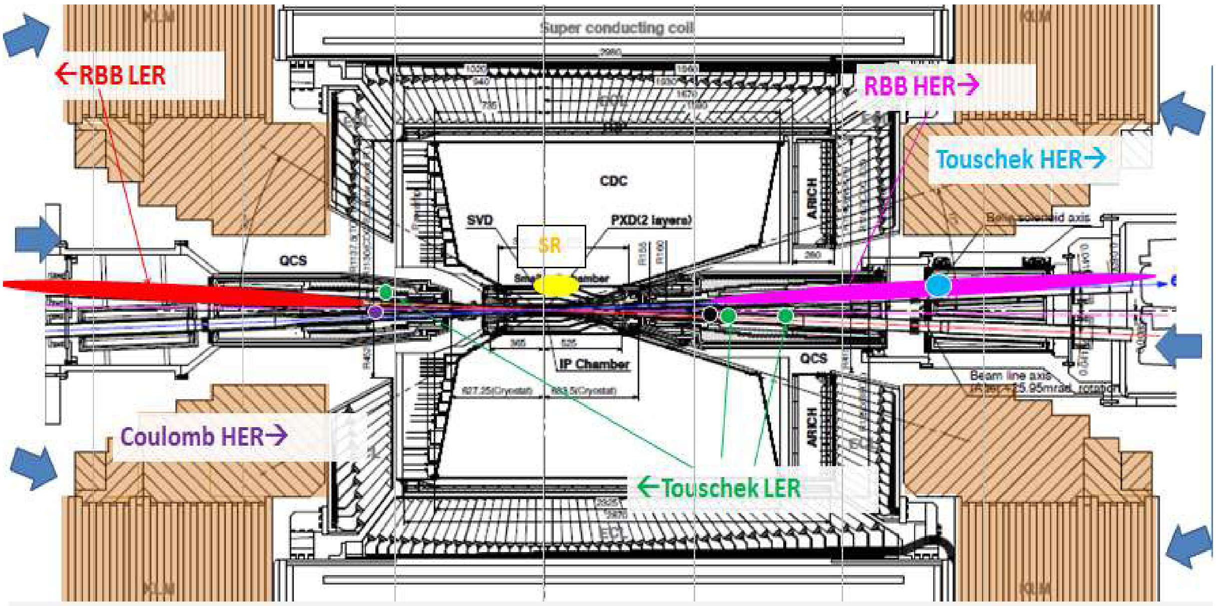

Figure 5.1 – Backgrounds at the interaction region (Belle II) [59]

Touschek scattering and inelastic Coulomb scattering are considered as single beam losses, they are generated overall the ring due to scattering of the beam particles on residual gas or scattering of the beam particles upon each other. In addition to being lost inside the interaction region (IR) and resulting in backgrounds in the detector, particles from single beam losses are lost all over the rings which reduces the beam intensities after a certain time. In rings such as SuperKEKB and due to the very high currents and the very small beam sizes, beams have therefore relatively short lifetimes of the order of 10 minutes. The main processes determining the beam lifetimes are the Touschek large angle intra-beam Coulomb scattering and the zero angle radiative Bhabha scattering at the IP. The beams should thus be continuously re-injected to maintain their intensity over time. During the single beam commissioning of SuperKEKB during phase 1, the main single beam losses were the beam gas Bremsstrahlung, the Touschek scattering and the Coulomb scattering.

5.1.1 Beam-Gas Bremsstrahlung

The beam-gas Bremsstrahlung (fig. 5.2) is the deceleration of the charged particles of the beam when interacting with the electromagnetic field of the atomic nucleus of the residual gas atoms in the vacuum chamber. The charged particles lose energy by emitting a photon, and can exit the beam pipe after a certain time. The energy spectrum of the scattered Bremsstrahlung positrons is similar to that of the radiative Bhabha process, with a difference that the Bhabha spectrum is produced at the IP only, whereas the Bremsstrahlung positrons are generated over all the ring. The beam-gas Bremsstrahlung and resulting losses are proportional to the beam current and residual pressure in the vacuum chamber. The beam currents at SuperKEKB are twice higher than at KEKB while the vacuum level, except at the interaction region, is expected to be the same, thus the loss rates are expected to be a bit higher at SuperKEKB. During phase 1 commissioning, the vacuum level in both rings ranged between 10 nTorr and less than 1 nTorr (1 Torr = 133.322 Pa).

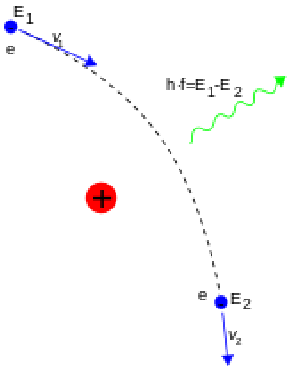

Figure 5.2 – Bremsstrahlung scattering of a charged particle in the field of the nucleus of an atom

5.1.2 Touschek scattering

In a storage ring, the electrons in the beam are subject to quantum excitations as they pass through the magnetic fields of the different magnets, where the discrete emission of photons results in a random walk of the beam particles diluting their trajectories and thereby enhancing the beam emittance. The beam emittance reaches an equilibrium value after beam injection when the radiation damping [60] due to synchrotron radiation balances the quantum excitations. Having acquired transverse velocities, particles in the same bunch can scatter upon each other in a process called Touschek scattering [61][62]. Extrapolated simulations showed that the Touschek backgrounds in SuperKEKB will increase by a factor of 20 compared to that at KEKB.

Since the horizontal emittances are larger than the vertical emittances, we assume that the initial momenta of the scattering particles are in the horizontal direction. We consider the Touschek scattering of the two particles in the center of mass system (CMS)(fig. 5.3), where $\vec{p}_{1,init}$=(p$_x$,0,0) and $\vec{p}_{2,init}$=(-p$_x$,0,0) are the initial momenta of the two particles expressed in the x, s and z coordinate system. Fig. 5.3 represents the particle scattering where θ is the scattering angle, and χ is the angle between the momentum of the scattered particle $\vec{p}_{1,scatt}$ and the s axis. The scattering momentum of the other particle is -$\vec{p}_{1,scatt}$. The momentum vector of the scattering particle is expressed as $\vec{p}_{1,scatt}$=(p$_x$ sinχ cosϕ, p$_x$ cosχ, p$_x$ sinχ sinϕ). Thus the momentum transfer to the longitudinal plane in the CMS is Δp_{cms} given in eq. 5.1, it is maximum when χ is zero.

$$\Delta p_{cms} = \gamma \times p_x \times cos\chi \tag{5.1}$$

In the laboratory frame, the maximum momentum transfer represented in eq. 5.1 transforms to ΔE in eq. 5.2 where γ is the Lorentz factor. γ is calculated as given in eq. 5.3 where E is the energy of the particle, m is the mass of the electron and c is the speed of light. In SuperKEKB, γ is 7843 and 13725 in the LER and HER respectively. The horizontal momentum is calculated as given in eq. 5.4, where ε_x is the horizontal emittance and β_x is the horizontal β function at the scattering position. In the Touschek process, one particle loses and the another gains energy. The particles are lost if their relative energy variation ΔE exceeds the energy acceptance of the machine. The energy acceptance of SuperKEKB is 1-1.5%, thus if a positron gains or loses more than 0.06 GeV or an electron gains or loses more than 0.1 GeV, they will be lost from the beam. The loss rate of Touschek is proportional to the square of the beam current and the inverse of the beam size.

$$\Delta E = \gamma \times p_x \tag{5.2}$$

$$E = \gamma m c^2 \tag{5.3}$$

$$\frac{p_x}{p} = \sqrt{\frac{\varepsilon_x}{\beta_x}} \tag{5.4}$$

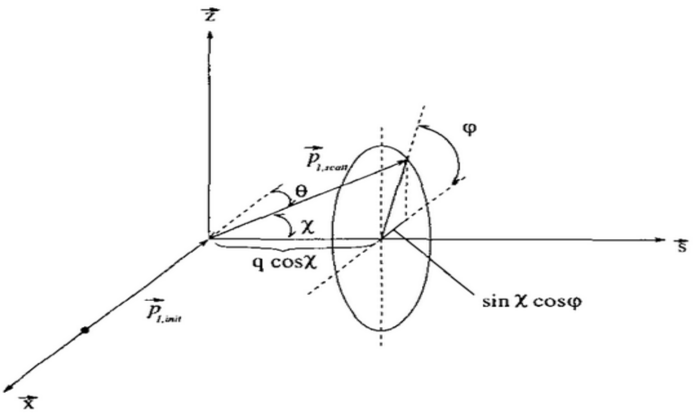

Figure 5.3 – Touschek scattering in the CMS [62]

5.1.3 Coulomb scattering

Coulomb scattering is the scattering of the charged particles of the bunch on the nucleus or the atomic electrons of the residual gas atoms. Coulomb scattering changes the direction of the beam particle (momentum) and thus the particle will be lost due to this transverse kick. The Coulomb scattering and the resulting losses are proportional to the beam current and the vacuum level (similar to Beam-gas Bremsstrahlung). Unlike Bremsstrahlung, simulations reveal that the Coulomb scattering rate is ≈100 times higher at SuperKEKB than at KEKB due to smaller beam pipe aperture at the interaction region and larger β functions at SuperKEKB [58].

5.2 Simulation of single beam losses in phase 1

A version of SAD was used to simulate the single beam losses (Beam-gas Bremsstrahlung, Touschek scattering and Coulomb scattering), consisting of two main parts, one which generates the single beam backgrounds and tracks them and produces files with the tracking results, and the other which analyses the tracking files and calculates the loss rates [63]. Each main part calls a group of libraries responsible for different tasks (definition of the physical apertures, definition of the physics of the backgrounds, e.g. cross sections or cuts in the phase space, definition of the mechanism of tracking, especially the scattering and observations points, definition of the calculation process of the loss rates, ...). This code was used to calculate the loss rates of the three different single beam backgrounds in the drift where we place our diamond sensors in the LER and to get the dynamics of the tracked particles of the three processes (energies, positions in the vacuum chamber, angular distributions, etc ..) after the quadrupole QKBLP just before the drift, to be used then to study the signal in the DS using GEANT4. In chapter 3, I showed that the optimal position of the DS in the LER is at 13.9 meters downstream of the IP. However, GEANT4 showed a uniform loss of the Bhabha particles all over the drift and thus the diamond sensors will be placed at 11.9 meters downstream of the IP. Below, I will discuss the simulations for the three different single beam loss processes.

5.2.1 Beam-Gas Bremsstrahlung

Modifications were performed to the code to obtain reliable results in the context of our study.

Case a: The scattering points in the standard version of the code are at the entrance of quadrupoles, except the final focus quadrupoles for phases 2 and 3 and some special vertical bending magnets (only 6 of them in the lattice). The observation point is at the entrance of each element. As a first attempt to study the lost particles in the drift of the DS, the code was used without modification. We expected having a whole spectrum of Bremsstrahlung positrons lost in the drift since Bremsstrahlung scattering takes place not only at the IP but in the entire ring. The energy spectrum of the lost Bremsstrahlung positron in the case of no modifications in the code is presented on l.h.s of fig. 5.4. The spectrum is discontinuous, and the reason behind this discontinuity is the poor resolution of scattering points. The r.h.s of fig. 5.4 shows the energy of the lost particles in the drift as a function of their scattering position. The discontinuity of the scattering positions on r.h.s of fig. 5.4 is clear, and corresponds to the positions of the quadrupoles in the lattice (fig. 5.5). It would prevent us from having the correct loss rate value in the drift, so we needed to improve the scattering resolution.

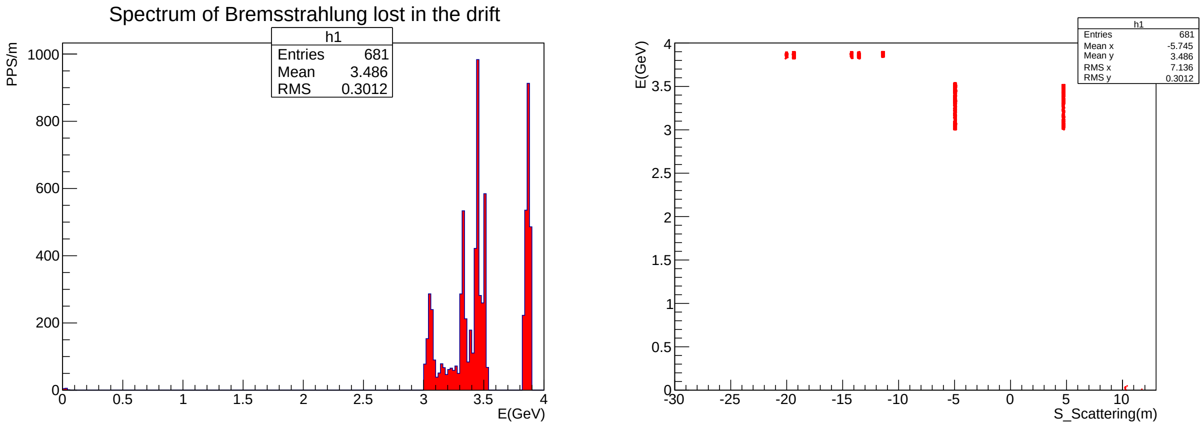

Figure 5.4 – The energy spectrum of Bremsstrahlung positrons lost in the drift on l.h.s and their energy as a function of their scattering position on r.h.s in case a (scattering at the entrance of quadrupoles and special vertical bends)

Case b: Small modifications to the code were implemented including scattering at

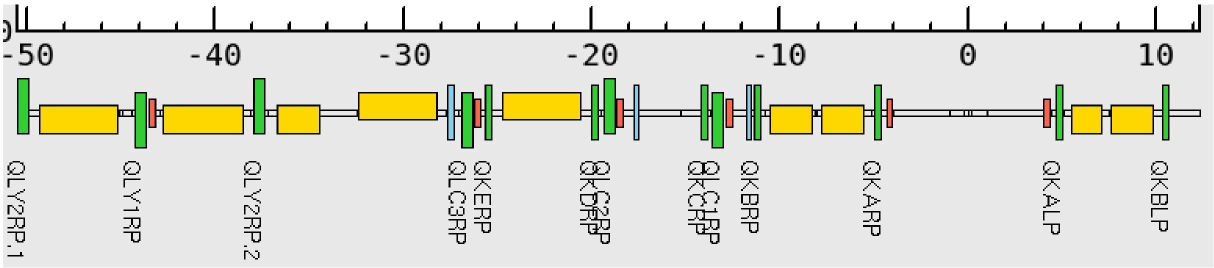

Figure 5.5 – The LER lattice from 50 meters upstream to 11 meters downstream from the IP

all the elements instead of just scattering at quadrupoles and very few vertical bends. The energy spectrum of the lost particles improved a bit but was still discontinuous (l.h.s of fig. 5.6). The resolution improvement was not enough since there exist relatively long elements (like bending magnets and drifts) in the scattering region, to which we are sensitive in the drift. On r.h.s of fig. 5.6, we can see that the distance between two consecutive scattering positions corresponds to the length of each element (since scattering takes place at the entrance of each element). With this change, we got a larger loss rate in the drift compared to "case a", but still the rate was not reliable since the energy spectrum was still discontinuous. **Case c:** To further enhance the scattering resolution,

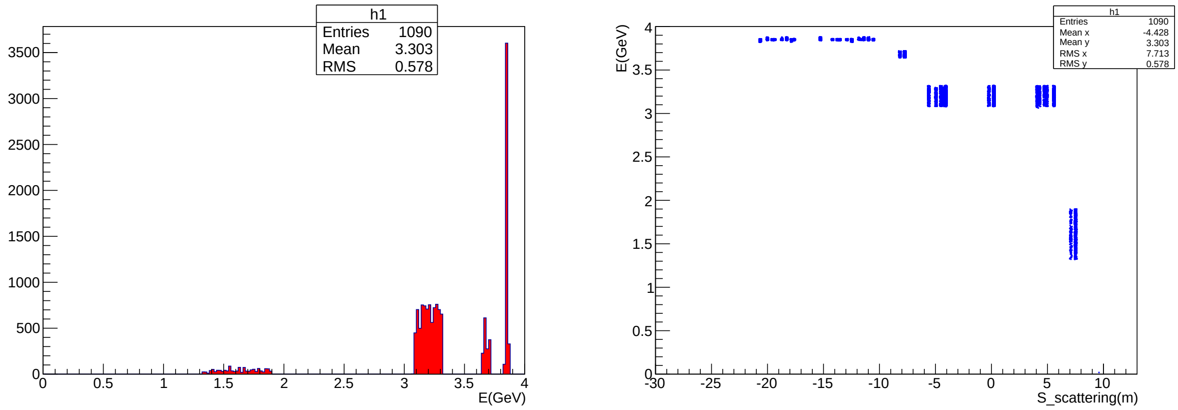

Figure 5.6 – The energy spectrum of Bremsstrahlung positrons lost in the drift on l.h.s and their energy as a function of their scattering position on r.h.s in case b (scattering at the entrance of all elements)

the long elements (drifts and bends) have been cut into slices of equal lengths. The scattering of the positrons was then considered at the entrance of each slice. The bending magnets were sliced into small bends of ≈15 cm each, keeping the same overall angle of the original element and the drifts were sliced into slices of 10 cm each (fig. 5.7), from 50 meters upstream to 13 meters downstream of the IP. In this way, we recovered the

entire energy spectrum of the Bremsstrahlung positrons lost in the drift (l.h.s of fig. 5.8) and gained better resolution on the scattering positions (r.h.s of fig. 5.8), where we can also see that the high energy particles that are lost in the drift are scattered at farther distances from the drift than the low energy particles.
Using this technique, the loss rate obtained in the drift was saturated while keeping the loss rate overall the ring the same: when increasing the number of scattering positions we increase the loss locally in the drift while the total loss overall the ring remains compatible within statistical errors. On l.h.s of fig. 5.9, the plot shows clearly the statistical

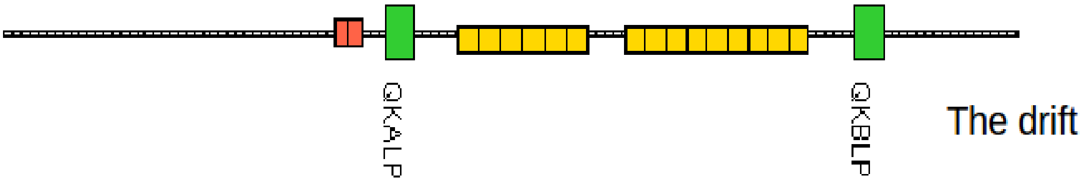

Figure 5.7 – Example of slicing of bending magnets: horizontal (yellow) and vertical (red), and drifts (grey) between IP and the drift (included)

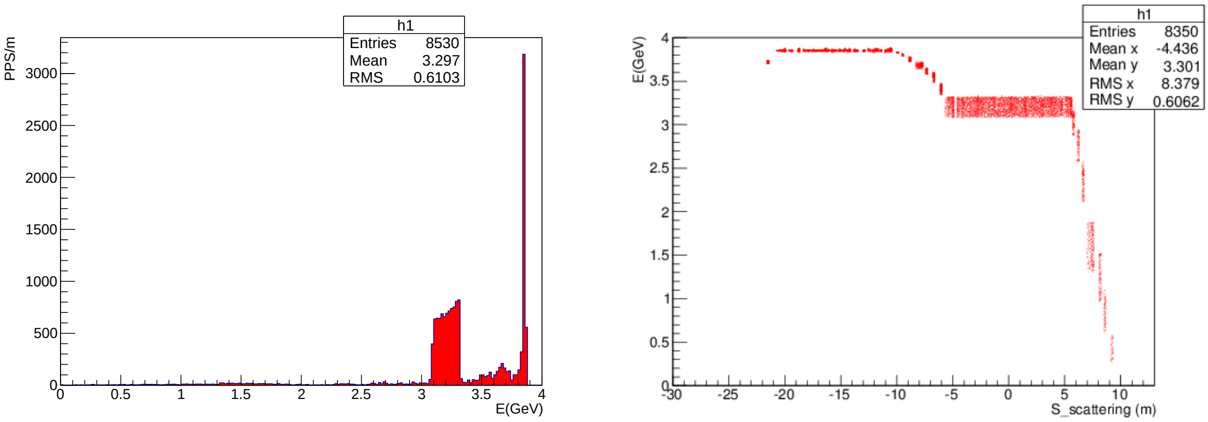

Figure 5.8 – The energy spectrum of Bremsstrahlung positrons lost in the drift on l.h.s and their energy as a function of their scattering position on r.h.s in case c (scattering at all the elements after slicing the bending magnets and the drifts)

variation of the total loss rate in the ring as a function of scattering resolution where “Q*,BV*” represents the scattering at quadrupoles and special vertical bends, “element*” represents the scattering at all the elements without any slicing, (30, 20, 10, 5) represents the length of the slices in cm of the drifts and the bends. Whereas the r.h.s of fig. 5.9 shows that the local loss rate in the drift decreases progressively when going from 10 cm slicing to scattering just at quadrupoles and vertical bends. In addition, the same figure shows that we lose 60% of the local losses in the drift if we go from slicing every 10 cm to scattering at “Q*,BV*”. It also shows that slicing every 10 cm saturates local losses, which implies that even going to finer slices of 5 cm should not change the result. As a result, 10 cm slicing was used in all the simulation results shown later. The improvement of the resolution of the observation position (the position of loss) is as important as that of the scattering position, where the former will be needed to define precisely the loss position of the Bhabha positrons in the drift which will afterwards be used in GEANT4 to study the signal of the losses in the DS. For this reason, the drift was cut into slices of 10 cm and the losses were observed at the entrance of each slice. The losses in the drift are distributed homogeneously over all the small slices (l.h.s of fig. 5.10), where low energy particles exit the beam pipe at a large horizontal angle and the high energy particles exit the beam pipe at smaller angles (r.h.s fig. 5.10). After generating and tracking the Bremsstrahlung losses, GEANT4 was used to study the signals of these losses in the DS. In GEANT4, the phase 1 design of the vacuum chamber at the drift was considered, which is a normal 6 mm thick Cu cylinder.

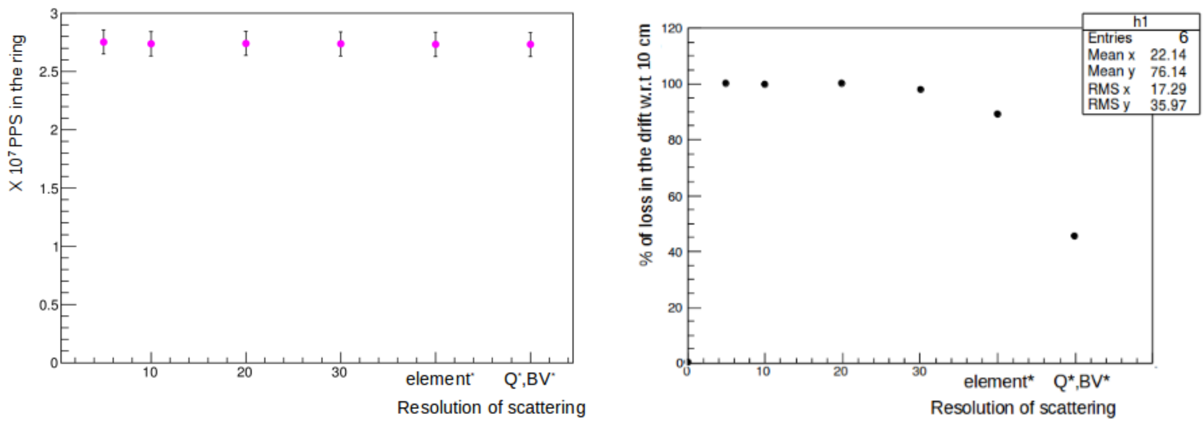

Figure 5.9 – The total loss from Beam-gas Bremsstrahlung overall the ring as a function of the scattering resolution on l.h.s and the percentage of loss in the drift with respect to the resolution of 10 cm as a function of scattering resolution on r.h.s

Due to their wide horizontal angular distribution that ranges from 3 mrad to 25 mrad, different Bremsstrahlung positrons will traverse different distances inside the material of the vacuum chamber. All Bremsstrahlung positrons in the drift are lost on the low energy side thus the charged secondaries from their interaction with the beam pipe exit on the same side (+x side) (l.h.s of fig. 5.11), nevertheless a few of them may exit all over the cylinder mainly due to backscattering. The energy spectrum of the charged secondaries peaks at ≈ 8 MeV and extends to 65 Mev (r.h.s of fig. 5.11).

The charged secondaries exit with all possible angles in the horizontal direction (l.h.s

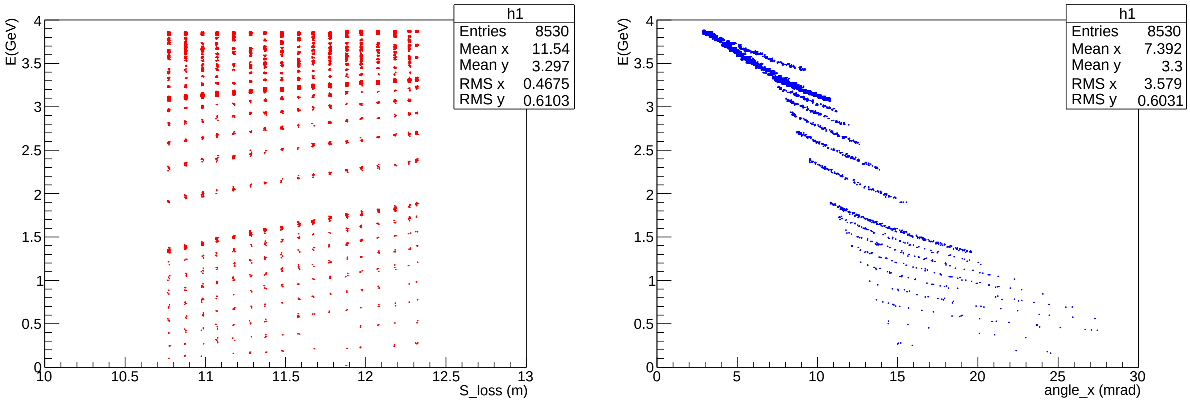

Figure 5.10 – The energy of the lost Bremsstrahlung positrons in the drift as a function of their loss position on l.h.s and as a function of their horizontal exiting angle on r.h.s

of fig. 5.12), with a peak in the distribution at ≈ 73^o. While some incident particles are totally absorbed in the thick beam pipe (no secondaries exit the beam pipe), other particles exit the beam pipe with different numbers of secondaries (r.h.s of fig. 5.12), the average number of charged secondaries per incident particle being ≈ 13.

Among all the Bremsstrahlung positrons that hit the inner beam pipe and are thus lost in the drift, only few particles generate a signal in the DS. The fraction of lost Bremsstrahlung positrons which will give signal in the DS to the total lost particles in the 1.65 m long drift is $5.9{\times}10^{-3}$. The signal in the DS is generated from the charged secondaries corresponding to the incident lost particles. The distribution of the number of secondaries per incident particle generating a signal in the DS is given in fig. 5.13, where most of the particles deposit only one secondary in the DS.

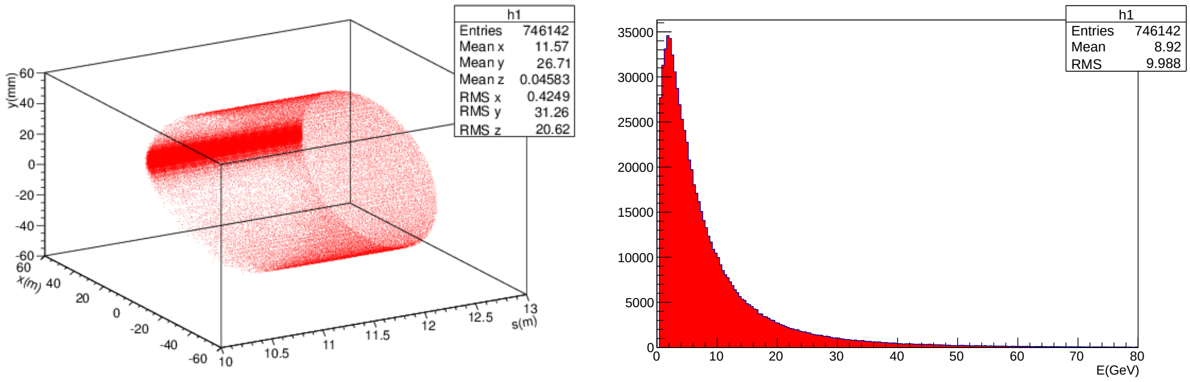

Figure 5.11 – The 3D distribution of the charged secondaries exiting the 6 mm thick Cu beam pipe on l.h.s and their energy spectrum on r.h.s

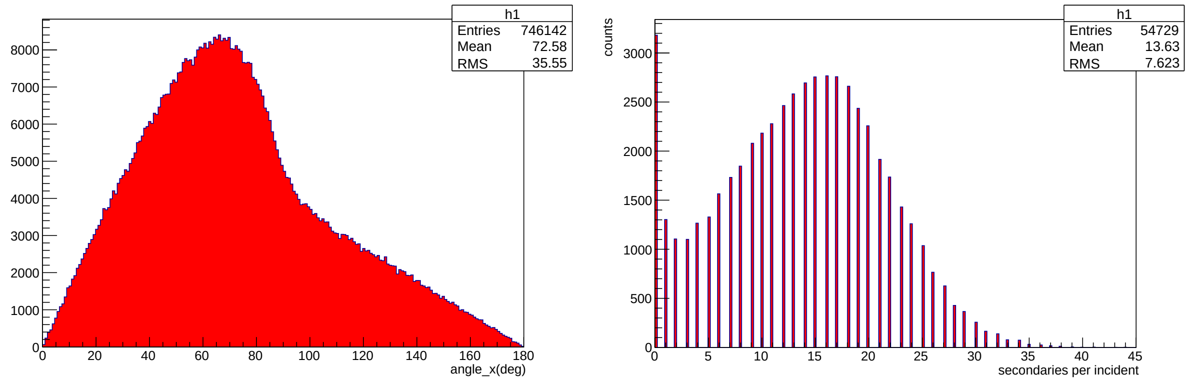

Figure 5.12 – The horizontal angular distribution of charged secondary particles exiting the 6 mm Cu cylinder beam pipe on l.h.s and their number per incident particle on r.h.s

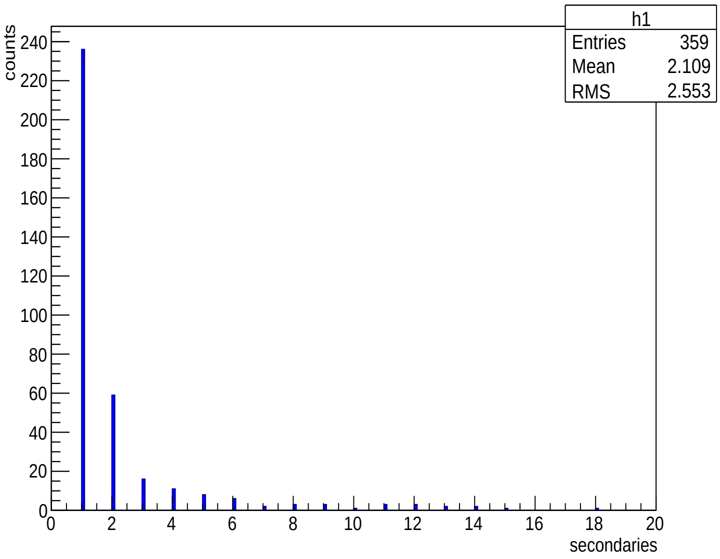

Figure 5.13 – Histogram of number of secondaries deposited in the DS by each incident particle

After having simulated and tracked the Bremsstrahlung losses by SAD and studied the signal from the losses in the DS, losses were estimated for several beam currents and vacuum pressures. The results are shown in fig. 5.14 where the losses in the DS are linear as a function of the product of the beam current and the vacuum pressure.

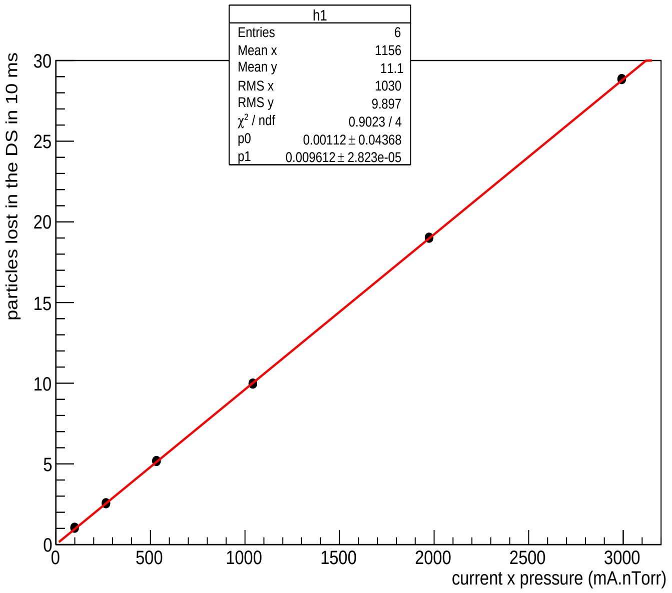

Figure 5.14 – The behaviour of the losses detected in the DS as a function of the product of beam current and vacuum pressure

5.2.2 The Touschek process

In the Touschek process, one particle loses energy and the another one gains energy and the energy variation corresponds to the relation given in eq. 5.2, which relates directly to the β function and the emittance. The Touschek scattered positrons which are lost in the drift are scattered at a maximum distance of 20 meters upstream from the IP, and they can lose or gain a maximum of 7% of their energy (l.h.s of fig. 5.15). The particles which gained energy exit the beam pipe on the high energy side (-x) with a very shallow horizontal angle, whereas the particles which lost energy exit the beam pipe on the low energy side (+x) (r.h.s of fig. 5.15).

The theoretical estimations of the energy variation of the particles due to Touschek scattering (eq. 5.2) are consistent with what we get from the simulation. The profile of the horizontal β function is given in fig. 5.16 between 50 meters upstream of the IP and the IP. The percentages of the energy variations calculated from the horizontal β function at the scattering position and the horizontal emittance of the beam ($\varepsilon_x = 1.95 \times 10^{-9}$ m) are shown in fig. 5.17, where energy losses between 4% and 7% are estimated in the region from 20 to 5 meters upstream of the IP, consistent with the simulation.

Since the Touschek particles exit the beam pipe on both sides in the horizontal plane, they will produce charged secondaries mainly in the same plane after having traversed the material of the beam pipe (l.h.s of fig. 5.18). Each exiting charged secondary corresponds to one incident particle, nevertheless some incident particles are absorbed totally in the

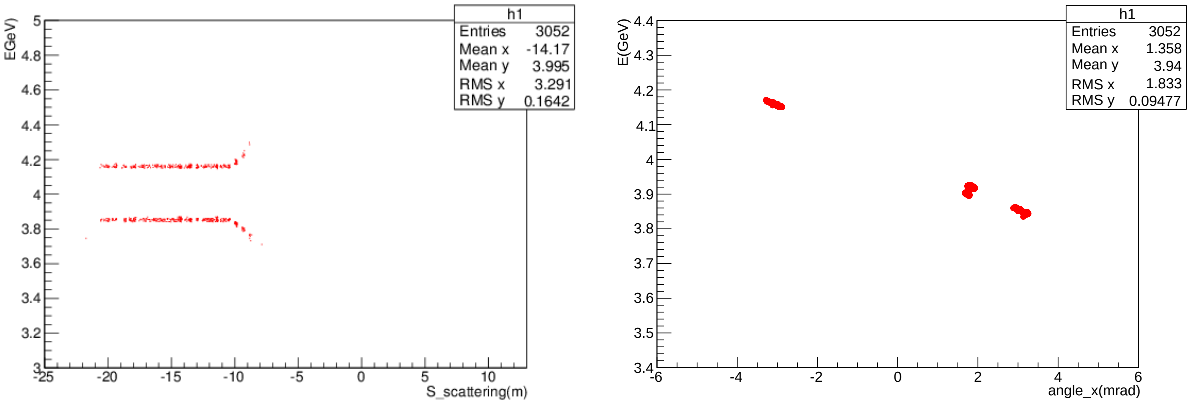

Figure 5.15 – The energy of the lost Touschek positrons in the drift as a function of their scattering position on l.h.s and as a function of their exiting horizontal angle on r.h.s

beam pipe with zero secondaries exiting (r.h.s of fig. 5.18). Among all the particles that are lost in the drift only very few generate a signal in the DS (a fraction of 4.85×10^{-3}), by depositing secondaries. Most incident particles giving a signal in the DS deposit only one secondary, and just a few may have more than one secondary (fig. 5.19).

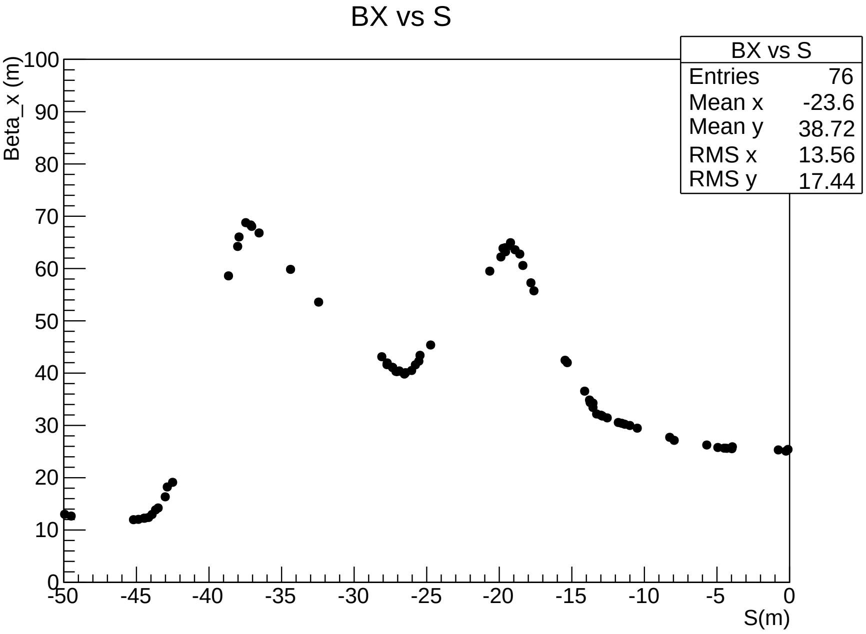

Figure 5.16 – The β function in the LER between 50 m upstream the IP and the IP

After having calculated the signal in the DS, the losses from Touschek scattering for different beam currents could be calculated. The results show a quadratic behaviour

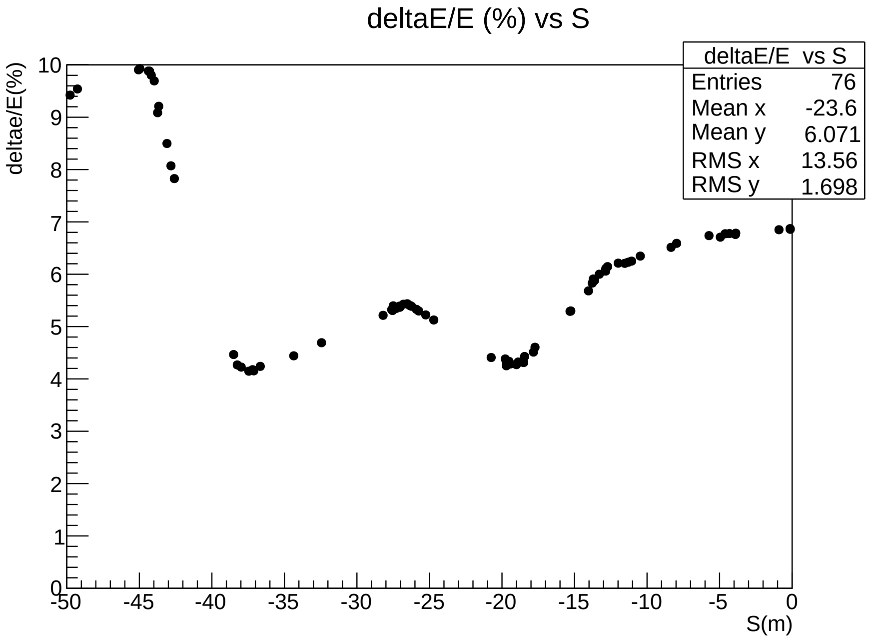

Figure 5.17 – The percentage of the energy variation due to Touschek scattering computed from eq. 5.2, between the scattering regions extending 50 meters upstream the IP and the IP

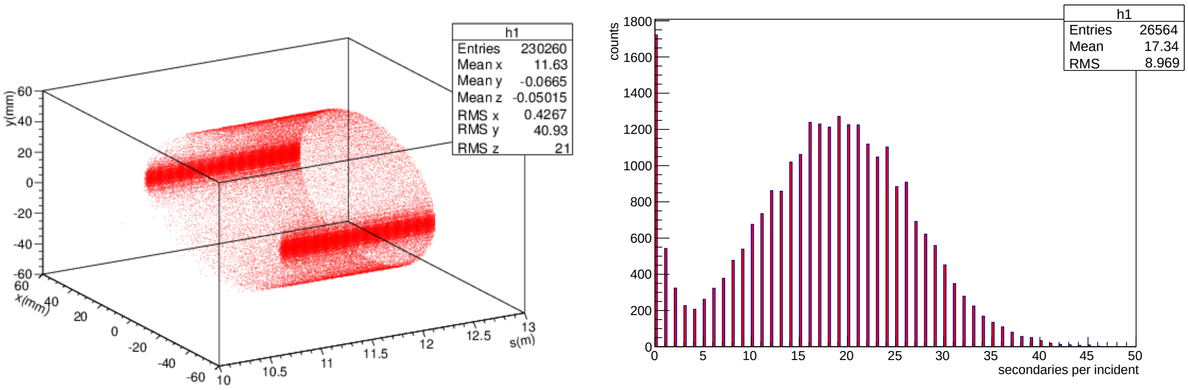

Figure 5.18 – The 3D distribution of the charged secondaries resulting from the interaction of the incident lost positrons with the 6 mm Cu cylinder beam pipe on l.h.s and their number per incident particle on r.h.s

(fig. 5.20), expected since the loss rates of the Touschek process are proportional to the square of the particle population in the bunch (N^2).

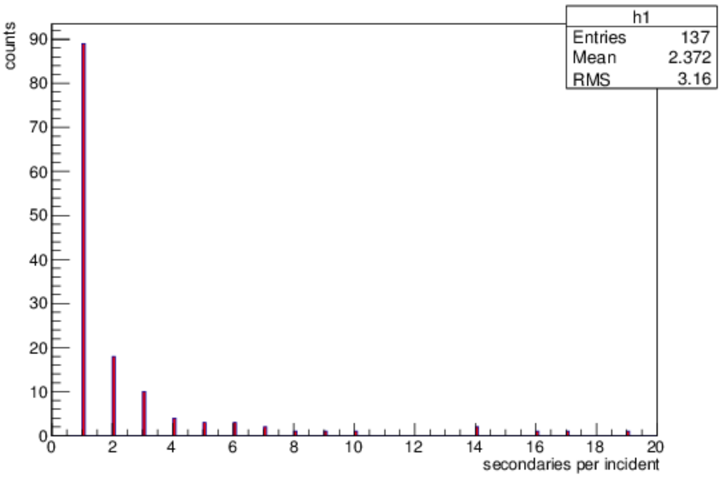

Figure 5.19 – Histogram of number of secondaries deposited in the DS by each incident particle

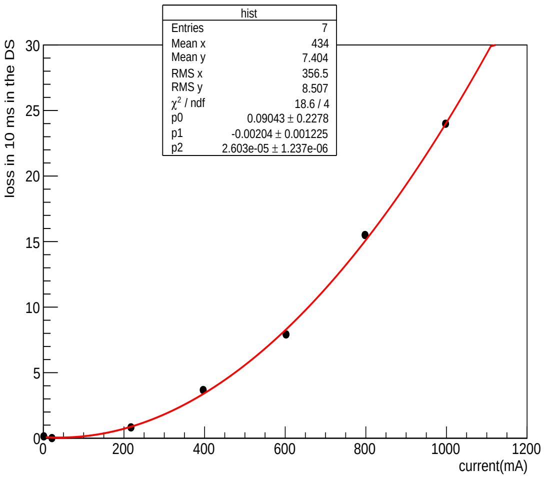

Figure 5.20 – The behaviour of the loss from Touschek scattering in 10 ms in the DS as a function of the beam current

5.2.3 Coulomb

Coulomb scattering is an elastic scattering between the particles of the beam and the nuclei of the residual gas atoms. Beam particles will get a transverse kick while keeping their initial energies. The Coulomb scattered positrons at positions up to ≈ 80 meters upstream of the IP will be lost in the drift due to their transverse angles in the horizontal and vertical planes (fig. 5.21). The Coulomb scattered positrons are lost mainly in the vertical plane (fewer particles are lost in the horizontal plane), and this can be observed clearly from the distribution of the charged secondaries which are the result of the interaction of the lost incident positrons with the material of the 6 mm Cu cylinder beam pipe (fig. 5.22).

The transverse offset of particle at a given loss position (B) due to a kick at an emission point (A) is proportional to the transfer matrix elements R12 for the horizontal plane and R34 for the vertical plane, between A and B, which can be expressed as $\sqrt{\beta_A \beta_B}\,\sin(\phi_{AB})$, where β_A and β_B are the transverse β functions at the emission and loss positions respectively. Due to the fact that β_x and β_y are about equal at the loss position (in the drift) (fig. 5.23), then the reason why Coulomb scattered positrons are lost in the vertical plane is that β_y is larger than β_x at the positions of scattering. Fig. 5.24 shows the distribution of the scattering positions of the Coulomb positrons lost in DS in the drift, it shows as well a peak at $\approx$ 80 meters upstream of the IP where the β_y is larger than β_x. Since our DS is placed in the horizontal plane at the low energy side (+x) and the Coulomb loss is mainly in the vertical plane, GEANT4 simulations reveal that we will have no signal from Coulomb scattering in the DS.

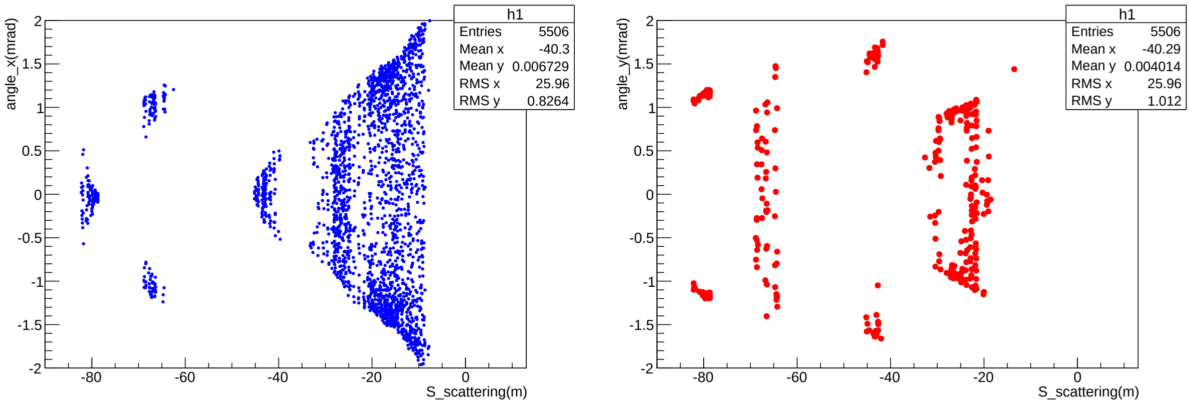

Figure 5.21 – The horizontal exiting angles on l.h.s and the vertical exiting angles on r.h.s, of the lost Coulomb scattered positrons in the drift

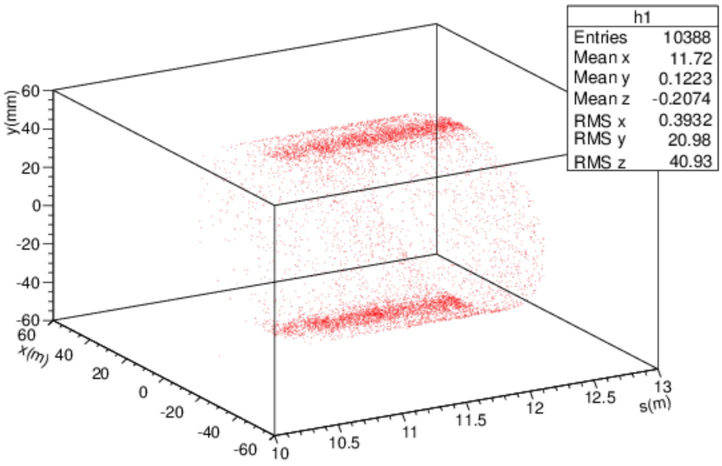

Figure 5.22 – 3D distribution of the position of the charged secondaries exiting the 6 mm Cu cylinder beam pipe

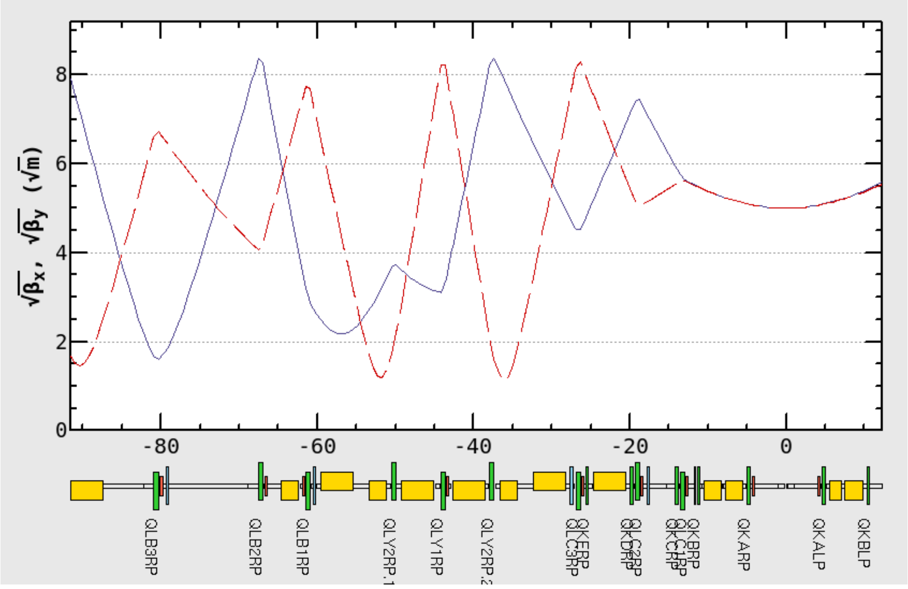

Figure 5.23 – The square root of the horizontal β function (blue) and the vertical β function (red) at the scattering positions up to $\approx$ 100 meters upstream from the IP until the drift at $\approx$ 11 meters

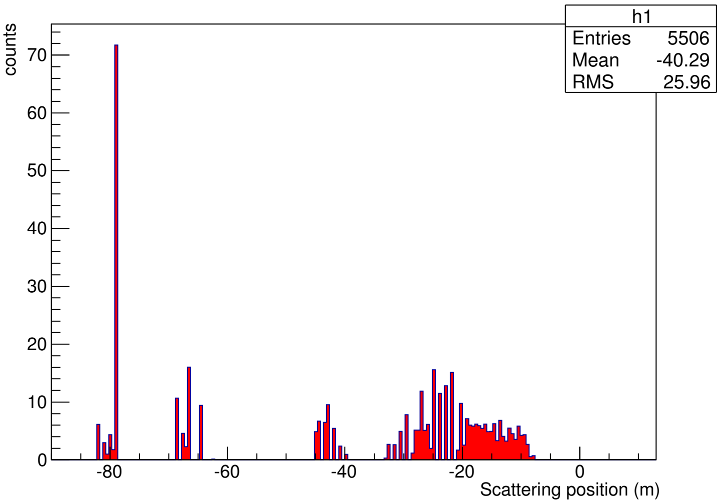

Figure 5.24 – The scattering positions of the Coulomb positrons lost in the DS in the drift

Chapter 6

Measurements of Single Beam Loss at Phase 1

6.1 Experimental configuration

To be able to measure the single beam losses at phase 1, a complete experimental setup was prepared and installed in both rings of SuperKEKB, consisting of:
- Mechanical setup
- Sensors and readout

6.1.1 Mechanical setup

The mechanical setup consists of pillars in each ring. Each pillar supports a movable plate with two sCVDs each connected to a CIVIDEC charge amplifier, and a fixed plate with the ZDLM monitors. The movable plate is associated to a remotely controlled motor to scan along the vertical direction over a range of 2.5 cm. In the HER, the pillar is installed 30 meters downstream of the IP and the sensors are facing the exit of the antechamber in the drift (fig.6.1). The pillar in the LER is installed at 11.9 meters downstream of the IP and the sensors are facing a normal cylindrical beam pipe in the drift (fig. 6.2). Both pillars are fixed on the ground with screws and contain one box each for cable interconnections.

6.1.2 Sensors and readout

For phase 1, four sCVDs connected to CIVIDEC charge amplifiers were installed, two of them in the LER (l.h.s of fig. 6.3) and two others in the HER (r.h.s of fig. 6.3). The signals from the sCVDs were sent to rack F-8 on the 2^{nd} floor of the Electronic Hut (E-Hut) of the Belle II experiment, by rigid half inch heliax cables connected at different stages with special connectors (fig. 6.4).

During phase 1, the Belle II detector with its E-Hut were rolled out from the interaction region (fig. 6.5) with the entire detector 13 meters to the side of the IP. Additional cables were used to connect the sensors to the electronic rack in the E-Hut. During phases 2 & 3, the Belle II detector will be rolled in and these extra cables will be removed.

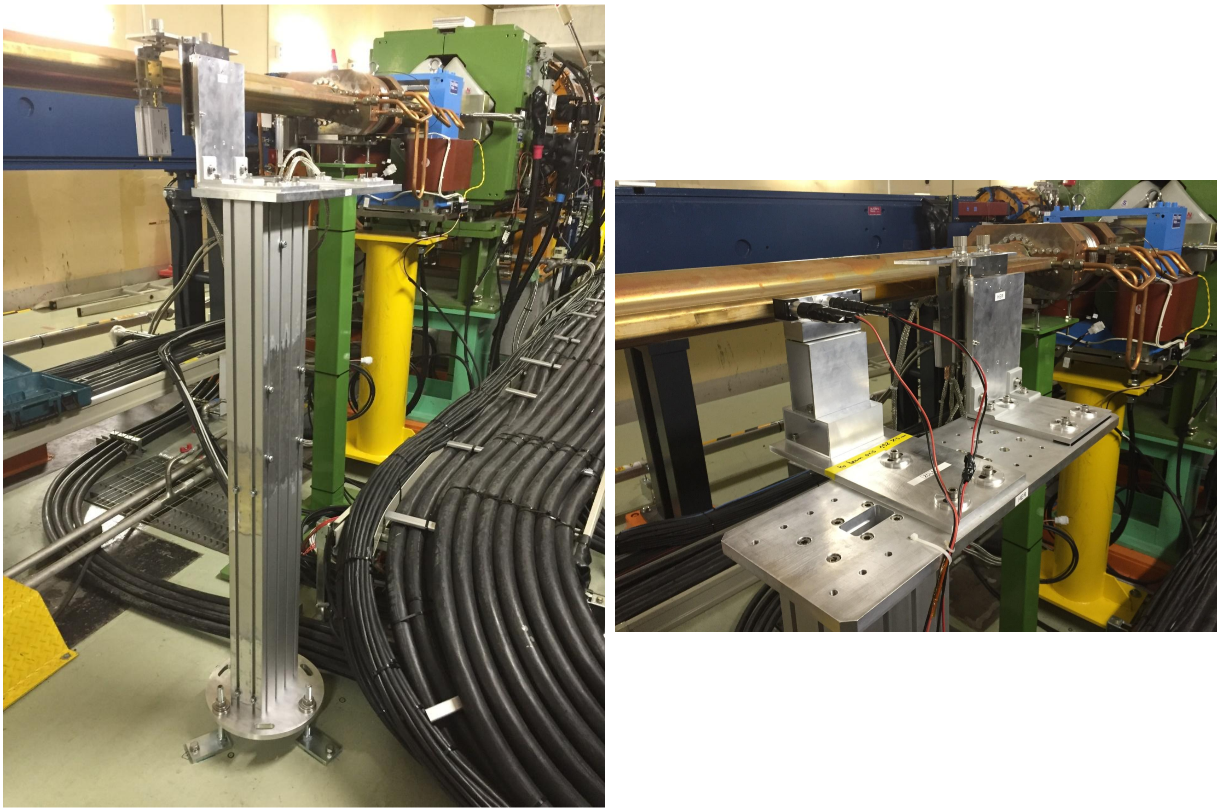

Figure 6.1 – The pillar in the HER at 30 meters downstream of the IP holding the two sCVDs and the ZDLM monitors

The electronic rack for phase 1 (fig. 6.6) was equipped with a special "RF SYNCHRO" crate to synchronize the future DAQ sampling clock to the RF clock, a 10 bit Keysight oscilloscope (2.5 GHz BandWidth and up to 20 GSPS sampling), a PC serving as gateway to the Linux operated Belle-II DAQ computers, a Windows based server on which analysis using MATLAB was performed, a high voltage power supply for the diamond sensors (400 V) and a low voltage power supply for the charge amplifiers (12 V).

Two signal acquisition procedures were implemented, either by continuous 10 ms records that could be processed on-the-fly every 5-6 seconds or up to fifty 410 ms long records spaced by few seconds, where the processing took place afterwards and lasted for a few hours. The raw data acquired by the Keysight oscilloscope were in ".H5" binary data format. These data were saved first in the hard disk of the oscilloscope and then copied to folders on the server. The copied ".H5" files were afterwards converted to ".mat" files and processed using MATLAB. The processing functions were built to search for the waveforms of the DS signals. Once the waveforms were defined, the maxima and their positions in time were extracted, as well as the FWHM of each waveform. In addition,

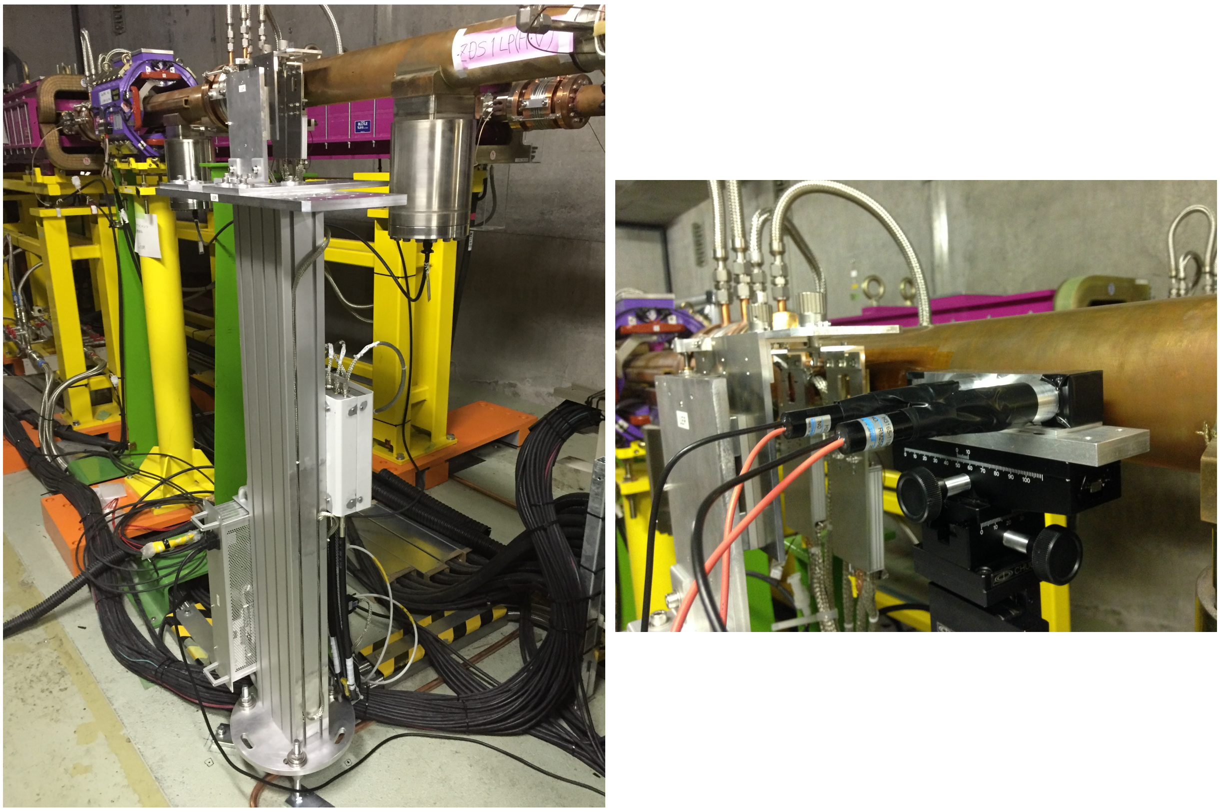

Figure 6.2 – The pillar in the HER at 11.9 meters downstream of the IP holding the two sCVDs and the ZDLM monitors

we created our own EPICS archive to save records of the machine parameters (like beam currents, vacuum pressure, beam size, time, ...) and we merged the data from the DS to the EPICS data after each acquisition. The time reference we used was given by the Belle II DAQ network (bdaq network). For our data to become accessible to the BEAST II working group of the Belle-II collaboration, we created a table with all the data recorded in phase 1. A subset of this table is processed to obtain a ROOT n-tuple and is included in the BEAST II ROOT n-tuples.

6.2 Single beam losses in the sCVD in phase 1

We aim from the measurement of the single beam losses in phase 1 to verify the simulations by comparing their results to the data we acquire. The verification of the simulation is necessary to extrapolate to phase 2, in order to have an idea about the amount of single beam losses we will have in the DS compared to the radiative Bhabha signal, as well as

Figure 6.3 – The two sCVDs connected to a charge amplifier each to be installed in the LER on l.h.s and in the HER on r.h.s

confirm the detector acceptance and efficiency.

During the phase 1 commissioning, we took data mainly during vacuum scrubbing in both rings. On the oscilloscope, we connected two channels to signals from diamond sensors in both rings, e.g. in combinations such as: (LER1,LER2), (LER2,HER2), (HER1,HER2), where LER and HER correspond to the sCVDs installed in the LER and HER, and 1 and 2 correspond to the sCVD closest and farthest from the IP, respectively. On the third channel of the oscilloscope we connected the revolution signal on which we trigger. The revolution signal is a signal given by the accelerator which corresponds to one turn of the beam in the ring ($\approx$ 3 km). The frequency of the revolution signal in SuperKEKB is about 100 KHz.

6.2.1 Losses as a function of different parameters

During the acquisition of signals from both rings, we noticed that we have much more signal in the LER than in the HER for similar beam currents. This can be clearly seen

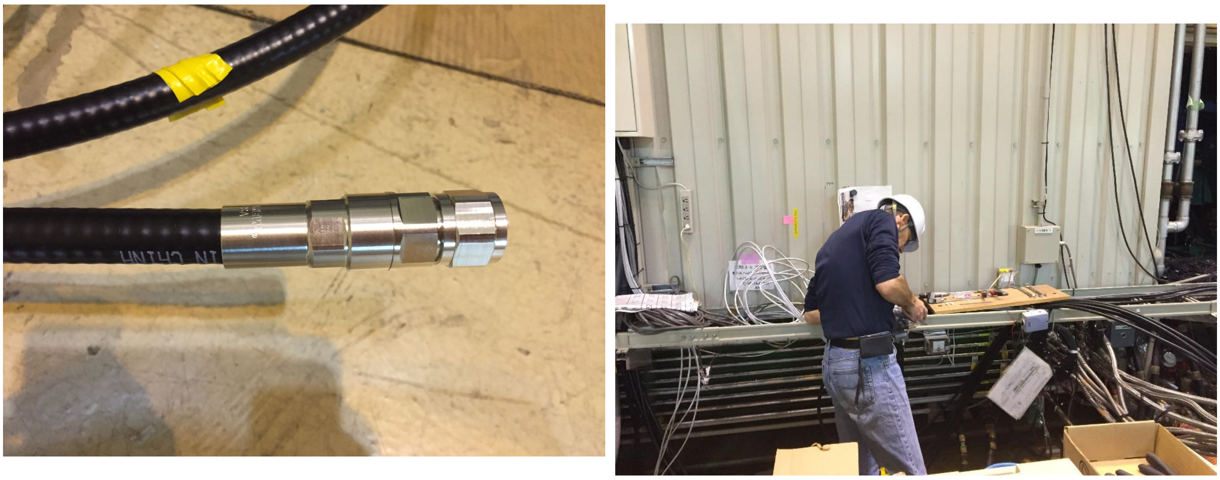

Figure 6.4 – Half inch heliax cables with the connectors on l.h.s and connections being done at B4 level in Tsukuba hall on r.h.s

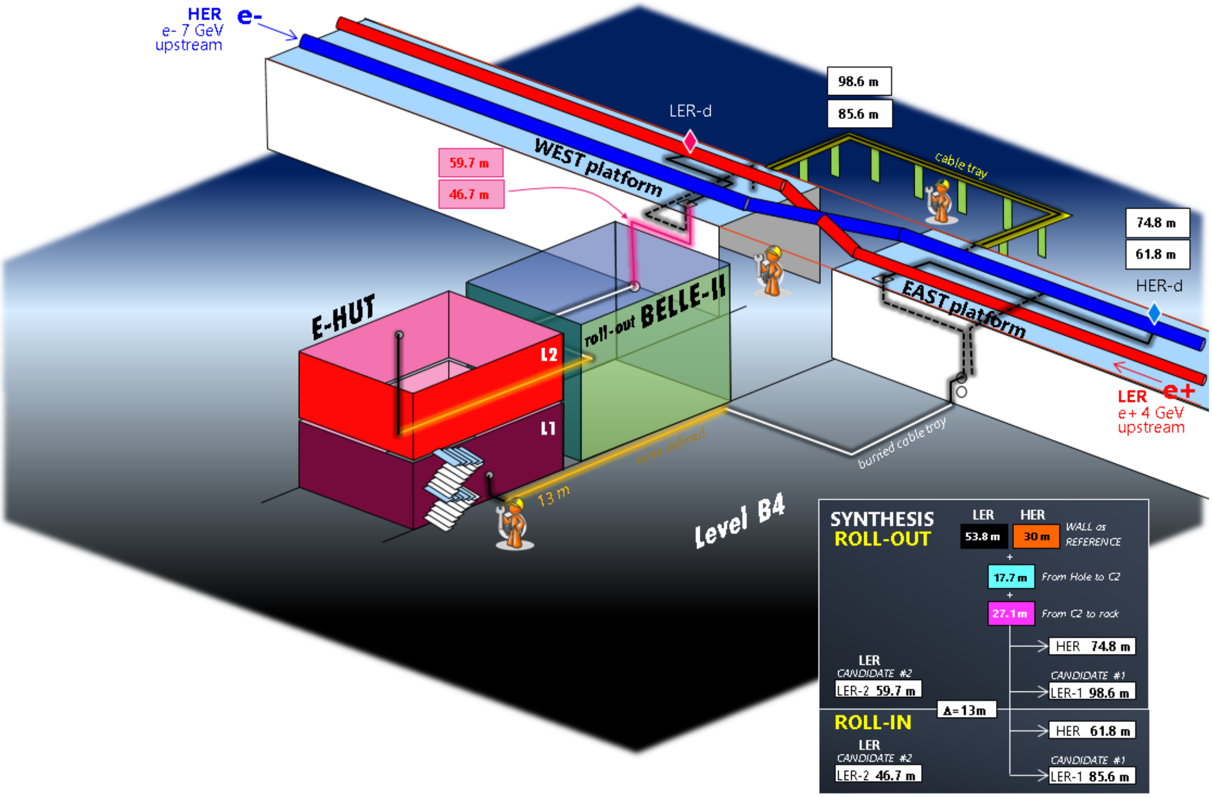

Figure 6.5 – The layout of the Tsukuba hall showing the Belle II detector with its Electronics-Hut and the paths for our cables in the LER and the HER

from an image taken from the oscilloscope during acquisitions from LER2 (yellow) and HER2 (green), where very large signals represent the injection (fig. 6.7).

Figure 6.6 – Our electronic rack in the E-Hut of the Belle II detector of the SuperKEKB experiment

At SuperKEKB, a top-up injection is considered where the beam is injected continuously at a frequency of 50 Hz. One of the important background sources is thus the injection noise [64]. The injected particles oscillate at an amplitude larger than that of the stored particles. If the injected particle oscillates outside the dynamic aperture, it will be lost after 10 to 1000 turns at some point in the ring. During phase 1, the injection noise was detected in our diamond sensors after each injection and it represented a large signal since several injected particles may be lost at once at the same place. This injection noise could be very high and cause a significant dead time in the acquisition of some of the Belle II sub-detectors, by causing electronics channels to go into saturation or large event sizes.

In HER, diamond sensors are located at 30m downstream of the IP, on the high energy side, to measure the Bhabha photons produced at the IP. The longitudinal extent of the spot size of the Bhabha photons hitting the inner wall of the beam pipe comes from the angular distribution of the beam particles (0.4 mrad). During phase 1, we mainly detected Bremsstrahlung photons which were produced in a region delimited by the last and the first bending magnets around the IP. This effective region represents 21.5 meters. Since the beams were not focused, the angular distribution of the photons is determined by the Bremsstrahlung process, whose characteristic emission angle is of the order of 1/gamma (0.07 mrad) [65]. Only the photons produced in the straight section at an angle larger than 4.5 times the characteristic angle can reach the sensors at 30 m, as well as a few photons produced in the bends. A preliminary study has estimated that the fraction of Bremsstrahlung reaching the HER 30 m section represents 10^{-4} of the amount of Bremsstrahlung produced in all the HER. In LER the fraction of the Bremsstrahlung losses at 11.9 m section represents $\approx 6 \times 10^{-3}$ of the total Bremsstrahlung losses in the ring. From this we can expect a large factor (>50) between LER and HER signal rates.

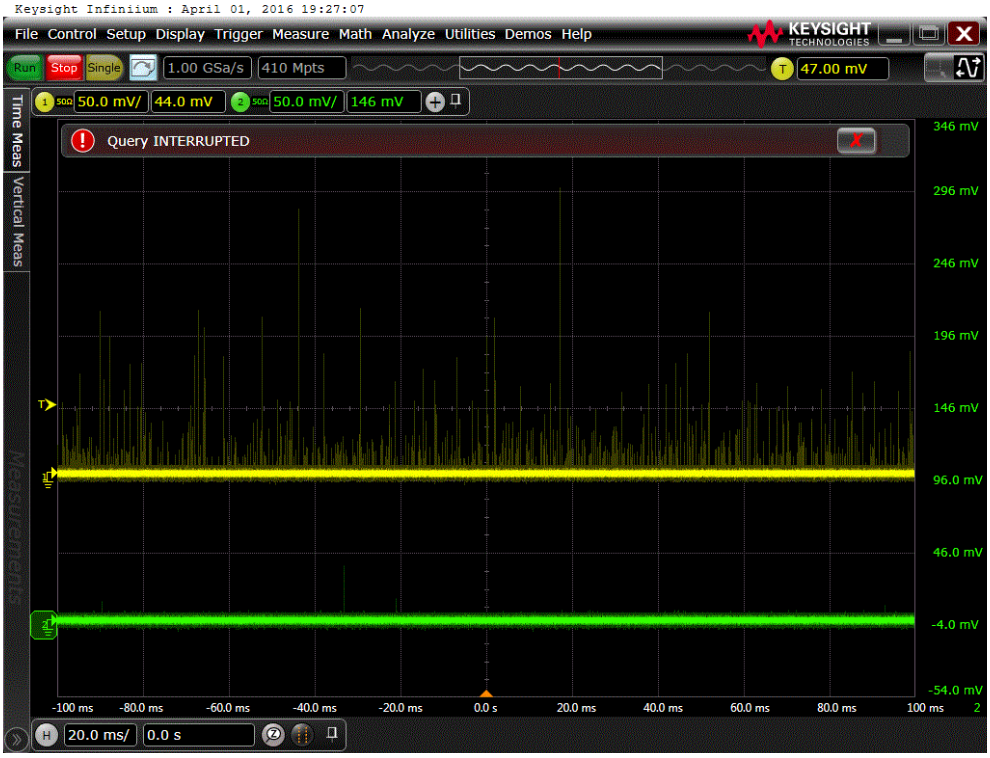

Keysight Infiniium : April 01, 2016 19:27:07

Query INTERRUPTED

Figure 6.7 – An image of the oscilloscope during the acquisition with (LER2(yellow), HER2(green))

6.2.1.1 Signals in the sCVD

1 MIP corresponds to 2.9 fC generated charge in the 4x4 mm^2 metallised part of the 500μm thick sCVD. The signal is then amplified by the charge amplifier (Gain 4 mV/fC)

to 11.6 mV. The energy deposited in the sCVD follows a Landau distribution, and this was simulated with GEANT4 (l.h.s of fig. 6.8) and confirmed by data (r.h.s of fig. 6.8).

However, there has been observed a difference between the simulation and the data at the level of the Landau fit. The limits of the Landau fit were considered from 6 mV to 200 mV in both cases, and the MPV (Most Probable Value) parameter was set to 8 mV. After performing the fit, the MPV of the Landau distribution in the measurements (11.6 mV) (r.h.s of fig. 6.8) was observed to be 1.26 times greater than that in the GEANT4 simulations (9.2 mV). Therefore, to have a reasonable comparison between the data and the simulation, the factor 1.26 has been taken into account to define the thresholds. The separation between the noise from the charge amplifier in the measurements was observed at 6 mV. Thus the threshold taken for the data during analysis was 6 mV, and the threshold for the simulation was taken at 4.75 mV.

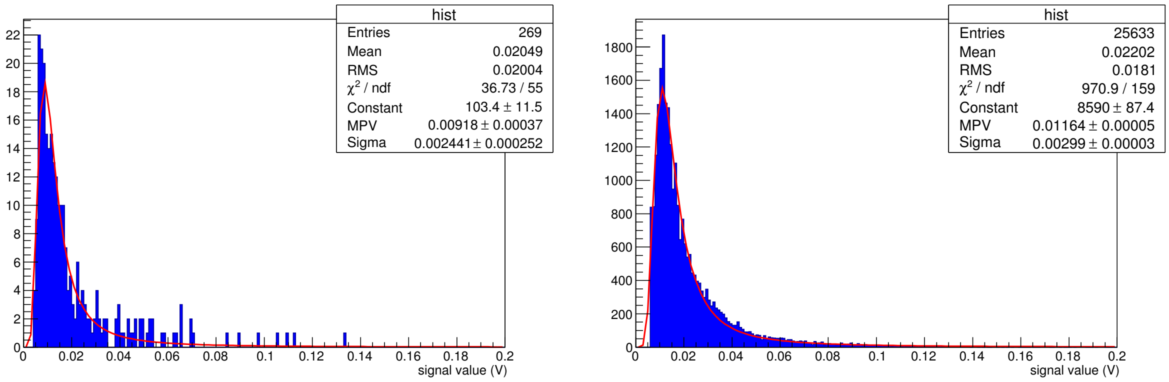

Figure 6.8 – Landau distribution of deposited charge of incident particles from simulations in GEANT4 on l.h.s and from data on r.h.s

6.2.1.2 Losses as function of current and pressure

The data analysis consisted in finding the number of peaks during a certain acquisition time which represents a sequence of sub acquisitions of 10 ms each, considering the threshold at 6 mV, and plotting this number as a function of different beam parameters (current, vacuum pressure,vertical beam size).

After analysis of the data, we can see that the losses (l.h.s of fig. 6.9) in the sCVD clearly follows the beam current profile (r.h.s of fig. 6.9) during the phases of injection and storage of the beam. The variation of the total loss rate in the sCVD per 10 ms given as a function of the beam current (l.h.s of fig. 6.10) shows a quadratic behaviour due to Touschek losses (chapter 5) and the variation as a function of vacuum pressure shows a linear behaviour(r.h.s of fig. 6.10).

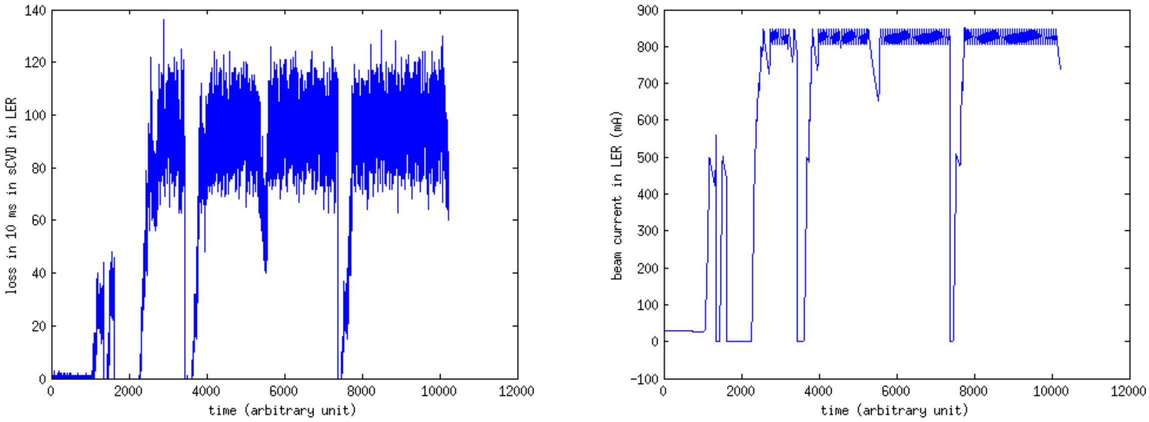

Figure 6.9 – Loss rate in the sCVD in 10 ms on l.h.s and beam current in the LER on r.h.s as function of time

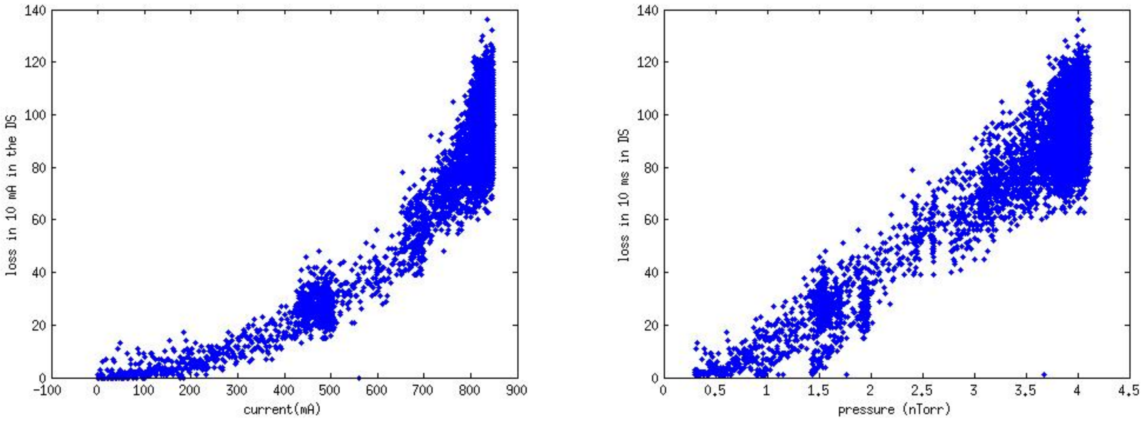

Figure 6.10 – The loss rate in 10 ms in the sCVD in LER as a function of beam current on l.h.s and as a function of vacuum pressure on r.h.s

6.2.1.3 Data from Cherenkov in LER

To compare the data from the sCVDs to that from the ZDLM monitors, we acquired data from the Cherenkov sensor using our Keysight oscilloscope. Since we have two channels dedicated for detector signals, we connected one sCVD in the LER to channel 1, and the Cherenkov detector in the LER to channel 2 of the oscilloscope. The threshold considered for the data taking and the analysis of the Cherenkov signals was 30 mV. The distribution of the peak values of the collected events is presented in fig. 6.11. The data was taken during the vacuum scrubbing in the LER, where the average current was 703 mA and the average vacuum pressure was 7.6 nTorr. From the loss distributions shown in fig. 6.12, we can observe clearly that the losses in the Cherenkov detector (1541 in 10 ms, red) are

≈ 11 times higher than those in the sCVD (136 in 10 ms, blue) under the same beam conditions. This factor is smaller than the ratio of the active areas of the sensors, but must also depend on the distances of the sensors from the beam pipe and the efficiency of the chosen threshold to define signals.

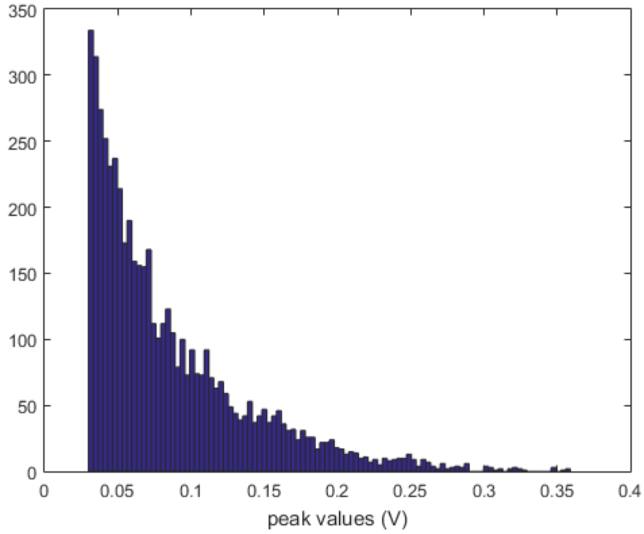

Figure 6.11 – The distribution of the peak values of the signals collected by the Cherenkov sensor

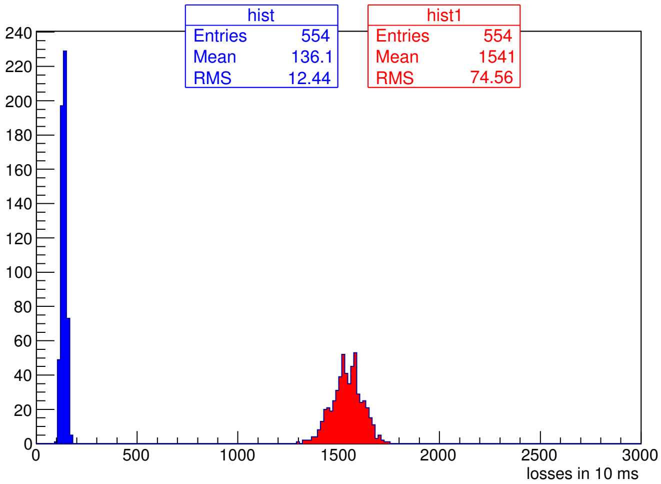

Figure 6.12 – The loss distributions in 10 ms in the sCVD (blue) and Cherenkov detector (red) for an average beam current of 703 mA and average vacuum pressure of 7.6 nTorr in the LER

6.2.2 Losses from vacuum bumps in the LER

Data were also acquired during dedicated BEAST II studies. On the 23^{rd} of May, a study was dedicated to the effects of vacuum bumps in the LER, during which several vacuum bumps were introduced in different sections around the IR. I analysed the data trying to separate the contributions from the losses due to Touschek and Bremsstrahlung in the sCVDs, but I noticed that the data taken during this study are not easy to analyse because the exact profile of the pressure along the section around the IP is not well known.

The map of the vacuum sections is given in fig. 6.13. During the study of the vacuum bumps, each time the NEG (Non-Evaporable Getters) in some defined subsections are heated to a certain temperature, to increase the vacuum pressure locally. Before each vacuum bump study, the beam is aborted and vacuum workers go into the tunnel to unplug the NEGs belonging to the corresponding subsections.

The distances from the IP of the subsections in which vacuum bumps took place are shown in table. 6.1. The bumps took place in the D02 section upstream of the IP in different subsections. The average pressure in the D02 section during the vacuum bumps in the subsections (L26,L25) and (L24,L23) is shown on l.h.s of fig. 6.14, and the profile of the losses in the sCVD (LER2) resulting from vacuum bumps is shown on r.h.s of fig. 6.14. We can see that the vacuum bumps are clearly correlated with losses in the sCVD and this confirms that our sensors in the drift at 11.9 meters downstream from the IP are sensitive to Beam-gas Bremsstrahlung scattering up to 35 meters upstream of the IP (see fig. 8a in chapter 5). Another vacuum bump was performed between 35 and 70 meters upstream of the IP in the LER (l.h.s of fig. 6.15). During this vacuum bump we did not notice any increase in losses in the sCVD. As can be seen on r.h.s of fig. 6.15, sCVD losses are just similar to the beam current profile in the LER (fig. 6.16). This confirms the simulation result in fig. 8b in chapter 5, which shows that our sCVDs are not sensitive to Beam-gas scattering occurring beyond ≈ 23 meters upstream of the IP.

Gauges	Distance upstream of the IP (meters)
L26	4
L25	12
L24	17
L23	33

Table 6.1 – Distances upstream of the IP of subsections where vacuum bumps took place in the D02 section

I used data from the first two bumps to calculate the fraction of losses in the sCVD from the scattering regions where the vacuum bumps were performed and compare them

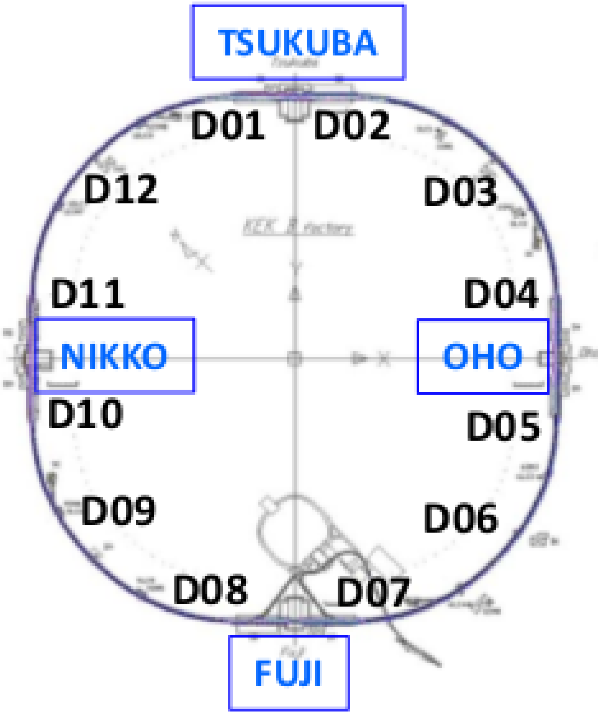

Figure 6.13 – The vacuum sections overall the LER at SuperKEKB

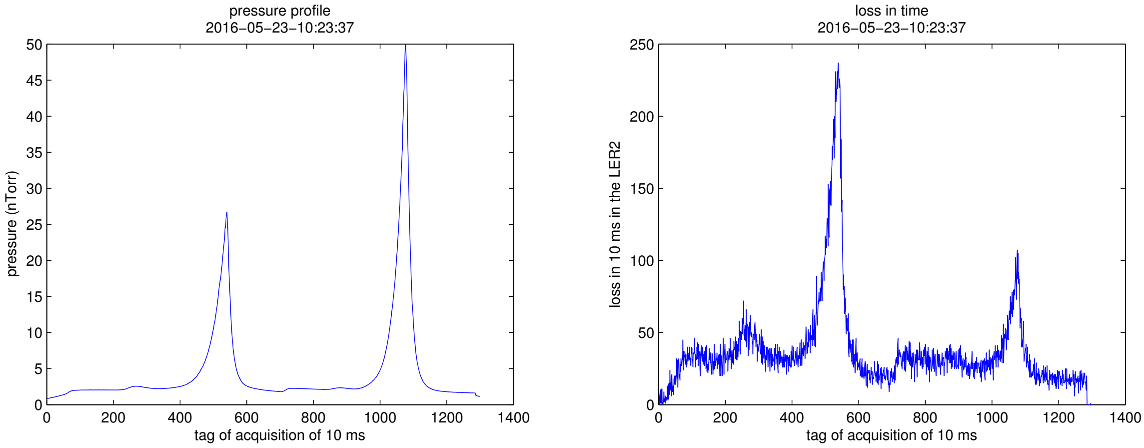

Figure 6.14 – The profile of the average pressure at D02 section on l.h.s and the profile of the losses in the sCVD (LER2) on r.h.s during the successive vacuum bumps in the subsections (L26,L25) and (L24,L23) of the D02 section

to the simulations. The fraction calculated is defined as f and is represented in equation 6.1, where loss$_{bump}$ represents the value of the loss in the sCVD at the maximum of the vacuum bump (r.h.s of fig. 6.14) and loss$_{all-sections}$ represents the total loss simulated in the sCVD when pressure is equal to that of the maximum of the bump everywhere in the ring. For each vacuum bump study, the bump was performed at two consecutive subsections. So to be able to calculate precisely the fraction given in equation 6.1, I needed to consider the average value of the vacuum bumps at the consecutive subsections (fig. 6.17, 6.18). The results are represented in table 6.2 and the fractions given by the data and that given by the simulation match for the two vacuum bumps at the two different positions.

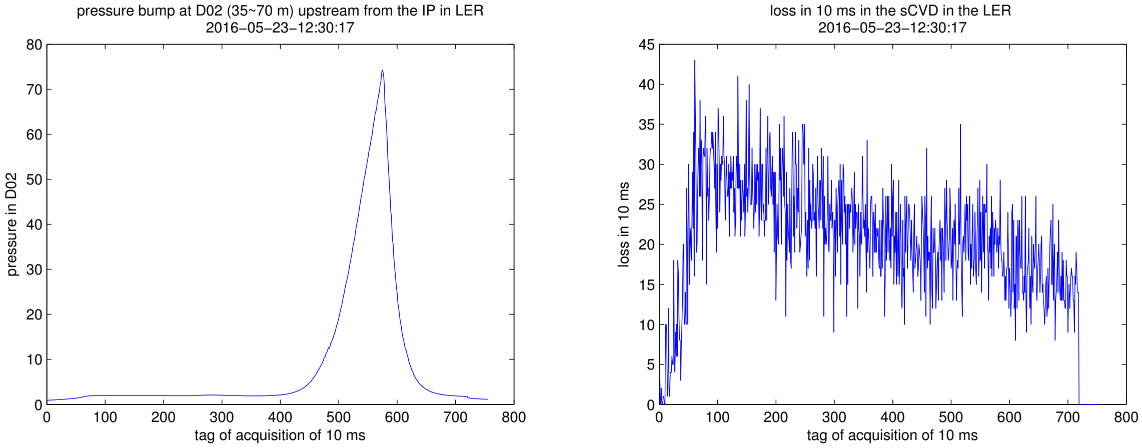

Figure 6.15 – The profile of the average pressure at D02 on l.h.s and the profile of the losses in 10 ms in the sCVD on r.h.s during the vacuum bump between 35 m and 70 m upstream from the IP in the LER

$$f = \frac{loss_{bump}}{loss_{all-sections}} \tag{6.1}$$

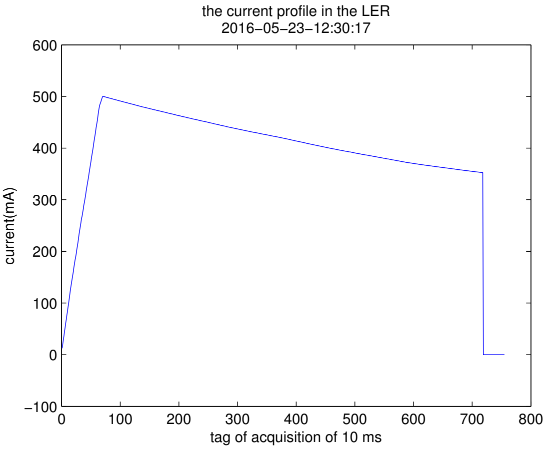

Figure 6.16 – The beam current profile in the LER during the vacuum bump between 35 and 70 meters upstream from the IP

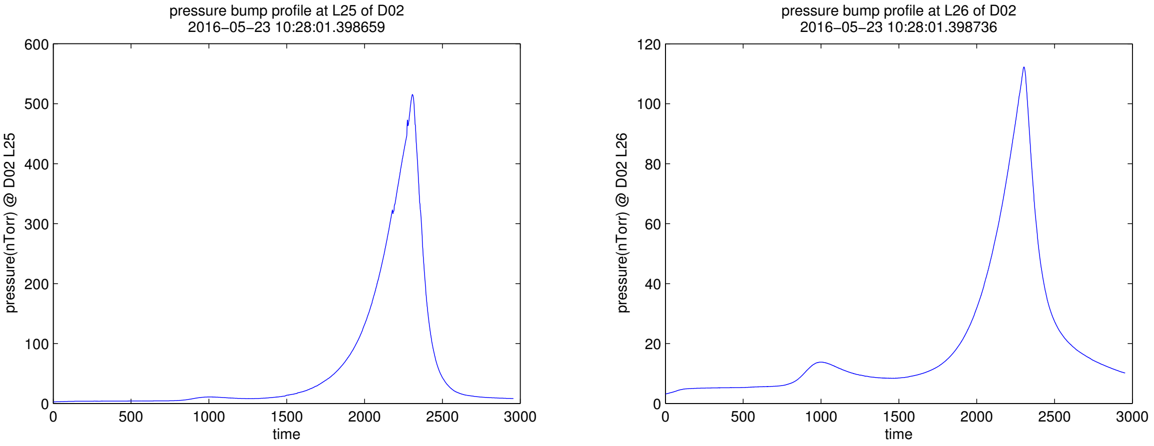

Figure 6.17 – Vacuum pressure in the subsection L25 on l.h.s and in L26 on r.h.s, between 4 and 12 meters upstream from the IP

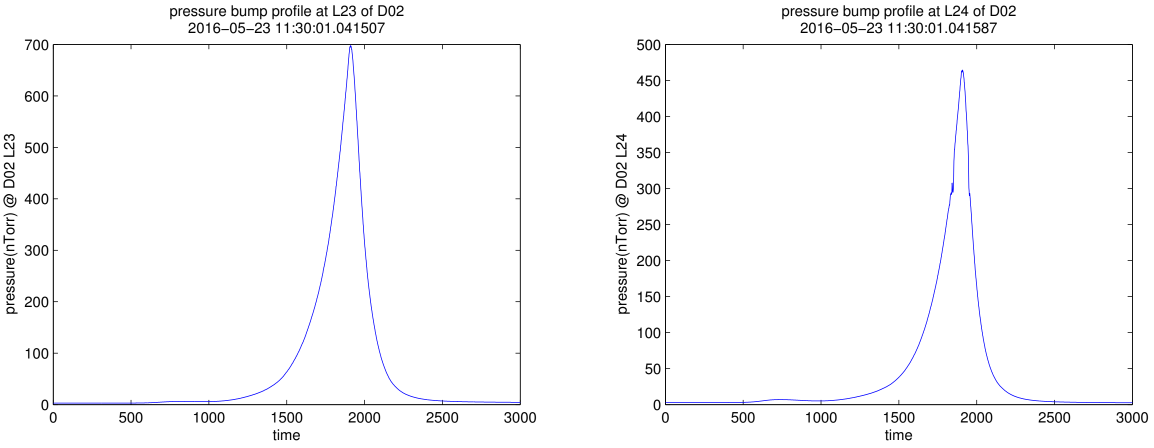

Figure 6.18 – Vacuum pressure in the subsection L23 on l.h.s and in L24 on r.h.s, between 17 and 35 meters upstream from the IP

Position of vacuum bump upstream of the IP	Average vacuum pressure (nTorr)	f_{data}	$f_{simulation}$
4 to 12 meters	300	0.17±0.01	0.20±0.02
17 to 35 meters	275	0.07±0.01	0.09±0.01

Table 6.2 – Comparison between data and simulation of the fraction of losses in the sCVD coming from the different sections during the vacuum bump

6.2.3 Losses for different vertical beam sizes

Another BEAST II study performed during the phase 1 commissioning of SuperKEKB was called Touschek study. Several days were dedicated to this study, both for the LER and HER. We were taking data in both rings but only data from the LER are analysed.

The aim of this study is to extract the contribution of the Touschek losses to the total losses by changing the vertical beam size σ_y. The beam size was increased by varying the value of the ECK (Emittance Control Knob), which consists in changing the field of the skew quadrupole component of the chromaticity correcting sextupoles, inducing a coupling of the horizontal emittance into the vertical plane in the ring, thus increasing the vertical beam size.

During the study, beam loss data were collected for six different beam currents in the LER, I = 180, 360, 540, 720, 900 and 1000 mA (l.h.s of fig. 6.19). For each current, σ_y is varied five times (r.h.s of fig. 6.19), with data taking lasting for $\approx$ 2 minutes at each value of σ_y.

The data from the sCVD (LER2) were analysed during this study. Losses observed in the sCVD result from both Beam-gas Bremsstrahlung and Touschek processes. For fixed values of the current (which also maintains more or less constant vacuum pressure) and varying the vertical beam size, the contribution of the Beam-gas Bremsstrahlung can be expected to remain constant while that of Touschek scattering should vary. Fitting the losses in the sCVD as a function of the inverse of the vertical beam size (σ_y^{-1}) allows separating both contributions in the following way. For σ_y^{-1} close to zero, which means σ_y is very large, the losses from Touschek scattering should vanish and thus all the losses in the sCVD should be from Beam-gas Bremsstrahlung. The contributions from Bremsstrahlung at each beam current are thus extracted from the y-intercept of the fits represented in fig. 6.20, fig. 6.21 and fig. 6.22.

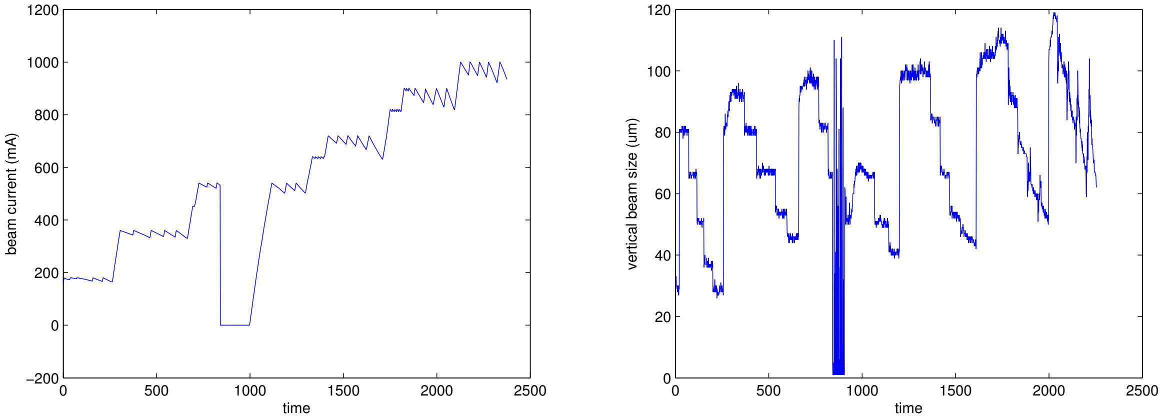

Figure 6.19 – Beam current on l.h.s and vertical beam size in the LER on r.h.s during the Touschek study

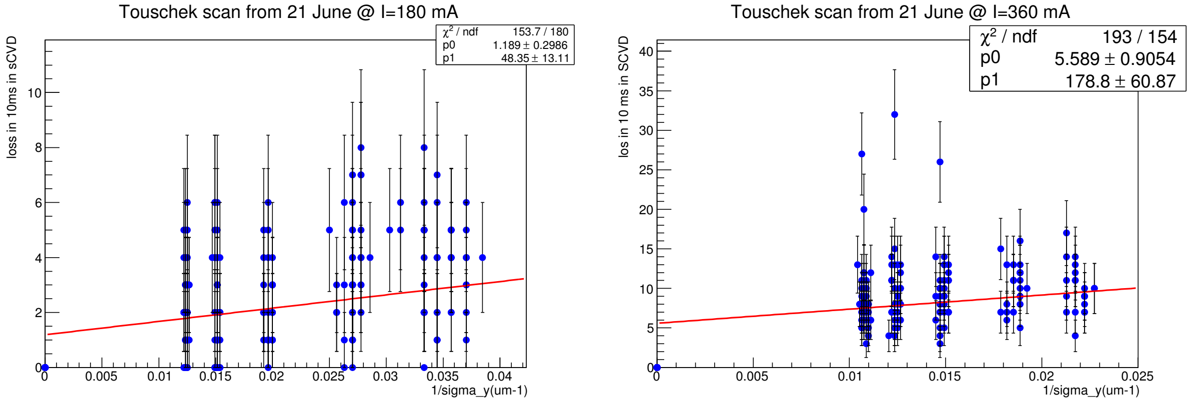

Figure 6.20 – Fit of the losses in the sCVD as a function of the inverse of the vertical beam size at 180 mA on l.h.s and at 360 mA on r.h.s

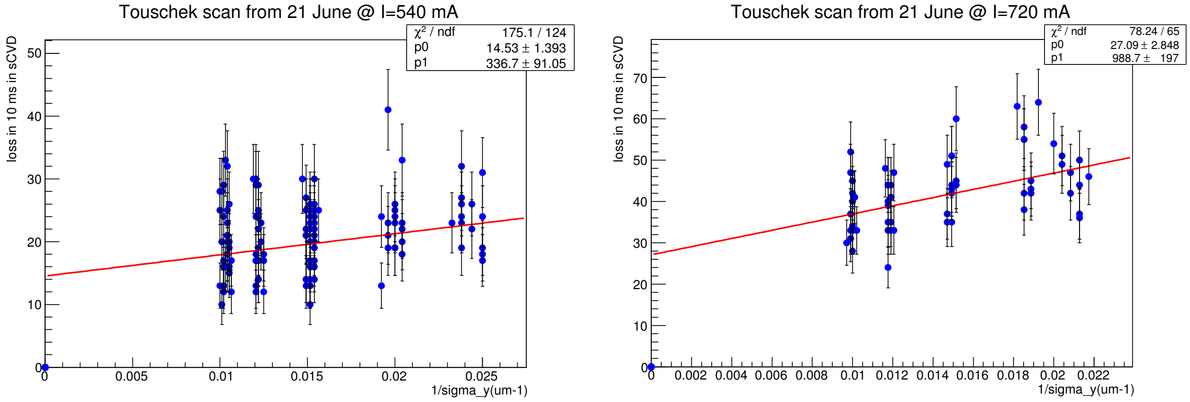

Figure 6.21 – Fit of the losses in the sCVD as a function of the inverse of the vertical beam size at 540 mA on l.h.s and at 720 mA on r.h.s

6.2.3.1 Losses from beam-gas Bremsstrahlung

The losses from Bremsstrahlung extracted from the fits (table. 6.3) are compared to the simulation as a function of the product of the beam current and the vacuum pressure in the LER and are represented on l.h.s of fig. 6.23. The fit of the losses from Bremsstrahlung is linear in both data and simulation (l.h.s of fig. 6.23), but we can see that there is a factor between the two fits, where the data is always greater than the simulation by about 3 (r.h.s of fig. 6.23). This factor is explained by the fact that the measured value of the pressure from the CCG (Cold Cathode Gauge) should be multiplied by a factor 3 to properly represent the actual CO equivalent pressure in the center of the vacuum chamber [66].

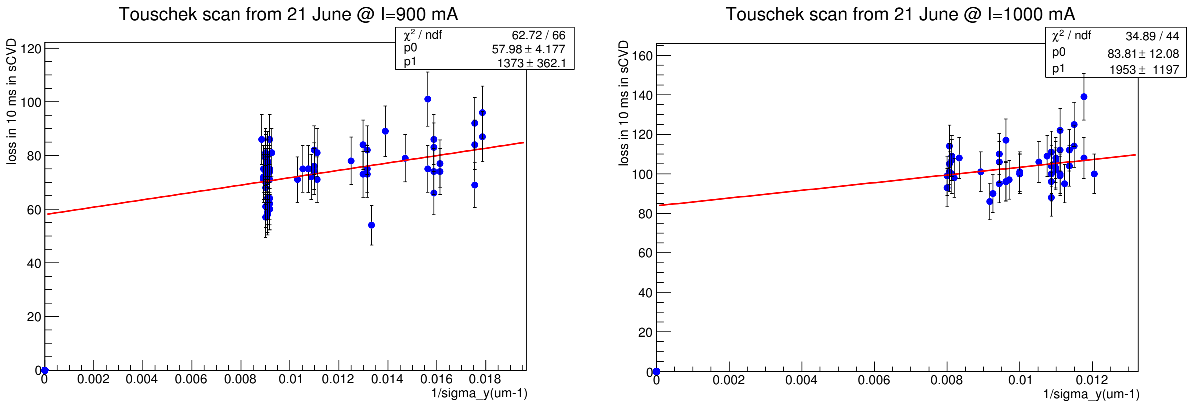

Figure 6.22 – Fit of the losses in the sCVD as a function of the inverse of the vertical beam size at 900 mA on l.h.s and at 1000 mA on r.h.s

Current (mA)	Pressure (nTorr)	Beam-gas Bremsstrahlung in DS in 10 ms
180	0.56	1.2 ± 0.3
360	0.75	5.6 ± 0.9
540	1	14.5 ± 1.4
720	1.45	27.1 ± 2.8
900	2.2	58.0 ± 4.2
1000	3	83.8 ± 12.0

Table 6.3 – Beam-gas Bremsstrahlung in 10 ms in the DS for different beam currents and vacuum pressure in the LER

6.2.3.2 Losses from Touschek scattering

The information on the Touschek contribution to the total beam losses in the sCVD is contained in the slopes of the fits in figs 6.20, 6.21 and 6.22. To confirm the direct proportionality of Touschek with the inverse of the vertical beam size, the relative losses from data as a function of the relative inverse vertical beam size are shown for the six values of the beam current, resulting in slopes ≈ 1 (see table. 6.4) (fig. 6.24, fig. 6.25, fig. 6.26). For a global comparison of the data to the simulation, the weighted arithmetic mean (see eq. 6.2) of the slopes for each current was computed, where x_i stands for the value of the slope and the σ_i is the fit error of the slope, as well as the corresponding error (see eq. 6.3). The result for the data is $\text{slope}_{data} = 0.97 \pm 0.05$, which is compatible within its statistical errors with the simulation (fig. 6.27): $\text{slope}_{simulation} = 1.095 \pm 0.06$.

$$\bar{x} = \frac{\sum_{i=1}^{n}(\frac{x_i}{\sigma_i^2})}{\sum_{i=1}^{n}\frac{1}{\sigma_i^2}} \tag{6.2}$$

$$\sigma_{\bar{x}}^2 = \frac{1}{\sum_{i=1}^{n} \frac{1}{\sigma_i}} \tag{6.3}$$

To compare the contribution of the losses from Touschek scattering in the sCVD between data and simulations, the slopes of the fits in figs. 6.20-fig. 6.22 were extrapolated quadratically to the same current (1000 mA). The weighted arithmetic mean of the extrapolated slopes was then computed along with the errors, according to eq. 6.2 and eq. 6.3, respectively.
The result of this calculation is Touschek$_{data}$= (1530±172)× $\frac{1}{\sigma_y}$.

Current (mA)	Slope ± error
180	0.95 ± 0.10
360	1.1 ± 0.6
540	1.02 ± 0.08
720	1.42 ± 0.55
900	0.97 ± 0.15
1000	0.97 ± 0.10

Table 6.4 – The slopes of the fit of the relative losses in the DS as a function of relative inverse vertical beam size, along with their errors for six different beam currents in the LER

A simulation was performed at a beam current of 1000 mA, for different beam sizes. To vary the beam size, the value of the x-y coupling was changed which will vary the value of the vertical emittance and thus the vertical beam size. The result of the losses from Touschek scattering as a function of the inverse vertical beam size at 1000 mA is shown in fig.6.28. The result of the fit gives Touschek$_{simu}$=(2623±508.6)× $\frac{1}{\sigma_y}$.

We observe a factor of $\frac{simu}{data}$=1.7±0.37. Trying to investigate the origins of this factor, the longitudinal beam size used in the simulation (σ_z=6 mm) was checked to be the same as that measured in SuperKEKB. Another possible source of discrepancy could be the vertical beam size itself, but it is believed that there is no significant error in the measurement of the vertical beam size, because it is consistent with the estimated value using the modelling, based on the level of residual mismatch observed in the measurements of optical functions in the LER.

The Touschek losses are proportional to the product of the inverse transverse beam sizes ($\frac{1}{\sigma_x} \times \frac{1}{\sigma_y}$), where σ_x=$\sqrt{\varepsilon_x \times \beta_x}$ and σ_y=$\sqrt{\varepsilon_y \times \beta_y}$, ε_x and ε_y are the transverse emittances and β_x and β_y are the transverse β functions. In the simulation, the transverse emittance ratio k=$\frac{\varepsilon_y}{\varepsilon_x}$ was varied, thus the simulation results are proportional to $\frac{1}{\varepsilon_x}$. Another possible explanation for the factor of 1.7 between data and simulation could therefore be that the horizontal emittance in the simulation is 1.7 times smaller than in reality in the LER ring. Reliable measurements of the horizontal beam size at SuperKEKB are unfortunately not available to check this hypothesis. We can also not completely exclude that some part of this discrepancy comes from in the simulation itself.

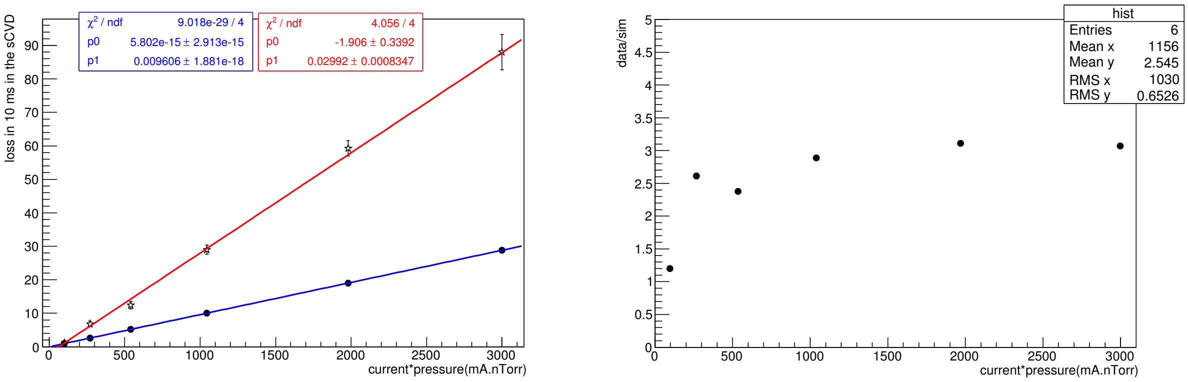

Figure 6.23 – Losses from beam-gas Bremsstrahlung in the sCVD in the LER as a function of the product of the beam current and the vacuum pressure, from data (red) and simulation (blue) on l.h.s and the fraction of the losses from beam-gas Bremsstrahlung in data and simulation

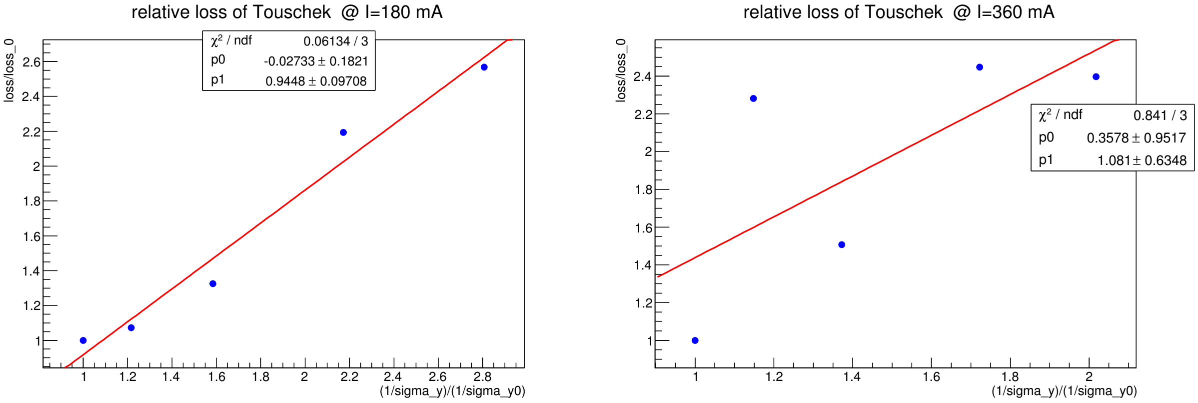

Figure 6.24 – The relative loss in the sCVD as a function of the relative vertical beam size for the beam currents of 180 mA on l.h.s and 360 mA on r.h.s

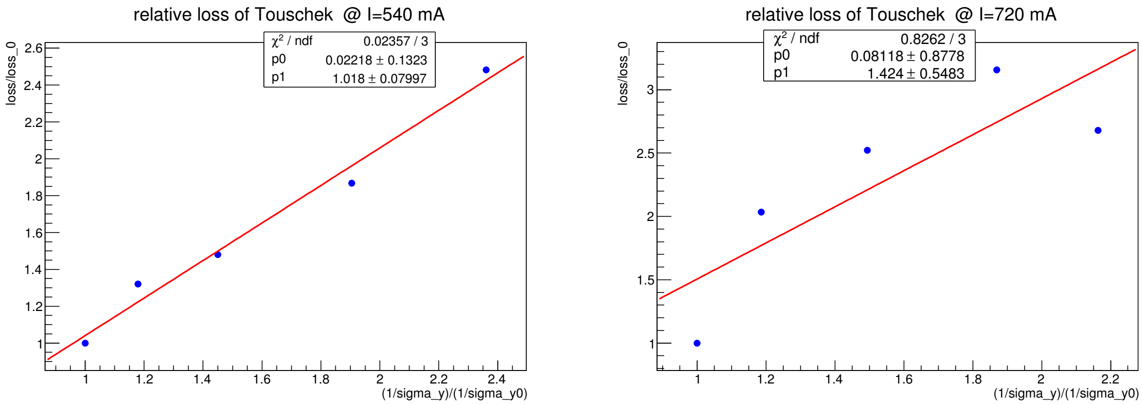

Figure 6.25 – The relative loss in the sCVD as a function of the relative vertical beam size for the beam currents of 540 mA on l.h.s and 720 mA on r.h.s

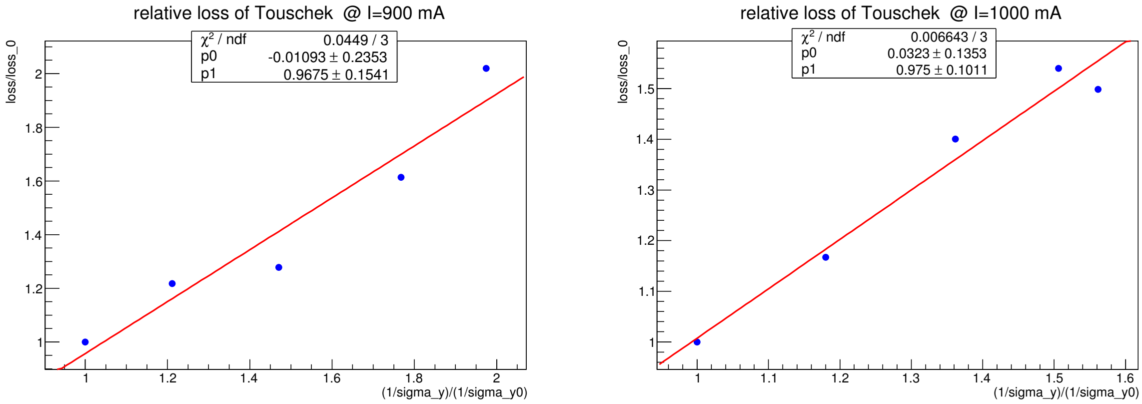

Figure 6.26 – The relative loss in the sCVD as function of the relative vertical beam size for the beam currents of 900 mA on l.h.s and 1000 mA on r.h.s

6.3 Estimations of the ratio of radiative Bhabha signal and single beam losses in phase 2

The good qualitative and quantitative agreement between our simulations and the measurements enabled us to estimate the level of background in the DS in phase 2. The same simulations performed for phase 1 have been carried for phase 2, considering the LER lattice with the final focus system. During phase 2, the collimators will be used to mitigate backgrounds before they reach the Belle II detector.

Since we are interested in the ratio of the radiative Bhabha signal to the background signal in the DS in phase 2, the normal beam pipe of phase 1 was considered instead of the window at 45°, which will be installed in the drift at 11.9 meters in the LER for phase 2.

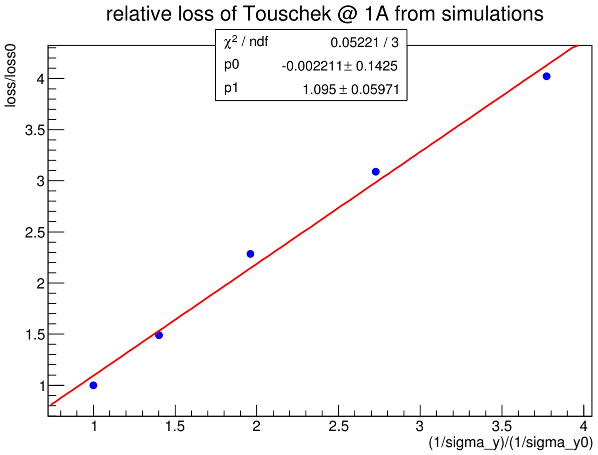

Figure 6.27 – The relative loss from Touschek as a function of the relative inverse vertical beam size from simulations at I= 1000 mA

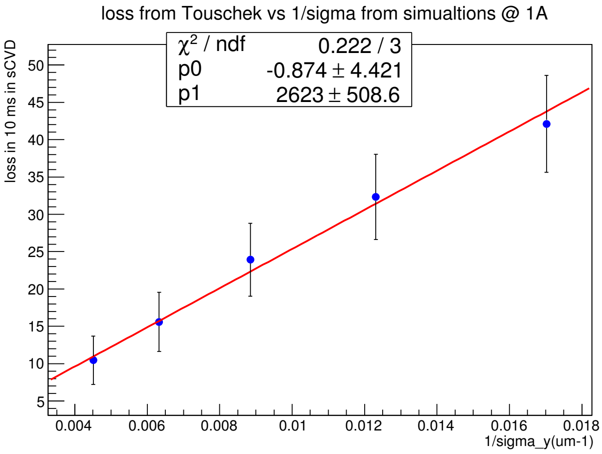

Figure 6.28 – The simulated losses from Touschek scattering as a function of the inverse vertical beam size at I= 1000 mA

6.3.1 Beam-gas Bremsstrahlung

For the simulation of Beam-gas Bremsstrahlung using the SAD code, a vacuum pressure of 1 nTorr and a total beam current of 1 A were considered, which correspond more or less to SuperKEKB parameters foreseen in the LER during phase 2. A Bremsstrahlung loss rate of 660 particles per second in the DS was estimated. This loss rate corresponds to ≈ 68% of the loss rate in the DS in phase 1 under the same vacuum pressure and beam current. This is due to the different optics in the IR with the final focus insertion.

6.3.2 Touschek scattering

With the phase 2 lattice and a beam current of 1 A in the LER, the Touschek loss rate in the DS was estimated to be 118 particles per second, this loss rate corresponds to ≈ 4.9% of the Touschek loss rate in the DS in phase 1 for the same beam current.

6.3.3 Signal to Noise in the LER in phase 2

The loss rate of the radiative Bhabha in the DS in phase 2 for $\mathcal{L}=10^{34}$ $\mathrm{cm}^{-2}\mathrm{s}^{-1}$ with the normal beam pipe is estimated to be 225000 particles per second. The total loss rate of Touschek scattering and beam-gas Bremsstrahlung is 778 particles per second. This means that the background level resulting from single beam losses is expected to be around two orders of magnitude smaller than the rate of the radiative Bhabha scattering signal during luminosity monitoring. This satisfies the conditions specified to achieve a high relative precision on the luminosity measurement.

CHAPTER 7

Conclusions and perspectives

Fast luminosity monitoring is essential in the presence of dynamical imperfections, for feedback and optimization. The aim of this thesis was to design and to implement an instrument for the fast luminosity measurement at SuperKEKB to correct many instabilities of the beam and thereby to optimize it. The target relative precision is 10^{-3} in 1 ms. The process studied is the radiative Bhabha scattering at zero photon scattering angle, which has a large cross-section. The technology used is based on diamond, which is radiation hard and provide a fast signal, located just outside the vacuum chamber downstream from the IP where the counting rate is sufficient to obtain the required precision and where the contamination from background processes is minimal.

Generation of the Bhabha particles has been performed using GUINEA-PIG++ and then tracked at several locations in the LER and HER of SuperKEKB using SAD. Thanks to the tracking results, the optimal position of the diamond sensors in the LER at which high Bhabha event rates could be detected, was chosen to be in the drift at 11.9 meters downstream from the IP to measure the signals from the interaction of the Bhabha positrons with the material of the beam pipe. On the other hand, for the HER, good candidate positions to measure the Bhabha electrons were not found. Therefore, studies in the HER indicate that it is better to measure signals from the Bhabha photons, and for this purpose the position of the diamond sensors was chosen to be at 30 meters downstream from the IP.

GEANT4 simulations have been performed considering different designs of the vacuum chamber in the LER at 11.9 meters, and results show that the normal 6 mm thick cylindrical beam pipe should be replaced by a window at 45°, for better detection of the electromagnetic shower and to achieve the aimed precision of 10^{-3} in 1 ms.

Characterisation tests of a thinned diamond sensor (4x4 mm^2, 140μm) and of a charge amplifier (with shaping time ≈ 10 ns) took place in the clean room at LAL using radioactive sources. The data from the tests have been analysed with MATLAB and root. Analysis results are consistent with the parameters of each of the tested elements.

A study of the single beam loss processes during phase 1 of the single beam commissioning at SuperKEKB has been performed. Simulations of beam-gas Bremsstrahlung, Touschek and Coulomb scattering were performed using a SAD code written at KEK.

Several modifications have been applied on the code to ensure reliable results. Afterwards, the losses from the three processes have been studied and calculated as a function of several parameters (beam current, vacuum pressure, beam size) in the LER. Simulation results indicate that at 11.9 meters in the LER, the diamond sensor is only sensitive to losses from beam-gas Bremsstrahlung and Touschek scattering. The signal in the diamond sensor from these two processes has been then studied by GEANT4.

The mechanical setup has been installed in December 2015 in both rings. Two diamond sensors connected to charge amplifiers were installed in each ring in the horizontal plane on the low energy side. Tests with radioactive sources were performed in situ to check the entire setup. By the end of February 2016, a complete readout system was installed and data taking lasted to the end of the phase 1 commissioning of SuperKEKB (end of June 2016). Data were acquired during vacuum scrubbing and also during dedicated studies of the single beam losses. Along with that, I participated in operational shifts in the control room of SuperKEKB, where interesting beam dynamics studies took place.

7.1 Data from single beam losses at phase 1

The analysis of the data taken during phase 1 has been performed using MATLAB, the results of the analysis are summarised in the following:

- Vacuum bumps in the LER: During vacuum bumps performed in the vacuum section upstream from the IP, loss bumps in the diamond sensors were observed and analysis results are consistent with the simulation, on the sensitivity of the diamond sensor at 11.9 meters to the scattering positions.

- Touschek study in LER: During this study, six beam currents have been considered and the vertical beam size was varied about five times for each beam current. From the analysis of data taken during this study, the contributions of the beam-gas Bremsstrahlung and the Touschek scattering to the total loss rate could be extracted. The results of beam-gas Bremsstrahlung is consistent with the simulation, whereas concerning Touschek scattering, a factor of 1.7 larger rate was observed in simulation compared to data. Parameters like the vertical emittance and the longitudinal beam size, which could affect the Touschek rate, may explain this factor, have been checked in the simulation and appear to be consistent with the data. Only the horizontal emittance could not be confirmed experimentally.

7.2 Implications for phase 2

7.2.1 Signal to background ratio during luminosity monitoring

The qualitative and quantitative agreement of our simulations and the measurements of single beam losses in phase 1 enabled us to estimate that the background level from the single beam losses will be two orders of magnitude smaller than the rate of radiative Bhabha signal during luminosity monitoring in phase 2. It also confirmed the modelling of the efficiency of the detector, thereby validating the estimated signal rates and luminosity precisions.

7.2.2 Vacuum chamber design and installation

A 6 mm thick Cu window at 45° will replace the normal 6 mm thick Cu cylindrical beam pipe for the data acquisition of the phase 2 of SuperKEKB. The installation of the window will start by the end of 2017. This new design requires some modifications to adapt the mechanical setup used during phase 1.

7.2.3 Precision on luminosity

Thanks to the window at 45° and a radiator, we should be able to achieve a precision of 3.7×10^{-3} for phase 2 at $\mathcal{L}$=10^{34} cm^{-2}s^{-1} and a precision of 1.2×10^{-3} for phase 3 at $\mathcal{L}$=8×10^{35} cm^{-2}s^{-1}.

7.2.4 Readout electronics

For phases 2 and 3, the oscilloscope will be replaced by a 10 bits ADC (Analog-to-Digital Converter) connected to an FPGA programmed to calculate the train integrated luminosity and the bunch integrated luminosity, and followed by a 16 bits DAC to provide these luminosities as analog output for feedback use.

In phase 2, for $\mathcal{L}$=10^{34} cm^{-2}s^{-1}, there won't be a luminosity signal each bunch crossing in the DS, thus the 500 μm DS with the charge amplifier used in phase 1 will be fast enough to do fast luminosity monitoring. However, in phase 3, for a luminosity up to 8×10^{35} cm^{-2}s^{-1}, the DS will have signals from successive bunches, separated only by 4 ns. In this case, different schemes could be adopted for the fast luminosity monitoring. Since we have two channels in each ring, we may use one channel for train luminosity ($\mathcal{L}_{\mathcal{T}}$) monitoring, and the second for bunch luminosity ($\mathcal{L}_{\mathcal{B}}$) monitoring.

For $\mathcal{L}_{\mathcal{T}}$ monitoring, two schemes could be considered, either keeping the same scheme as in phase 2 with the 500 μm DS and the charge amplifier ($\sigma \approx 10$ ns) while considering a different data processing in the presence of pile-up, or using a thinner DS (140 μm) connected to either a faster charge amplifier ($\sigma \approx$ 2-3 ns) or to a voltage amplifier which gives a signal as fast as the DS ($\sigma \approx$ 2-3 ns). The voltage amplifier has a higher noise compared to charge amplifier, however this should not be a problem for phase 3 since several MIPs will be intercepted in the DS at once, resulting in larger signals.

For $\mathcal{L}_{\mathcal{B}}$ monitoring, it is not necessary to have a precision as high as for $\mathcal{L}_{\tau}$ monitoring. In this case, considering the same scheme as phase 2 could be good enough by moving one channel away from the window, to decrease its signal level, which is acceptable given the reduced precision requirement.

Concerning the data collected in phase 1 in HER, it will be analysed to calculate the rates of the single beam losses in the DS for different beam parameters. For phase 2, a GEANT4 simulation should be performed considering the geometry of the antechamber where we place the DS in the HER (30 meters downstream of the IP) to study the signals of the radiative Bhabha photons in the DS and define the reachable precision. On the other hand, a detailed simulation of the single beam losses during phase 2 should be performed considering the geometry of the window at 45° in the LER.

From the experience during phase 1, data acquisition codes for phase 2 using the FPGA should be written and tested in advance before the start of the phase 2 commissioning, not to lose time when the beams are circulating and the collisions are performed. Once the shape of the output signals is confirmed, processing and analysis codes should be prepared to enable an online analysis of the data to be sent to the lock-in amplifier each 1 ms to enable a feedback based on the dithering algorithm.

CHAPTER 8

Appendix A

8.1 Copper

Copper has the smallest radiation length (X_0=1.47 cm) and the largest atomic number (Z=29) among all the other considered materials. Consequently, we believe that Cu will give the worst precision among the materials due to the fact that a great part of the electromagnetic shower will be absorbed in the thickness of the beam pipe.

8.1.1 6 mm

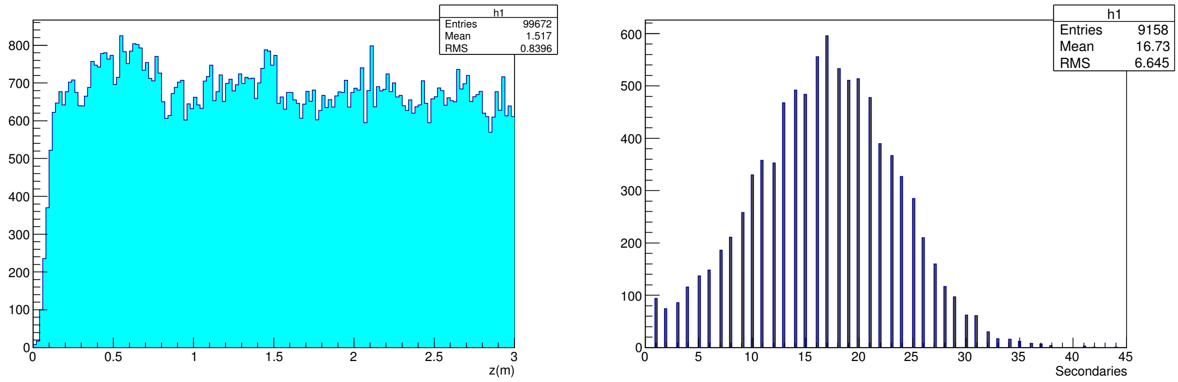

(a) The position in z of the exiting charged secondaries

(b) The number of charged secondaries per incident Bhabha positron exiting the beam pipe

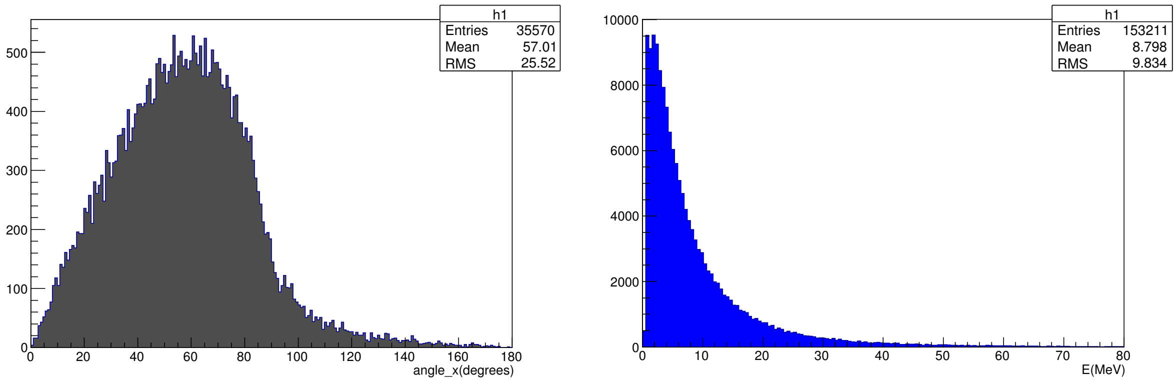

(c) The transverse angular profile of the exiting secondaries

(d) The energy spectrum of the exiting secondaries

Figure 8.1 – Dynamics of the secondaries exiting 6 mm thick Copper beam pipe

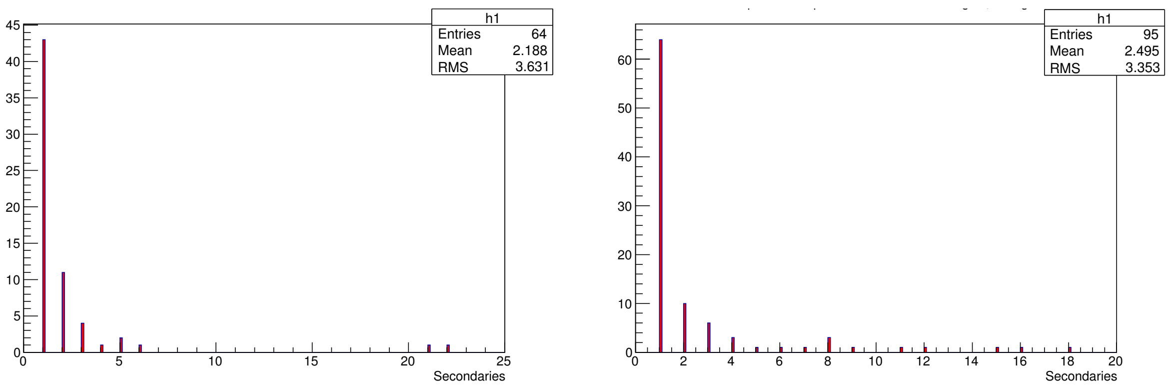

(a) DS parallel (0°) to the beam pipe

(b) DS at 45° to the beam pipe

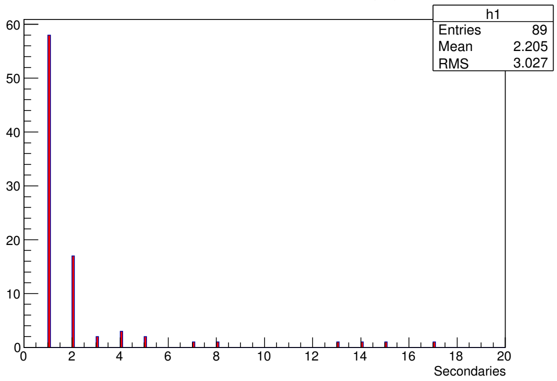

(c) DS perpendicular (90°) to the beam pipe

Figure 8.2 – Histograms of the number of charged secondaries in the DS per incident exiting Bhabha positron for different orientations of the DS at 6 mm thick Copper beam pipe

8.1.2 5 mm

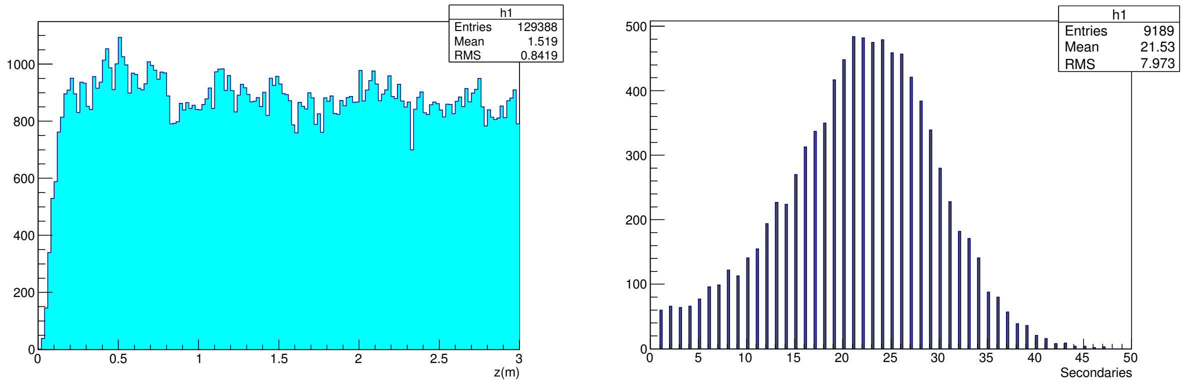

(a) The position in z of the exiting charged secondaries

(b) The number of charged secondaries per incident Bhabha positron exiting the beam pipe

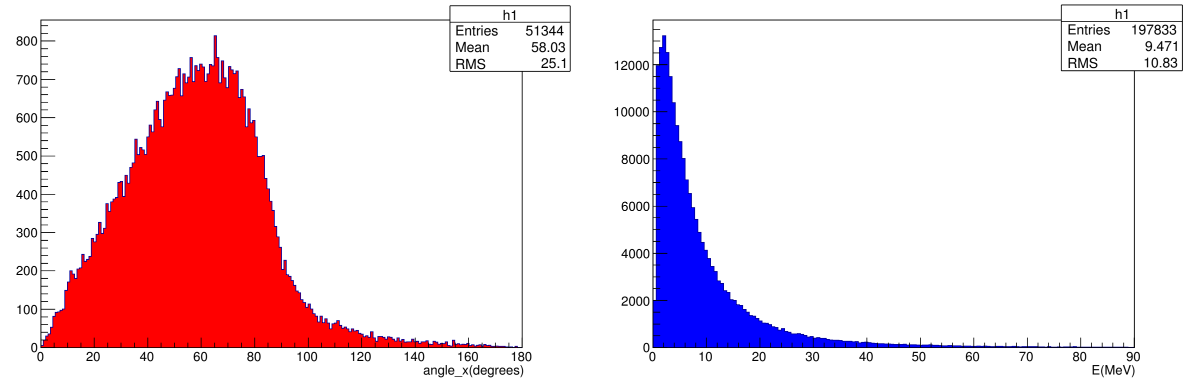

(c) The transverse angular profile of the exiting secondaries

(d) The energy spectrum of the exiting secondaries

Figure 8.3 – Dynamics of the secondaries exiting 5 mm thick Copper beam pipe

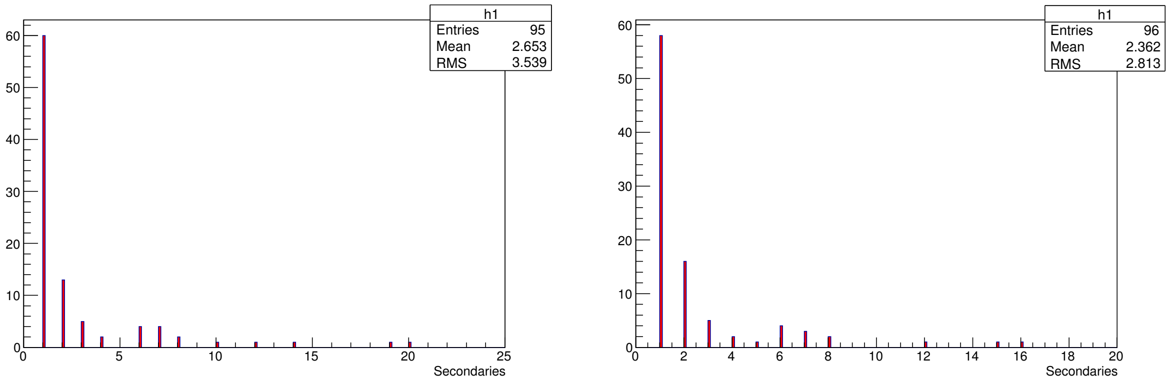

(a) DS parallel (0°) to the beam pipe

(b) DS at 45° to the beam pipe

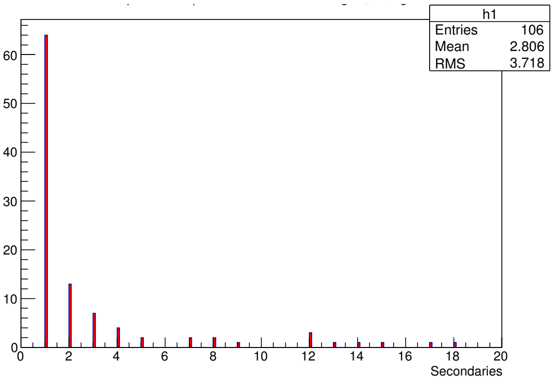

(c) DS perpendicular (90°) to the beam pipe

Figure 8.4 – Histograms of the number of charged secondaries in the DS per incident exiting Bhabha positron for different orientations of the DS at 5 mm thick Copper beam pipe

8.1.3 4 mm

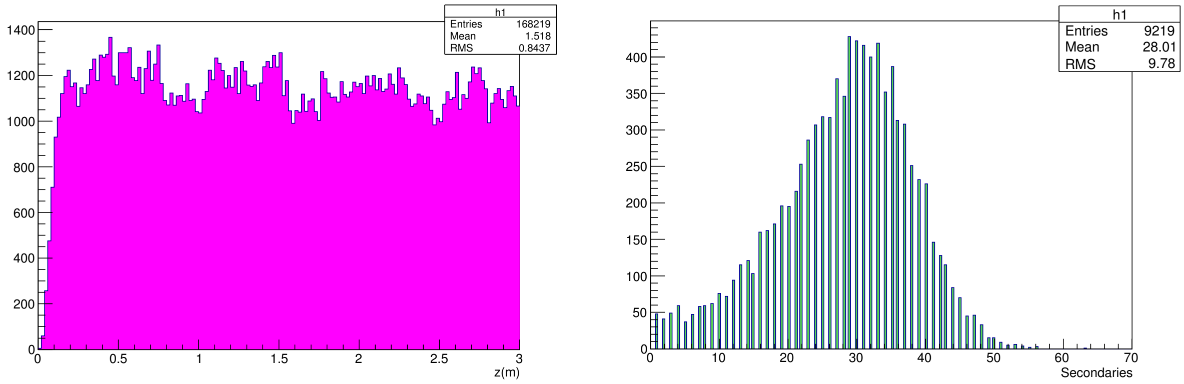

(a) The position in z of the exiting charged secondaries

(b) The number of charged secondaries per incident Bhabha positron exiting the beam pipe

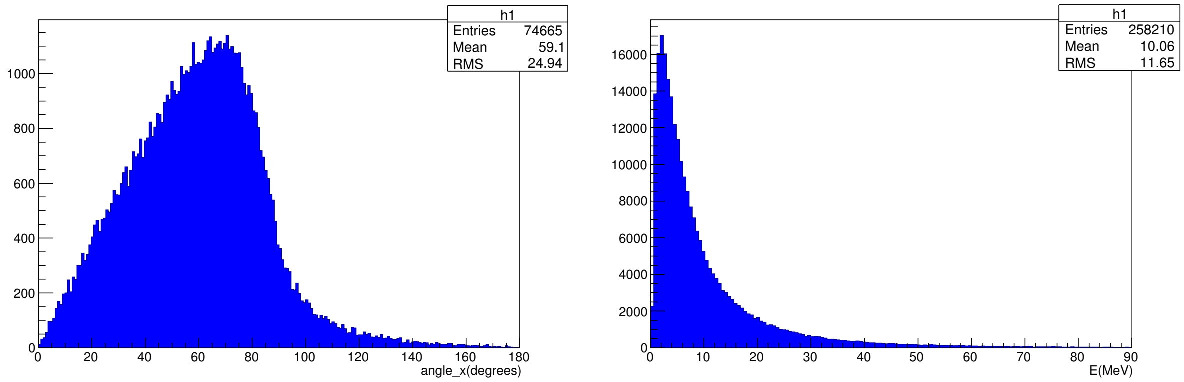

(c) The transverse angular profile of the exiting secondaries

(d) The energy spectrum of the exiting secondaries

Figure 8.5 – Dynamics of the secondaries exiting 4 mm thick Copper beam pipe

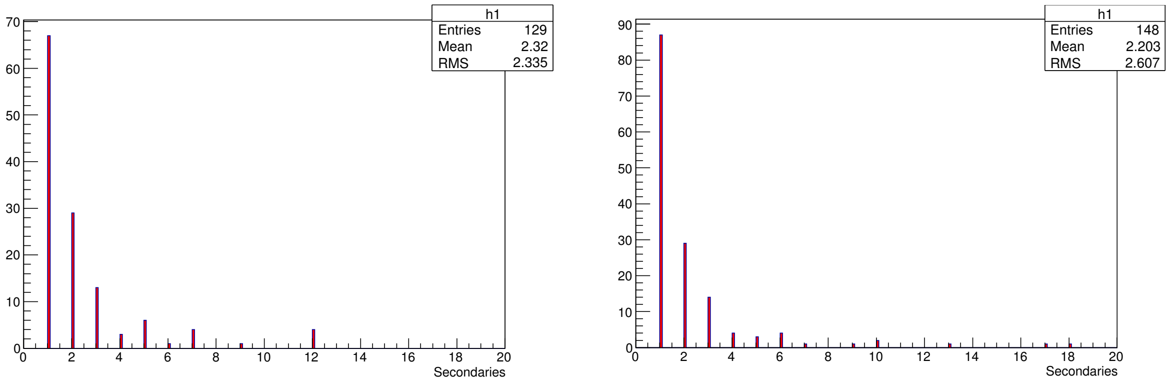

(a) DS parallel (0°) to the beam pipe

(b) DS at 45° to the beam pipe

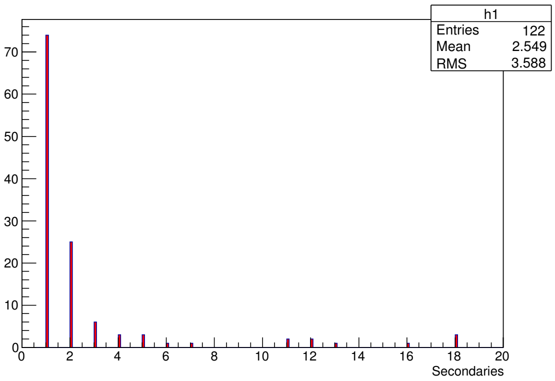

(c) DS perpendicular (90°) to the beam pipe

Figure 8.6 – Histograms of the number of charged secondaries in the DS per incident exiting Bhabha positron for different orientations of the DS at 4 mm thick Copper beam pipe

8.1.4 3 mm

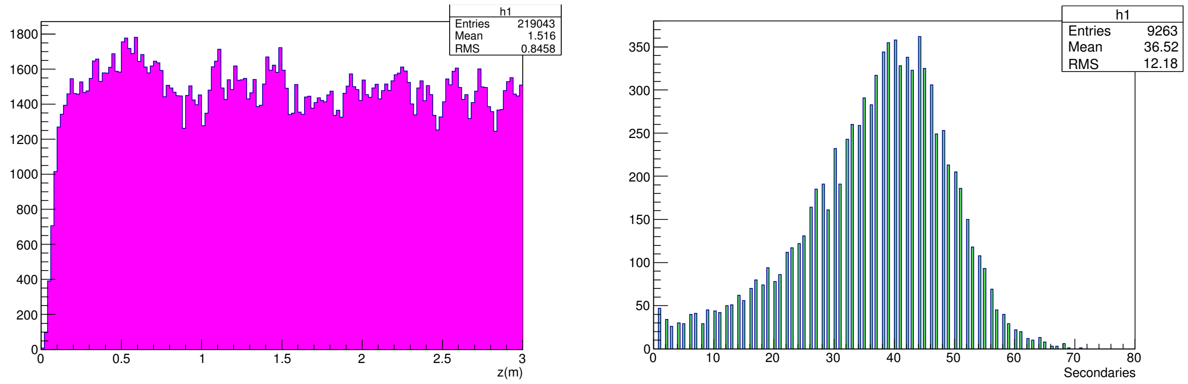

(a) The position in z of the exiting charged secondaries

(b) The number of charged secondaries per incident Bhabha positron exiting the beam pipe

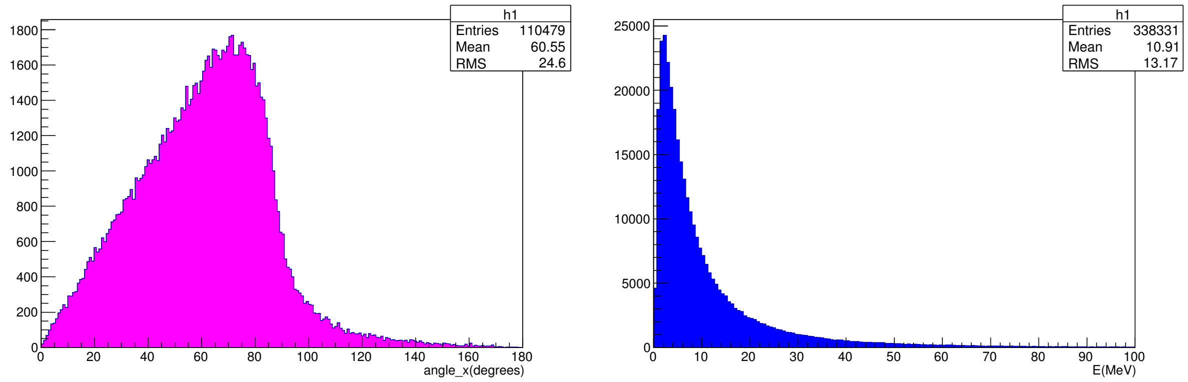

(c) The transverse angular profile of the exiting secondaries

(d) The energy spectrum of the exiting secondaries

Figure 8.7 – Dynamics of the secondaries exiting 3 mm thick Copper beam pipe

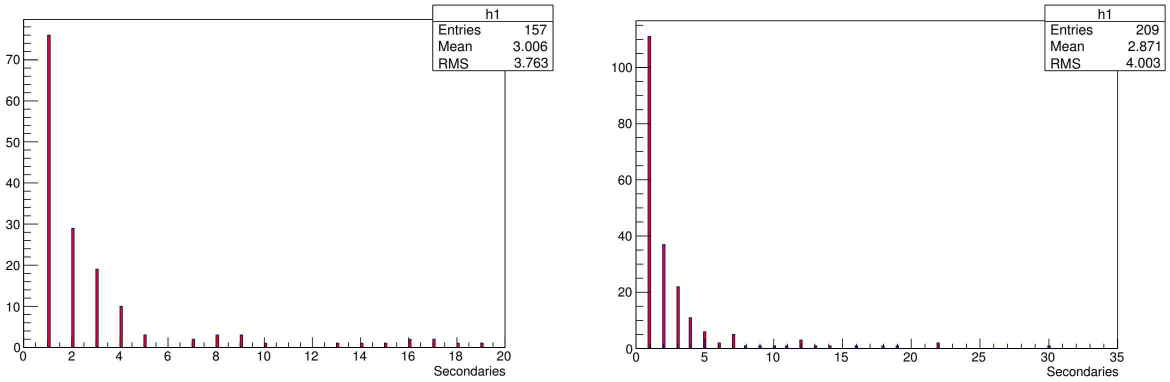

(a) DS parallel (0° to the beam pipe

(b) DS at 45° to the beam pipe

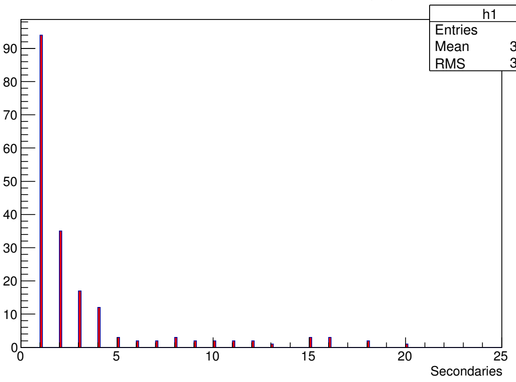

(c) DS perpendicular (90°) to the beam pipe

Figure 8.8 – Histograms of the number of charged secondaries in the DS per incident exiting Bhabha positron for different orientations of the DS at 3 mm thick Copper beam pipe

8.1.5 2 mm

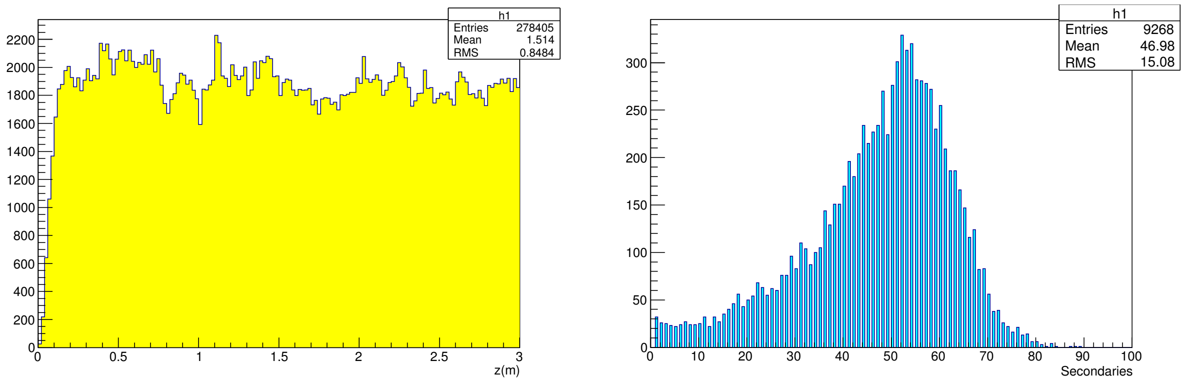

(a) The position in z of the exiting charged secondaries (b) The number of charged secondaries per incident Bhabha positron exiting the beam pipe

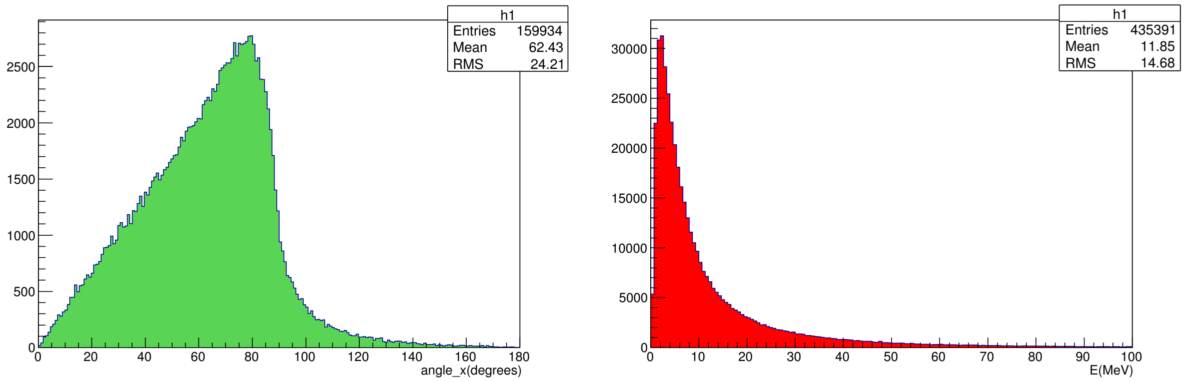

(c) The transverse angular profile of the exiting secondaries (d) The energy spectrum of the exiting secondaries

Figure 8.9 – Dynamics of the secondaries exiting 2 mm thick Copper beam pipe

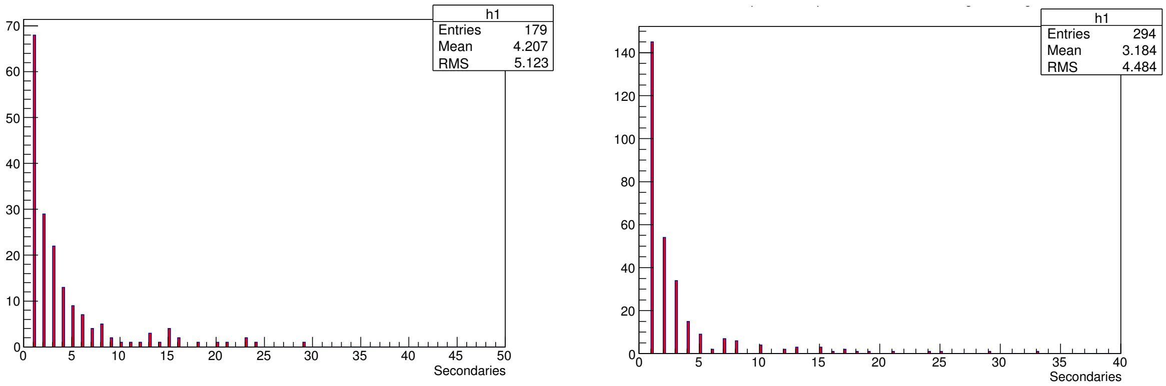

(a) DS parallel (0°) to the beam pipe

(b) DS at 45° to the beam pipe

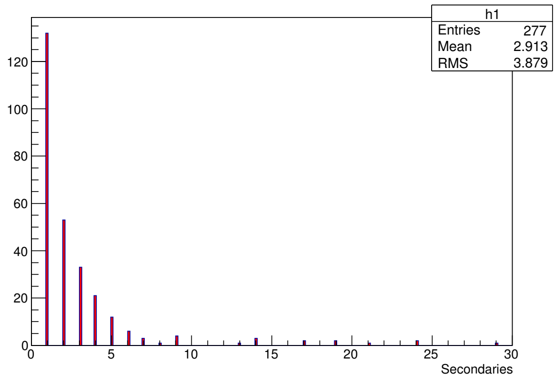

(c) DS perpendicular (90°) to the beam pipe

Figure 8.10 – Histograms of the number of charged secondaries in the DS per incident exiting Bhabha positron for different orientations of the DS at 2 mm thick Copper beam pipe

8.1.6 1 mm

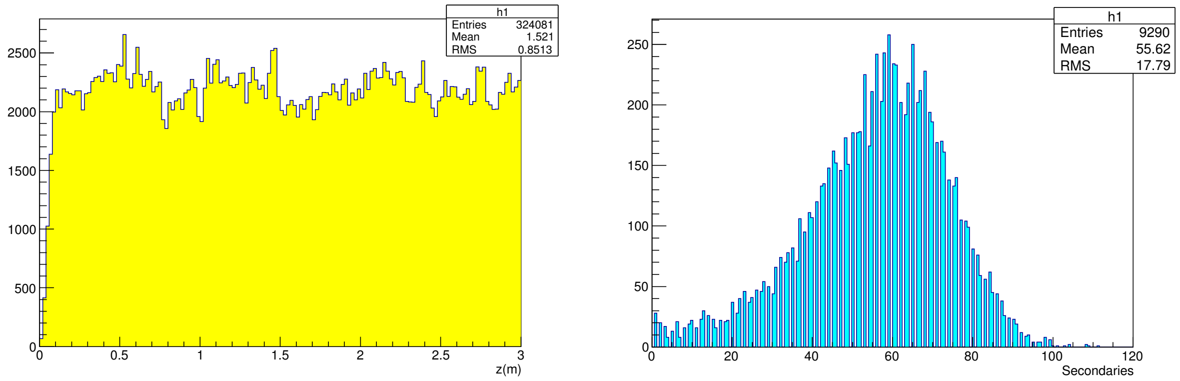

(a) The position in z of the exiting charged secondaries

(b) The number of charged secondaries per incident Bhabha positron exiting the beam pipe

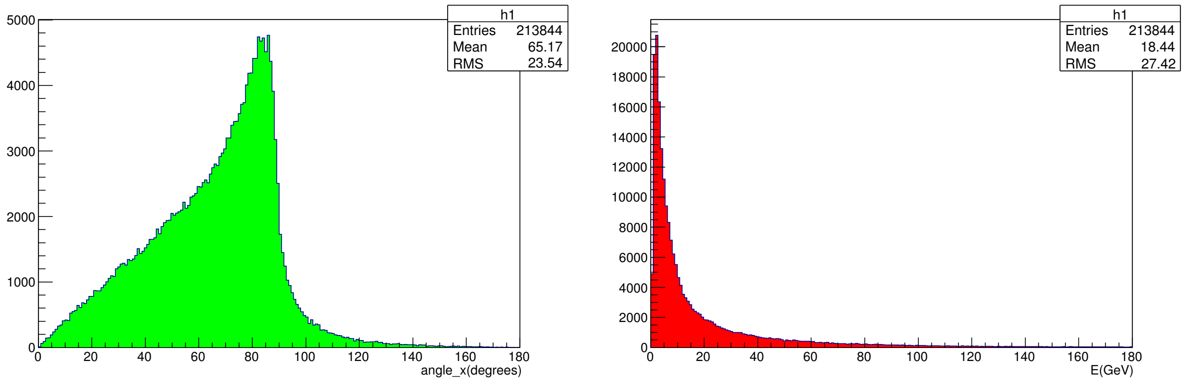

(c) The transverse angular profile of the exiting secondaries

(d) The energy spectrum of the exiting secondaries

Figure 8.11 – Dynamics of the secondaries exiting 1 mm thick Copper beam pipe

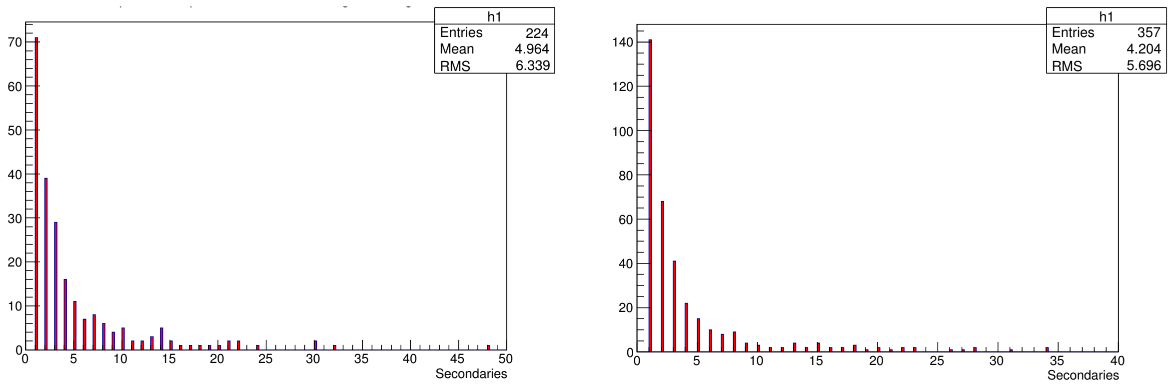

(a) DS parallel (0°) to the beam pipe

(b) DS at 45° to the beam pipe

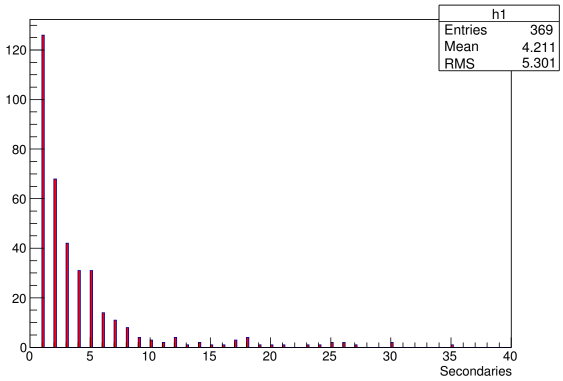

(c) DS perpendicular (90°) to the beam pipe

Figure 8.12 – Histograms of the number of charged secondaries in the DS per incident exiting Bhabha positron for different orientations of the DS at 1 mm thick Copper beam pipe

8.1.7 Precision of $\mathcal{L}$ evaluation

After analysis of the simulation, we can conclude on the precision of the luminosity measurement in 1 ms for phase 2 ($\mathcal{L}$=10^{34}cm^{-2}s^{-1}) and phase 3 ($\mathcal{L}$=10^{35}cm^{-2}s^{-1}). The precision improves only moderately when decreasing the thickness of the beam pipe, with the best values for 1 mm (fig. 8.13). The orientation of the DS also affects the precision slightly, with a preference for the cases of 45° and 90° at 1 mm. For 6 mm, all orientations give the same result. Achievable precision is still very far from the specification, even in the best conditions at phase 2 (l.h.s of fig. 8.13) and phase 3 (r.h.s of fig. 8.13). Even when decreasing the thickness of the beam pipe to 1 mm, we will not be able to improve the precision in the way we can do with the window and radiator. The factor of improvement in the case of the window and the radiator compared to the 1 mm thick beam pipe is 7 for phase 2.

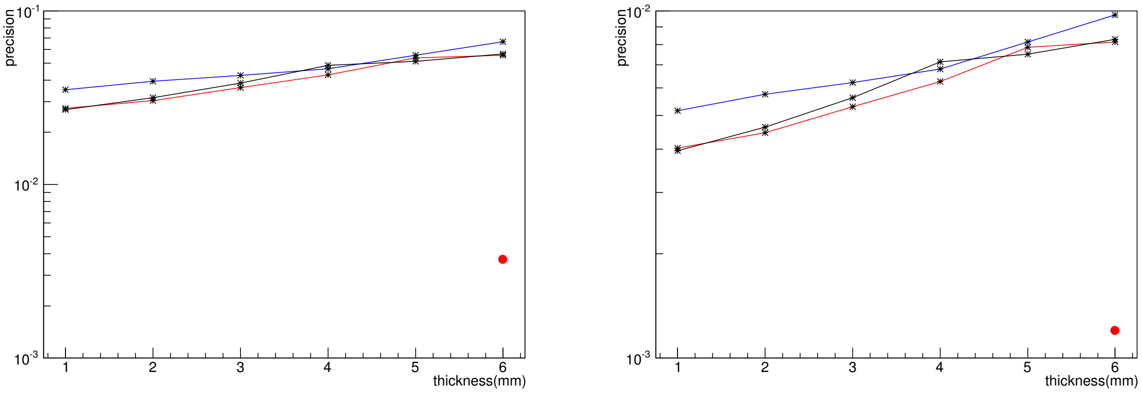

Figure 8.13 – Precision in 1 ms on the luminosity as a function of the thickness of the beam pipe for DS at 0° (blue), DS at 45° (red) and DS at 90° (black) compared to the window + radiator (red spot) in phase 2 on l.h.s and in phase 3 on r.h.s

8.2 Aluminium

The secondaries exit the beam pipe uniformly whatever the thickness of the beam pipe. For a thickness of 6 mm (fig. 8.14a), the number of exiting charged secondaries increases progressively until 50 cm from the exit of the quadrupole QKBLP where it stabilizes, the reason lies behind the absorption of the shower due to the shallow exiting angle of the Bhabha positrons and the large thickness of the beam pipe.

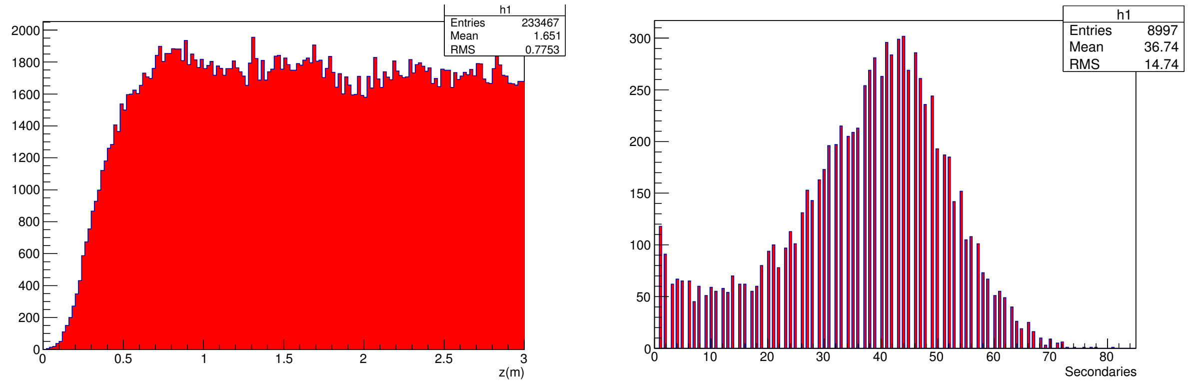

(a) The position in z of the exiting charged secondaries

(b) The number of charged secondaries per incident Bhabha positron exiting the beam pipe

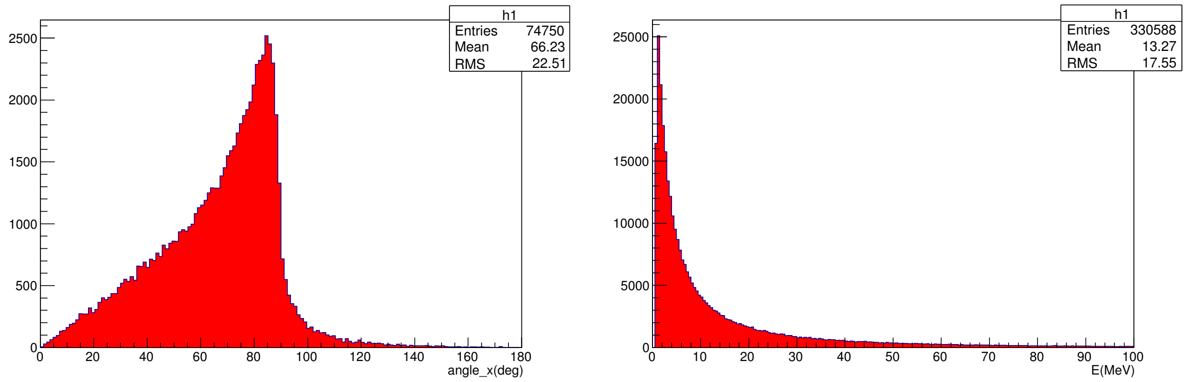

(c) The transverse angular profile of the exiting secondaries

(d) The energy spectrum of the exiting secondaries

Figure 8.14 – Dynamics of the secondaries exiting 6 mm thick Aluminium beam pipe

8.2.1 Precision of $\mathcal{L}$ evaluation

Similar to the case of a Copper beam pipe, the precision improves when decreasing the thickness. The best precision is for the smallest thickness (1 mm), with a DS at 90° (1.6 % in phase 2 (l.h.s of fig. 8.15) and 5×10^{-3} in phase 3 (r.h.s of fig. 8.15)). These precisions are still not satisfactory. The values achieved in the case of the window and radiator, are 4.3 times better for phase 2.

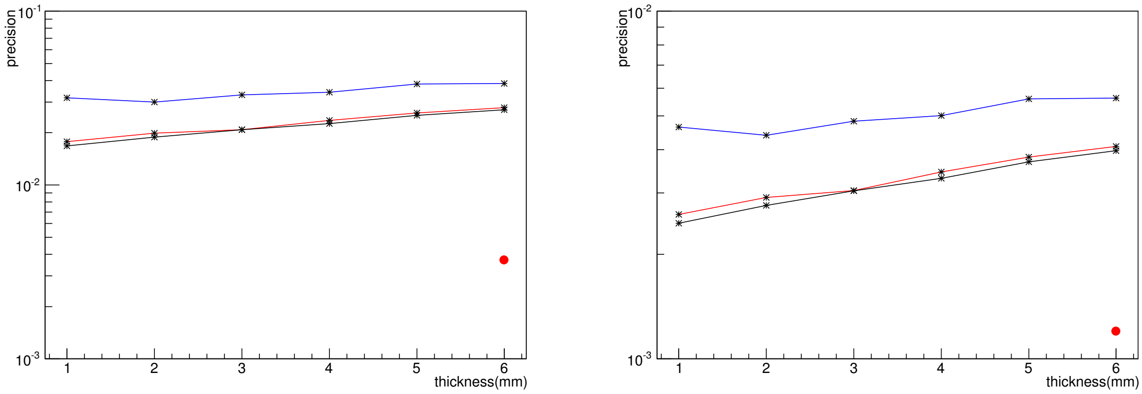

Figure 8.15 – Precision in 1 ms on the luminosity as a function of the thickness of the beam pipe for DS at 0° (blue), DS at 45° (red) and DS at 90° (black) compared to the window + radiator (red spot) in phase 2 on l.h.s and in phase 3 on r.h.s

8.3 Titanium

The dynamics of the secondaries exiting a 6 mm thick Ti beam pipe are represented in fig. 8.16.

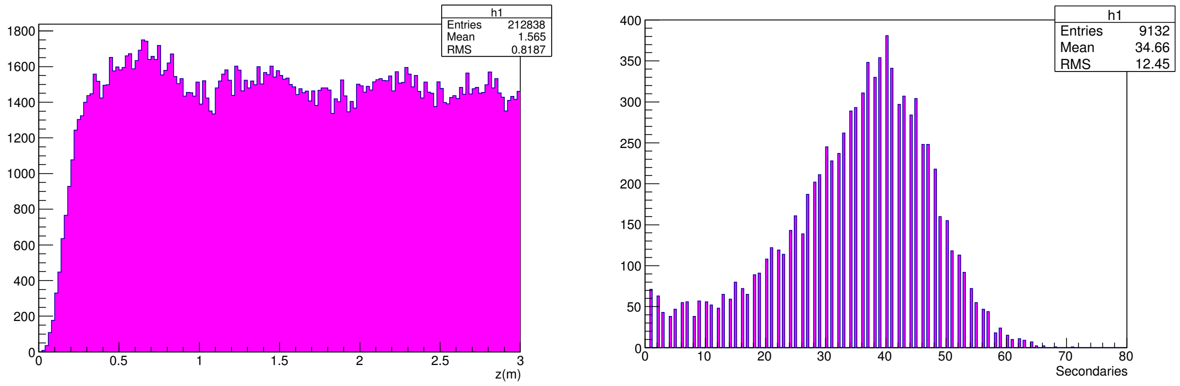

(a) The position in z of the exiting charged secondaries

(b) The number of charged secondaries per incident Bhabha positron exiting the beam pipe

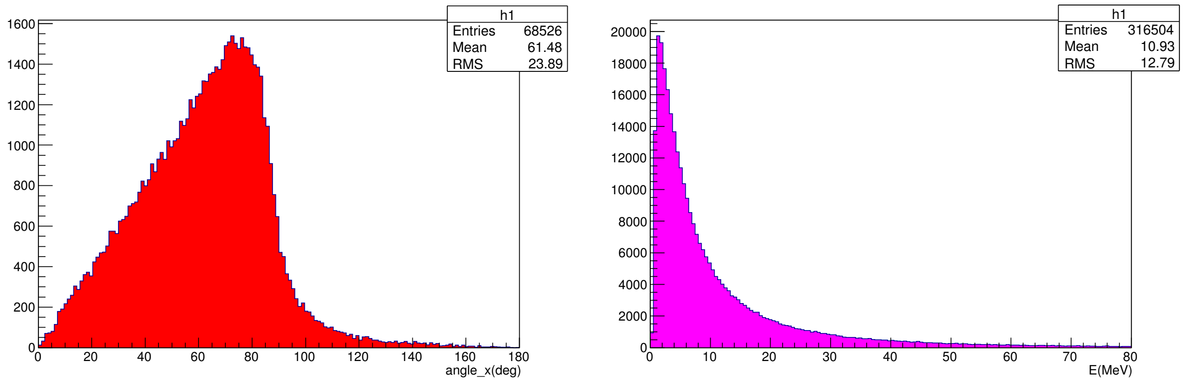

(c) The transverse angular profile of the exiting secondaries

(d) The energy spectrum of the exiting secondaries

Figure 8.16 – Dynamics of the secondaries exiting 6 mm thick Titanium beam pipe

8.3.1 Precision of $\mathcal{L}$ evaluation

The best precision is obtained also for a 1 mm thick Titanium beam pipe and with a DS at 90° (2% in phase 2 (l.h.s of fig. 8.17) and 6.3×10^{-3} in phase 3 (r.h.s of fig. 8.17)). The precision is 5 times better in the case of the window and the radiator compared to 1 mm thick Ti beam pipe.

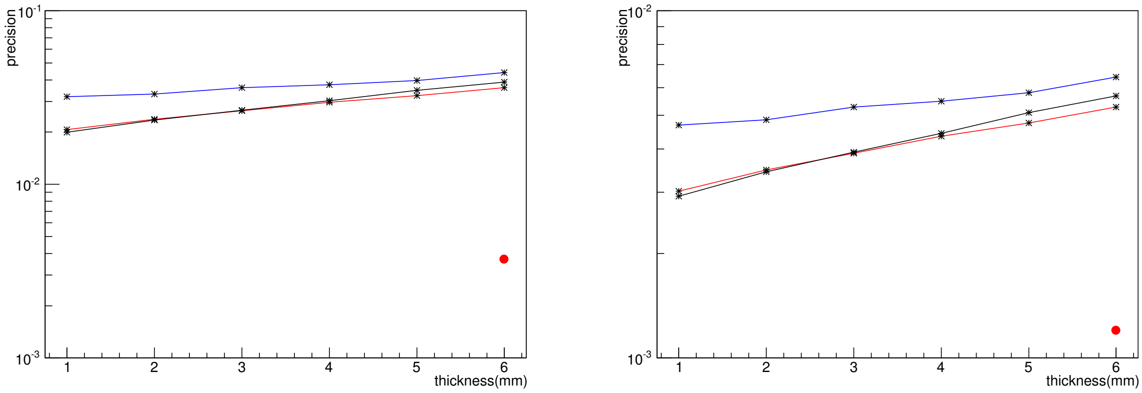

Figure 8.17 – Precision in 1 ms on the luminosity as a function of the thickness of the beam pipe for DS at 0° (blue), DS at 45° (red) and DS at 90° (black) compared to the window + radiator (red spot) in phase 2 on l.h.s and in phase 3 on r.h.s

8.4 Beryllium

The dynamics of the secondaries exiting the 6 mm thick Beryllium beam pipe are shown in fig. 8.18. Beryllium has the longest radiation length (X_{Be}=35.28 cm) and the smallest atomic number (Z=4), which reduces the absorption of the shower, and thus more secondaries exit the beam pipe.

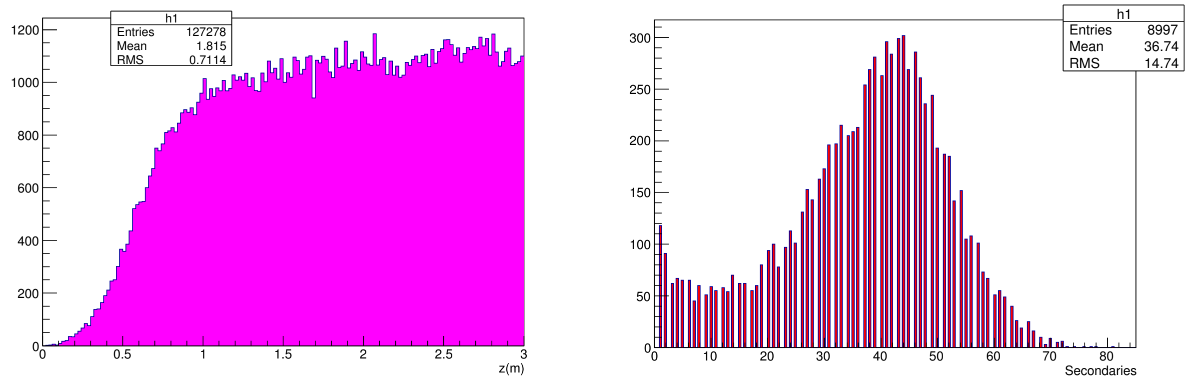

(a) The position in z of the exiting charged secondaries

(b) The number of charged secondaries per incident Bhabha positron exiting the beam pipe

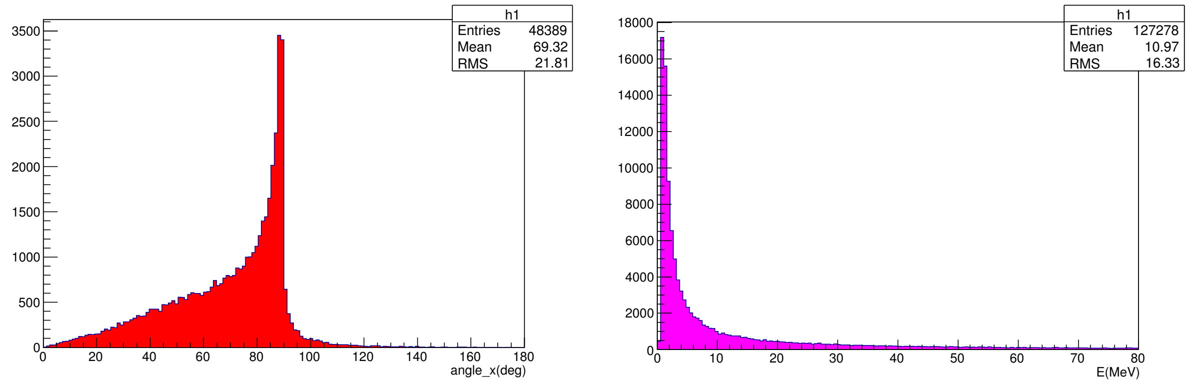

(c) The transverse angular profile of the exiting secondaries

(d) The energy spectrum of the exiting secondaries

Figure 8.18 – Dynamics of the secondaries exiting 6 mm thick Beryllium beam pipe

8.4.1 Precision of $\mathcal{L}$ evaluation

The precision is shown as function of thickness of the Beryllium beam pipe in phase 2 (l.h.s of fig. 8.19) and phase 3 (r.h.s of fig. 8.19). The best precision is for a 1 mm thick beam pipe with a DS at 90°. The factor of improvement of the case of a window and radiator compared to the case of 1 mm thick Be beam pipe is 3.5.

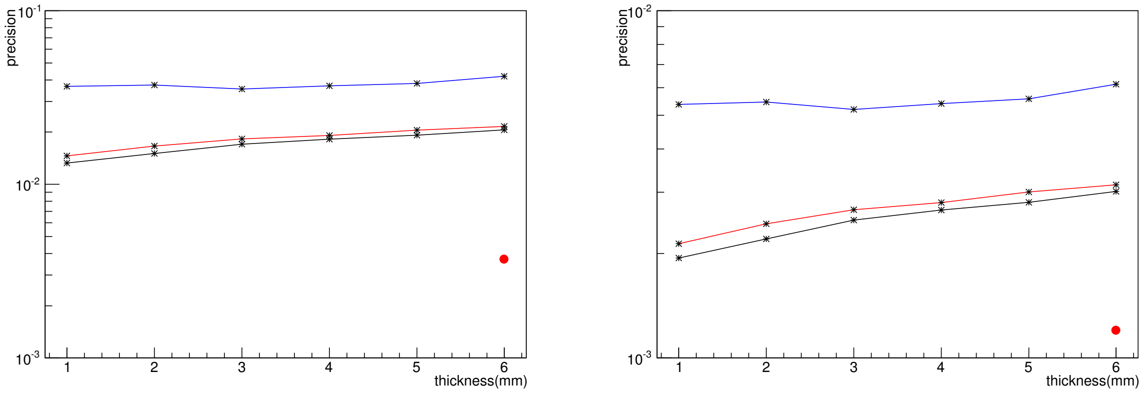

Figure 8.19 – Precision in 1 ms on the luminosity as a function of the thickness of the beam pipe for DS at 0° (blue), DS at 45° (red) and DS at 90° (black) compared to the window + radiator (red spot) in phase 2 on l.h.s and in phase 3 on r.h.s

8.5 Comparison between different designs and final choice

In fig. 8.20, 8.21 and 8.22, the precision of $\mathcal{L}$ evaluation, evaluated for four materials (Cu, Ti, Al, Be), as a function of the thickness of the beam pipe during phases 2 and 3, for the different orientations of the DS at 0°, 45° and 90°, are compared. The red dot indicates the precision expected using the window insertion and a radiator (see chapter 3).

The best precision obtained among materials is with a Beryllium beam pipe of 1 mm thickness and a DS oriented at 90°. This precision (1.3% in phase 2 and 4.1×10^{-3} in phase 3) is still far from the aimed precision. The window with radiator shows the best precision among all the designs of the beam pipe (3.7×10^{-3} in phase 2 and 1.2×10^{-3} in phase 3).

After showing the results of all the simulations done to the vacuum group at KEK, it has been decided to fabricate the 6 mm Cu window at 45°, to be installed in the drift at 11 m downstream of the IP for the phase 2 of SuperKEKB.

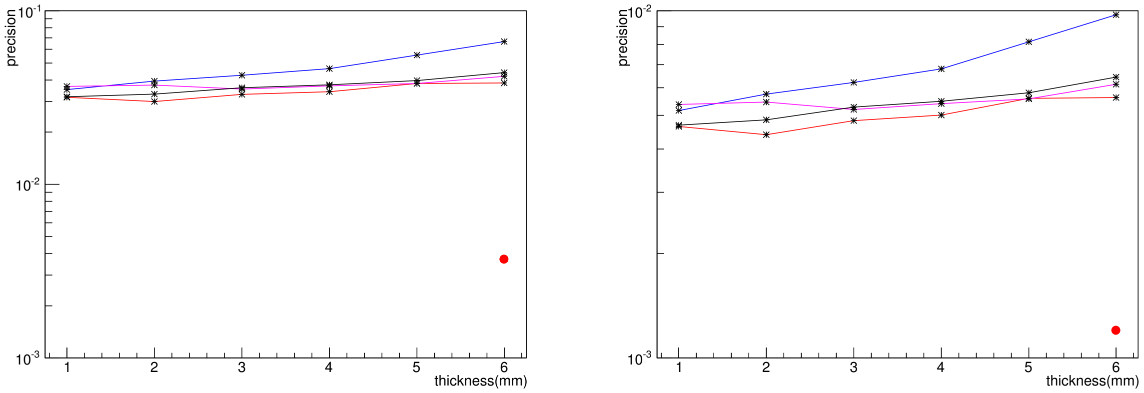

Figure 8.20 – Precision in 1 ms on the luminosity as a function of the thickness of the beam pipe for the four different materials, Cu (blue), Ti (black), Al (red), Be (magenta) and window+radiator (red spot), for a DS at 0°, in phase 2 on l.h.s and in phase 3 on r.h.s

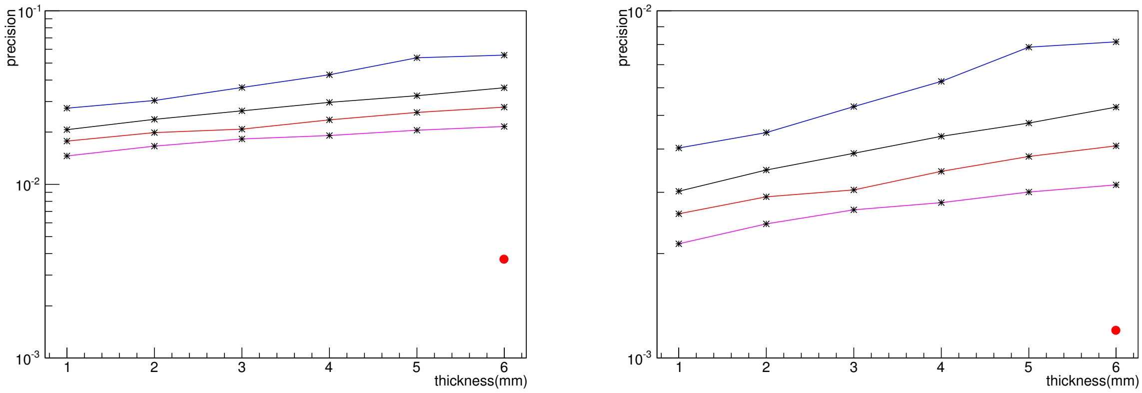

Figure 8.21 – Precision in 1 ms on the luminosity as a function of the thickness of the beam pipe for the four different materials, Cu (blue), Ti (black), Al (red), Be (magenta) and window+radiator (red spot), for a DS at 45°, in phase 2 on l.h.s and in phase 3 on r.h.s

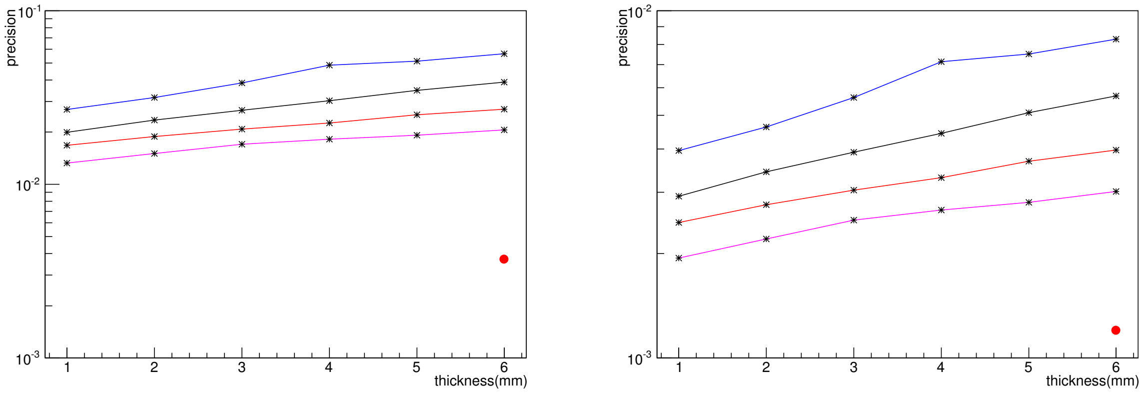

Figure 8.22 – Precision in 1 ms on the luminosity as a function of the thickness of the beam pipe for the four different materials, Cu (blue), Ti (black), Al (red), Be (magenta) and window+radiator (red spot), for a DS at 90°, in phase 2 on l.h.s and in phase 3 on r.h.s

Bibliography

[1] F. Abe et al, “Observation of Top Quark Production in $\bar{p}$p Collisions with the Collider Detector at Fermilab”, Phys. Rev. Lett. 74, 2626 (Cited on page 1.)

[2] T. Patzak, “First direct observation of the tau neutrino”, Europhysics news, 2001 (Cited on page 1.)

[3] The ATLAS collaboration, “A Particle Consistent with the Higgs Boson Observed with the ATLAS Detector at the Large Hadron Collider”, Science 21 Dec 2012, Vol. 338, Issue 6114, pp. 1576-1582 (Cited on page 1.)

[4] The CMS collaboration, “Observation of a new boson at a mass of 125 GeV with the CMS experiment at the LHC”, Phys. Lett. B 716 (2012) 30 (Cited on page 1.)

[5] Mike Koratzinos, “FCC-ee accelerator parameters, performance and limitations” (Cited on page 2.)

[6] https://en.wikipedia.org/wiki/Circular_Electron_Positron_Collider (Cited on page 2.)

[7] https://en.wikipedia.org/wiki/Compact_Linear_Collider (Cited on page 2.)

[8] Y. Ohnishi et al, “Accelerator design at SuperKEKB”, Prog. Theor. Exp. Phys. 2013, 03A011, DOI: 10.1093/ptep/pts083 (Cited on page 5.)

[9] T. Abe et al, Belle II Technical Design Report, arXiv:1011.0352 [physics.ins-det], Oct. 2010. (Cited on page 5.)

[10] N. Ohuchi et al, “Design of the superconducting magnet system for the SuperKEKB interaction region”, WEODA1, Proceedings of PAC2013, Pasadena, CA USA (Cited on pages 6, 8 and 143.)

[11] M. Yoshida et al, “Generation and acceleration of low-emittance, high-current electron beams for SuperKEKB, MOIOB03, proceedings of LINAC2014, Geneva, Switzerland. (Cited on page 7.)

[12] T. Natsui et al, “Quasi-travelling wave side coupled RF gun commissioning for SuperKEKB”, MOPRI033, proceedings of IPAC14, Dresden, Germany. (Cited on page 7.)

[13] X. Zhou et al, “Neodymium and Ytterbium hybrid solid laser of RF gun for SuperKEKB”, THPMY041, proceedings of IPAC2016, Busan, Korea. (Cited on page 8.)

[14] Satoh et al, “Commissioning status of SuperKEKB injector linac”, THPOY027, proceedings of IPAC2016, Busan, Korea. (Cited on page 8.)

[15] T. Kamitani et al, “SuperKEKB positron source construction and status”, MOPRI004, proceedings of IPAC2014, Dresden, Germany. (Cited on page 8.)

[16] L. Zang et al, “SuperKEKB positron source target protection scheme”, MOPFI017, proceedings of IPAC2013, Shanghai, China. (Cited on page 8.)

[17] L. Zang et al, “Design, manufacture and operation of the beam spoiler for positron target protection”, MOPRI002, proceedings of IPAC2014, Dresden, Germany. (Cited on page 8.)

[18] L. Zang et al, “Design optimization of flux concentrator for SuperKEKB”, TUPPD032, proceedings of IPAC2012, New Orleans, Louisiana, USA. (Cited on page 8.)

[19] S. Matsumoto et al, “Large-aperture Travelling-wave accelerator structure for positron capture of SuperKEKB injector linac”, THPRI047, proceedings of IPAC2014, Dresden, Germany. (Cited on page 9.)

[20] M. Kikuchi et al, “Design of positron damping ring for Super-KEKB”, TUPEB054, proceedings of IPAC10, Kyoto, Japan. (Cited on page 10.)

[21] M. Kikuchi, “Reverse-bend FODO lattice applied to damping ring for SuperKEKB”, Nuclear Instrumentation and Methods in Physics Research A 556 (2006) 13-19 (Cited on page 10.)

[22] M. Satoh et al, “Commissioning status of SuperKEKB injector linac”, THPOY027, proceedings of IPAC16, Busan, Korea. (Cited on page 10.)

[23] H. Kaji, “Upgrade of event timing system at SuperKEKB”, THCOCA04, proceedings of ICALEPCS2013, San Francisco, CA, USA. (Cited on page 11.)

[24] Y. Suetsugu, “Present Status of the SuperKEKB Vacuum System”, 21^{st} KEKB review, June 2016, KEK, Tsukuba, Japan. (Cited on page 12.)

[25] Y. Susaki, “Electron cloud instability in SuperKEKB Low Energy Ring”, TUPEB014, proceedings of IPAC’10, Kyoto, Japan. (Cited on page 12.)

[26] Kazuhito Ohmi and Demin Zhou, “Study of electron cloud effects in SuperKEKB”, TUPRI012, proceedings of IPAC’14, Dresden, Germany. (Cited on page 12.)

[27] k. Shibata, “SuperKEKB Vacuum System”, KEK, Tsukuba, Japan. (Cited on page 12.)

[28] M. Venturini and W. Kozanecki, “Hourglass effect and the measurement of the transverse size of colliding beams by luminosity scans”, Stanford Linear Accelerator Center, Stanford University, Stanford, CA 94309, SLAC PUB 8699, November 2000 (Cited on page 13.)

[29] SuperB collaboration, “SuperB Technical Design Report”, INFN-13-01/PI, LAL 13-01, SLAC-R-1003, arXiv:1306.5655v1 (Cited on page 14.)

[30] Boqun Wang, “The Belle II experiment and SuperKEKB upgrade”, 10^{th} International Workshop on e^+e^- collisions from ϕ to ψ (Cited on page 15.)

[31] S. Tanaka, H. Nakayama, Y. Funakoshi, T. Browder, I. Jaegle, S. Vahsen, D. Cinabro, F.H. Lin, M.Z. Wang, C. Marinas, “BEAST II Technical Design Report DRAFT For use in US Belle II Project TDR”, 31 May 2013 (Cited on page 16.)

[32] H. Nakayama, “BEAST phase 1”, KEKB review committee, June 2016, KEK, Tsukuba, Japan (Cited on pages 16, 18 and 143.)

[33] Y. Funakoshi et al, “Interaction Point Orbit Feedback System at SuperKEKB”, proceedings IPAC 2015, Richmond, Virginia, United States. (Cited on page 19.)

[34] T. Hirai, S. Uehara and Y. Watanabe, ”Real-time luminosity monitor for a B-factory experiment, *”Nuclear Instruments And Methods In Physics Research, Section A”*, 11 Feb. 2001. (Cited on page 19.)

[35] https://en.wikipedia.org/wiki/Nyquist−Shannon_sampling_theorem (Cited on page 21.)

[36] https://www.wolfram.com/mathematica/ (Cited on page 21.)

[37] Private discussion with S. Uehara, July 2016. (Cited on page 21.)

[38] https://en.wikipedia.org/wiki/Lock-in_amplifier (Cited on page 21.)

[39] Markus Friedl, Diploma thesis, “Diamond Detectors for Ionizing Radiation”, University of Technology, Vienna (Cited on page 24.)

[40] https://cividec.at/ (Cited on page 26.)

[41] S. Liu, thesis diploma, “Development of Diamond Sensors for Beam Halo and Compton Spectrum Diagnostics after the Interaction Point of ATF2”, LAL, university of Paris Sud, Orsay, France. (Cited on pages 31 and 144.)

[42] J. Brossard et al, “PHIL Accelerator at LAL - Diagnostic status”, Proceedings of BIW10, Santa Fe, New Mexico, US, May 2-6 2010 (Cited on page 33.)

[43] D. Attie, S. Barsuk, O. Bezshyyko, L. Burmistrov, A. Chaus, P. Colas, O. Fedorchuk, L. Golinka-Bezshyyko, I.Kadenko, V. Krylov, V. Kubytskyi, R. Lopez, H. Monard,V. Rodin, M. Titov, D. Tomassini, A. Variola, “LEETECH facility as a flexible source of low energy electrons”, arxiv:1601.04348, Instrumentation and Detectors. (Cited on page 33.)

[44] V. Kubytskyi et al, “DIAMOND SENSOR RESOLUTION IN SIMULTANEOUS DETECTION OF 1,2,3 ELECTRONS AT THE PHIL PHOTOINJECTOR FACILITY AT LAL”, proceedings of IPAC16, Busan, South Korea, May 2016 (Cited on page 34.)

[45] D. Schulte Ph. D. Thesis, University of Hamburg 1996. TESLA-97-08 (Cited on page 37.)

[46] G. Le Meur et al., Univ . Paris-Sud, CNRS/IN2P3, Orsay, France.
D. Schulte, CERN, Geneva, Switzerland.
Description of guineapig++, the C++ upgraded version of the GUINEA-PIG beam-beam simulation program (Cited on page 37.)

[47] http://acc-physics.kek.jp/SAD/ (Cited on page 38.)

[48] http://geant4.web.cern.ch/geant4/ (Cited on page 43.)

[49] Y. Funakoshi, “Overview of Phase 1 Commissioning”, 21st KEKB review, 13 June 2016, http://www-kekb.kek.jp/MAC/2016/ (Cited on pages 59, 61, 69, 70 and 146.)

[50] H. Ikeda et al, “Beam loss monitor at SuperKEKB”, TUPD22, proceedings of IBIC2014, Monterey, CA, USA (Cited on pages 63, 65 and 146.)

[51] Y. Suetsugu et al, “First commissioning of the SuperKEKB vacuum system”, TUOCB01, proceedings of IPAC2016, Busan, Korea (Cited on pages 65, 66 and 146.)

[52] Y. Suetsugu, “First commissioning of the SuperKEKB vacuum system”, presentation TUOCB01, IPAC 2016, Busan, Kurea (Cited on pages 66, 69 and 146.)

[53] J. Wei et al, “Electron- cloud effects in high-intensity proton accelerators”, Brookhaven National Laboratory (Cited on page 66.)

[54] J. Flanagan et al, “Observation of vertical betatron sideband due to electron clouds in the KEKB LER”, Phys.Rev.Lett. 94 (2005) 054801. (Cited on page 68.)

[55] K. Ohmi, oral presentation “Instabilities simulation and observation”, 21th KEKB accelerator review committee, June 2016, KEK, Tsukuba, Japan. (Cited on page 68.)

[56] H. Fukuma et al, “Beam instrumentation for the SuperKEKB rings”, MOCB01, proceedings of IBIC2012, Tsukuba, Japan. (Cited on page 68.)

[57] M. Iwasaki et al, “Evaluation of the detector BG for SuperKEKB”, Proceedings of IPAC’10, Kyoto, Japan. (Cited on page 71.)

[58] H. Nakayama, M. Iwasaki, K. Kanazawa, H. Nakano, Y. Ohnishi, S.Tanaka, T. Tsuboyama, “Beam background and MDI design for SuperKEKB/BELLE-II”, Proceedings of IPAC2012, New Orleans, Louisiana, USA. (Cited on pages 71 and 74.)

[59] H. Nakayama, Y. Funakoshi, Y. Ohnihsi, K. Kanazawa, T. Ishibashi,“SuperKEKB background simulation, including issues for detector shielding”, Proceedings of HF2014, Beijing, China (Cited on pages 71 and 146.)

[60] https://en.wikipedia.org/wiki/Radiation_damping (Cited on page 73.)

[61] J. Le Duff, “Single and multiple Touschek effects”, Laboratoire de l’Accélérateur Linéaire, Orsay, France. (Cited on page 73.)

[62] S. Y. Lee, “Accelerator Physics” second edition, Chapter 4 “Physics of electron storage rings” section II “Beam lifetime”, department of physics, Indiana university. (Cited on pages 73, 74 and 146.)

[63] Y. Ohnishi, Private Communication. (Cited on page 74.)

[64] Y. Funakoshi, presentation “some considerations on beam background after beam injection”, IN2P3-KEK collaboration on Belle-II and BEAST meeting, 19-20 January 2015. (Cited on page 94.)

[65] M.L. Taylor, B. Dalton a, R.D. Franich, “The Schiff angular bremsstrahlung distribution from composite media”, Nuclear Instruments and Methods in Physics Research B 293 (2012) 1-5 (Cited on page 95.)

[66] Y. Suetsugu, Private communication, June 2016
Ken-ichi Kanazawa et al, “Experience of Operating the Large Vacuum System of the KEKB Collider”
Ken-ichi Kanazawa et al, “ Experiences at the KEK B-factory vacuum system”, Prog. Theor. Exp. Phys. 2013, 03A005, DOI: 10.1093/ptep/pts068 (Cited on page 104.)

List of Figures

2.1 Luminosity at SuperKEKB compared to other colliders 6
2.2 Layout of SuperKEKB/Belle II experiment 7
2.3 The final focus Superconducting magnet system at SuperKEKB [10] . . 8
2.4 The RF gun on l.h.s and the photocathode on r.h.s, at SuperKEKB . . . 9
2.5 The scheme of positron source on l.h.s and the large aperture S-band accelerating structure at SuperKEKB on r.h.s 9
2.6 Electron/positron separator chicane at SuperKEKB 10
2.7 The layout of the damping ring at SuperKEKB 11
2.8 The layout of the SuperKEKB injector linac 12
2.9 The concept of antechamber on l.h.s and the antechambers for wigglers on r.h.s at SuperKEKB 13
2.10 The nano beam scheme at SuperKEKB 14
2.11 The layout of the Belle II detector 16
2.12 The layout of the BEAST II in the interaction region of SuperKEKB at phase 1 18
2.13 The list of sub detectors of BEAST II [32] 18

3.1 Example of Ante-chamber asymmetric dithering coil at SuperKEKB . . . 20
3.2 Single crystalline diamond sensor (sCVD) on l.h.s and the Cherenkov and Scintillator detectors on r.h.s 20
3.3 The dithering parameters on the luminosity profile 22
3.4 The luminosity signal in the luminosity monitor from Monte-Carlo simulation at a given counting rate and dithering with modulation amplitude “p” 22
3.5 The FFT of the square root of the measured luminosity profile with a peak at the double frequency ($2\times f_0$) on l.h.s and a peak at the baseline frequency (f_0) on the r.h.s 22
3.6 The profile of the signal size at p=0.2 and rate=400 KHz per 1 ms of the baseline frequency on l.h.s and the double frequency on r.h.s 23
3.7 The diamond lattice 24
3.8 The readout circuit on l.h.s and the operation scheme of the diamond sensor on r.h.s 26
3.9 Landau distribution of energy deposited by MIPs in 500 μm diamond sensor simulated by GEANT4 26
3.10 The experimental setup of the tests on the diamond sensor in the clean room 27
3.11 140 μm CIVIDEC diamond sensor on l.h.s and the CIVIDEC charge amplifier on r.h.s 28

3.12 Low voltage supply for the charge amplifier on l.h.s and high voltage supply for the diamond sensor on r.h.s 28
3.13 The ^{90}Sr decay scheme 29
3.14 Screenshots from the oscilloscope, pink: 140μm diamond and yellow: scintillator, diamond signal in the tail of Landau on l.h.s and diamond signal close to the maximum of Landau on r.h.s 29
3.15 Landau reconstruction of 140 μm sCVD on l.h.s and noise reconstruction of the charge amplifier on r.h.s in case of triggering on all events in the DS 30
3.16 Signal and noise amplitude distributions in the 500μm diamond sensor [41] 31
3.17 Landau reconstruction of 140 μm sCVD on l.h.s and noise reconstruction of the charge amplifier on r.h.s in the case of multistage trigger 31
3.18 Landau reconstruction of the signal from 500 μm sCVD on l.h.s and the width of the signal of the 500 μm sCVD on the r.h.s in the case of multistage trigger 32
3.19 Position of the maximum of the signals in the 500 μm sCVD on l.h.s and in the scintillator on r.h.s 32
3.20 Difference of the position of the maximum of the diamond and scintillator 33
3.21 The maximum of the signal as a function of its position in time in the sCVD on l.h.s and as function of its width on r.h.s 33
3.22 The PHIL accelerator design 34
3.23 The LEETECH facility design 34
3.24 The maximum of the signal in the sCVD on l.h.s and the position in time of the maximum of laser signal at PHIL on r.h.s 35
3.25 Difference of the time position of the diamond and laser signals 35
3.26 Radiative Bhabha process at zero photon scattering angle 36
3.27 Deflected Bhabha particles after optical elements downstream of the IP at SuperKEKB 36
3.28 The energy distribution of Bhabha positrons on l.h.s and of Bhabha electrons on r.h.s 37
3.29 Angular distributions of Bhabha positrons in the horizontal plane on l.h.s and in the vertical plane on the r.h.s 38
3.30 Angular distributions of Bhabha electrons in the horizontal plane on l.h.s and in the vertical plane on r.h.s 39
3.31 Accelerated beam in a bending magnet 39
3.32 Transverse distribution in x and y of beam positrons (blue) and Bhabha positrons (red) after third and fourth bending magnets 40
3.33 The horizontal position distribution of Bhabha positrons as a function of their energies, after third and fourth bending magnets 41
3.34 Energy distribution of Bhabha positrons which are already lost (green), detectable in the DS (blue) and still remaining in the beam pipe (red) after the third bend (BLC1LP2) and fourth bend (BLC2LP) 41

3.35 Beta functions and dispersion functions over first 27 m downstream the IP for the LER . . . 42
3.36 The horizontal position distribution of Bhabha positrons as function of their energies after first and second bending magnets . . . 43
3.37 The x-E distribution of the Bhabha positrons on l.h.s and the energy distribution of Bhabha positrons which are already lost (green), detectable in the DS (blue) and still remaining in the beam pipe (red) on r.h.s, in the drift at 13.9 meters . . . 44
3.38 Energy spectrum on l.h.s and exiting angle distribution on r.h.s of the lost Bhabha particles in the drift after QKBLP . . . 45
3.39 The 3D plot of the charged secondary particles resulting from the interaction of the exiting Bhabha positrons with the 6 mm thick Cu cylindrical beam pipe . . . 46
3.40 The transverse angular distribution of the exiting charged secondaries from the 6 mm Cu beam pipe . . . 46
3.41 Illustration of an electromagnetic shower of a Bhabha positron exiting the 6 mm Cu beam pipe and of the parallel and perpendicular positioning of the DS (violet) . . . 47
3.42 The fraction f of exiting Bhabha positrons with a detectable signal in the DS for a parallel sensor (blue) and perpendicular sensor (red) as a function of the distance from the beam pipe . . . 47
3.43 Precision on luminosity in 1 ms in phase 2 ($\mathcal{L}$=10^{34}cm^{-2}s^{-1}) on l.h.s and in phase 3 ($\mathcal{L}$=8 x 10^{35}cm^{-2}s^{-1}) on r.h.s . . . 47
3.44 The design of the window at 45° suggested by K. Kanazawa . . . 48
3.45 The number of exiting charged secondaries per 1000 incident positrons crossing a given thickness of Cu beam pipe . . . 48
3.46 The development of the shower in the radiator on l.h.s and the simulated window with an iron radiator at its shower maximum on r.h.s . . . 49
3.47 The energy spectrum of the particles exiting the window and the radiator 49
3.48 The energy of the incident particles giving signal in the centred 5x5 mm^2 DS (blue) and with no signal (red) in the case of the window with a radiator 50
3.49 Histograms of the number of charged secondaries in the DS per incident exiting Bhabha positron for a window with radiator on l.h.s and for a window without a radiator on r.h.s . . . 50
3.50 The β and dispersion functions of the lattice of the HER up to 24 meters downstream of the IP . . . 53
3.51 The energies of the Bhabha electrons as a function of their transverse position x after first bending magnet (l.h.s) and second bending magnet (r.h.s) . . . 53

3.52 The energies of the Bhabha electrons as a function of their transverse position (x) after third bending magnet (l.h.s) and fourth bending magnet (r.h.s) . . . 54
3.53 The energies of the Bhabha electrons as a function of their transverse position x in the drift at 20 m (l.h.s) and at 15.6 m (r.h.s) . . . 54
3.54 The energy spectrum of Bhabha photons in the HER on l.h.s and their horizontal angle distribution on r.h.s . . . 55
3.55 The distance from the IP at which the photons exit the HER beam pipe 56
3.56 The lattice of the HER where the γ spot hits, showing the free spaces for the luminosity monitors . . . 56
3.57 The distances at which the Bhabha photon spot hits the vacuum chamber in the HER . . . 57

4.1 History of the vacuum scrubbing in SuperKEKB during phase 1, in the LER on l.h.s and in the HER on r.h.s . . . 60
4.2 The position of collimators in SuperKEKB rings during phase 1 . . . 61
4.3 The physical vertical emittance in the LER during phase 1 after several corrections [49] . . . 61
4.4 Loss monitor system at SuperKEKB . . . 64
4.5 PIN diodes at SuperKEKB, around the collimator [50] on l.h.s and near a bellow [50] on r.h.s . . . 65
4.6 The cross section of the ion chamber at SuperKEKB [50] . . . 65
4.7 The electron current measured in the LER as a function of the beam current for different types of the beam pipe [51] . . . 66
4.8 The non-linear pressure rise at nine different gauges at the arc section as a function of beam current in LER . . . 67
4.9 A solenoid magnet on l.h.s and a permanent magnet on r.h.s at an aluminium bellow at SuperKEKB . . . 68
4.10 The pressure rise against the beam current, at the 30 m bellow section before and after applying the solenoidal magnetic fields on l.h.s and in two arc sections before and after the installation of 800 permanent magnets around the aluminium bellows in the arc section on r.h.s [52] . . . 69
4.11 The vertical beam size in the LER as a function of the total beam current for different bucket spacing, before the installation of permanent solenoids at the Al bellows on l.h.s and after the installation of permanent solenoids at the Al bellows on r.h.s [49] . . . 70

5.1 Backgrounds at the interaction region (Belle II) [59] . . . 71
5.2 Bremsstrahlung scattering of a charged particle in the field of the nucleus of an atom . . . 72
5.3 Touschek scattering in the CMS [62] . . . 74

5.4 The energy spectrum of Bremsstrahlung positrons lost in the drift on l.h.s and their energy as a function of their scattering position on r.h.s in case a (scattering at the entrance of quadrupoles and special vertical bends) . 75
5.5 The LER lattice from 50 meters upstream to 11 meters downstream from the IP 76
5.6 The energy spectrum of Bremsstrahlung positrons lost in the drift on l.h.s and their energy as a function of their scattering position on r.h.s in case b (scattering at the entrance of all elements) 76
5.7 Example of slicing of bending magnets: horizontal (yellow) and vertical (red), and drifts (grey) between IP and the drift (included) 77
5.8 The energy spectrum of Bremsstrahlung positrons lost in the drift on l.h.s and their energy as a function of their scattering position on r.h.s in case c (scattering at all the elements after slicing the bending magnets and the drifts) 77
5.9 The total loss from Beam-gas Bremsstrahlung overall the ring as a function of the scattering resolution on l.h.s and the percentage of loss in the drift with respect to the resolution of 10 cm as a function of scattering resolution on r.h.s 78
5.10 The energy of the lost Bremsstrahlung positrons in the drift as a function of their loss position on l.h.s and as a function of their horizontal exiting angle on r.h.s 79
5.11 The 3D distribution of the charged secondaries exiting the 6 mm thick Cu beam pipe on l.h.s and their energy spectrum on r.h.s 79
5.12 The horizontal angular distribution of charged secondary particles exiting the 6 mm Cu cylinder beam pipe on l.h.s and their number per incident particle on r.h.s 80
5.13 Histogram of number of secondaries deposited in the DS by each incident particle 80
5.14 The behaviour of the losses detected in the DS as a function of the product of beam current and vacuum pressure 81
5.15 The energy of the lost Touschek positrons in the drift as a function of their scattering position on l.h.s and as a function of their exiting horizontal angle on r.h.s 82
5.16 The β function in the LER between 50 m upstream the IP and the IP . . 82
5.17 The percentage of the energy variation due to Touschek scattering computed from eq. 5.2, between the scattering regions extending 50 meters upstream the IP and the IP 83
5.18 The 3D distribution of the charged secondaries resulting from the interaction of the incident lost positrons with the 6 mm Cu cylinder beam pipe on l.h.s and their number per incident particle on r.h.s 83

5.19 Histogram of number of secondaries deposited in the DS by each incident particle . . . 84
5.20 The behaviour of the loss from Touschek scattering in 10 ms in the DS as a function of the beam current . . . 84
5.21 The horizontal exiting angles on l.h.s and the vertical exiting angles on r.h.s, of the lost Coulomb scattered positrons in the drift . . . 85
5.22 3D distribution of the position of the charged secondaries exiting the 6 mm Cu cylinder beam pipe . . . 86
5.23 The square root of the horizontal β function (blue) and the vertical β function (red) at the scattering positions up to $\approx$ 100 meters upstream from the IP until the drift at $\approx$ 11 meters . . . 86
5.24 The scattering positions of the Coulomb positrons lost in the DS in the drift 87

6.1 The pillar in the HER at 30 meters downstream of the IP holding the two sCVDs and the ZDLM monitors . . . 90
6.2 The pillar in the HER at 11.9 meters downstream of the IP holding the two sCVDs and the ZDLM monitors . . . 91
6.3 The two sCVDs connected to a charge amplifier each to be installed in the LER on l.h.s and in the HER on r.h.s . . . 92
6.4 Half inch heliax cables with the connectors on l.h.s and connections being done at B4 level in Tsukuba hall on r.h.s . . . 93
6.5 The layout of the Tsukuba hall showing the Belle II detector with its Electronics-Hut and the paths for our cables in the LER and the HER . 93
6.6 Our electronic rack in the E-Hut of the Belle II detector of the SuperKEKB experiment . . . 94
6.7 An image of the oscilloscope during the acquisition with (LER2(yellow), HER2(green)) . . . 95
6.8 Landau distribution of deposited charge of incident particles from simulations in GEANT4 on l.h.s and from data on r.h.s . . . 96
6.9 Loss rate in the sCVD in 10 ms on l.h.s and beam current in the LER on r.h.s as function of time . . . 97
6.10 The loss rate in 10 ms in the sCVD in LER as a function of beam current on l.h.s and as a function of vacuum pressure on r.h.s . . . 97
6.11 The distribution of the peak values of the signals collected by the Cherenkov sensor . . . 98
6.12 The loss distributions in 10 ms in the sCVD (blue) and Cherenkov detector (red) for an average beam current of 703 mA and average vacuum pressure of 7.6 nTorr in the LER . . . 98
6.13 The vacuum sections overall the LER at SuperKEKB . . . 100

6.14 The profile of the average pressure at D02 section on l.h.s and the profile of the losses in the sCVD (LER2) on r.h.s during the successive vacuum bumps in the subsections (L26,L25) and (L24,L23) of the D02 section . . 100
6.15 The profile of the average pressure at D02 on l.h.s and the profile of the losses in 10 ms in the sCVD on r.h.s during the vacuum bump between 35 m and 70 m upstream from the IP in the LER 101
6.16 The beam current profile in the LER during the vacuum bump between 35 and 70 meters upstream from the IP 101
6.17 Vacuum pressure in the subsection L25 on l.h.s and in L26 on r.h.s, between 4 and 12 meters upstream from the IP 102
6.18 Vacuum pressure in the subsection L23 on l.h.s and in L24 on r.h.s, between 17 and 35 meters upstream from the IP 102
6.19 Beam current on l.h.s and vertical beam size in the LER on r.h.s during the Touschek study 103
6.20 Fit of the losses in the sCVD as a function of the inverse of the vertical beam size at 180 mA on l.h.s and at 360 mA on r.h.s 104
6.21 Fit of the losses in the sCVD as a function of the inverse of the vertical beam size at 540 mA on l.h.s and at 720 mA on r.h.s 104
6.22 Fit of the losses in the sCVD as a function of the inverse of the vertical beam size at 900 mA on l.h.s and at 1000 mA on r.h.s 105
6.23 Losses from beam-gas Bremsstrahlung in the sCVD in the LER as a function of the product of the beam current and the vacuum pressure, from data (red) and simulation (blue) on l.h.s and the fraction of the losses from beam-gas Bremsstrahlung in data and simulation 107
6.24 The relative loss in the sCVD as a function of the relative vertical beam size for the beam currents of 180 mA on l.h.s and 360 mA on r.h.s 107
6.25 The relative loss in the sCVD as a function of the relative vertical beam size for the beam currents of 540 mA on l.h.s and 720 mA on r.h.s 108
6.26 The relative loss in the sCVD as function of the relative vertical beam size for the beam currents of 900 mA on l.h.s and 1000 mA on r.h.s 108
6.27 The relative loss from Touschek as a function of the relative inverse vertical beam size from simulations at I= 1000 mA 109
6.28 The simulated losses from Touschek scattering as a function of the inverse vertical beam size at I= 1000 mA 109

8.1 Dynamics of the secondaries exiting 6 mm thick Copper beam pipe . . . 116
8.2 Histograms of the number of charged secondaries in the DS per incident exiting Bhabha positron for different orientations of the DS at 6 mm thick Copper beam pipe 117
8.3 Dynamics of the secondaries exiting 5 mm thick Copper beam pipe . . . 118

8.4 Histograms of the number of charged secondaries in the DS per incident exiting Bhabha positron for different orientations of the DS at 5 mm thick Copper beam pipe . . . 119

8.5 Dynamics of the secondaries exiting 4 mm thick Copper beam pipe . . . 120

8.6 Histograms of the number of charged secondaries in the DS per incident exiting Bhabha positron for different orientations of the DS at 4 mm thick Copper beam pipe . . . 121

8.7 Dynamics of the secondaries exiting 3 mm thick Copper beam pipe . . . 122

8.8 Histograms of the number of charged secondaries in the DS per incident exiting Bhabha positron for different orientations of the DS at 3 mm thick Copper beam pipe . . . 123

8.9 Dynamics of the secondaries exiting 2 mm thick Copper beam pipe . . . 124

8.10 Histograms of the number of charged secondaries in the DS per incident exiting Bhabha positron for different orientations of the DS at 2 mm thick Copper beam pipe . . . 125

8.11 Dynamics of the secondaries exiting 1 mm thick Copper beam pipe . . . 126

8.12 Histograms of the number of charged secondaries in the DS per incident exiting Bhabha positron for different orientations of the DS at 1 mm thick Copper beam pipe . . . 127

8.13 Precision in 1 ms on the luminosity as a function of the thickness of the beam pipe for DS at 0° (blue), DS at 45° (red) and DS at 90° (black) compared to the window + radiator (red spot) in phase 2 on l.h.s and in phase 3 on r.h.s . . . 128

8.14 Dynamics of the secondaries exiting 6 mm thick Aluminium beam pipe . 129

8.15 Precision in 1 ms on the luminosity as a function of the thickness of the beam pipe for DS at 0° (blue), DS at 45° (red) and DS at 90° (black) compared to the window + radiator (red spot) in phase 2 on l.h.s and in phase 3 on r.h.s . . . 130

8.16 Dynamics of the secondaries exiting 6 mm thick Titanium beam pipe . . 131

8.17 Precision in 1 ms on the luminosity as a function of the thickness of the beam pipe for DS at 0° (blue), DS at 45° (red) and DS at 90° (black) compared to the window + radiator (red spot) in phase 2 on l.h.s and in phase 3 on r.h.s . . . 132

8.18 Dynamics of the secondaries exiting 6 mm thick Beryllium beam pipe . . 133

8.19 Precision in 1 ms on the luminosity as a function of the thickness of the beam pipe for DS at 0° (blue), DS at 45° (red) and DS at 90° (black) compared to the window + radiator (red spot) in phase 2 on l.h.s and in phase 3 on r.h.s . . . 134

8.20 Precision in 1 ms on the luminosity as a function of the thickness of the beam pipe for the four different materials, Cu (blue), Ti (black), Al (red), Be (magenta) and window+radiator (red spot), for a DS at 0°, in phase 2 on l.h.s and in phase 3 on r.h.s 135
8.21 Precision in 1 ms on the luminosity as a function of the thickness of the beam pipe for the four different materials, Cu (blue), Ti (black), Al (red), Be (magenta) and window+radiator (red spot), for a DS at 45°, in phase 2 on l.h.s and in phase 3 on r.h.s 136
8.22 Precision in 1 ms on the luminosity as a function of the thickness of the beam pipe for the four different materials, Cu (blue), Ti (black), Al (red), Be (magenta) and window+radiator (red spot), for a DS at 90°, in phase 2 on l.h.s and in phase 3 on r.h.s 136

List of Tables

2.1 Comparison between achieved parameters at KEKB and design parameters at SuperKEKB . . . 6
2.2 The machine parameters for a very high luminosity at SuperKEKB . . . 13

3.1 Minimum required fractions of Bhabha cross-section in the sensors 23
3.2 Properties of different solid state detectors at T=300 K . . . 25
3.3 The list of the first four bending magnets downstream of the IP in the LER 40
3.4 Precision on luminosity at different phases of SuperKEKB and different designs . . . 51
3.5 Characteristics of the different materials considered for the design of the vacuum chamber . . . 51
3.6 The list of the first four bending magnets downstream of the IP in the HER 52

6.1 Distances upstream of the IP of subsections where vacuum bumps took place in the D02 section . . . 99
6.2 Comparison between data and simulation of the fraction of losses in the sCVD coming from the different sections during the vacuum bump 102
6.3 Beam-gas Bremsstrahlung in 10 ms in the DS for different beam currents and vacuum pressure in the LER . . . 105
6.4 The slopes of the fit of the relative losses in the DS as a function of relative inverse vertical beam size, along with their errors for six different beam currents in the LER . . . 106